UNIVERSITÀ DEGLI STUDI DI MILANO

Doctorate School in Industrial Chemistry, XXXII cycle

Department of Chemistry

CHIRAL POLYAMIDOAMINO ACIDS WITH POTENTIAL FOR BIOTECHNOLOGICAL APPLICATIONS

CHIM/04

PhD candidate
Federica Lazzari

Tutor: Prof. Elisabetta RANUCCI
PhD course coordinator: Prof. Dominique ROBERTO

Academic year 2019

INDEX

CHAPTER ONE: introduction to synthetic chiral polymers and α-amino acid-based polymers

CHAPTER TWO: pH Dependence and self-assembly of polyamidoamino acids derived from natural α-amino acids

Arginine-based polymers

Alkyl-substituted PAACs

Glutamine-based polymer

CHAPTER THREE: Fluorescent properties and pH dependent self-organization of *D*-, *L*- and *D,L*-Tryptophan based polyamidoamino acids

CHAPTER FOUR: chiral recognition of *D*- and *L*-Arginine derived polyamidoamino acids with pH dependent self-assembled sodium deoxycholate

	Acronym
Acyclic Diene Metathesis	ADMET
Atom Transfer Radical Polymerization	ATRP
(*S*)-Atropisomer of 1,1′-binaphthyl-2,2′-diylhydrogenphosphate	BNDHP
Circular Dichroism	CD
Critical Micelle Concentration	CMC
Chiral Stationary Phases	CSP
Dynamic Light Scattering	DLS
Diffusion-Ordered Spectroscopy	DOSY
Fourier-Transform Infrared Spectroscopy in Attenuated Total Reflectance	FT-IR/ATR
Guanidinium chloride	GuaCl
Infrared Spectroscopy	IR
Isothermal Titration Calorimetry	ITC
Polyamidoamino acid derived from *L*-arginine	*L*-ARGO7
L-tryptophan/glycine copolymers	M-G-*L*-Trp
Polyamidoamino acid derived from *L*-alanine	M-*L*-Ala
Polyamidoamino acid derived from *L*-glutamine	M-*L*-Gln
Polyamidoamino acid derived from *L*-leucine	M-*L*-Leu
Polyamidoamino acid derived from *L*-tryptophan	M-*L*-Trp
Polyamidoamino acid derived from *L*-valine	M-*L*-Val
N,N′-Methylenebisacrylamide	MBA
Molecular Dynamics	MD
Micellar Electro-kinetic Capillary Chromatography	MECC
Number-average molecular weight	M_n
Weight-average molecular weight	M_w
Sodium Deoxycholate	NaDC
Nitroxide-Mediated Polymerization	NMP
Nuclear Magnetic Resonance	NMR
Nuclear Overhauser Effect Spectroscopy	NOESY
Phenylalaninol	PA
Polyamido amine	PAA

Polyamidoamino acid	PAAC
1,4 Phenylene Diisocyanate	PDI
Polydispersity Index	PDI
Poly(ester amide)	PEA
Poly (ether ester amide)	PEEA
Polyethylene oxide	PEO
Poly(ester ether urethane urea)	PEUU
Pulsed-gradient spin-echo Nuclear Magnetic Resonance	PGSE-NMR
Reversible Addition–Fragmentation Chain-Transfer Polymerization	RAFT
(*R*)-1,1′-bi(2-Naphthol)	RBNOL
Gyration Radius	R_g
Hydrodynamic Radius	R_h
Raman Optical Activity	ROA
Ring Opening Metathesis Polymerization	ROMP
Ring-Opening Polymerization	ROP
Small-Angle Neutron Scattering	SANS
Size Exclusion Chromatography	SEC
Tris(hydroxymethyl)aminomethane	TRIS
Thiphenylmethyl Methacrylate	TrMA
N-Triphenylmethyl methacrylamide	TrMAM
UV-Visible Spectroscopy	UV-Vis
Variable Temperature Nuclear Magnetic Resonance	VT-NMR

THESIS ABSTRACT

The design of chiral synthetic polymers capable of self-assembling into stable secondary structures represents an attracting approach with important biological applications, such as selective subcellular localization, protein surface mimicry and recognition. Chirality in polymers may be expressed based on the location of the stereogenic centers: i) main-chain chirality; ii) side-chain chirality and iii) self-assembled structures. Synthetic polymers as polyacetylenes, polyolefines and polymethacrylamides showing side-chain chirality may be synthesized by radical polymerization processes starting from modified α-amino acids.

In previous work, a new family of biomimetic polymers showing side-chain chirality, named polyamidoamino acids (PAACs), were introduced. The first polymer of this family was named *L*-ARGO7, derived by the step-wise polyaddition of *L*-arginine with *N,N′*-methylenebisacrylamide (MBA). The reaction was carried out in water, at 50°C and pH > 9 for 6 days, yielding a polymer with M_w ≈8000 and PDI 1.4. *L*-ARGO7 turned to be highly cytocompatible ($IC_{50} \geq 8$ mg mL^{-1}) and easily internalized in mouse embryo fibroblasts balb/3T3 clone A31 cell line proving, in this respects, to share some of the unique biological properties of polyarginine cell-permeating peptides.

The objectives of this work were multiple: to obtain a library of PAACs from the reaction of *N,N′*-methylenebisacrylamide with various natural α-amino acids following the same general procedure adopted for the synthesis of *L*-ARGO7, thus demonstrating the versatility of the synthetic process devised; to study the solution properties of PAACs, namely as acid-base behavior, ionization state, size and viscosity; to elucidate their conformational properties and ability to fold in aqueous media into compact and stable secondary structures; to study the responsiveness of these conformations to external stimuli; to study the fluorescent properties of PAACs from *L*-tryptophan; most important, to assess the PAAC ability to exhibit chirality-dependent interactions with biomolecules.

The PAACs synthesized in this work can be classified based on the structural features of the α-amino acid residue:

i) cationic arginine derived PAACs obtained from ***D*-, *L*-** and ***D,L*-arginine**; these polymers are moderately basic, since the guanidine group is internally neutralized by the carboxylate. Basicity is mainly due to the presence of the *tert*-amine;

ii) hydrophobic alkyl-substituted PAACs derived from ***L*-alanine** (M-*L*-Ala), ***L*-valine** (M-*L*-Val) and ***L*-leucine** (M-*L*-Leu); these polymers are obtained by reacting slightly hydrophobic α-amino acids bearing lateral substituents of increased steric hindrance;

iii) polar glutamine-derived PAAC obtained from ***L*-glutamine** (M-*L*-Gln); glutamine was chosen for its ability to form hydrogen bonds as protons donor or acceptor;

iv) amphipathic homo- and copolymeric *L*-tryptophan-based PAACs synthesized from, respectively, ***L*-tryptophan** (M-*L*-Trp) and ***L*-tryptophan/glycine** mixtures (M-G-*L*-Trp); tryptophan was chosen for its fluorescence properties, used to characterized conformational and structural features of homo- and copolymers.

EXPERIMENTAL PART: PAACs SYNTHESIS

The synthetic procedure of the investigated PAACs is reported in Scheme 1. *L*-, *D*- and *D,L*-PAACs were obtained in variable yield (60-70 %) carrying out the polymerization in aqueous solutions at 50 °C and pH > 9 for 6 days. In no case, traces of hydrolytic degradation or formation of aggregates were seen.

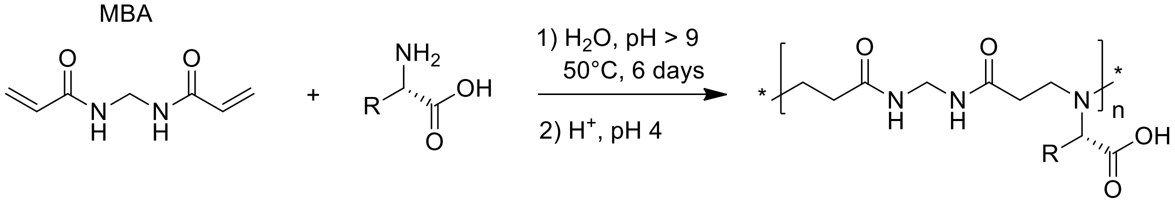

R = CH_3- (Alanine)
$(CH_3)_2CH$- (Valine)
$(CH_3)_2CH$-CH_2- (Leucine)

R = $NH_2COCH_2CH_2$- (Glutamine)
$NH_2C(NH)NHCH_2CH_2CH_2$- (Arginine)

Scheme 1. Synthesis of the investigated PAACs (*L*-enantiomeric form).

After 6 days, solutions were acidified to pH 4, purified by ultrafiltering through membranes with 100 and 5 kDa nominal molecular weight cut-off. The intermediated fractions were freeze-dried and structurally analysed by means of ^{1}H and ^{13}C NMR in D_2O, at pH 4.5. Molecular weights (M_w and M_n) was measured by means of size exclusion chromatrographic (SEC) analysis, carried out in 0.1 M TRIS buffer pH 8.00 ± 0.05, with 0.2 M NaCl.

RESULTS

i) ARGO7 and Alkyl-substituted PAACs

Circular dichroism (CD) measurements were recorded between 200 – 280 nm in the 3-12 pH interval. Spectra were consistent with the presence of pH-dependent ordered secondary structures, whose changes with pH were rapidly achieved and fully reversible. In addition, conformations resulted thermodynamically stable and reversible in the 3-70°C range. CD spectra were collected at ionic strength up to 2 M NaCl and in presence of denaturating agents, as urea and guanidinium chloride. Conformation of ARGO7 isomers resulted unaffected by ionic strength and presence of denaturants, whereas M-*L*-Ala, M-*L*-Val and M-*L*-Leu conformations changed with the introduction of guanidinium chloride.

Molecular dynamics (MD) simulations were performed at Politecnico di Milano (prof. G. Raffaini and F. Ganazzoli) and revealed that ARGO7 and alkyl-substituted PAACs had a compact, coiled structure (R_gs 0.8-1.11 nm). MD showed that PAACs' main chains were organized into a transoid arrangement characteristics of hairpin-like conformations. Structuring and size were mainly dictated by intramolecular interactions of electrostatic nature in the polymer main chain, with minor dependence from the amino acids side chain.

Hydrodynamic radius (R_h) was determined by DLS as a function of pH, time, ionic strength and presence of denaturating agents (urea and guanidinium chloride). Results revealed that these PAACs had monomodal volumetric distributions of 1.5 ± 0.3 nm average radius, stable at 25 °C for at least 1 month and unaffected by pH, ionic strength and presence of denaturants. In addition, nanoparticles' dimensions did not change by increasing the PAACs concentration in the 0.5 – 20 mg mL^{-1} range, suggesting these polymers may intramolecularly self-assembled into stable single chain nanoparticles.

ii) glutamine-derived PAACs

Differently from the other PAACs, M-*L*-Gln M_w and M_n values were more than two times higher than the others. This was tentatively ascribed to the presence of intra- and intermolecular hydrogen bonding, further studied with CD and NMR spectroscopy.

CD spectra resulted sensitive to the presence of urea, a protein denaturant known to form H-bonding, with time dependent spectral variations. DOSY, variable-temperature NMR (VT-NMR) and NOESY were used to obtain the structural and conformational features of M-*L*-Gln. DOSY showed only one diffusion coefficient, from which a R_h of 3.53 nm was calculated. VT-NMR was carried out at pH 4.5 and revealed that side-chain amide groups were involved in the formation of H-bonding, whereas only a small percentage of amides of the MBA backbone did the same. In addition, NOESY experiments measured two NOEs, both involving CH_2 next to the *tert*-amine and CH_2 in β and γ position of the glutamine side chain, respectively. Thus, M-*L*-Gln showed a coiled structure in which glutamine side chain moved closer to the main chain.

iii) tryptophan-based PAACs

Polymers bearing tryptophan as side substituent were synthesized by Michael-type polyaddition of MBA with *L*-tryptophan, its isomer, and different molar ratio of *L*-tryptophan/glycine mixtures. Differently from the other PAACs, these reactions were carried out under nitrogen flux and by portion wise addition of the base to avoid indole oxidation.

UV–Vis absorption and scattering of polarized IR beam tests showed all of them to have composition- and pH-dependent solubility. CD studies and DLS measurements were comparable with the other PAACs. CD were consistent with the formation of pH dependent self-assembled structures, whose conformation was dictated by the polymer main chain and its average ionization degree. R_h*s* resulted stable for at least 1 month, unaffected by pH but, to some extent, sensitive to concentration in the range 1–30 $mg{\cdot}mL^{-1}$.

Photoluminescence analyses, quantum yields, steady state and time-resolved fluorescence were measurements at different pH, polymers concentration and tryptophan content. Results indicated that the photoluminescence properties of tryptophan derived polymers were governed solely by tryptophan. All polymers exhibited pH-dependent quantum yields, lifetimes and emission maximum. Interestingly, fluorescence studies conducted on oxygen-free solution gave comparable results, indicating compact conformations where *L*-tryptophan moieties were not accessible to the quencher. Also, intermolecular quenching by approaching chains was studied and observed in M-*L*-Trp and M-G-*L*-Trp_{10}.

iv) *L*- and *D*-ARGO7 chiral recognition

To assess ARGO7 chiral recognition ability, sodium deoxycholate (NaDC), one of the components of bile salts, was chosen as a chiral model surface. Through a stepwise mechanism, NaDC can form chiral micelles, whose self-assembly behaviour is mainly affected by pH. In particular, NaDC showed three main pH dependent behaviour: homogenous solution (pH > 8), gel phase (pH 7 – 7.5), flocculation and aggregation (pH < 7). Pulsed-gradient spin echo NMR (PGSE-NMR), surface tension, circular dichroism (CD), dynamic light scattering (DLS), zeta potential (ZP) and small-angle neutron scattering (SANS) experiments were carried out on NaDC/*L*- and NaDC/*D*-ARGO7 mixtures, to assess chirality-dependent interactions. Surface tension, DLS, zeta potential and PGSE NMR measurements were recorded to characterize NaDC behaviour in solutions (CMC and self-assembly) as a function of pH and concentration and will not be considered in this report.

CD measurements were carried out on 5 mg mL^{-1} of NaDC mixed with 0.5 mg mL^{-1} of either *L*-, *D*- or *D,L*-ARGO7 solutions, in the 190 – 300 nm range in a 1 mm cell. Prior to the analysis, solutions were corrected to pD (pH of D_2O solutions) 9.06, and 7.50. At pD 9.06, the addition of NaDC did not result in any significant modification of the polymers' spectra, in either *L*- or *D*- form of the polymers. Thus, no chiral discrimination could be found at this pH. At pD 7.30, CD spectra of NaDC gel phase showed different pattern upon addition of *L*- and *D*-ARGO7, whereas no changes were seen with *D,L*-ARGO7. Thus, the self-reorganization of NaDC into an ordered gel, was likely due to the chiral recognition of the different isomers.

Small-angle neutron scattering (SANS) measurements were carried out at the ISIS Neutron and Muon Source facility (Rutherford Appleton Laboratory in Oxfordshire, UK, under the supervision of Prof. Peter Griffiths) to study chiral recognition, by looking at the conformational modifications of NaDC micelles upon introduction of the different isomeric forms of the polymer, at different pHs and concentrations. SANS collected at pD 8.5 - 8.8 for various NaDC concentrations were consistent with the presence of micelles, described by prolate ellipsoids with polar radius of 22 – 28 Å and equatorial radius of 7 – 10 Å. By decreasing pH, NaDC micelles' structure changed from a prolate ellipsoid (pD 8.80) to an elongated rod (pD 7.30) described by elliptical cylinders of 487.6 ± 21.2 Å length and 2.88 ± 0.19 axis ratio (Figure. 1a, black curve). NaDC/ARGO7 mixtures were prepared adding 5 mg mL^{-1} of NaDC to 0.5 mg mL^{-1} solution of *D*-, *L*-, *D,L*-ARGO7 and an equimolar mixture obtained by mixing *L*- and *D*-isomer of the polymer (*D*-/*L*-ARGO7). All NaDC/ARGO7 mixtures showed superimposable curves. They were fitted with the same model used for NaDC solutions, that is micelles with prolate ellipsoidal morphology (Figure 1a). Only small changes in the total charge and in the semi-minor and semi-major axis were seen. This confirmed the modest effect of the electrostatic interactions between the two components, ARGO7 and NaDC, and the absence of chiral discrimination.

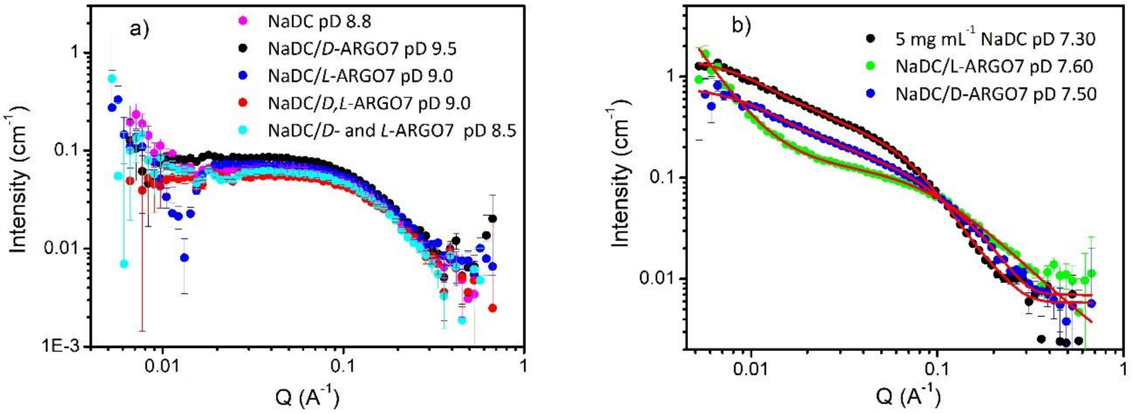

Figure 1. NaDC scattering data with: a) *D*-, *L*-, *D,L*-ARGO7 and the equimolar mixture *D*-/*L*-ARGO7 at pD 8.5-9.0 and b) the same solutions at pD 7.30-7.60. Mathematical fittings were reported as red lines.

Chiral recognition was then assessed collecting SANS data for 5 mg mL^{-1} NaDC gels (pD 7.3 – 7.5) with 0.5 mg mL^{-1} of *D*-, *L*-, *D,L*-ARGO7 or an equimolar mixture composed of 0.5 mg mL^{-1} *D*-ARGO7 and 0.5 mg mL^{-1} *L*-ARGO7. They showed that NaDC structure was differently affected by the chirality of the polymer (Figure 1b), confirming results obtained from CD spectra. In particular, *D*-, *D,L*-ARGO7 and the equimolar mixture changed SANS pattern in the same way. They retained the same rod-like structure of NaDC micelles, albeit with a lower axis ratio (1.51 ± 0.41). Different was the case of the NaDC/*L*-ARGO7 solutions, where *L*-ARGO7 appeared to trigger the formation of NaDC ellipsoidal clusters.

In conclusion, PAACs represent singular examples of synthetic bioinspired chiral polymers that showed potential for biotechnological applications on account of their i) stimuli-responsiveness, ii) self-assembly ability and iii) selective interactions with chiral structures, including biological structures.

PUBLICATIONS

- **Lazzari F.**, Manfredi A., Alongi J., Marinotto D., Ferruti P., Ranucci E. D-, L- and D,L-Tryptophan-Based Polyamidoamino Acids: pH-Dependent Structuring and Fluorescent Properties, *Polymers* **2019**, 11 (*3*), 543-562. https://doi.org/10.3390/polym11030543.
- **Lazzari F.**, Manfredi A., Alongi J., Mendichi R., Ganazzoli F., Raffaini G., Ferruti P., Ranucci E. Self-Structuring in Water of Polyamidoamino Acids with Hydrophobic Side Chains Deriving from Natural α-Amino Acids, *Polymers* **2018**, 10 (*11*), 1261-1279. https://doi.org/10.3390/polym10111261.
- Manfredi A., Mauro N., Terenzi A., Alongi J., **Lazzari F.**, Ganazzoli F., Raffaini G., Ranucci E., Ferruti P. Self-Ordering Secondary Structure of D - And L-Arginine-Derived Polyamidoamino Acids, *ACS Macro Lett.* **2017**, 6 (*9*), 987–991. https://doi.org/10.1021/acsmacrolett.7b00492.

PUBLICATIONS IN PREPARATION

- **Lazzari F.**, Raffaini G., Ganazzoli F., Manfredi A., Vasile F., Alongi J., Ferruti P., Ranucci E. Evidence of Hydrogen Bonding in a L-Glutamine-Based Polyamidoamino Acids and its pH-Dependent Conformations.
- **Lazzari F.**, Alongi J., Ferruti P., Ranucci E., Griffiths C.P. Chiral Recognition Between pH Dependent Self-assembled Sodium Deoxycholate and D-, L-Arginine Derived Polyamidoamino Acids.

1

Introduction to synthetic chiral polymers and *α*-amino acid based polymers

1.1 CHIRAL SYNTHETIC POLYMERS

Chirality is thoroughly present in nature as an intrinsic property of biomacromolecules, found for example in nucleic acids, proteins, polysaccharides and lipids. It can be expressed in different forms: D- or L- enantiomers, inherently chiral structures and tridimensional self-assembled architectures. Exploiting the chirality of the starting building blocks, nature is then able to build up complex chiral architectures, held together by noncovalent interactions (hydrogen bonding, electronic and hydrophobic forces). Albeit chirality is found everywhere, the importance of having a certain twist to carry out certain biological functions, as the discrimination of pairs of enantiomers, remains still unknown.

Chiral polymers are defined as polymers showing chirality in their primary and/or secondary structure. The most-known chiral polymers are the naturally occurring polymers like polypeptides, polysaccharides and polynucleotides [1]. They have been widely employed for the synthesis of chiral polymer-based materials [2-4]. Recently, also fully synthetic and hybrid chiral polymers have gained a great deal of attention as novel smart materials for their widespread applications in catalysis [5-8], drug-delivery [9,10], chiral recognition [11,12], chiral resolution [13-15], biosensing [16-18] and bioimaging [19]. Among these, their most established applications are as polymer-supported catalyst [20] and chiral stationary phases (CSP) to discriminate pairs of enantiomers (resolution), with already commercially available materials [21]. Further promising studies are based on dynamic helical polymers as innovative smart materials, capable to respond to specific external stimuli. Applications of chiral polymers are based on their chiral structure. As such, of utmost importance is the development of new and efficient synthetic methods to obtain polymers with well-defined architectures. Chiral polymers may be divided into four main groups: i) polymers bearing chiral centers in their main; ii) polymers bearing chiral centers as side pendant; iii) polymers showing secondary structures, originated by the specific tridimensional twisting of the polymeric chain, and iv) polymers able to self-assemble into supramolecular architectures. The first two classes may also have specific conformations in solution, and they may be able to self-assembled into more complex structures. All these polymers are obtained through either the polymerization of chiral monomers or the asymmetric polymerization of achiral monomers. In asymmetric polymerization, an optically-inactive prochiral monomer or a prochiral monomer with an optically-active auxiliary is polymerized to give a polymer with conformational main chain, configurational main chain or side chain chirality. This type of polymerization includes asymmetric synthesis, chirality induction, helix-sense selective and enantiomer selective polymerization.

1.1.1 Main-chain chirality

Polymers with main-chain chirality are widely used in chiral separation and recognition [21-25], and asymmetric catalysis [26], due to their rigid or semi-flexible conformation. Their tendency to assume helical or rigid-rod conformation, allowed a higher capability in chiral applications [27-29]. The most common synthetic polymers showing main chain chirality, are pseudo peptides like poly (2-oxazoline)s [30,31], poly(α-amino acid)s [32,33], polylactides [34,35], polyamides [36], polyesters [37], polyester amides [38], polyester urethanes [39] and polydepsipeptides [40] (Scheme 1), namely copolymers of α-hydroxy acids and α-amino acids.

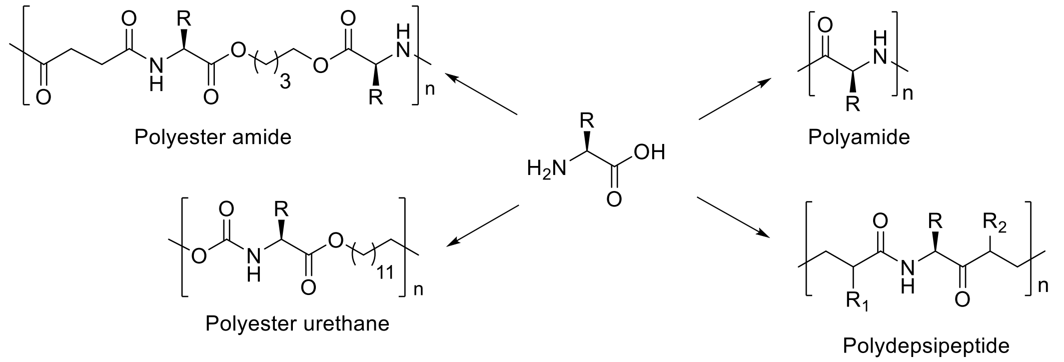

Scheme 1. Some examples of polymers with main-chain chirality derived from α amino-acids.

Recently, also polyurethanes and polythiourethanes were synthesized with main-chain chirality [41]. For example, a chiral polythiourethane was obtained exploiting the cationic ring-opening polymerization of 4(*S*)-(methoxycarbonyl)-1,3-oxazolidine-2-thione (Scheme 2).

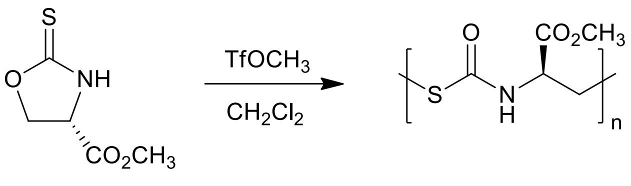

Scheme 2. An example of polythiourethane obtained by cationic ring-opening polymerization of cyclic thiourethane [41].

Chiral cyclic and linear polyurethanes [42] were synthesized starting from optically active (*R*)-1,1′-bi(2-naphthol) (R-BINOL) and 1,4 phenylene diisocyanate (PDI) (Figure 1).

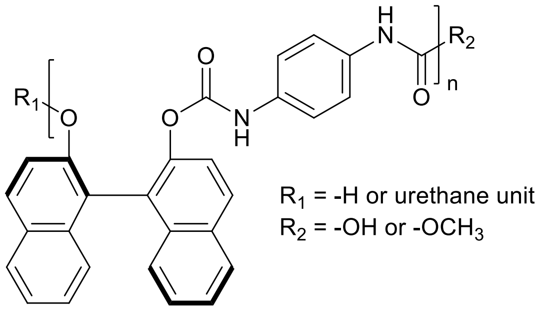

Figure 1. Repeating unit of a chiral polyurethane obtained from the polyaddition of (*R*)-1,1′-bi(2-naphthol) and 1,4 phenylene diisocyanate [42].

Polyurethanes and polythiourethanes might show higher order conformations, as α-helix and β-sheet [42], other than a variety of self-assembled architectures, as spheres or rod-like micelles, vesicles and fibers [43].

Generally, synthetic polymers with main-chain chirality may be synthesized through asymmetric polymerization [44-46], by a careful catalyst design, by ring-opening polymerization (ROP) [30,34,35] or by polycondensation [25]. To note, the direct polymerization of chiral monomers has shown to reduce the polymers processability. This drawback may be overcome by some expedients, like introducing long chain alkyl [27], consequently changing the rheological behavior and its conformation. For example, the introduction of an alkyl side chain in the chiral poly(propiolic esters), resulted in inversion of the helix sense [47]. Main-chain chiral polymers may assume specific conformations in solution, and they may self-assemble into ordered structures. For example, poly (2-oxazoline)s, whose repeating unit is reported in Figure 2, may be synthesized by ring opening polymerization and can self-assembly into ordered secondary structures, held together by dipolar interactions between tertiary amides [31]. The microwave assisted polymerization of 2,4-disubstituted-2-oxazoline monomer, like (*R*)-2-butyl-4-ethyl-2-oxazoline, gave polymers with temperature dependence CD spectra, probably associated to a flexible helical conformation [30]. In contrast, the racemic polymer obtained from the (*RS*)-2-butyl-4-ethyl-2-oxazoline polymerization, formed a random coil. By increasing the length of the alkyl side chain, in order ethyl, butyl, octyl, nonyl and undecyl, the crystallization rate increases [31]. This phenomenon is a combination of side-chain and main-chain crystallization, that generates a wide spectrum of differently oriented crystals, whose CD spectra changes with temperature in different manner.

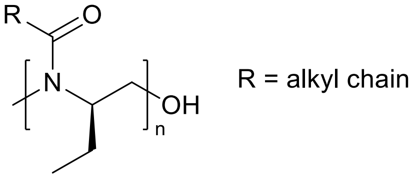

Figure 2. Repeating unit of poly (2-oxazoline)s.

1.1.2 Side-chain chirality

Polymers with side chain chirality may be obtained from the following monomers: acryl- and methacrylamides [48,49], dienes [50], phenylacetylenes [51,52], isocyanides [53] and phenylisocyanides [54], isocyanates [55], norbonene diesters and diamides [56], phosphazenes [57], propargylamides [58] and propargyl esters [59], vinyl esters [60] and vinyl ethers [61], acrylates and methacrylates [62] (Scheme 3). They are generally synthesized by direct polymerization of chiral monomers by atom transfer radical polymerization (ATRP), nitroxide-mediated polymerization (NMP), RAFT polymerization, ring opening metathesis polymerization (ROMP), living anionic and cationic polymerization, acyclic diene metathesis (ADMET) polymerization, and metal catalyzed metathesis or insertion polymerization.

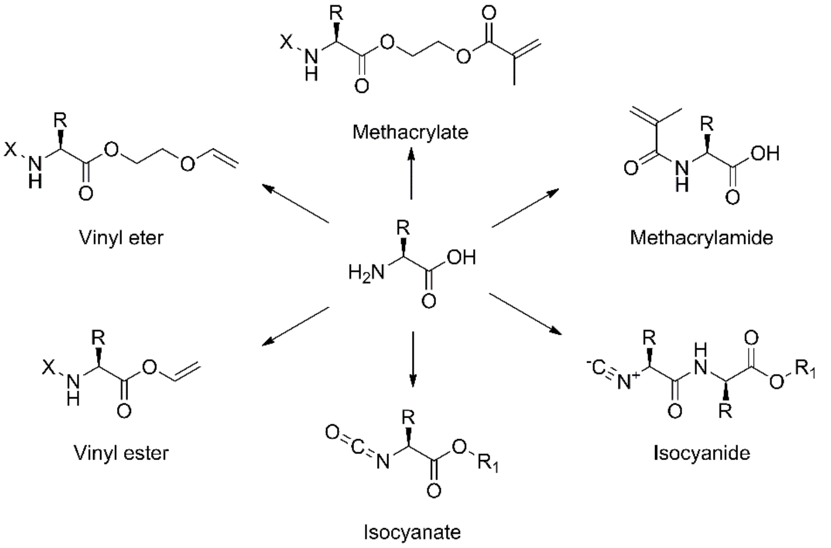

Scheme 3. Some examples of amino acid-derived monomers used to prepare side chain amino acid-based polymers.

Another well-known class of bioinspired polymers bearing stereogenic centers in their side chain is constituted by polypeptoids, or *N*-substituted glycines derivatives [63]. In contrast to polypeptides, the *N*-substitution deprives polypeptoids of main-chain chirality. Also, they lack the ability to form hydrogen bonding interactions along the main chain. As a result, the conformations of polypeptoids are strongly dependent on the *N*-substituent structures and may give rise to well-defined secondary structures. One way to synthesized linear polypeptoids is by controlled ring-opening polymerization (ROP) of *N*-substituted *N*-carboxyanhydride with primary amine initiators (Scheme 4), whereas cyclic polypeptoids may be obtained by zwitterionic ring-opening polymerizations (ZROPs) using, for example, *N*-heterocyclic carbenes as nucleophilic initiator [63].

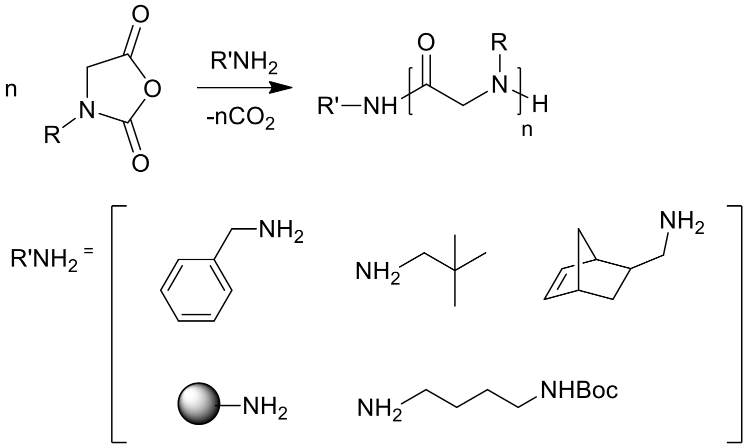

Scheme 4. Some primary amine initiators for *N*-substituted *N*-carboxyanhydride ring opening polymerization to obtain linear polypeptoids. Note: the solid sphere indicates a solid support or surface.

Side-chain chiral polymers show a multitude of applications in asymmetric synthesis, molecular recognition, and photoelectrical materials. Similarly to polymers having main-chain chirality, the ones with side-chain chirality might show different kind of conformations and supramolecular structures, depending on the experimental conditions and the nature of the side substituent. One way to induce conformations with prevailing handedness of the backbone is to introduce stereocenters in the side-chain [64]. In a series of chiral poly(methacrylamides), the introduction of (*R*)-phenylglycine was reported to enhance the stability and formation of one-handed helix via H-bonding between the amide groups in the side chains [65]. To increase the asymmetric coupling between the stereocenter in the side group and the main chain, the chiral atom is usually linked directly to (or close to) the polymerizable group [66,67]. Stereoregular poly(N-alkynylamides) showed that the main-chain helical conformation, induced by the chiral center located in the side group, was maintained when stereocenter was separated by few covalent bonds [68]. Whereas, no backbone structuring was observed when the distance was higher than seven atoms. Another way to synthesized one-handed helical polymers consists in the introduction of bulky side groups in the monomers structure. For example, thiphenylmethyl methacrylate (TrMA) and *N*-triphenylmethyl methacrylamide (TrMAM) induced the formation of isotactic one-handed helical polymethacrylates and methacrylamides though either anionic or radical polymerization in chiral conditions [21]. Polyacetylenes constitutes a different example of synthetic polymers whose main chains may be forced in an anisotropic reorganization of atomic groups upon introduction of chiral bulky substituents linked to the main chain. Chiral spirobifluorene-derived polyacetylenes reported cis-transoidal main chain conformation, organized into helical structures (Figure 3) [69]. Polyecetylenes conformations may be further induced and stabilized by the presence of chiral initiators or ligands [70].

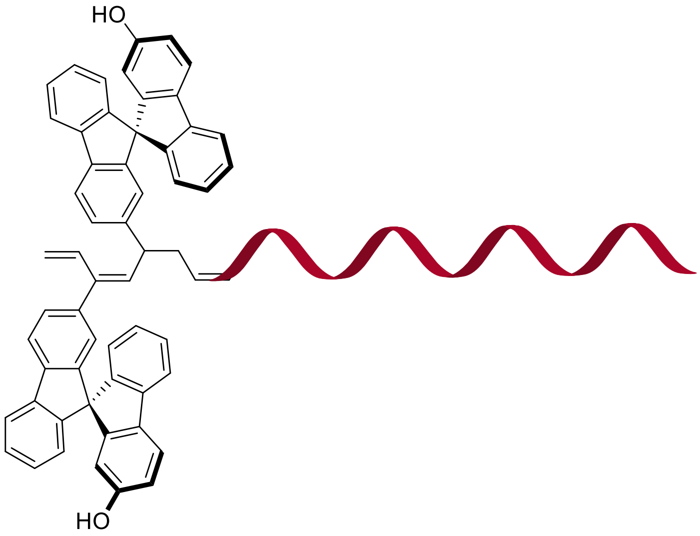

Figure 3. Example of a polyacetylene bearing chiral spirobifluorene moieties and its main chain helical conformation.

1.2 *α*-AMINO ACIDS DERIVED POLYMERS

The incorporation of *α*-amino acids into polymers represents an attracting approach to impart unique optical properties and to increase biocompatibility and biodegradability [71]. Amino acids may be incorporated either in the polymers' main chain or in the side chain. Polymers belonging to the first group are generally poly(ester amide)s (PEAs), poly (ether ester amide)s (PEEAs) and poly(ester ether urethane urea)s (PEUUs), obtained mainly by polycondensation reactions [71]. As an example, biodegradable PEAs were synthesized by interfacial polycondensation starting from L-phenylalanine [72], in order to obtain porous scaffolds for vascular tissue engineering applications. Synthesis of bioinspired polymers bearing α-amino acids as side pendant has been achieved mainly by controlled radical polymerization techniques as: atom transfer (ATRP), nitroxide-mediated NMP), RAFT and ROP polymerization, to name a few. Prior to the synthesis, modification of the N- or C-terminus of the amino acid is carried out to introduce polymerizable functions. Another way could be to exploit -SH or -OH additional functional groups. *N*-Terminus modified polymers such as *N*-acryloyl- or *N*-methacryloyl-α-amino acids are used to obtain polyacrylamides or polymethacrylamides [73-75]. C-terminus modified α-amino acid may be introduced as side pendants into the backbone of polymethacrylates [76], polyacrylates [77], polyacetylenes [78,79], polyolefines [80], polyvinyl ethers [61] and polyphosphazenes [81]. For example, various α-amino acid derived polypropargylamides were synthesized in order to obtain a polymer with stimuli responsive helical conformation. Both *N*- and *C*-derived polymers may show interesting properties, as stimuli responsiveness [82], the ability to self-assemble into complex architecture [83] and pH-dependent solubility [84]. In addition, they may show chirality-induced structuring in solution [79,80] and chiral recognition capacities including differential interactions with organic cell components [85].

1.3 POLYAMIDO AMINO ACIDS (PAACs)

Polyamidoamino acids (PAACs) are a relatively new family of bioinspired chiral polymers carrying α-amino acids as side substituent. These polymers are an offspring of linear polyamido amines (PAAs) obtained from *prim*-amines or *bis*-sec-amines and bisacrylamides. PAAs are a well-known family of soluble synthetic functional polymers with a recognized potential for various applications: biotechnological [86,87], water purification [88,89], heterogeneous catalysis [90], coating for sensing applications [91–93] and flame retardant agents for cotton textiles [94, 95]. Due to the widespread applications of PAAs, PAACs were further explored to assess if and how these polymers may address the challenges encountered in biology and biomedical sciences, as their parent. Differently from the other α-amino acids derived polymers obtained either by *N*- or *C*-modified monomers, PAACs retain the acid-base properties and the chirality of the parent amino acids. These polymers are synthesized by the stepwise polyaddition of natural α-amino acids, and their stereoisomers, to

N,N′-methylenebisacrylamides (MBA) (Scheme 5). Reactions are carried out in water, at 50°C and pH > 9 for 6 days [96]. The synthesis is highly specific since the amino-acids′ *prim*-amine groups are the only functional groups reacting and converted into *tert*-amines after the addition [97].

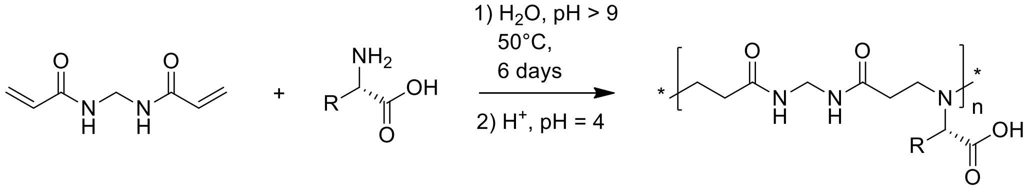

Scheme 5. Synthesis of PAACs.

The first polymer of this family was named *L*-ARGO7, synthesized by the Michael type polyaddition of *L*-arginine to *N,N′*-methylenebisacrylamide (MBA) [97]. Arginine was chosen for its cell-permeating properties, as reported in literature in both synthetic polyarginines and arginine-rich peptides [98,99]. Supposedly, guinidine groups could interact with biological membranes by forming divalent hydrogen bonds with carboxylate-, sulfate- and phosphate groups [98,99].

Under normal conditions, that is at room temperature (25°C), natural α-amino acids other that glycine react very sluggishly with bisacrylamides. The first attempt to synthesize *L*-ARGO7 was carried out at 25 °C, pH > 9 for 6 months, obtaining a polymer in 41% yield, number-average molecular weight (M_n) of 10100, and polydispersity index (PDI) of 1.19 [97]. The higher reaction time was due to the low arginine reactivity, probably connected to the sterically hindered structure of the amine groups. This could explain why, even though the addition of the first N-H group was fast, the second one reacted very slowly. The ability of *L*-ARGO7 and of *L*-ARGO7-co-MBAP, its copolymer with piperazine, to cross cell membranes was evaluated by in vitro studies with mouse embryo fibroblasts balb/3T3 clone A31 cells. Both polymers resulted cytobiocompatible, with an IC_{50} ≥ 8 mg mL^{-1} for *L*-ARGO7. They easily entered cells, with a more effective cellular uptake shown by the copolymer [97]. The determination of the acid-base properties of *L*-ARGO7 showed an isolectric point of ≈10 and positive net average charges per repeating unit of +0.25 at pH 7.4 [96].

In order to reduce the reaction time, calcium ions were used as catalysts for the Michael addition reaction. Calcium was chosen for its acid-base properties, able to catalyze the addition of amino nucleophiles to α,β-unsaturated carbonyl compounds [100]. After the addition of 0.1 mol calcium chloride/mol *L*-arginine, a decrease in the overall reaction time was observed: *L*-ARGO7 was obtained in 63% yield after 21 days with M_n 16700 and PDI 1.61 [97]. The PAACs synthesized by the conventional procedure and those obtained by using Ca^{2+} as a catalyst showed no difference in physico-chemical properties. However, Ca^{2+} may be retained as counterion and this may affect the biological properties. Therefore, extensive and often difficult purification processes are required. To solve this problem, higher reaction temperatures were explored. In fact, it is well known that in Michael polyadditions an increase in temperature leads to higher polymerization rates [87]. On the other hand, higher temperatures may also increase the rates of side reactions, such as retro-Michael and amide hydrolysis, leading to a concomitant chain length reduction.

When ARGO7 synthesis was carried out at 50°C, pH > 9 for 6 days, a polydisperse polymer was obtained in 92 % yield with $M_n \approx 4600$ and PDI 1.4 [96]. The reaction was easily extended to *D*- and *D,L*-arginine obtaining polymers with the same M_n and PDI [97]. Interestingly, preliminary circular dichroism measurements carried out for *L*-ARGO7 at pH 7 showed the polymers ability to self-assembled in solution into ordered structures [97]. As for PAAs, an evaluation of the acid-base properties of *L*-ARGO7 was carried out. Results indicated *L*-ARGO7 never display the typical polyelectrolyte behaviour in solution. In fact, its pK_as depends only slightly on the protonation degree of the macromolecule. By exploiting the different reaction rates of the two hydrogens of the amino-acid *prim*-amine groups with bisacrylamides, the synthesis of *L*-, *D*- and *D,L*-ARGO7 polymers was recently improved by a step-by-step polyaddition [101]. This allowed the formation of monodisperse ARGO7 with controlled sequences and controlled molecular weights [101]. For these stereoisomers, hints of chirality-dependent cell internalization were collected at the University of Greenwich (Dr. Simon Richardson). Results are currently under investigation.

1.4 HOW TO STUDY CHIRO-OPTICAL PROPERTIES

In order to characterize chiral polymers, techniques like circular dichroism (CD), polarimetry and Raman optical activity (ROA) are generally employed. Circular dichroism (CD) is based on the differential absorption by chromophores of left and right circularly polarised components of plane-polarised radiation [102]. CD signal arises when optically active chromophores are a) intrinsically chiral, due to their structure, b) covalently linked to a chiral center, or c) placed in an asymmetric environment [102]. CD spectroscopy is mainly used to study polymers configuration and conformation as well as conformational stability in various experimental conditions. The variation of the chiro-optical properties of copolymers obtained from various (*R*)-*N*-(1-phenylethyl) methacrylamide and 2-hydroxyethyl methacrylate ratios was assessed [103]. The nonlinear variation of the CD values with the content of chiral units suggested the presence of secondary structures, held together by intramolecular interactions as H-bonding. In the case of (*R*)-phenylglycine-modified *N*-phenylmethacrylamide polymer, named poly(RR-PEBM), CD proved the formation of a helical conformation with a preferred screw sense [104]. Its stability was assessed at different temperatures and solvents. Intensity of the CD spectra resulted only slightly affected by temperature modifications in the -10 – 50°C interval. Instead, a sharp decreased in CD intensity was observed when methanol was chosen as solvent suggesting the transition from helix conformation to random coil due to the loss of intramolecular interactions in the macromolecule [104]. In literature, stimuli responsiveness of polymers' conformations was recorded measuring dependence of CD spectra over pH as well [105]. Among other applications, CD spectroscopy has been used to study chiro-optical properties of supramolecular aggregates and complexes, as in case the of cyclodextrins inclusion complexes, metal-bound complexes, protein/drugs adducts, biopolymers/small molecules complexes, polymer-induced conformation and self-assembled chiral molecules [106]. Interestingly, CD was also employed to monitor conformational changes during the aggregation of (*R*)-1,1'-binaphthyl-based polymers [107], whose behavior in solution and CD spectra resulted affected by the torsional angles between the chromophores.

Recently, CD was extended to the study of self-assembled soft materials [108], that is hydrogels obtained from intrinsically chiral low molecular weight molecules, as amino acids and carbohydrates. The ordered structure is driven by various intermolecular interactions, resulting in the gelation process and encapsulation of solvent molecules. In the CD spectrum, the interactions of the chromophores in the self-assembled state generated a stronger signal compared to the solutions, albeit with lower absorbances.

Similarly, ROA measures the difference in Raman scattering between right and left circularly polarised light. This technique is becoming another complementary tool for configurational and conformational analysis of biomolecules, including amino acids, peptides, proteins [109], sugars, nucleic acids [110] and terpenes [111]. In fact, the ROA spectrum of enantiomers is the same but with opposite sign. Combining experimental and theoretical study, helix poly(trityl methacrylate) was studied by ROA in order to assign both the helical screw sense and the side-group chirality of the synthetic chiral polymer [112].

1.5 APPLICATIONS OF CHIRAL SYNTHETIC POLYMERS

Chiral synthetic polymers are employed in a variety of applications, some of them were already mentioned in the paragraph above. Principally they are adopted as chiral stationary phases (CSP) for high-performance liquid chromatography [21]. There are three types of chiral polymers used as CSP: i) biopolymers, ii) polymers prepared by modification of naturally occurring polymer backbone, such as polysaccharides and iii) those having fully synthetic structure. Group i) is formed principally by enzymes and proteins, as bovine serum albumin, α_1-acid glycoprotein, ovomucoid, avidin and riboflavin binding protein, trypsin, α-chymotrypsin, cellobiohydrolase I and lysozyme to name a few. Group ii) consists of a variety of polysaccharides derivatives, like cellulose and amylose-derived tribenzoates and tris(phenylcarbamates) [113]. The chiral recognition and resolving ability depended on the substituents introduced on the phenyl moieties. The introduction of electron-donating or electron-withdrawing substituents improved the chiral recognition ability. Among the many derivatives of polysaccharides, 3,5-dimethylphenylcarbamates of cellulose and amylose and cellulose tris(4-methylbenzoate) showed high chiral recognition, which permitted the resolution of more than 80% of the racemates tested [114]. In group iii) polymethacrylates showing helical conformation and polymethacrylamides with side chain chirality were considered. They resulted especially effective as CSP [21]. Triphenylmethyl methacrylate (TrMA) formed an isotactic polymer named poly(TrMA), characterized by single-handed helical conformation of the main-chain, through anionic polymerization in presence of n-BuLi with (-)-sparteine. The presence of the bulky trityl groups allowed stabilization of the helix. Chiral recognition of the silica-supported poly(TrMA) was proved toward more than 200 compounds [115,116]. Polyacrylamides and polymethacrylamides bearing the stereogenic centers as side pendants showed chiral recognition abilities depending on the polymers' structure, the racemates and the chromatographic conditions. Silica packed column containing polyacrylamide bearing benzyl and ethyl groups, is currently on the market. Other chiral synthetic polymers as polyolefines, polystyrene derivatives, poly(vinyl ether)s, polychloral, polyisocyanide, polyacetylenes, polyethers and polyamides may be synthesized bearing optically active side groups or having a preferred conformations in solution, as such possessing chiral recognition abilities [21].

Another application is the optical resolution of enantiomers by crystallization, achieved exploiting several chiral polymers. A set of optically active DHBCs were synthesized based on PEG-*b*-PEI block (PEG: poly-(ethylene glycol and PEI: branched poly-(ethyleneimine)) [117]. In order to impart polymers of chiral properties, chiral molecules such as (*S*)-ascorbate (vitamin C), (*S*)-proline, or (*R*)-gluconate were attached to the PEI amino branches. DHBCs was able to separate enantiomers in crystallization of conglomerate systems of sodium ammonium tartrate ($NaNH_4T$) and in racemic systems of calcium tartrate tetrahydrate (CaT), by slowing down the formation of the thermodynamically stable racemic crystals. In another article, DHBCs based on polyethylene oxide (PEO) with chiral (*R*) or (*S*)-glutamic acid blocks influenced the crystallization kinetics, crystal morphology and chiral resolution of *D,L*-threonine. In particular, the chiral resolution depended on the conformation of the polymer, showing the chiral recognition of *D,L*-threonine take place only for the PEO copolymer with *R*-glutamic acid in is α-helix form.

Chiral polymers also hold potential for application in chiral catalysts, liquid crystals, nonlinear optical materials and chiral sensors. Example of polymer-based chiral probes consisted in polymer containing (*S*)-2,2′-binaphthol moieties in their main chains [118]. This exhibited enantioselectve fluorescence enhancement behavior toward the enantiomers of phenylalaninol (PA), whose increase in fluorescence intensity resulted linearly correlated with the molar concentration ratios of the *D*- and *L*-enantiomers. Another example is represented by (*R,R*)-Salen-based polymer, prepared by copolymerization of (*R,R*)-1,2-diaminocyclohexance with 2,5-dibutoxy-1,4-di(5-tert-butylsalicyclaldehyde)-phenylene [118]. This polymer can distinguish the two enantiomers of phenylglycinol by changing the degrees of fluorescence intensity enhancement. For instance, exposure of the sensor to (*S*)-phenylglycinol leads to a large increase in the fluorescence efficiency, whereas lower intensities were recorded in presence of (*R*)-phenylglycinol.

1.6 REFERENCES

1. Ravve, A. Naturally occurring polymers, *principles of polymer chemistry* **2000**, 449-475, Springer, Boston, MA.

2. Tomoyuki, I. The dawn of chiral material development using saccharide-based helical polymers. *Polym. J.* **2017**, 49, 355–362, DOI:10.1038/pj.2016.123.

3. Song, Z.; Han, Z.; Lv, S.; Chen, C.; Chen, L.; Yin, L.; Cheng, J. Synthetic polypeptides: from polymer design to supramolecular assembly and biomedical application. *Chem. Soc. Rev.* **2017**, 46, 6570-6599, DOI:10.1039/C7CS00460E.

4. Duro-Castano, A.; Conejos-Sánchez, I.; Vicent, M.J. Peptide-based polymer therapeutics, *Polymers* **2014**, 6, 515-551, https://doi.org/10.3390/polym6020515.

5. Luo, R.; Zhu, M.; Shen, X.; Li, S. Polymer catalyst with self-assembled hierarchical access for sortable catalysis. *J. Catal.* **2015**, 331, 49-56, doi:10.1016/j.jcat.2015.08.018.

6. Evans, C. A.; Skey, J.; Wright, M.; Qu, W.; Ondeck, C.; Longbottom, D.A.; O' Reilly, R.K. Functional and tuneable amino acid polymers prepared by RAFT polymerization, *J. Polym. Sci. A* **2009**, 47, 6814-6826.

7. Kristensen, T.E.; Vestli, K.; Jakobsen, M.G.; Hansen, F. K.; Hansen, T. A general approach for preparation of polymer-supported chiral organocatalysts via acrylic copolymerization. *J. Org. Chem.* **2010**, 75, 1620–1629, doi: 10.1021/jo902585j.

8. Itsuno, S.; Hassan, M. Md. Polymer-immobilized chiral catalysts. *RSC Adv.* **2014**, 4, 52023, DOI: 10.1039/c4ra09561h.

9. Liang, J.; Yang, B.; Deng, J. Polylactide-based chiral particles with enantio-differentiating release ability. *Chem. Eng. Sci.* **2018**, 344, 262-269, doi:10.1016/j.cej.2018.03.076.

10. Quiñones, J. P.; Peniche, H.; Peniche, C., Chitosan based self-assembled nanoparticles in drug delivery. *Polymers* **2018**, 10, 235-267, doi:10.3390/polym10030235.

11. Morioka, K.; Suito, Y.; Isobe, Y.; Habaue, S.; Okamoto, Y. Synthesis and chiral recognition ability of optically active poly{N-[(R)-α-methoxycarbonylbenzyl]methacrylamide} with various tacticities by radical polymerization using Lewis acids. *J. Polym. Sci. A Polymer Chemistry* **2003**, 41, 3354 –3360, doi:10.1002/pola.10927.

12. Shen, J.; Okamoto, Y. Efficient separation of enantiomers using stereoregular chiral polymers. *Chem. Rev.* **2016**, 116, 1094–1138, DOI: 10.1021/acs.chemrev.5b00317.

13. Mastai, Y.; Sedlak, M.; Colfen, H.; Antonietti, M. The separation of racemic crystals into enantiomers by chiral block copolymers. *Chem. Eur. J.* **2002**, 8, 2430, doi:10.1002/1521-3765(20020603)8:11<2429:AID-CHEM2429>3.0.CO;2-6.

14. Menahem, T.; Mastai, Y. Chiral soluble polymers and microspheres for enantioselective crystallization. *J. Polym. Sci. A Polymer Chemistry* **2006**, 44, 3009, DOI: 10.1002/pola.21376.

15. Menahem, T.; Pravda, M.; Mastai, Y. Correlation between structures of chiral polymers and their efficiency for chiral resolution by crystallization. *Chirality* **2009**, 21, 862-870, doi: 10.1002/chir.20724.

16. Fukuhara, G. Polymer-based supramolecular sensing and application to chiral photochemistry. *Polym. J.* **2015**, 47, 649–655. DOI: 10.1038/pj.2015.52.

17. Fukuhara, G.; Inoue, Y. Chirality-sensing binaphthocrown ether–polythiophene conjugate. *Chem. Eur. J.* **2010**, 16, 7859 – 7864, DOI: 10.1002/chem.200903545.

18. Yashima, E.; Maeda, K.; Nishimura, T. Detection and amplification of chirality by helical polymers. *Chem. Eur. J.* **2004**, 10, 42-51, DOI: 10.1002/chem.200305295.

19. Dai, C.; Yang, D.; Zhang, W.; Bao, B.; Cheng, Y.; Wang, L. Far-red/near-infrared fluorescent conjugated polymer nanoparticles with size-dependent chirality and cell imaging applications, *Polym. Chem.* **2015**, 6, 3962, DOI: 10.1039/c5py00344j.

20. Fan, Q.; Wang, R.; Chan, A. S. C. Polymer-Supported Chiral Catalysts with Positive Support Effects, *Bioorg. Med. Chem. Lett.* **2002**, 12, 1867–1871, https://doi.org/10.1016/S0960-894X(02)00273-1.

21. Nakano, T. Optically active synthetic polymers as chiral stationary phases in HPLC, *J. Chromatogr. A* **2001**, 906, 205-225, DOI: 10.1016/s0021-9673(00)00944-4.

22. Teraguchi, M.; Mottate, K.; Kim, S-Y.; Aoki, T.; Kaneko, T.; Hadano, S.; Masuda, T. Synthesis of chiral helical poly(hydroxyl-containing phenylacetylene) membranes by in-situ depinanylsilylation and their enantioselective permeabilities. *Macromolecules* **2005**, 38, 6367–6373, https://doi.org/10.1021/ma050089z.

23. Nakano, T.; Satoh, Y.; Okamoto, Y. Synthesis and chiral recognition ability of a cross-linked polymer gel prepared by a molecular imprint method using chiral helical polymers as templates. *Macromolecules* **2001**, *34*, 2405–2407, https://doi.org/10.1021/ma001933i.

24. Teraguchi, M.; Masuda, T. Poly(diphenylacetylene) membranes with high gas permeability and remarkable chiral memory. *Macromolecules* **2002**, *35*, 1149–1151, https://doi.org/10.1021/ma011537f.

25. Wei, P.; Wang, D.; Wu, Z.; Bi, X. Synthesis of a series of soluble main-chain chiral nonracemic poly(alkyl-aryl ketone). *Express polym. Lett.* **2008**, 6, 440, DOI: 10.3144/expresspolymlett.2008.53.

26. Haraguchi, N.; Ahamed, P.; Parvez, M.M.; Itsuno, S. Synthesis of main-chain chiral quaternaty ammonium polymers for asymmetric catalysis using quaternization polymerization. *Molecules* **2012**, 17, 7569, DOI: 10.3390/molecules17067569.

27. Pu, L. 1,1′-Binaphthyl dimers, oligomers, and polymers: Molecular recognition, asymmetric catalysis, and new materials. *Chemical Reviews* **1998**, 98, 2405, https://doi.org/10.1021/cr970463w.

28. Xue, Q. B.; Kimura, T.; Fukuda, T.; Shimada, S.; Matsuda, H. Synthesis and lyotropic liquid crystal properties of chiral helical polycarbodiimides. *Liquid Crystals* **2004**, 31, 137, DOI: 10.1080/02678290410001637185.

29. Van Beijnen, A. J. M.; Nolte, R. J. M.; Naaktgeboren, A. J.; Zwikker, J. W.; Drenth, W.; Hezemans, A. M. F. Helical configuration of poly(iminomethylenes). Synthesis and CD spectra of polymers derived from optically active isocyanides. *Macromolecules* **1983**, 16, 1679, https://doi.org/10.1021/ma00245a001.

30. Bloksma, M.M.; Hendrix, M. M. R. M.; Rathgeber, S.; Schubert, U.S.; Hoogenboom, R. Main-chain chiral poly(2-oxazoline)s: influence of alkyl side-chain on secondary structure formation in the solid state. *Macromol. Symp.* **2015**, 350, 43, DOI: 10.1002/masy.201400023.

31. Bloksma, M.M; Rogers, S.; Schubert, U.S.; Hoogenboom, R. Secondary structure formation of main-chain chiral poly(2-oxazoline)s in solution. *Soft Matter* **2010**, 6, 994, DOI: 10.1039/b921467d.

32. Deng, M. X.; Wu, J.; Reinhart-King; C. A.; Chu, C. C. Synthesis and Characterization of Biodegradable Poly(ester amide)s with Pendant Amine Functional Groups and In Vitro Cellular Response. *Biomacromolecules* **2009**, *10*, 3037, https://doi.org/10.1021/bm9006437.

33. Arimura, H.; Ohya, Y.; Ouchi, T. Formation of Core−Shell Type Biodegradable Polymeric Micelles from Amphiphilic Poly(aspartic acid)-block-Polylactide Diblock Copolymer *Biomacromolecules* **2005**, *6*, 720, https://doi.org/10.1021/bm0494491.

34. Mehta, R.; Kumar, V.; Bhunia, H.; Upadhyay, S.N. Synthesis of poly(lactic acid): a review. *J. Macromol. Sci. Polym. Rev.* **2005**, C45, 325–349, https://doi.org/10.1080/15321790500304148.

35. Bourissou, D.; Moebs-Sanchez, S.; Martín-Vaca, B. Recent advances in the controlled preparation of poly(α-hydroxy acids): metal-free catalysts and new monomers. *C. R. Chim.* **2007**, 10, 775, https://doi.org/10.1016/j.crci.2007.05.004.

36. Itsuno, S; Tkahashi, S. Synthesis of chiral polyamides containing an (R,R)-1,2-diphenylethylenediamine monosulfonamide structure and their application to asymmetric transfer hydrogenation catalysis. *ChemCatChem* **2017**, 9, 385, DOI: 10.1002/cctc.201601220.

37. Philip, B.; Sreekumar, K. Synthesis and characterization of chiral main chain polyesters with polar segments tailored for second harmonic generation. *J. Mater. Sci.* **2003**, *38*, 1573, https://doi.org/10.1023/A:1022949320834.

38. Synthesis and properties of optically active polyester-amides from ester-containing chiral dicarboxylic acid and aromatic diamines, *Polym. J.* **1993**, *25*, 65, https://doi.org/10.1295/polymj.25.65.

39. Báez, J.E.; Fernández, Á.M.; Navarro, R.; García, C. Study on the effect of linear alkyl [CH2CH2]m and ether [CH2CH2O]m groups in the α,ω-hydroxy telechelic poly(L-lactide) (HOPLLAOH) and their poly(ester-urethanes) (PEUs). Synthesis and Characterization. *J. Polym. Res.* **2017**, 24, 199, https://doi.org/10.1007/s10965-017-1364-7.

40. Dijkstra, P.J.; Feijen, J. Synthetic pathways to polydepsipeptides. *Macromol. Symp.* **2000**, *153*, 67, DOI: 10.1002/1521-3900(200003)153:13.0.CO;2-F.

41. Nagai, A.; Ochiai, B.; Endo, T. Observation of optical activity in polythiourethane obtained by the controlled cationic ring-opening polymerization of chiral cyclic thiourethane derived from serine. *J. Polym. Sci., Part A: Polym. Chem.* **2005**, 43, 1554, https://doi.org/10.1002/pola.20624.

42. Prashant, G.G.; Takeshi, S.; Yukatsu, S; Katsuaki, K.; Tamaki, N. Chiral polyurethane synthesis leading to π-stacked 2/1-helical polymer and cyclic compounds. *ACS Macro Lett.* **2015**, *49*, 901, https://doi.org/10.1021/acsmacrolett.5b00477.

43. Cheng, X.; Jin, Y.; Fan, B.; Qi, R.; Li, H.; Fan, W. Self-assembly of polyurethane phosphate ester with phospholipid-like structures: spherical, worm-like micelles, vesicles, and large compound vesicles. *ACS Macro Lett.* **2016**, *52*, 238, https://doi.org/10.1021/acsmacrolett.5b00789.

44. Touchard, F.; Fache, F.; Lemaire, M. Polythioureas: Main chain chiral polymers in hydride transfer hydrogenation. *Eur. J. Org. Chem* **2000**, 2000, 3787, https://doi.org/10.1002/1099-0690(200011)2000:22%3C3787::AID-EJOC3787%3E3.0.CO;2-0.

45. Nozaki, K. Asymmetric catalytic synthesis of polyketones and polycarbonates. *Pure Appl. Chem.* **2004**, 76, 541, https://doi.org/10.1351/pac200476030541.

46. Kakuchi, T.; Obata, M. Synthesis and mechanism of a main-chain chiral polymer based on asymmetric cyclopolymerization. *Macromol. Rapid Commun.* **2002**, 23, 395, https://doi.org/10.1002/1521-3927(20020401)23:7<395::AID-MARC395>3.0.CO;2-K.

47. Nakako, H.; Nomura, R.; Masuda, T. Helix inversion of poly(propiolic esters). *Macromolecules* **2001**, 34, 1496, https://doi.org/10.1021/ma001812i.

48. Casolaro, M.; Bottari, S.; Ito, Y. Vinyl polymers based on L-histidine residues. Part 2. Swelling and electric behavior of smart poly(ampholyte) hydrogels for biomedical applications, *Biomacromolecules* **2006**, *7*, 1439, https://doi.org/10.1021/bm0509671.

49. Sanda, F.; Kamatani, J.; Handa, H.; Endo, T. Radical polymerization behavior of a proline-substituted acrylamide. Effect of s-Cis-s-Trans isomerization on the polymerization. *Macromolecules* **1999**, *32*, 2490, https://doi.org/10.1021/ma9814090.

50. Hopkins, T.E.; Wagener, K.B. ADMET synthesis of polyolefins targeted for biological applications. *Macromolecules* **2004**, *37*, 1180, https://doi.org/10.1021/ma035289u.

51. Liu, J.; Lam, J. W. Y.; Tang, B. Z. Acetylenic polymers: syntheses, structures, and functions. *Chem. Rev.* **2009**, 109, 5799, https://doi.org/10.1021/cr900149d.

52. Li, B.S.; Cheuk, K.K.L.; Yang, D.; Lam, J.W.Y.; Wan, L.J.; Bai, C.; Tang, B.Z. Self-assembling of an amphiphilic polyacetylene carrying L-leucine pendants: a homopolymer case. *Macromolecules* **2003**, *3615*, 5447, https://doi.org/10.1021/ma034275l.

53. Kajitani, T.; Okoshi, K.; Sakurai, S.; Kumaki, J.; Yashima, E. Helix-sense controlled polymerization of a single phenyl isocyanide enantiomer leading to diastereomeric helical polyisocyanides with opposite helix-sense and cholesteric liquid crystals with opposite twist-sense. *J. Am. Chem. Soc.* **2006**, *128*, 708, https://doi.org/10.1021/ja0576536.

54. Schwartz, E.; Liegeois, V.; Koepf, M.; Bodis, P; Cornelissen, J.J.L.M.; Brocorens, P.; Beljonne, D.; Nolte, R.J.M.; Rowan, A.E.; Woutersen, S.; Champagne, B. Beta sheets with a twist: The conformation of helical polyisocyanopeptides determined by using vibrational circular dichroism. *Chem.-Eur. J.* **2013**, *19*, 13168, https://doi.org/10.1002/chem.201300073.

55. Sanda, F.; Takata, T.; Endo, T. Synthesis of a novel optically active nylon-1 polymer: anionic polymerization of L-leucine methyl ester isocyanate, *J. Polym. Sci., Part A: Polym. Chem.* **1995**, *33*, 2353, https://doi.org/10.1002/pola.1995.080331408.

56. Biagini, S.C.G.; Davies, R.G.; Gibson, V.C.; Giles, R.M.; Marshall, E.L.; North, M. Ruthenium initiated ring opening metathesis polymerization of amino-acid and -ester functionalized norbornenes and a highly selective chain-end functionalization reaction using molecular oxygen, *Polymer* **2001**, *42*, 6669, https://doi.org/10.1016/S0032-3861(01)00146-X.

57. Allcock, H. R.; Morozowich, N.L. Bioerodible polyphosphazenes and their medical potential. *Polym. Chem.* **2012**, *3*, 578, DOI: 10.1039/C1PY00468A.

58. Shiotsuki, M.; Sanda, F.; Masuda, T. Polymerization of substituted acetylenes and features of the formed polymers. *Polym. Chem.* **2011**, 2, 1044, DOI: 10.1039/C0PY00333F.

59. Qu, J.; Sanda, F.; Masuda, T. Synthesis and chiroptical properties of amino acid-derived poly(methylpropargyl ester)s. *Eur. Polym. J.* **2009**, *45*, 448. https://doi.org/10.1016/j.eurpolymj.2008.10.032.

60. Thomas, G.B.; Lipscomb, C.E.; Mahanthappa, M.K. Amino acid vinyl esters: a new monomer palette for degradable polycationic materials. *Polym. Chem.* **2012**, 3, 741, DOI: 10.1039/C2PY00531J.

61. Sanda, S.; Endo, T. Synthesis and cationic polymerization of a novel optically active vinyl ether with L-proline structure. *Macromol. Chem. Phys.* **1997**, *198*, 1209. https://doi.org/10.1002/macp.1997.021980422.

62. Adams, D.J.; Atkins, D.; Cooper, A.I.; Furzeland, S.; Trewin, A.; Young, I. Vesicles from peptidic side-chain polymers synthesized by atom transfer radical polymerization. *Biomacromolecules* **2008**, *9*, 2997, https://doi.org/10.1021/bm8006693.

63. Chan, B.A.; Xuan, S.; Li, A.; Simpson, M.J.; Sternhagen, G.L.; Yu, T.; Darvish, O.A.; Jiang, N.; Zhang, D. Polypeptoid polymers: synthesis, characterization, and properties. *Biopolymers* **2018**, 109, e23070, https://doi.org/10.1002/bip.23070.

64. Zhi, J.; Zhu, Z.; Liu, A.; Cui, J.; Wan, X.; Zhou, Q. Odd-even effect in free radical polymerization of optically active 2,5-bis[(40-alkoxycarbonyl)-phenyl]styrene. *Macromolecules* **2008**, 41, 1594, DOI: 10.1021/ma8000115.

65. Bai, J.; Zhang, C.; Liu, L.; Liu, W.; Shen, X.; Xu, X.; Fan, L. Synthesis of polymethylacrylamide carrying R-phenylglycine pendant groups and effect of hydrogen bonds on main chain helicity. *Eur. Polym. J.* **2014**, *50*, 214. https://doi.org/10.1016/j.eurpolymj.2013.10.032.

66. Sakai, R.; Sakai, N.; Satoh, T.; Li, W.; Zhang, A.; Kakuchi, T. Strict size specificity in colorimetric anion detection based on poly(phenylacetylene) receptor bearing second generation lysine dendrons. *Macromolecules* **2011**, 44, 4249, https://doi.org/10.1021/ma200710r.

67. Xu, X.D.; Zhu, Y.Q.; Li, H.; Feng, S.W.; Dai, H.C.; Shen, X.D.; Bai, J.W.; Zhang L.L.; Okamoto, Y. Stereospecific radical polymerization of optically active (meth)acrylamides: study on the mechanism of stereocontrol. *Acta Polym. Sin.* **2013**, *3*, 286, DOI: 10.3724/SP.J.1105.2013.12380.

68. Tabei, J.; Shiotsuki, M.; Sanda, F.; Masuda, T. Effect of chiral substituents on the secondary structure of poly(N-alkynylamides). *Macromolecules* **2005**, *38*, 5860, https://doi.org/10.1021/ma050313k.

69. Takata, T.; Ishiwari, F.; Sato, T.; Seto, R.; Koyama, Y. Synthesis, structure, and properties of polyacetylenes possessing chiral spirobifluorene moieties in the side chain, *Polymer Journal* 2008, 40, 846, doi:10.1295/polymj.PJ2008104.

70. Maeda, K; Yashima, E. Helical polyacetylenes induced via noncovalent chiral interactions and their applications as chiral materials. *Top Curr. Chem. Z*, **2017**, 375, 72, DOI 10.1007/s41061-017-0161-4.

71. Bauri, K.; Roy, S.G.; De, P. Side-chain amino-acid-derived cationic chiral polymers by controlled radical polymerization. *Macromol. Chem. Phys.* **2016**, 217, 365, https://doi.org/10.1002/macp.201500271.

72. Karimi, P.; Rizkalla, A.S.; Mequanint, K. Versatile biodegradable poly(ester amide)s derived from amino-acids for vascular tissue engineering. *Materials* **2010**, *3*, 2346, DOI:10.3390/ma3042346.

73. Sanda, F.; Nakamura, M.; Endo, T. Syntheses and radical copolymerization behavior of optically active methacrylamides having L- and D-leucine moieties. Interaction between L- and D-forms. *Macromolecules* **1996**, *29*, 8064, https://doi.org/10.1021/ma960906i.

74. Casolaro, M.; Casolaro, I. Stimuli-responsive hydrogels bearing α-amino acid residues: a potential platform for future therapies. *J. Biomed. Eng. Med. Device* **2016**, *1*, 111, DOI: 10.4172/2475-7586.1000111.

75. Mori, H.; Kato, I.; Endo, T. Dual-stimuli-responsive block copolymers derived from proline derivatives. *Macromolecules* **2009**, *42*, 4985, https://doi.org/10.1021/ma900706s.

76. Maji, T.; Banerjee, S.; Bose, A.; Mandal, T.K. A stimuli-responsive methionine-based zwitterionic methacryloyl sulfonium sulfonate monomer and the corresponding antifouling polymer with tunable thermosensitivity. *Polym. Chem.* **2017**, *8*, 3164. DOI 10.1039/C7PY00460E.

77. Maji, T.; Banerjee, S.; Biswas, Y.; Mandal, T.K. Dual-stimuli-responsive L-serine-based zwitterionic UCST-type polymer with tunable thermosensitivity. *Macromolecules* **2015**, *48*, 4957, https://doi.org/10.1021/acs.macromol.5b01099.

78. Gao, G.; Sanda, F.; Masuda, T. Synthesis and properties of amino acid-based polyacetylenes. *Macromolecules* **2003**, *36*, 3932, https://doi.org/10.1021/ma021738z.

79. Cheuk, K.K.L.; Li, B.S.; Lam, J.W.Y.; Xie, Y.; Tang, B.Z. Synthesis, chain helicity, assembling structure, and biological compatibility of poly(phenylacetylene)s containing L-alanine moieties. *Macromolecules* **2008**, *41*, 5997, https://doi.org/10.1021/ma800976e.

80. Hopkins, T.E.; Pawlow, J.H.; Koren, D.L.; Deters, K.S.; Solivan, S.M.; Davis, J.A.; Gómez, F.J.; Wagener, K.B. Chiral polyolefins bearing amino acids. *Macromolecules* **2001**, *34*, 7920–7922. https://doi.org/10.1021/ma010930i.

81. Allcock, H.R.; Pucher, S.R.; Scopelianos, A.G. Poly[(amino acid ester)phosphazenes] as substrates for the controlled release of small molecules. *Biomaterials* **1994**, *15*, 563. https://doi.org/10.1016/0142-9612(94)90205-4.

82. Sugiyama, K.; Rikimaru, S.; Okada, Y.; Shiraishi, K. Preparation and application of chiral recognizable thermosensitive polymers and hydrogels consisting of N-methacryloyl-S-phenylalanine methyl ester. *J. Appl. Polym. Sci.* **2001**, *82*, 228. DOI: 10.1002/app.1842.

83. Ladmiral, V.; Charlot, A.; Semsarilar, M.; Armes, S.P. Synthesis and characterization of poly(amino acid methacrylate)-stabilized diblock copolymer nano-objects. *Polym. Chem.* **2015**, *6*, 1805, DOI: 10.1039/C4PY01556H.

84. Roy, S.G.; De, P. pH responsive polymers with amino acids in the side chains and their potential applications. *J. Appl. Polym. Sci.* **2014**, *131*, 41084. https://doi.org/10.1002/app.41084.

85. Wang, X.; Gan, H.; Sun, T.; Su, B.; Fuchs, H.; Vestweber, D.; Butz, S. Stereochemistry triggered differential cell behaviours on chiral polymer surfaces. *Soft Matter* **2010**, *6*, 3851. DOI 10.1039/C0SM00151A.

86. Ranucci, E.; Manfredi, A. Polyamidoamines: versatile bioactive polymers with potential for biotechnological applications. *Chemistry Africa* 2019, 2, 167, https://doi.org/10.1007/s42250-019-00046-1.

87. Ferruti, P. Poly(amidoamine)s: past, present, and perspectives. *J. Polym. Sci. Part A Polym. Chem.* **2013**, *51*, 2319, https://doi.org/10.1002/pola.26632.

88. Ferruti, P.; Ranucci, E.; Manfredi, A.; Mauro, N.; Ferrari, E.; Bruni, R.; Colombo, F.; Mussini, P.R.; Rossi, M. L-lysine and EDTA polymer mimics as resins for the quantitative and reversible removal of heavy metal ion water pollutants. *J. Polym. Sci., Part A: Polym. Chem.* **2012**, *50*, 5000, https://doi.org/10.1002/pola.26330.

89. Manfredi, A.; Ranucci, E.; Morandi, S.; Mussini, P.R.; Ferruti, P. Fast and quantitative manganese sorption by polyamidoamine resins. *J. Polym. Sci., Part A: Polym. Chem.* **2013**, *51*, 769, DOI: 10.1002/pola.26462.

90. Ferruti, P.; Ranucci, E.; Tempesti, E.; Giuffrè, L.; Arlati, P.; Airoldi, G. *J. Appl. Polym. Sci.* **1990**, *41*, 1923.

91. Ranucci, E.; Putelli, L.; Ferruti, P.; Ferrari, V.; Marioli, D.; Taroni, A. Use of poly(amidoamines) as CO_2- and Si_2-sensitive material for gravimetric sensors. *Mikrochim. Acta* **1995**, *120*, 257. https://doi.org/10.1007/BF01244436.

92. Ranucci, E.; Ferruti, P.; Ferrari, V.; Marioli, D.; Taroni, A. Multifunctional polymers for sensing applications. *Polym. Advan. Technol.* **1996**, *7*, 529, https://doi.org/10.1002/(SICI)1099-1581(199605)7:5/6<529::AID-PAT542>3.0.CO;2-A.

93. Sartore, L.; Penco, M.; Della Sciucca, S.; Borsarini, G.; Ferrari, V. New carbon black composite vapor detectors based on multifunctional polymers. *Sensors Actuat. B Chem.* **2005**, *111*, 160, https://doi.org/10.1016/j.snb.2005.07.032.

94. Manfredi, A.; Carosio, F.; Ferruti, P.; Ranucci, E.; Alongi, J. Linear polyamidoamines as novel biocompatible phosphorus-free surface-confined intumescent flame retardants for cotton fabrics. *Polym. Degrad. Stabil.* **2018**, *151*, 52, DOI: 10.1016/j.polymdegradstab.2018.02.020.

95. Manfredi, A.; Carosio, F.; Ferruti, P.; Alongi, J.; Ranucci, E. Disulfide-containing polyamidoamines with remarkable flame retardant activity for cotton fabrics. *Polym. Degrad. Stabil.* **2018**, *156*, 1, DOI: 10.1016/j.polymdegradstab.2018.07.028.

96. Manfredi, A.; Mauro, N.; Terenzi, A.; Alongi, J.; Lazzari, F.; Ganazzoli, F.; Raffaini, G.; Ranucci, E.; Ferruti, P. Self-ordering secondary structure of D- and L-arginine-derived polyamidoamino acids. *ACS Macro Lett.* **2017**, 6, 987–991, doi:10.1021/acsmacrolett.7b00492.

97. Ferruti, P.; Mauro, N.; Falciola, L.; Pifferi, V.; Bartoli, C.; Gazzarri, M.; Chiellini, F.; Ranucci, E. Amphoteric, prevailingly cationic L-arginine polymers of poly(amidoamino acid) structure: Synthesis, acid/base properties and preliminary cytocompatibility and cell- permeating characterizations. *Macromol. Biosci.* **2014**, 14, 390–400, doi:10.1002/mabi.201300387.

98. Futaki, S.; Suzuki, T.; Ohashi, W.; Yagami, T.; Tanaka, S.; Ueda, K.; Sugiura, Y. Arginine-rich peptides: an abundant source of membrane-permeable peptides having potential as carriers for intracellular protein delivery. *Biol. Chem.* **2001**, *276*, 5836, doi: 10.1074/jbc.M007540200.

99. Vives, E.; Brodin, P.; Lebleu, B. A truncated HIV-1 Tat protein basic domain rapidly translocates through the plasma membrane and accumulates in the cell nucleus. *J. Biol. Chem.* **1997**, *272*, 16010, doi: 10.1074/jbc.272.25.16010.

100. Zintchenko, A.; Van der Aa, L.J.; Engbersen, J.F.J. Improved synthesis strategy of poly(amidoamine)s for biomedical applications: catalysis by "green" biocompatible earth

alkaline metal salts. *Macromol. Rapid Commun.* **2011**, *32*, 321, https://doi.org/10.1002/marc.201000545.

101. Ferruti, F.; Alongi, J.; Manfredi, A.; Ranucci, E.; Ferruti, P. Controlled synthesis of linear polyamidoamino acids. *Polymers* **2019**, 11, 1324, DOI: 10.3390/polym11081324.

102. Kelly, S.M.; Price, N.C. The use of circular dichroism in the investigation of protein structure and function. *Curr. Protein Pept. Sci.* **2000**, *1*, 349, DOI: 10.2174/1389203003381315.

103. Bag, S.D.; Rao, B. Chiral copolymers of (R)-N-(1-phenylethyl) methacrylamide and 2-hydroxyethyl methacrylate: copolymerization characteristics and chiroptical properties. *Polym. Int.* **2010**, *59*, 501, https://doi.org/10.1002/pi.2728.

104. Bai, J.; Zhang, C.; Liu, L.; Liu, W.; Shen, X.; Xu, X.; Fan, L. Synthesis of polymethylacrylamide carrying R-phenylglycine pendant groups and effect of hydrogen bonds on main chain helicity, *Eur. Polym. J.* **2014**, 50, 214, https://doi.org/10.1016/j.eurpolymj.2013.10.032.

105. Tang, H.; Zhao, W.; Yu, J.; Li, Y.; Zhao, C. Recent development of pH-responsive polymers for cancer nanomedicine. *Molecules* **2019**, *24*, 4, doi:10.3390/molecules24010004

106. Pescitelli, G.; Di Bari, L.; Berova, N. Application of electronic circular dichroism in the study of supramolecular systems**.** *Chem. Soc. Rev***.** **2014**, *43***,** 5211, DOI 10.1039/C4CS00104D.

107. Zhang, H.; Zheng, X.; Kwok, R.T.K.; Wang, J.; Leung, N.L.C.; Shi, L.; Sun, J.Z.; Tang, Z.; Lam, J.W.Y; Qin, A.; Tang, B.Z. In situ monitoring of molecular aggregation using circular dichroism. *Nat. Commun.* **2018**, *9*, 4961. DOI: 10.1038/s41467-018-07299-3.

108. Sitsanidis, E.D.; Piras, C.C.; Alexander, B.D.; Siligardi, G.; Jávorfi, T.; Hall, A.J.; Edwards, A.A. Circular dichroism studies of low molecular weight hydrogelators: The use of SRCD and addressing practical issues. *Chirality* 2018, 30, 708, DOI: 10.1002/chir.22850.

109. Hecht, L.; Barron, L.D. Raman optical activity. In *Modern techniques in Raman spectroscopy*. Laserna JJ. (Ed.), Wiley, 1996, Chichester, 295-298.

110. Barron, L.D.; Hecht, L. Vibrational Raman optical activity: from fundamentals to biochemical application. In *Circular dichroism: interpretation and applications*. Nakanishi, K.; Berova, N.D.; Woody, R.W. (Eds), VCH Publishers, 1994, New York, p.667-702.

111. Barron, L.D.; Zhu, F.; Hecht, L. Raman optical activity: an incisive probe of chirality, and of biomolecular structure and behavior. *Vib. Spectrosc.* **2006**, *42*, 15, https://doi.org/10.1016/j.vibspec.2006.04.020.

112. Merten, C.; Barron, L.D.; Hecht, L.; Johannessen, C. Determination of the helical screw sense and side-group chirality of a synthetic chiral polymer from Raman Optical Activity. *Angew. Chem. Int.* **2011**, *50*, 9973, https://doi.org/10.1002/anie.201104345.

113. Bonato, P.S.; Lanchote, V.L.; Bortocan, R.; Jabor, V.A.P.; Paias, F.O.; Ricci-Júnior, E.; Carvalho, R. Chiral stationary phases based on cellulose and amylose tris-3,5-dimethylphenylcarbamate derivatives for the resolution of selected chiral drugs and metabolites. *J. Liq. Chrom. Relat. Tech.* **1999**, *22*, 1813, DOI: 10.1081/JLC-100101768.

114. Zhang, T.; Nguyena, D.; Franco, P.; Murakami, T.; Ohnishi, A.; Kurosawa, H. Cellulose 3,5-dimethylphenylcarbamate immobilized on silica a new chiral stationary phase for the analysis of enantiomers. *Analytica Chimica Acta* **2006**, *557*, 221, https://doi.org/10.1016/j.aca.2005.10.017.

115. Harada, N.; Saito, A.; Koumura, N.; Roe, D.C.; Jager, W.F.; Zijlstra, R.W.J.; de Lange, B.; Feringa, B.L. Chemistry of unique chiral olefins. 2. Unexpected thermal racemization of cis-1,1′,2,2′,3,3′,4,4′-Octahydro-4,4′- biphenanthrylidene. *J. Am. Chem. Soc.* **1997**, *119*, 7249, https://doi.org/10.1021/ja970668m.

116. Sedo, J.; Ventosa, N.; Ruiz-Molina, D.; Mas, M.; Molins, E.; Rovira, C.; Veciana, C. Crystal structures of chiral diastereoisomers of a carbon-based high-spin molecule. *J. Angew. Chem. Int. Ed. Engl.* **1998**, *37*, 330, https://doi.org/10.1002/(SICI)1521-3773(19980216)37:3<330::AID-ANIE330>3.0.CO;2-0.

117. Medina, D.D.; Mastai, Y. Chiral polymers and polymeric particles for enantioselective crystallization. *Isr. J. Chem.* **2018**, *58*, 1330, DOI: 10.1002/ijch.201800174.

118. Zhang, X.; Yin, J.; Yoon, J. Recent advances in development of chiral fluorescent and colorimetric sensors. *Chem. Rev.* **2014**, *114*, 4918, dx.doi.org/10.1021/cr400568b

2

pH Dependence and self-assembly of polyamidoamino acids derived from natural α-amino acids

Manfredi, A.; Mauro, N.; Terenzi, A.; Alongi, J.; Lazzari, F.; Ganazzoli, F.; Raffaini, G.; Ranucci, E.; Ferruti, P. *ACS Macro Lett.* **2017**, 6, 987-991, DOI: 10.1021/acsmacrolett.7b00492.

Lazzari, F.; Manfredi, A.; Alongi, J.; Mendichi, R.; Ganazzoli, F.; Raffaini, G.; Ferruti, P.; Ranucci, E. *Polyme*rs **2018**, 10, 1261. https://doi.org/10.3390/polym10111261

2.1 INTRODUCTION

In literature [1] many examples of chiral polymers obtained from natural α-amino acids can be found. These are generally synthesized either by the radical polymerization of the N- or C-terminus functionality of amino acids [2-4] or by the Michael type polyaddition with acrylamide-terminal monomers, as for PAACs. These bioinspired polymers show interesting properties: pH-dependent solubility [5], self-assembly ability [6], thermosensitivity [7,8], chirality-induced structuring in solution [9-11] and chiral recognition [12,13] abilities, as preferential interactions with chiral biomolecules or cell components [13].

In this chapter, three classes of PAACs will be presented and their solution properties determined: i) basic PAACs, obtained from *L*-, *D*- or *D,L*-arginine (ARGO7 stereoisomers) [14,15]; ii) alkyl-substituted PAACs, obtained from *L*-alanine (M-*L*-Ala), *L*-valine (M-*L*-Val) and *L*-leucine (M-*L*-Leu) [16]; polar-bearing residues PAACs, obtained from *L*-glutamine (M-*L*-Gln). Polyelectrolyte acid-base behavior, pH-dependent self-structuring in water and size were firstly determined for all PAACs. Then, for M-*L*-Gln formation of hydrogen bonding was additionally assessed. In all cases, theoretical modeling studies were carried out at Politecnico di Milano to better understand conformational properties. A comparison between these three classes of polymers will also be discussed.

2.2 EXPERIMENTAL SECTION

2.2.1 Materials

Solvents and reagents, unless otherwise indicated, were analytical-grade commercial products and used as received. Tris(hydroxymethyl)aminomethane (TRIS) (≥99.8%), sodium chloride (99.5%), guanidine hydrochloride (99%), *L*-arginine (*L*-Arg, >98.5%), *D*-arginine (*D*-Arg, >99%), *D,L*-arginine (*D,L*-Arg, >98.5%), *L*-leucine (*L*-Leu, ≥98%), *L*-valine (*L*-Val, ≥98%,) and *L*-alanine (*L*-Ala, ≥98%) were purchased from Sigma-Aldrich (Milano, Italy). *N,N′*-Methylenebisacrylamide (MBA, 96%) purchased from Acros Organics (Milano, Italy) and LiOH monohydrate (≥ 98%) was supplied by Honeywell Fluka (Steinheim, Westphalia, Germany). HCl and NaOH volumetric standard solutions were purchased from Fluka analytics (Milano, Italy). Ultrapure water (18 MΩ·cm^{-1}), produced with a Millipore Milli-Q® apparatus (Darmstadt, Hesse, Germany), was used to prepare all solutions.

2.2.2 Instruments and methods

^{1}H and ^{13}C NMR spectra of ARGO7 and alkyl-substituted PAACs were recorded in D_2O at 25 °C using a Bruker Avance DPX-400 NMR (Bruker, Milano, Italy) operating at 400.13 MHz and 100.40 MHz, respectively. Spectra were recorded at pH 4.5.

^{1}H and ^{13}C NMR spectra of M-*L*-Gln were obtained in D_2O and H_2O-D_2O 9:1 at 25 °C using a Bruker Avance III 400 MHz and a Bruker Avance 600 MHz. For variable temperature analysis, NMR spectra of polymer at pH 4.5 and pH 1 were recorded in a range from 298 K to 338 K. The TOCSY spectra, with a mixing time of 80 ms, allowed the identification of the spin systems correlations. NOESY experiments with mixing times of 200 and 700 ms were used to evaluate the spatial correlations. In the 1D, TOCSY, NOESY, solvent suppression was achieved by using the excitation sculpting pulse sequence. HSQC and HMBC with J=8Hz were used to confirm carbon assignment. DOSY spectra were acquired with the standard Bruker sequence with presaturation during relaxation delay for water suppression. For the determination of the diffusion coefficient D, a big delta of 200 ms and a little delta of 2500 us were used.

Fourier-Transform Infrared spectroscopy was recorded in Attenuated Total Reflectance configuration (FTIR-ATR) performing 16 scans at 4 cm^{-1} resolution in the 4000–500 cm^{-1} range, using a Perkin Elmer Spectrum 100 spectrometer (Milano, Italy) equipped with a diamond crystal (penetration depth = 1.66 µm). Before analysis, samples were dried under a vacuum to constant weight.

Size exclusion chromatography (SEC) traces were obtained for all PAACs with Toso-Haas TSK-gel G4000 PW and TSK-gel G3000 PW columns connected in series, using a Waters model 515 HPLC pump (Milano, Italy) equipped with a Knauer autosampler 3800 (Knauer, Bologna, Italy), a light scattering (670 nm), a viscometer Viscotek 270 dual detector (Malvern, Roma, Italy) and a refractive index detector (Waters, Model 2410, Milano, Italy). The mobile phase was a 0.1 M Tris buffer (pH 8.00 ± 0.05) solution with 0.2 M sodium chloride. Sample concentration: 20 mg mL^{-1}; flow rate: 1 mL min^{-1}; injection volume: 20 µL; loop size: 20 µL; column dimensions: 300 × 7.5 mm^2. The instrument optical constants were determined using PEO 19 kDa as a narrow polymer standard. All samples were filtered through a 0.2 µm syringe Whatman filter before measurements.

Dynamic light scattering (DLS) analyses were carried out on 0.5-20 mg mL^{-1} polymer solutions prepared in ultrapure water, using a Malvern Zetasizer NanoZS instrument (Malvern, Roma, Italy), equipped with a laser fitted at 532 nm and fixed 173° scattering angle. Before analyses, samples were filtered through a 0.2 μm syringe Whatman filter. The solution pH was adjusted to the selected value using 0.1 M HCl or 0.1 M NaOH aqueous solutions. Measurements were performed in triplicate, and each value was reported as the average of 10 runs.

Circular dichroism (CD) spectra of ARGO7 isomers were recorded at Università degli Studi di Palermo using a JASCO J-715 spectropolarimeter, employing 1 cm path-length quartz cells and the following parameters: range 210–400 nm, stop r: 0.2 nm, speed: 200 nm min-1, accumulation: 4, response: 0.5 s, bandwidth: 1 nm. The temperature was controlled through a Peltier system. Stock solutions were prepared by directly solubilizing ARGO7 homopolymers (*L, D* or *D,L*) in MilliQ water. Final samples were obtained by dilution to the desired concentration (≈ 0.26 mM, expressed as concentration of the repeating units) with NaCl and guanidinium chloride solutions at the indicated concentrations and pHs.

Circular dichroism spectra of M-*L*-Ala, M-*L*-Val and M-*L*-Leu were obtained using a JASCO J-500CD spectrometer (Jasco Europe Srl, Lecco, Italy), by scanning from 200 to 300 nm in a 1 cm path-length quartz cell at 50 nm min^{-1} scan speed. Each spectrum was the average of 3 measurements. These solutions were prepared at 0.5 $\text{mg}\cdot\text{mL}^{-1}$ concentration, dissolving each polymer in either 0.1 M NaCl or 2 M urea or guanidinium chloride solutions. Before recording spectra, samples were thermostated for 1 h at the desired temperature and pHs. The latter was adjusted using 0.1 M HCl or 0.1 M NaOH aqueous solutions and measured by a combined Metrohm microelectrode (Varese, Italy). CD spectra were normalized based on the molar concentration of the repeating units (≈1.83 ± 0.17 mM) and reported as Molar Ellipticity (θ expressed as mdeg $\text{M}^{-1}\cdot\text{cm}^{-1}$).

Acid-base properties were determined by potentiometric titrations, according to the following procedure: samples were dissolved in 0.1 M NaCl solutions (7 mL) to reach the final concentration of 0.05 M of repeating unit. Solutions, deaerated by continuous ultrapure N_2 bubbling and thermostated at 25 °C, were potentiometrically titrated forward with 0.1 M NaOH and backward with 0.1 M HCl. In forward titrations, the pH was previously adjusted to 1.8-2.0 with 1.0 M HCl, while in backward titrations pH was previously adjusted to 11.8-12.0 with 1.0 M NaOH. The pH-meter, a Primatrode with a NTC electrode connected to an 827 pH lab Metrohm, was calibrated against two pH standard buffers, thermostated at 25 °C. All titration experiments were performed in quadruplicate.

pKa determination. The pK_{a1} (side -COOH) and pK_{a2} (chain *tert*-amine) values were determined by potentiometric titrations. As an example, ARGO7 equilibria and ionizable functions were reported in Figure 1. Each pK_a were identified as the pH values at the half-equivalent points, located in the buffer zone of each specific function (side -COOH and *tert*-amine). The half-equivalent points were obtained as the half-titrant volume amounts added between consecutive inflections in the pH versus titrant volume curves (Figure 18). The inflection points were in turn determined by numerically calculating the second derivative of the pH versus volume curves. For ARGO7, the pK_{a3} value of the guanidine group was not experimentally determined but assumed to be equal to 13.0.

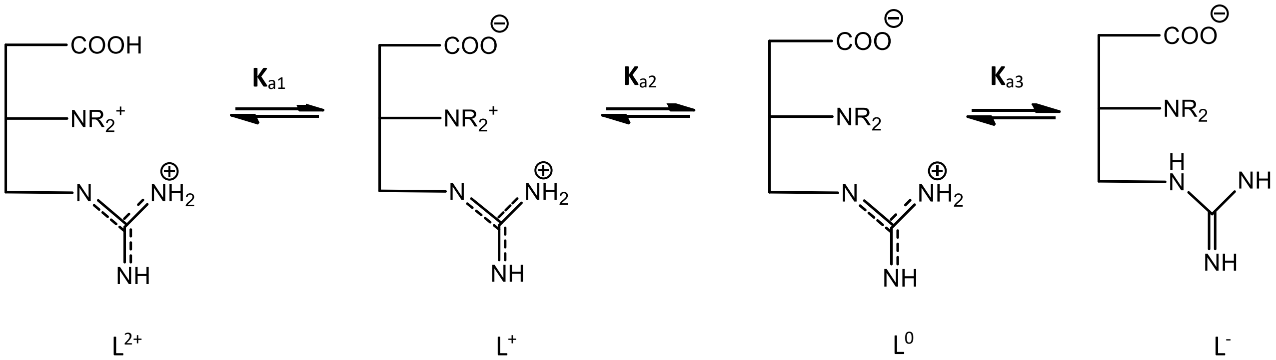

Figure 1. Simplified sketch of ARGO7 ionic species: L^{2+} doubly positively charged; L^{+} positively charged zwitterionic; L^{0} neutral zwitterionic; L^{-} negatively charged.

β parameter determination. The *β* parameters of the generalized Henderson-Hasselbalch equation (Eq. 1a) were determined for both pK_{a1} (side -COOH) and pK_{a2} (chain *tert*-amine) to ascertain the presence of interactions between ionizable groups on adjacent monomeric units. They were determined by firstly selecting the specific buffer region intervals marked by each pK_a. The dissociation degree, *α*, was then calculated in each zone as the ratio between the reacted moles and the total amount of moles necessary to reach complete neutralization. *β* Values were finally obtained from Eq. 1b as the slope of the pH versus –log((1-*α*)/*α*) curve (Figure A4). Points near inflections deviated from ideality and were not considered.

$$pK_a = pH + b' \log\frac{1-a}{a} \quad \text{(Eq. 1a)} \qquad \leftrightarrow \quad pH = pK_a - b \times \log\frac{1-a}{a} \quad \text{(Eq. 1b)}$$

Determination of simulated titration curves. Simulated titration curves were determined following the De Levie approach [17] to iteratively refine *pKa* and *β* values to achieve the best fitting to the experimental data. For ARGO7 isomers, calculations were made based on the following considerations:

- Initial conditions:

V_0 = initial solution volume
c_0 = initial PAACs concentration expressed as molarity of the repeat unit
c_S = initial concentration of ionic strength stabilizer
c_t = titrant concentration (strong base in forward titration or acid in backward titration)
V_t = volume of the titrant added (strong base in forward titration or acid in backward titration)
c_A or c_B = acid concentration (or base in backward titration) used to correct pH
N = moles of strong acid possibly present as residual from the synthetic process or PAACs pretreatments

- *Mass balance:*

$$C_{PAACS} = C_{L^{2+}} + C_{L^{+}} + C_{L^{0}} + C_{L^{-}} = \frac{C_0 V_0}{V_0 + V_t} \qquad \text{(Eq. 2)}$$

- *Equilibrium constants* (Eq. 3a-d):

$$K_{a1} = \frac{C_{L^{+}} C_{H^{+}}}{C_{L^{2+}} y^2} \text{ (a);} \quad K_{a2} = \frac{C_{L^{0}} C_{H^{+}}}{C_{L^{+}}} \text{ (b);} \quad K_{a3} = \frac{C_{L^{-}} C_{H^{+}} y^2}{C_{L^{0}}} \text{ (c);} \qquad K_w = C_{H^{+}} C_{OH^{-}} y^2 \text{ (d)}$$

- *Concentration fractions* (Eq. 4a-d):

$$\alpha_3 = \frac{C_{L^{2+}}}{C} = \frac{C_{H^{+}}^3}{D} \text{ (a);} \quad \alpha_2 = \frac{C_{L^{-}}}{C} = \frac{C_{H^{+}}^2 y^2 K_{a1}}{D} \text{ (b);} \quad \alpha_1 = \frac{C_{L^{0}}}{C} = \frac{C_{H^{+}} y^2 K_{a1} K_{a2}}{D} \text{ (c);}$$

$$\alpha_0 = \frac{C_{L^{-}}}{C} = \frac{K_{a1} K_{a2} K_{a3}}{D} \text{ (d)}$$

with:

$$\mathrm{D} = \mathrm{C}_{\mathrm{H}^{+}}^3 + \mathrm{C}_{\mathrm{H}^{+}}^2 \mathrm{y}^2 \mathrm{K}_{\mathrm{a1}} + \mathrm{C}_{\mathrm{H}^{+}} \mathrm{y}^2 \mathrm{K}_{\mathrm{a1}} \mathrm{K}_{\mathrm{a2}} + \mathrm{K}_{\mathrm{a1}} \mathrm{K}_{\mathrm{a2}} \mathrm{K}_{\mathrm{a3}} \qquad \text{(Eq. 5)}$$

The activity coefficients (Davies equation):

$$y = 10^{-0.5\left[\frac{\sqrt{I}}{1+\sqrt{I}} - 0.3I\right]} \qquad \text{(Eq. 6)}$$

Ionic strength:

$$I = \frac{1}{2}(C_{H^+} + C_{OH^-} + C_{Na^+} + C_{Cl^-} + 4C_{L^{2+}} + C_{L^+} + C_{L^-}) \qquad \text{(Eq. 7)}$$

- <u>Charge balance</u>:

$$H^+ + Na^+ + 2L^{2+} + L^+ = L^- + OH^- + Cl^- \qquad \text{(Eq. 8)}$$

where (Eq. 9a-f):

$$C_{Na^+} = \frac{C_T V_T + C_S V_0}{V_0 + V_T}\ \text{(a)}; \qquad C_{Cl^-} = \frac{C_S V_0 + C_A V_A + N}{V_0 + V_T}\ \text{(b)}; \qquad C_{L^{2+}} = \frac{\alpha_3 C_0 V_0}{V_0 + V_T}\ \text{(c)}; \quad C_{L^+} = \frac{\alpha_2 C_0 V_0}{V_0 + V_T}\ \text{(d)};$$

$$C_{L^-} = \frac{\alpha_0 C_0 V_0}{V_0 + V_T}\ \text{(e)}; \qquad C_{OH^-} = \frac{K_w}{C_{H^+} y^2}\ \text{(f)}$$

Combining all former conditions, the following solving equation, representing the whole forward titration curve, was obtained in terms of V_T as a function of pH:

$$V_T = \frac{V_0[C_0(\alpha_0 - \alpha_2 - 2\alpha_3) + C_A - \Delta] + N}{\Delta + C_T} \qquad \text{(Eq. 10)}$$

where:

$$\Delta = H^+ - OH^- = H^+ - {}^{K_w}/_{H^+ y^2} \qquad \text{(Eq. 11)}$$

For M-*L*-Ala, M-*L*-Val and M-*L*-Leu, the L^{2+} terms should not be considered. All expressions were simplified into the following final equations:

$$V_T = \frac{V_0[C_0(\alpha_0 - \alpha_2) + C_A - \Delta] + N}{\Delta + C_T} \qquad \text{(Eq. 12)}$$

and the whole backward titration:

$$V_T = \frac{V_0[C_0(\alpha_0 - \alpha_2) + C_A - \Delta] + N - (\Delta + C_B)V_B}{\Delta - C_T} \qquad \text{(Eq. 13)}$$

Simulated titration curves were obtained from Eq. 10-13 in the buffer regions relative to both side -COOH and *tert*-amine groups. Calculation were carried out considering C_{Na^+} and C_{Cl^-} constant throughout the whole titration experiment, and equal to 0.1 M. Concentration fractions α and pK_a values were refined iteratively to achieve the best fitting to the experimental points.

Determination of speciation diagrams. Speciation diagrams were obtained by plotting the concentration fractions of the differently ionic species as a function of pH (Eq. 14a-d).

ARGO7 concentration fractions:

$$\alpha_3 = \frac{C_{L^{2+}}}{C} = \frac{C_{H^+}^3}{D} \quad \text{(a);} \qquad \alpha_2 = \frac{C_{L^-}}{C} = \frac{C_{H^+}^2 y^2 K_{a1}}{D} \quad \text{(b);} \qquad \alpha_1 = \frac{C_{L^0}}{C} = \frac{C_{H^+} y^2 K_{a1} K_{a2}}{D} \quad \text{(c);}$$

$$\alpha_0 = \frac{C_{L^-}}{C} = \frac{K_{a1} K_{a2} K_{a3}}{D} \quad \text{(d)}$$

M-*L*-Ala, M-*L*-Val, M-*L*-Leu concentration fractions:

$$\alpha_2 = \frac{C_{L^-}}{C} = \frac{C_{H^+}^2}{D} \quad \text{(a);} \qquad \alpha_1 = \frac{C_{L^0}}{C} = \frac{C_{H^+} y^2 K_{a1}}{D} \quad \text{(b);} \qquad \alpha_0 = \frac{C_{L^-}}{C} = \frac{K_{a1} K_{a2}}{D} \quad \text{(c)}$$

With D and y as previously described, and where the K_{a1} and K_{a2} values were corrected for β_1 and β_2.

Molecular Dynamics Simulations were performed at Politecnico di Milano [18-20], with InsightII/Discover 20002 using the consistent valence force field CVFF [21]. For L-ARGO7, simulations at different pH were carried out assuming i) at pH 1 full protonation of the amino group in the main chain and of the *L*-arginine guanidinium side group, with a total charge of +20e; ii) at pH 6, full protonation of the guanidinium moiety for a total charge of +10e; iii) at pH 14, full deprotonation of the carboxyl group and of the guanidinium moiety with a total charge of -10e at pH 14. In the case of M-*L*-Ala, M-*L*-Val and M-*L*-Leu simulations were carried out in order to have a positive (L^+), a null (L^0) and a negative (L-) charge per repeat unit, that is: i) at pH 1 when the total charge was +10e, ii) at the isoelectric point (pH 5) and iii) at pH 11 when the total charge was -10e.

Starting from an extended conformation of the polymer chains, after an initial geometry optimization, the molecules were subjected to long MD runs: the first lasting 5 ns, in an effective medium with a distance-dependent dielectric constant, and the second for 0.5 ns in explicit water, adopting a cubic cell with a size of 44 Å of about 2640 water molecules. Equilibration of the system was reached within the initial 1000 ps in the effective dielectric medium, and within 200 ps in water, due to the random collisions with the solvent molecules. It was monitored through the time change of the total and potential energy together with its components (such as the Coulomb, the Van Der Waals and the torsional components), and of the end-to-end distance. The dynamic equations were integrated using the Verlet algorithm with a time step of 1 fs at a temperature of 300 K, controlled through the Berendsen thermostat. The instantaneous coordinates were periodically saved for further analysis. All the energy minimizations where carried out with the conjugate gradient method up to an energy gradient lower than $4x10^{-3}$ kJ mol^{-1} $Å^{-1}$.

2.2.3 Synthesis of PAACs

L-, *D*- or *D,L*-arginine (2.191 g, 12.453 mmol) was added to a dispersion of *N,N'*-methylenebisacrylamide (2.000 g, 12.453 mmol) in water (4.1 mL) under stirring. The resultant slurry was warmed under stirring to 50 °C, gradually becoming homogeneous solution. The reaction mixture was kept in the dark at the same temperature with occasional stirring for 6 days. After this time, the reaction mixture was acidified to pH 3.5 with 6 M hydrochloric acid and ultrafiltered through a membrane with nominal molecular weight cut-off 100 kDa to eliminate possible particulate impurities. The passed-through portion was then further ultrafiltered through a membrane with nominal cut-off 5 kDa. The product, an off-white powder, was then retrieved from the retained portion by freeze-drying.

Table 1. Yields, weight-average molecular weights and polydispersity index of *D*-, *L*- and *D,L*-ARGO7.

Sample	Yield (%)	M_w	M_w/M_n [a)]
D-ARGO7	88	7700	1.54
L-ARGO7	92	6500	1.43
D,L-ARGO7	90	6800	1.48

[a] M_w and M_n: weight- and number-average molecular mass.

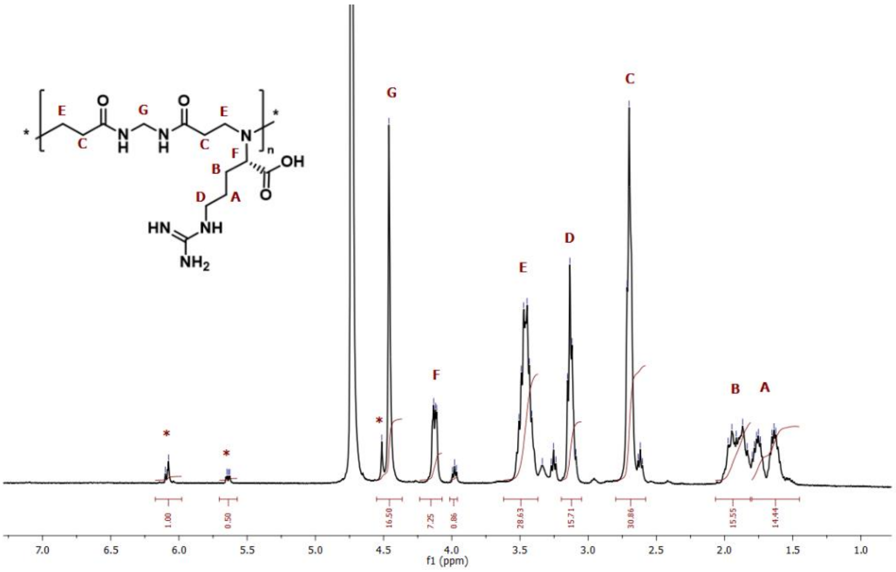

Figure 2. ^{1}H NMR spectra of *L*-ARGO7 in D$_2$O at pH 4.5. Asterisks represent the signals of methylene and double bond protons of the terminal acrylamide.

^{1}H NMR (D$_2$O, 400.132 MHz, ppm): δ 1.62-1.80 (m, 2H, C**H**$_2$CH$_2$CHCOO-), 1.83-1.97 (m, 2H, CH$_2$C**H**$_2$CHCOO-), 2.70-2.71 (m, 4H, COC**H**$_2$CH$_2$N), 3.09-3.15 (m, 2H, C**H**$_2$CH$_2$CH$_2$CHCOO-), 3.41-3.51 (m, 4H, COCH$_2$C**H**$_2$N), 4.11-4.13 (m, 1H, CH$_2$C**H**COO−), 4.46 (s, 2H, NHC**H**$_2$NH), 4.51 (s, 2H, NHC**H**$_2$NH of terminal acrylamide), 5.63–5.65 and 6.08–6.10 ppm (m, 3H, **H**$_2$C=C**H** of terminal acrylamide) (Figure 2).

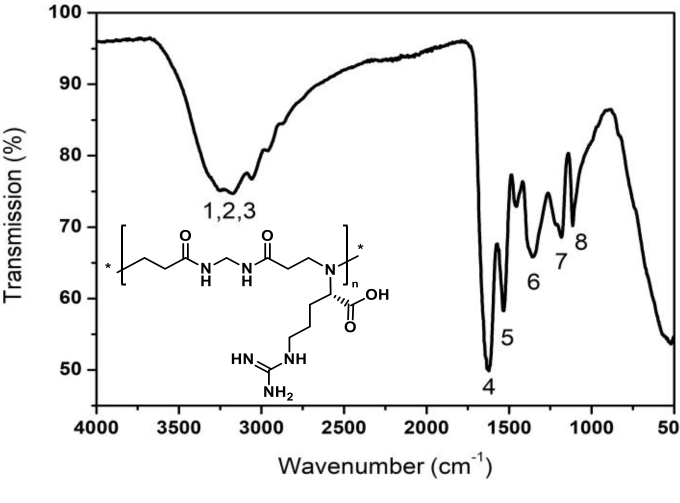

Figure 3. FTIR-ATR spectra of *L*-ARGO7 powder.

Peak assignment for *L*-ARGO7 are (Figure 3): 3276 cm^{-1} (signal 1, O-H stretching); 3180 cm^{-1} (signal 2, N-H stretching); 2954 cm^{-1} (signal 3, C-H stretching); 1641 cm^{-1} (signal 4, C=O stretching); 1536 cm^{-}

^{1} (signal 5, N-H bending); 1387 cm^{-1} (signal 6, O-H bending); 1187 cm^{-1} (signal 7, C-N stretching); 1115 cm^{-1} (signal 8, C-O stretching).

M-*L*-Ala was prepared as *L*-ARGO7 with the following proportions: *L*-alanine (2.27 g, 25.00 mmol), MBA (4.02 g, 25.00 mmol) and water (8 mL). In addition, LiOH monohydrate (1.07 g, 25.00 mmol) was added to the mixture of *L*-Ala and MBA to deprotonate the amine groups. Yield 81%. M_{w}=7800; $M_{\mathrm{w}}/M_{\mathrm{n}}$=1.44.

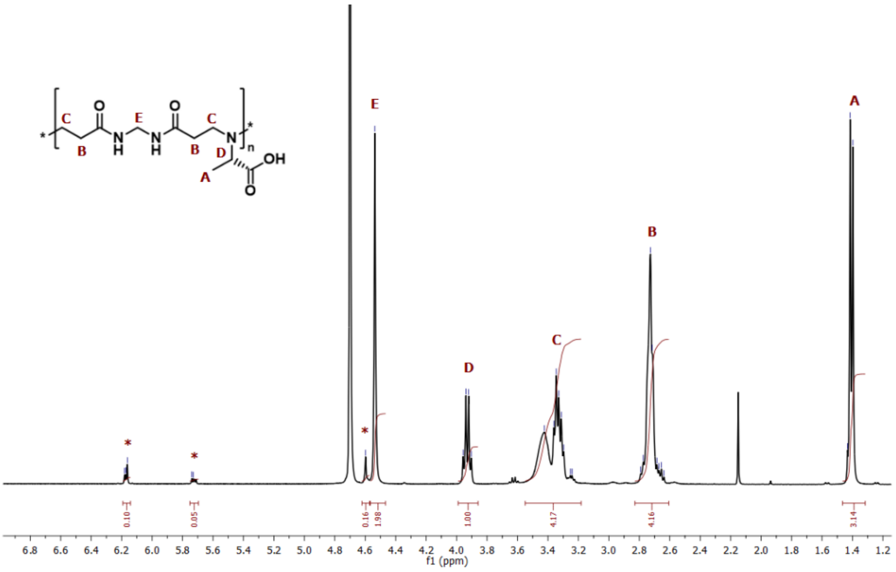

Figure 4. ^{1}H NMR spectra of M-*L*-Ala in D_2O at pH 4.5. Asterisks represent the signals of methylene and double bond protons of the terminal acrylamide.

^{1}H NMR (D_2O, 400.132 MHz, ppm): δ 1.40-1.43 (m, 3H, **CH_3**CH), 2.64-2.79 (m, 4H, CO**CH_2**CH_2N), 3.24-3.42 (m, 4H, $COCH_2$**CH_2**N), 3.90-3.96 (m, 1H, CH_3**CH**COO–), 4.54 (s, 2H, NH**CH_2**NH), 4.60 (s, 2H, NH**CH_2**NH of terminal acrylamide), 5.73–5.74 and 6.16–6.18 ppm (m, 3H, **H_2C=CH** of terminal acrylamide) (Figure 4). ^{13}C NMR (100.623, D_2O, ppm): δ 15.14, 33.31, 44.19, 46.35, 61.48, 175.16, 181.28.

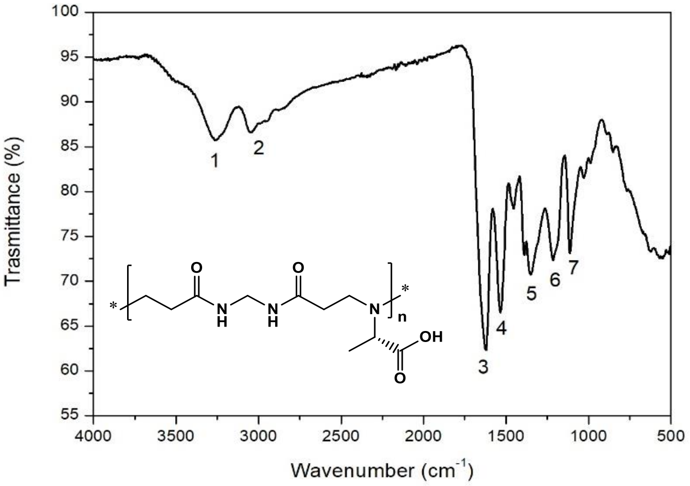

Figure 5. FTIR-ATR spectra of M-*L*-Ala powder.

Peak assignment for M-*L*-Ala are (Figure 5): 3259 cm^{-1} (signal 1, N-H stretching); 3045-2948 cm^{-1} (signal 2, C-H stretching); 1618 cm^{-1} (signal 3, C=O stretching); 1531 cm^{-1} (signal 4, N-H bending); 1357 cm^{-1} (signal 5, O-H bending); 1211 cm^{-1} (signal 6, C-N stretching); 1113 cm^{-1} (signal 7, C-O stretching).

M-*L*-Val was prepared as **M-*L*-Ala** by substituting L-valine (2.99 g, 25.00 mmol) for L-alanine. Yield 47%. M_{w}=5600; $M_{\mathrm{w}}/M_{\mathrm{n}}$=1.30.

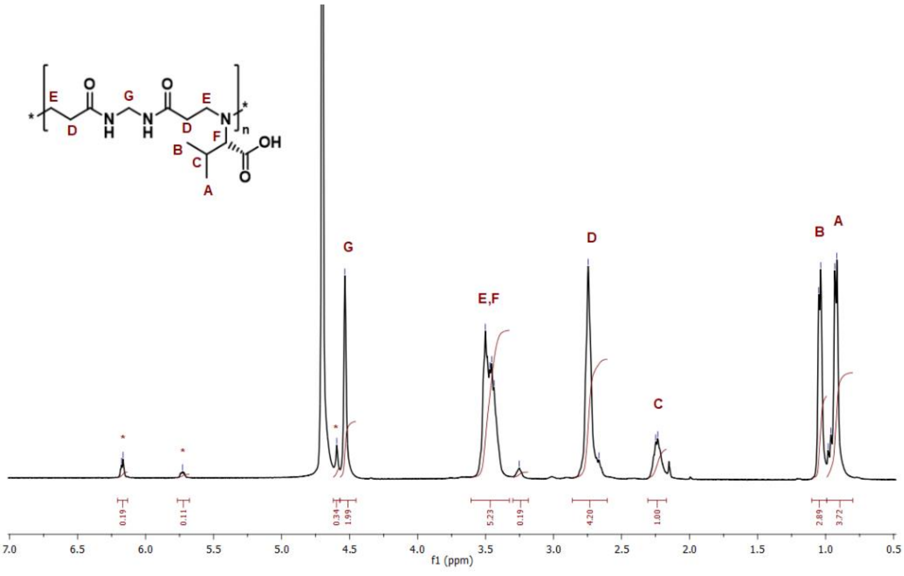

Figure 6. ^1H NMR spectra of M-*L*-Val in D_2O at pH 4.5. Asterisks represent the signals of methylene and double bond protons of the terminal acrylamide.

^1H NMR (D_2O, 400.132 MHz, ppm): δ 0.92-0.93 (d, 3H, $(C\mathbf{H}_3)_2CH$), 1.04-1.05 (d, 3H, $(C\mathbf{H}_3)_2CH$), 2.23-2.25 (m, 1H, $(CH_3)_2C\mathbf{H}CHCOO$-), 2.67-2.75 (m, 4H, $CO\mathbf{CH_2}CH_2N$), 3.44-3.50 (m, 5H, $COCH_2\mathbf{CH_2}N$

and CH**CH**COO−), 4.53 (s, 2H, NHCH$_2$NH), 4.59 (s, 2H, NH**CH$_2$**NH of terminal acrylamide), 5.73 and 6.17–6.18 ppm (m, 3H, **H$_2$**C=C**H** of terminal acrylamide) (Figure 6). ^{13}C NMR (100.623, D$_2$O, ppm): δ 17.23, 19.37, 25.85, 28.82, 44.23, 47.28, 73.43, 170.94, 172.52.

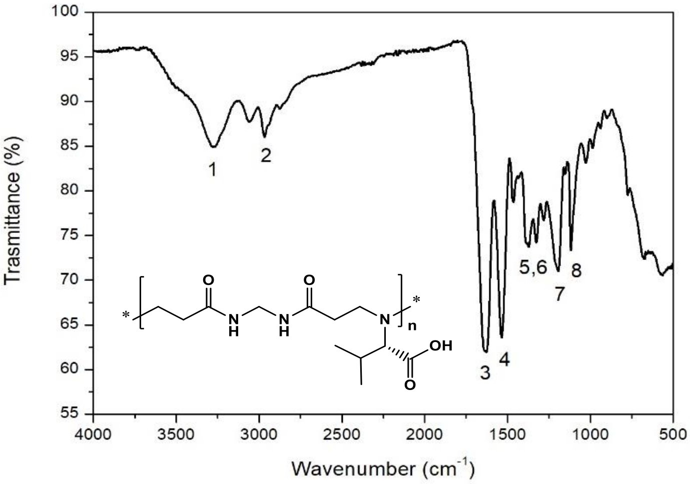

Figure 7. FTIR-ATR spectra of M-*L*-Val powder.

Peak assignment for M-*L*-Val are (Figure 7): 3273 cm^{-1} (signal 1, N-H stretching); 3058-2873 cm^{-1} (signal 2, C-H stretching); 1631 cm^{-1} (signal 3, C=O stretching); 1537 cm^{-1} (signal 4, N-H bending); 1375 cm^{-1} (signal 5, C-H bending); 1326 cm^{-1} (signal 6, O-H bending); 1194 cm^{-1} (signal 6, C-N stretching); 1117 cm^{-1} (signal 7, C-O stretching).

M-*L*-Leu was prepared as **M-*L*-Ala** by substituting L-leucine (3.35 g, 25.00 mmol) for L-alanine. Yield 59%. M_w= 6200; $M_\mathrm{w}/M_\mathrm{n}$= 1.51.

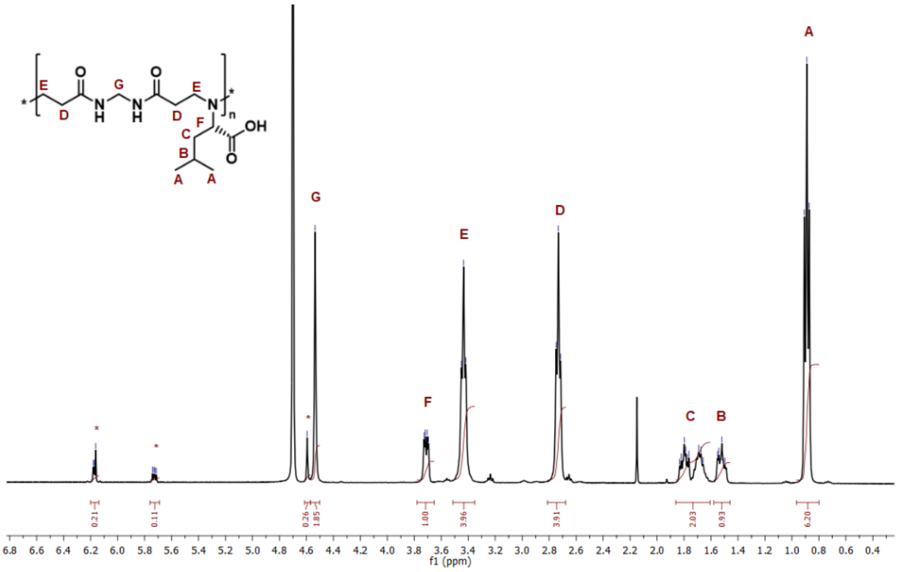

Figure 8. ^{1}H NMR spectra of M-*L*-Leu in D_2O at pH 4.5. Asterisks represent the signals of methylene and double bond protons of the terminal acrylamide.

^{1}H NMR (D_2O, 400.132 MHz, ppm): δ 0.89 (t, 6H, $\mathbf{CH_3}$CH), 1.50-1.55 (m, 1H, C**H**$(CH_3)_2$), 1.76-1.83 (m, 2H, CHC$\mathbf{H_2}$CH), 2.72-2.75 (m, 4H, COC$\mathbf{H_2}$$CH_2$N), 3.42-3.45 (m, 4H, CO$CH_2C\mathbf{H_2}$N), 3.69-3.73 (m, 1H, CH_2**CH**COO-), 4.54 (s, 2H, NHC$\mathbf{H_2}$NH), 4.59 (s, 2H, NHC$\mathbf{H_2}$NH of terminal acrylamide), 5.73 and 6.17–6.18 ppm (m, 3H, $\mathbf{H_2}$C=C**H** of terminal acrylamide) (Figure 8). ^{13}C NMR (100.623, D_2O, ppm): δ 15.14, 33.31, 44.19, 46.35, 61.48, 175.16, 181.28.

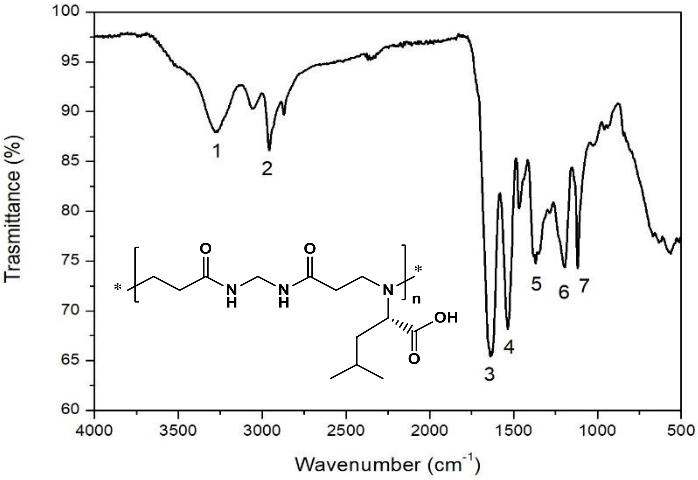

Figure 9. FTIR-ATR spectra of M-*L*-Leu powder.

Peak assignment for M-*L*-Leu are (Figure 9): 3278 cm^{-1} (signal 1, N-H stretching); 3065-2871 cm^{-1} (signal 2, C-H stretching); 1639 cm^{-1} (signal 3, C=O stretching); 1532 cm^{-1} (signal 4, N-H bending); 1367 cm^{-1} (signal 5, O-H bending); 1192 cm^{-1} (signal 6, C-N stretching); 1115 cm^{-1} (signal 7, C-O stretching).

M-*L*-Gln was prepared as **M-*L*-Ala** by substituting *L*-glutamine (3.67 g, 24.99 mmol) for L-alanine. Yield 72%. M_w=21500; M_w/M_n=2.31.

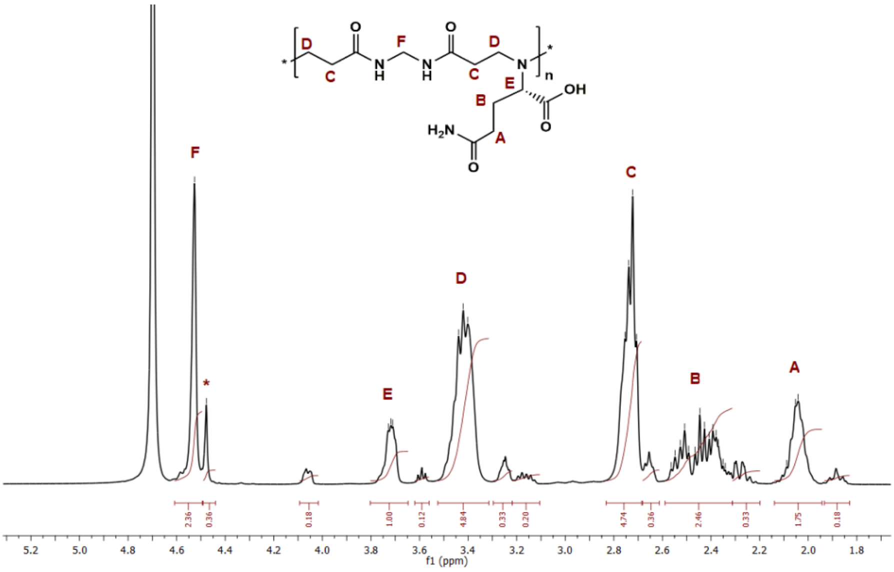

Figure 10. ${}^{1}H$ NMR spectra of M-*L*-Gln in D_2O at pH 4.5. Asterisks represent the signals of methylene derived from MBA, on terminal chains.

${}^{1}H$ NMR (D_2O, 400.132 MHz, ppm): δ 2.04–2.09 (m, 2H, $H_2NCOCH_2CH_2$) 2.37–2.55 (m, 2H, $H_2NCOCH_2CH_2$), 2.71-2.75 (m, 4H, $COCH_2CH_2N$), 3.40-3.44 (m, 4H, $COCH_2CH_2N$), 3.71-3.73 (m, 1H, CH_2CHCOO–), 4.48 (s, 2H, $NHCH_2NH$ of terminal acrylamide), 4.53 (s, 2H, $NHCH_2NH$) (Figure 10). ${}^{13}C$ NMR (D_2O, 100.623, ppm): δ 21.57, 29.39, 31.56, 44.24, 47.99, 65.50, 171.99, 177.25.

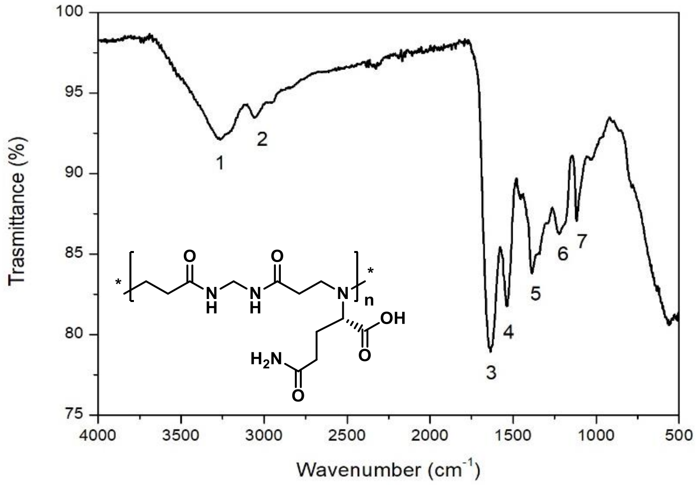

Figure 11. FTIR-ATR spectra of M-*L*-Gln powder.

Peak assignment for M-*L*-Gln are (Figure 11): 3265 cm^{-1} (signal 1, N-H stretching); 3105-2904 cm^{-1} (signal 2, C-H stretching); 1641 cm^{-1} (signal 3, C=O stretching); 1538 cm^{-1} (signal 4, N-H bending); 1387 cm^{-1} (signal 5, O-H bending); 1221 cm^{-1} (signal 6, C-N stretching); 1117 cm^{-1} (signal 7, C-O stretching).

ARGININE-BASED POLYMERS

2.3 RESULTS AND DISCUSSION

2.3.1 Synthesis of ARGO7 isomers

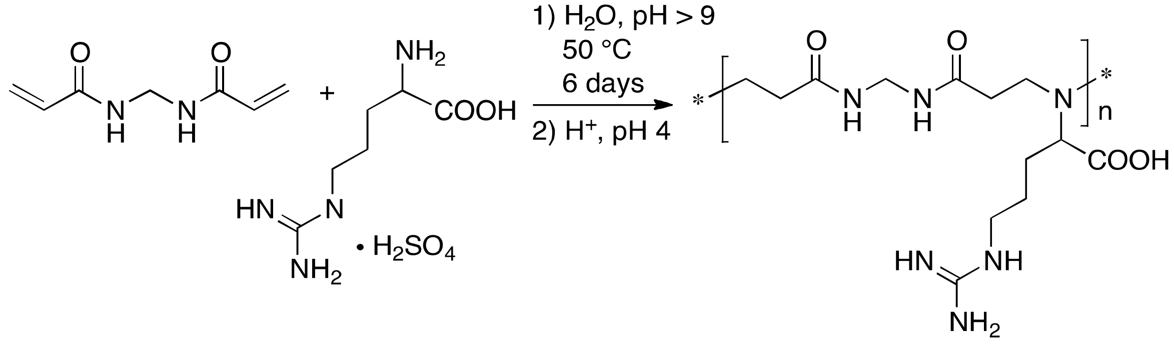

Scheme 1. Synthesis of ARGO7 polymers.

D-, *L*- and *D,L*-arginine were added to an aqueous solution of *N,N'*- methylenebisacrylamide, and the synthesis carried out at 50 °C, pH > 9 for 6 days. This pH was chosen to fully deprotonate amine groups, since they can react only as free bases (Scheme 1). Previous attempts to synthesize *L*-ARGO7 were done carrying out the reaction for six months, at room temperature with $CaCl_2$ as catalyst [14]. Now, fairly high molecular weights were obtained lowering reaction time and in absence of added catalysts. In fact, syntheses were quenched after 6 days and the concurrent PAA hydrolysis, typically showed at temperature > 40°C, was not observed.

2.3.2 Acid-Base Properties

Along ARGO7 chains, several carboxyl- and amine groups can be found. As such, ARGO7 is an amphoteric polyelectrolyte and its "apparent" pKa_1 (carboxyl groups) and pKa_2 (*tert*-amine groups) values depend on the dissociation degree α. These protonation constants were determined using the generalized Henderson-Hasselbalch equation (Eq. 15):

$$pH = pK_a - \beta \log \frac{1-\alpha}{\alpha} \qquad \text{(Eq. 15)}$$

where K_a is the apparent acidic dissociation constant of the group being pH-determining in the buffer titration zone considered and β is the Katchalsky and Spitnik parameter [22]. This parameter accounts for possible interactions between ionizable groups of repeat units being spatially or topologically adjacent. The pK_a and β values of ARGO7 polymers (Table 2) were determined by potentiometric titration following the procedure described in Experimental Section.

Table 2. pKa and β values of ARGO7 isomers in the a) α range 0.2-0.8 (β_1) and b) α range 0.1-0.9 (β_2).

Isomer	pK_{a1}[a,b]	β_1[a,b]	pK_{a2}[b,c]	β_2[b,c]
D-ARGO7	2.24 ± 0.10	0.60 ± 0.06	6.41 ± 0.07	1.12 ± 0.02
L-ARGO7	2.31 ± 0.02	0.60 ± 0.13	6.43 ± 0.06	1.14 ± 0.06
D,L-ARGO7	2.34 ± 0.06	0.57 ± 0.07	6.39 ± 0.02	1.25 ± 0.01

[a] Carboxyl group. [b] Average values obtained from four forward titration experiments. [c] Amine group. The pKa of the guanidine group was not determined and assumed ≥ 12.3. Reprinted with permission from [15]. Copyright (2017) American Chemical Society.

Titration curves were obtained for *D*-, *L*- and *D,L*-ARGO7 and resulted superimposable (see L-ARGO7 in Figure 12 as an example), with comparable isoelectric points (9.7), pK_a and β values. These results excluded differences ascribed to ARGO7 chirality. The Katchalsky and Spitnik parameter β were calculated considering α in the range, respectively, 0.2–0.8 for β_1 and 0.1–0.9 for β_2, to exclude points that clearly deviates from the trend.

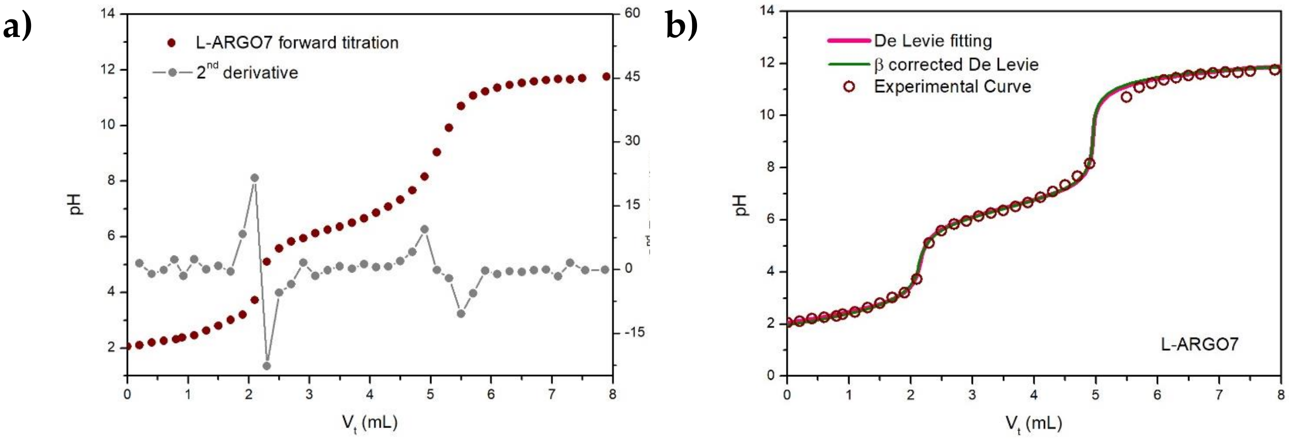

Figure 12. *L*-ARGO7 a) forward titration curve with its second derivative and b) De Levie fitting with and without β values. Curves referred to the 1st experiment of Table A1.

Each ARGO7 repeat unit could exist in four ionization states (Figure 13a) whose relative distributions with pH, named speciation curves (Figure 13b), were calculated with the pKa and β

values of Table 2, following the method reported in Experimental Section. Speciation curves calculated with and without β values resulted superimposable, with negligible differences. Hence, the moderately low polyelectrolyte effect did not affect equilibria of charged groups.

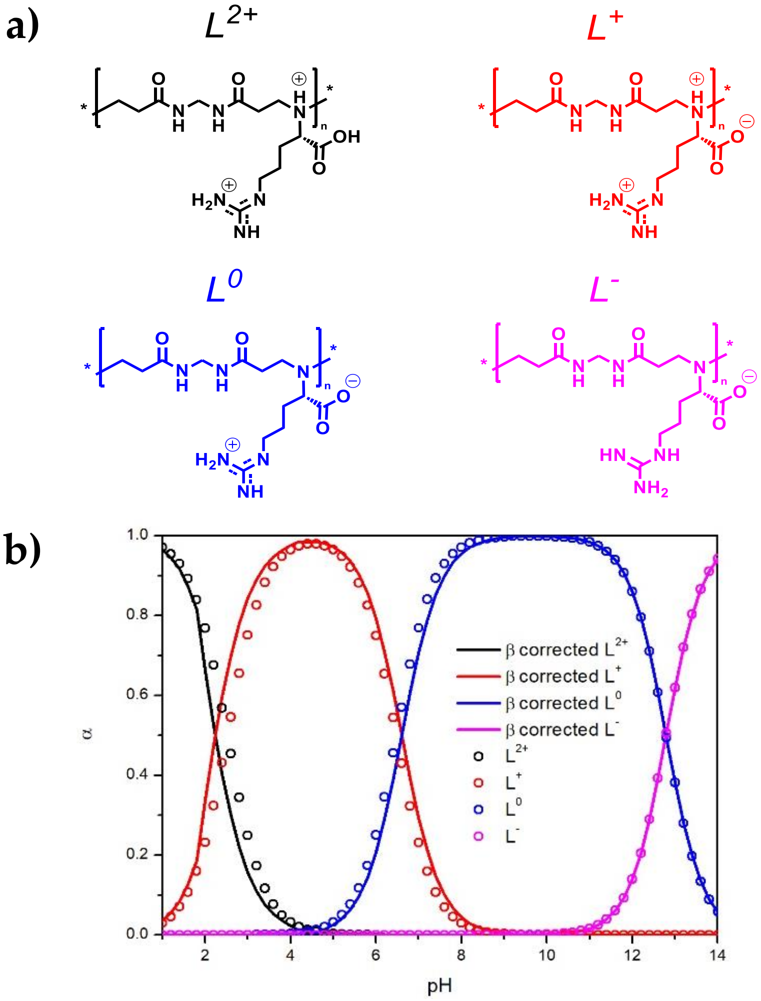

Figure 13. Distribution of charged species a) and speciation diagram b) referred to the 1st titration of *L*-ARGO7 (Table A1 and Figure 13): L^{2+} doubly positively charged; L^{+} positively charged zwitterionic; L^{0} neutral zwitterionic; L^{-} negatively charged. Speciation diagram reported β-corrected curves (straight line) and uncorrected data (dots).

2.3.3 Circular Dichroism (CD) Analysis

CD spectra of *D*- and *L*-ARGO7 were recorded at 25 °C in 0.1 M NaCl and in the 2.1÷12.1 pH range. Results indicated that ARGO7 polymers were able to self-assemble into ordered structures, whose CD spectra changed with pH (Figure 14a for *L*- and Figure A1 in Appendix for *D*-ARGO7). As expected, *D*- and *L*-ARGO7 showed mirror-image spectra, whereas *D,L*-ARGO7 resulted flat (Figure A2 in Appendix).

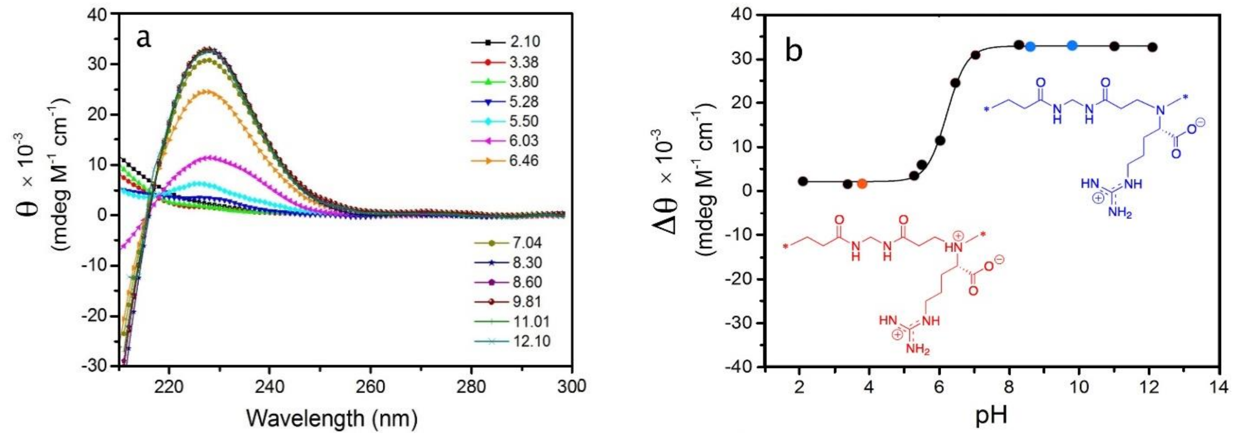

Figure 14. *L*-ARGO7 CD spectra: a) pH dependence and b) differential molar ellipticity at 228 nm. Reprinted with permission from [15]. Copyright (2017) American Chemical Society.

In the CD spectra, the molar ellipticity (Θ) maximum was centered at 228 nm and increased with increasing pH (Figure 14a). In particular, its intensity kept increasing in the 5.50 – 8.30 pH range. Then, it remained constant.

The differential molar ellipticity (ΔΘ) at 228 nm was calculated for *D*- and *L*-ARGO7 in the whole pH range, taking as reference the Θ value at pH 2. Plotting the values as a function of pH, three noticeable regions could be detected (Figure 14b): i) the lower plateau at pH 2.0÷5.5, ii) the inflection point at pH ~ 6 and iii) the upper plateau at pH > 7.5. These points mirrored the ionization state of the ARGO7 chains reported in the speciation diagram (Figure 13). In the first region i), ARGO7 resulted positively charged, and the major absorption in the CD profile was detected below 220 nm, associated to the C=O functional groups. Then, in region ii) the slightly basic *tert*-amine groups were partially deprotonated, changing the chromophores surroundings and hence the repulsion between chains. In iii), the *tert*-amine groups were fully deprotonated and ARGO7 resulted electrically balanced, until pH 12.

ARGO7 was able to assume immediately its conformation, right after pH was adjusted. To assess conformational stability and reversibility with pH, two cycles were done: pH was changed from 2 to 8 and backward. Results indicated that changing pH triggered reversible modification of ARGO7 conformations (Figure 15).

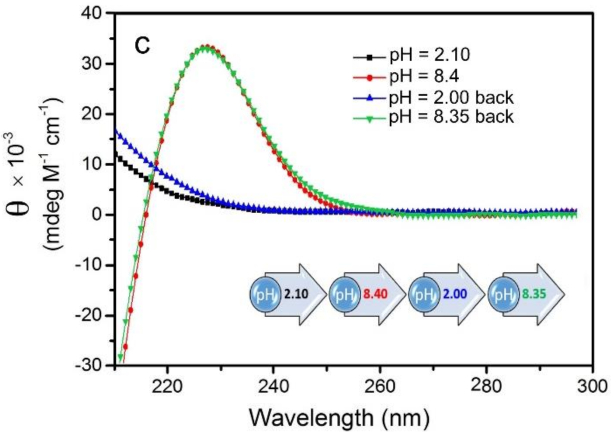

Figure 15. Reversibility of *L*-ARGO7 CD spectra with respect to a pH change. Reprinted with permission from [15]. Copyright (2017) American Chemical Society.

At pH ~ 8.3 the dependence of *L*-ARGO7 spectral patterns were assessed over temperature, ionic strength, polymer concentration and M_w, presence of denaturants as guanidinium chloride and urea. CD spectra did not change upon modification of any of these parameters. First, effect of temperature was studied by heating ARGO7 sample at 25°C, then swiping temperature in the 5÷70 °C interval, and after, back again to 25 °C. These changing produced only a modest and reversible effect (Figure 16), indicating ARGO7 conformations were thermodynamically stable.

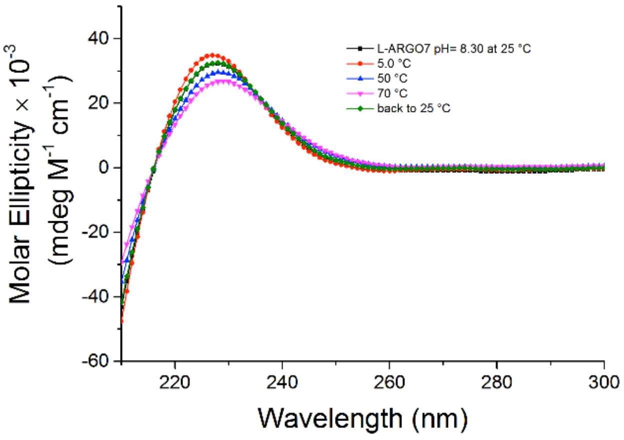

Figure 16. Temperature dependence of *L*-ARGO7 CD spectra in the interval 5 ÷ 70 °C and back to 25 °C, at pH 8.30.

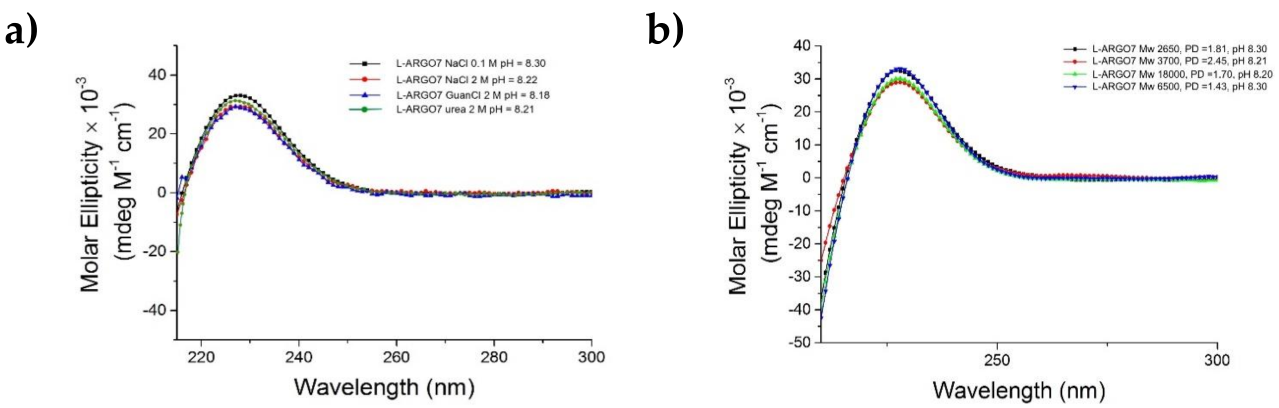

Figure 17. Modification of CD spectra with: a) increasing ionic strength (0.1 and 2 M NaCl) and presence of denaturating agents as 2 M guanidinium chloride and urea, at pH 8.18 ÷ 8.30 and b) different molecular weight of L-ARGO7, at pH 8.21 ÷ 8.30.

Equally, increasing ionic strength from 0.1 to 2 M NaCl did not significantly change CD spectra. The same was true when denaturating agents, guanidinium chloride and urea (2 M) (Figure 17a), were introduced. It can be stated that ARGO7 structuring was not direct by electrostatic interactions or hydrogen bonding, respectively. Even changing M_w, in the range 2.5÷10.5 kDa, had no influence on CD spectra (Figure 17b).

2.3.4 Dynamic Light Scattering (DLS) Measurements

DLS analyses were carried out on 1 mg mL^{-1} ARGO7 solution, in 0.1 M NaCl, to evaluate the pH-dependence of the hydrodynamic radii (R_h) of the polymers. Data were collected within the 2-11 pH range and indicated that R_h was not affected by pH variation (Figure 18). In all cases no traces of aggregates were seen.

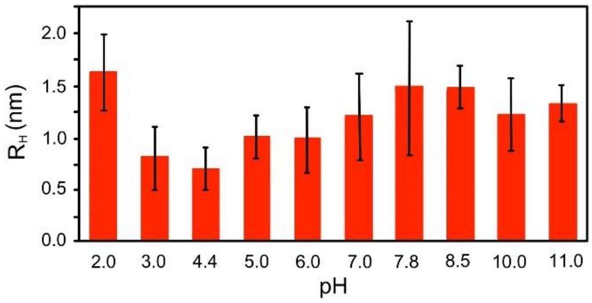

Figure 18. pH dependence of *L*-ARGO7 particle size from DLS. Reprinted with permission from [15]. Copyright (2017) American Chemical Society.

2.3.5 Theoretical Modeling

The molecular dynamics (MD) simulations of *L*-ARGO7 were carried out with 10 repeat units (M_n = 3280) at different pH values (Table 2), using a previously adopted Simulation Method [18-20]. Gyration radius (R_g), surface accessible to the solvent (S), dipole moment (μ) and end-to-end distance (R) were reported in Table 3.

Results showed *L*-ARGO7 did not assume an extended conformation, typical of polyelectrolytes, but a coiled structure instead, with R_g between 0.9 – 1.03, much smaller than R (Figure 19a and Table 3). In the MD runs, these bundled structures were rapidly obtained, with minor fluctuations after equilibration (Figure A3 in Appendix).

Table 3. Properties of simulated *L*-ARGO7 at different pH values in water at the end of the molecular dynamics run.

pH	Charge (*e*)	R_g (nm)	R (nm) [a)]	S (nm^2)[b)]	μ (D)
1	+20	1.03	2.51	26.2	26.40
6	+10	0.92	1.32	20.7	45.51
14	-10	0.90	1.84	21.4	37.73

[a)] distance between the outermost N atoms along the main chain; b) surface accessible to a 1.4 Å radius spherical probe. In all cases, SD was less than 2% of the calculated values. Reprinted with permission from [15]. Copyright (2017) American Chemical Society.

Three different pHs were considered: 1, 6 and 14. At pH 1, R_g resulted only slightly bigger than all the other pH values, despite the larger overall charge. The same was true for the solvent accessible surface (Figure 19b), and the end-to-end distance R (Table 3).

The dipole moment (μ) mainly depended on the local dipoles of C=O groups along the chain, and might explained CD spectral pattern (Figure 11a). In fact, variation of the dipole moment with pH (Table 3 and Figure 19c) matched the behavior of the CD spectra. In particular, at pH 1 the dipole moment reached its lowest value, probably due to the compensation of some dipole vectors pointing in opposite direction. At pH 6, ARGO7 units were electrically balanced and μ recorded its highest value. Once ARGO7 chains were negatively charged, at pH 14, μ decreased again (Figure 19c). These extreme pH values, 1 and 14, were not considered in the CD experimental studies due to polymers' stability problems.

Molecular dynamics simulations were consistent with the experimental results, considering the different molecular masses. Both pointed toward a coiled conformation, that can exist due to the flexible main chain and the topological separation of the charged groups. Self-structuring was driven by electrostatic interactions and hydrogen bonds within the main chain, the arginine side groups, and among them. These generated folded structures reminiscent of the protein hairpin conformation [23-25]. At pH 6 and 14, torsional angles distribution was quite the same, and ranged between 30° and ±180° values (Figure 19a). Instead, at pH 1 distribution of such angles was much more concentrated around ±180° (Figure 19a).

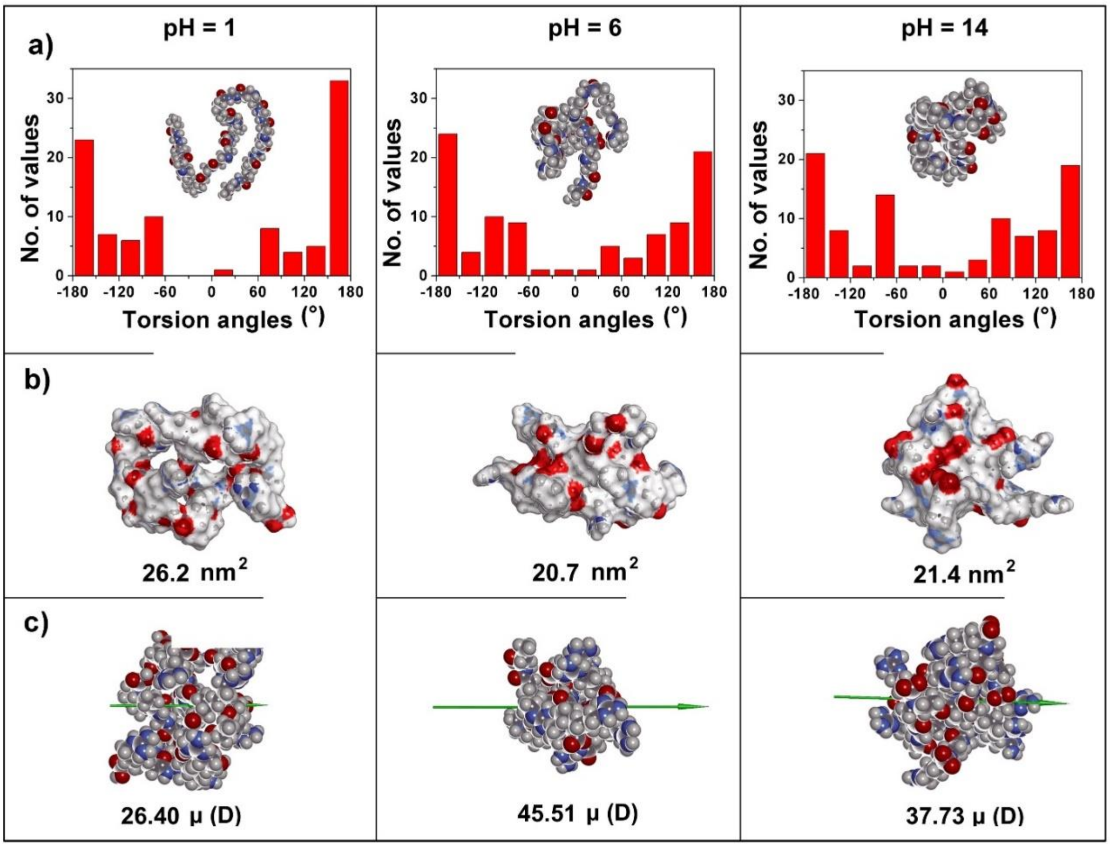

Figure 19. a) Main chain molecular conformations in water at the end of the MD runs at pH 1, 6 and 14 and torsion angle distributions around the main chain bonds: the histogram are shown with a binning of 30°. Color codes: C atoms dark grey; H atoms light gray; N atoms blue; O atoms red. b) Solvent accessible surface area in water. The surface area is in dark grey near C atoms, in light gray near H atoms, in blue near N atoms and in red near O atoms. c) Dipole moments in water. Color codes are the same as in panel a). Reprinted with permission from [15]. Copyright (2017) American Chemical Society.

ALKYL-SUBSTITUTED PAACs

2.3 RESULTS AND DISCUSSION

2.3.1 Synthesis of M-*L*-Ala, M-*L*-Val and M-*L*-Leu

Other PAACs were synthesized with the same synthetic procedure adopted for ARGO7. Polyaddition was carried out in water at 50 °C and pH ≥10 for 6 days, starting from *L*-alanine, *L*-valine or *L*-leucine to obtain M-*L*-Ala, M-*L*-Val and M-*L*-Leu, respectively (Scheme 2). Differently from ARGO7, LiOH monohydrate was added in stochiometric amount to deprotonate carboxylic groups, in this way leaving NH_2 groups as free bases.

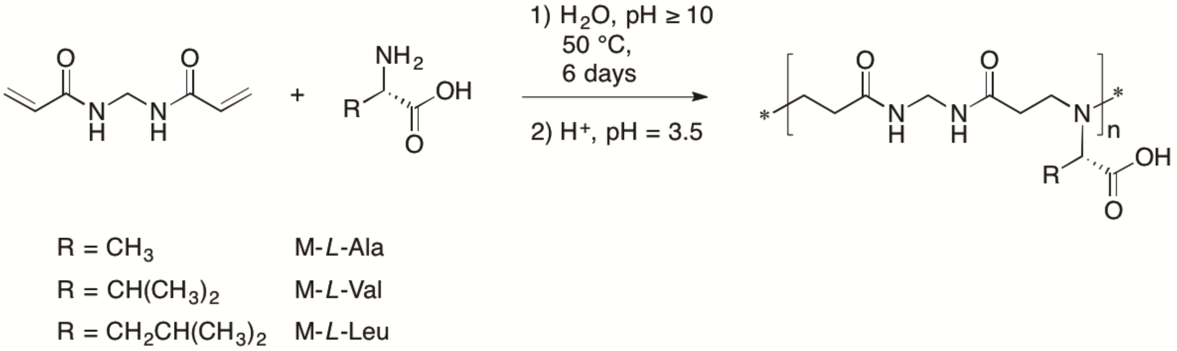

Scheme 2. Michael polyaddition of PAACs.

Interestingly, setting the reaction temperature at 50°C did not trigger the radical polymerization of MBA vinyl groups, since no traces of insoluble cross-linked matter were observed. In addition, reaction time and pH did not cause any hydrolytic degradation, as proved by the absence of characteristic peaks in NMR spectra. Yields, weight-average molecular weights (M_w) and polydispersity index were reported in Experimental Section.

As for ARGO7 isomers, physicochemical properties and structuring ability in water of alkyl-based PAACs were assessed and compared.

2.3.2 Acid-base properties

M-*L*-Ala, M-*L*-Val and M-*L*-Leu protonation constants (pKa_1 and pKa_2) were determined using the same procedure described for ARGO7 isomers. Their trend with the dissociation constants α is reported in Figure 20, while their values are reported in Table 4.

Table 4. pK_a and β values of PAACs in the α range 0.2– 0.8 (β_1) and 0.1– 0.9 (β_2).

Sample	pKa_1[a,b]	β_1 [a]	pKa_2[b,c]	β_2 [c]	IP[d]
M-*L*-Ala	2.12 ± 0.04	0.76 ± 0.05	8.13 ± 0.17	1.32 ± 0.04	5.1
M-*L*-Val	2.08 ± 0.06	0.68 ± 0.09	6.78 ± 0.03	1.45 ± 0.08	4.4
M-*L*-Leu	2.11 ± 0.02	0.61 ± 0.07	7.37 ± 0.16	1.38 ± 0.07	4.7

[a]Carboxyl group; [b] Average values obtained from four forward titration experiments; [c] Amine group; [d] Isoelectric point.

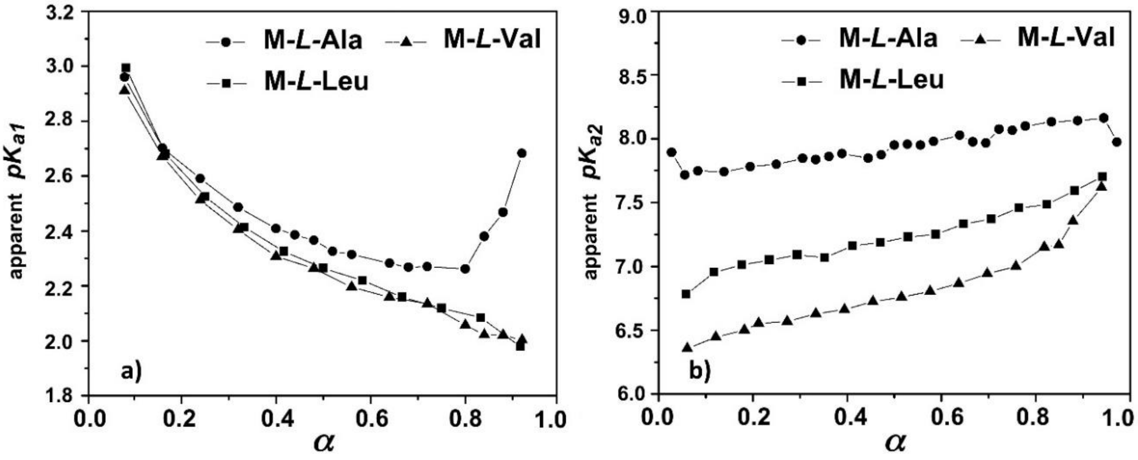

Figure 20. Dependence of PAAC apparent a) carboxyl- and b) amine pK_a values on the dissociation degree. Operational conditions: 0.05 M repeating units in aqueous 0.1 M NaCl at 25 °C.

Generally, polyelectrolytes showed increasing $pK_a s$ values with increasing ionization degree [26]. As polymers become more charged, a greater amount of work is required to remove a proton from a carboxyl group or to add a proton to an amine group, owing to charge repulsion. By contrast, PAACs' pK_{a1s} followed an opposite trend: they decreased by increasing the ionization degree, in the α range 0.1-0.8 for M-*L*-Ala, 0.1-0.9 for M-*L*-Val and M-*L*-Leu (Figure 20a). Instead, the apparent pK_{a2} increased in all cases, along 0.05-0.95 α range (Figure 20b). These changes in pK_{a1} followed those of polymeric carboxylic acids in presence of cationic polyelectrolytes [27]. In this case, deprotonation was promoted by the formation of strong inter-polyelectrolyte complexes [27], that affect charge shielding. Conformational compactness showed in solution by PAACs may favor strong intramolecular interactions between neighboring carboxylate and ammonium groups, carrying opposite charges. The formation of these complexes increased the pK_{a2}, since more effort was needed to first break the interaction and then release protons from ammonium groups. To notice when M-*L*-Ala reached α >0.8, pK_{a1} increased approaching the normal behavior of polymeric acids [27]. This may be ascribed to the fact that α-substituent of alanine is the least bulky and hydrophobic of the series, leading to weaker electrostatic interactions between its charged groups.

Forward titration curves and De Levie fitting calculated with and without β parameter are reported in Figure 21. M-*L*-Ala, M-*L*-Val and M-*L*-Leu showed comparable pKa and β values (Table 4), independent from the amino-acid side chain. The Katchalsky and Spitnik parameter β were calculated considering α in the range, respectively, 0.2–0.8 for β_1 and 0.1–0.9 for β_2. The average values are in line with the ones calculated for the ARGO7 polymers and may be considered, as such, a characteristic of all PAACs.

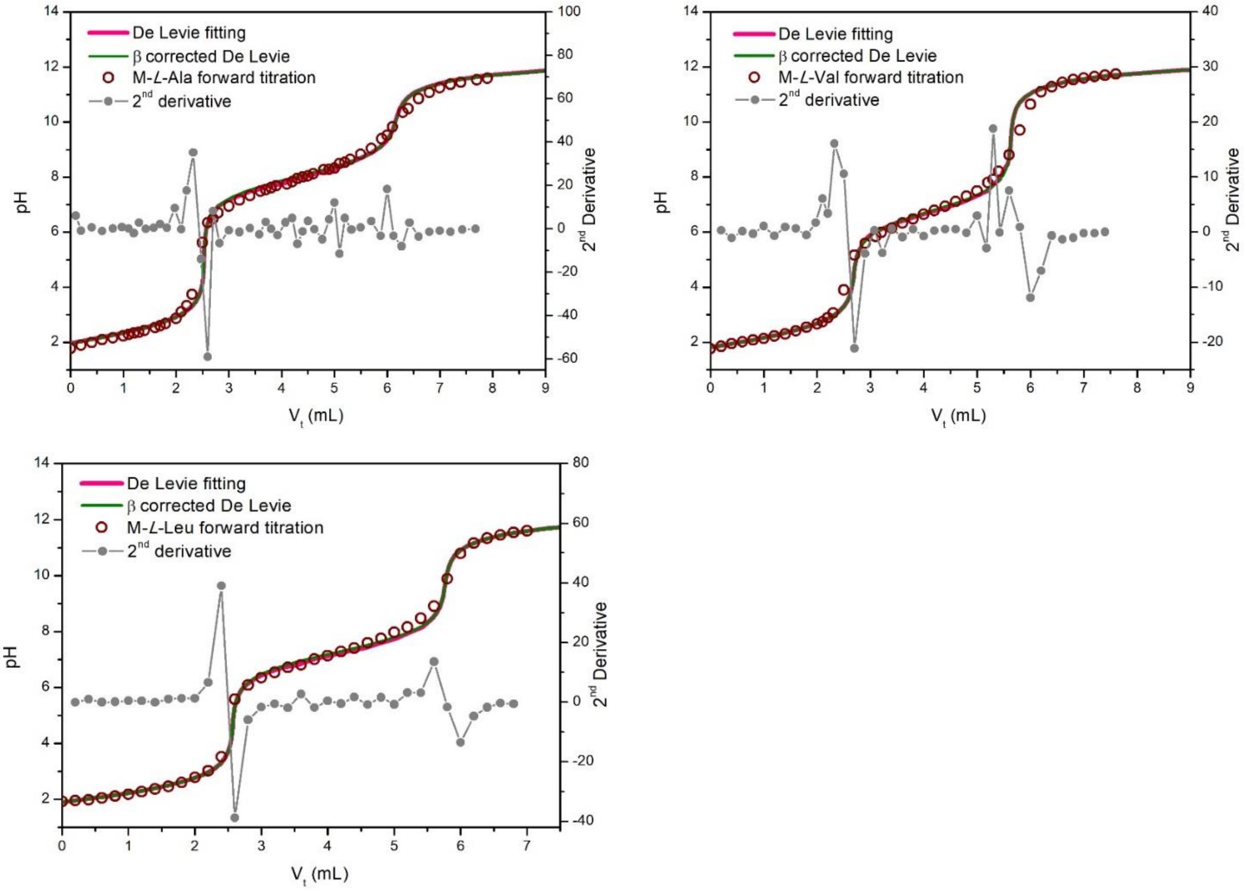

Figure 21. Forward titration curves of M-*L*-Ala, M-*L*-Val and M-*L*-Leu, referred to the 1st experiment of Table A2 in Appendix.

PAAC repeating units existed in three ionization states, whose speciation curves were determined from the pK_a and β values reported in Table 4, following methods described in the Experimental Section. The related diagrams are shown in Figure 22.

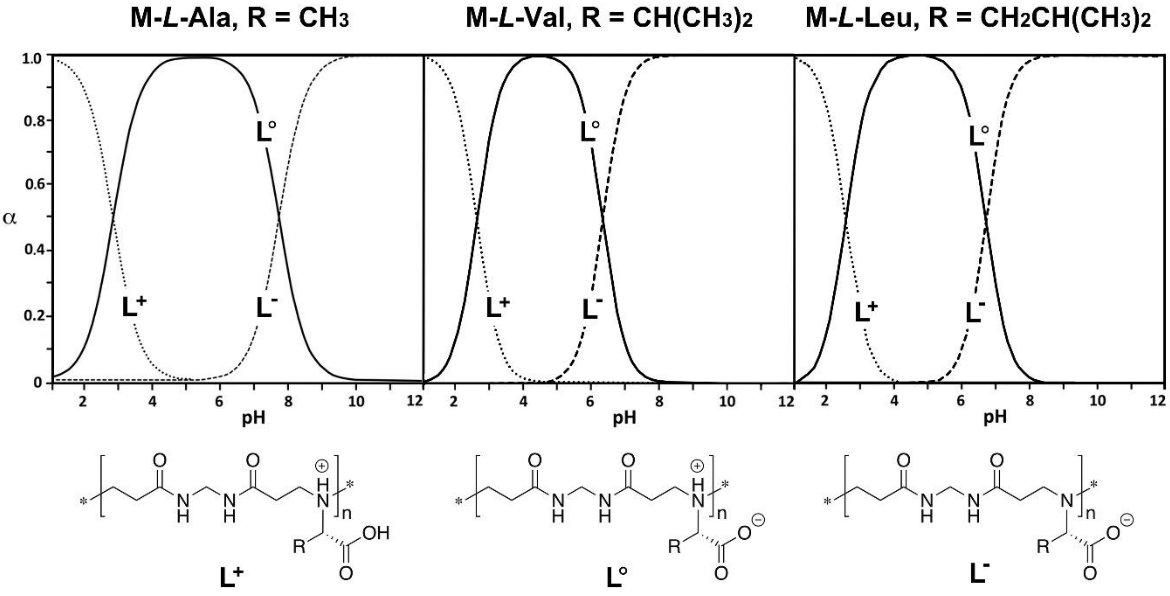

Figure 22. Speciation diagrams of M-*L*-Ala, M-*L*-Val and M-*L*-Leu.

2.3.3 Circular Dichroism Analysis

M-*L*-Ala, M-*L*-Val and M-*L*-Leu CD spectra were collected in 0.1 M NaCl, in the 3 – 11 pH range and wavelength interval 200-280 nm. Results confirmed ARGO7 behavior, that is all PAACs were able to self-assemble in solution into pH dependent structures (Figure 22). At pH ≥7, spectra showed a positive molar ellipticity peak (referred to PAAC repeat units) with maximum centered at 228 (M-*L*-Ala), 234 (M-*L*-Val) and 231 (M-L-Leu) nm respectively. The maximum value increased with increasing pH and, in all cases, was lowest for M-*L*-Ala.

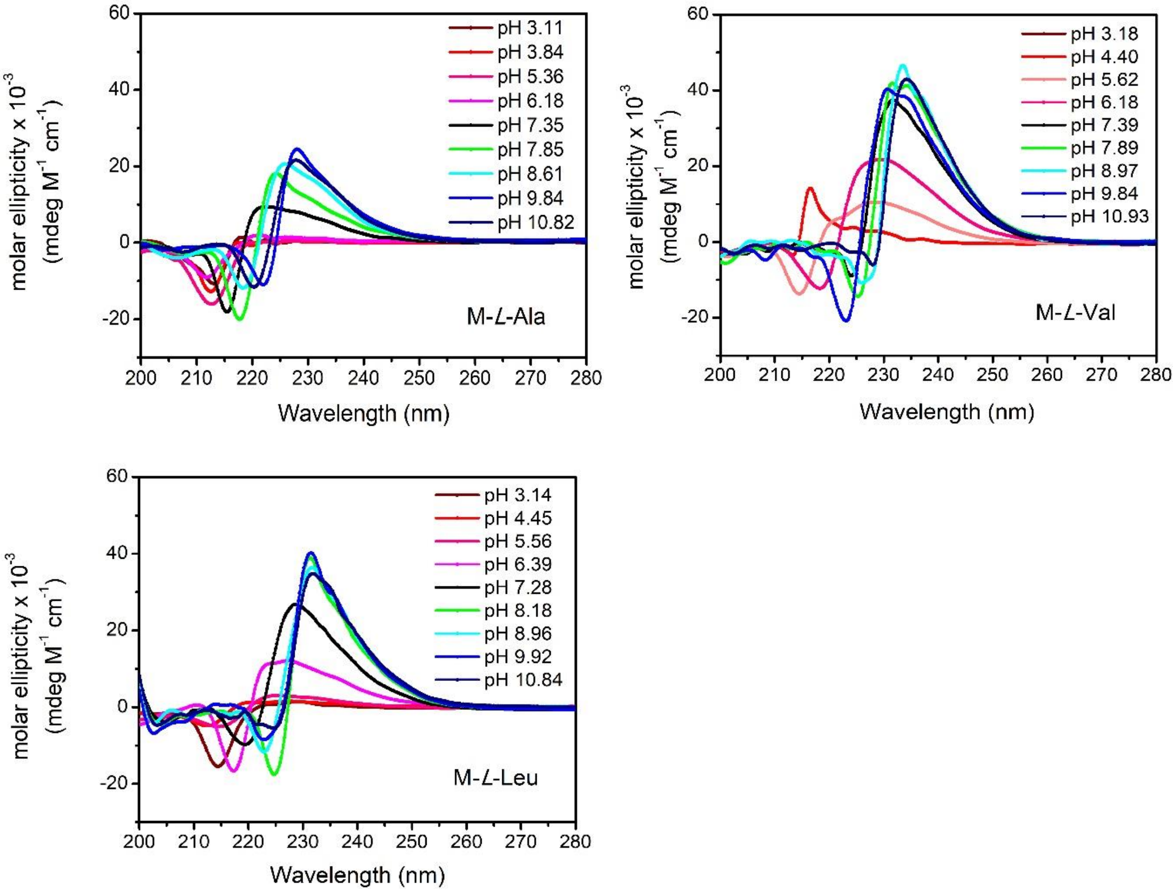

Figure 22. pH Dependence of PAAC CD spectra of a) M-*L*-Ala, b) M-*L*-Val and c) M-*L*-Leu at 25 °C. Operational conditions: 1.83 ± 0.17 mM repeating units in 0.1 M NaCl solution, 25 °C.

The differential molar ellipticity was calculated taking as reference the molar ellipticity value of each maximum at pH 3 (Figure 23). Negative peaks were not considered. In all cases, sigmoidal curves were obtained and showed: i) a lower plateau in the pH intervals 3.0-5.5 (M-*L*-Ala), 3.0-4.8 (M-*L*-Val) and 3.0-5.0 (M-*L*-Leu); ii) an inflection point at pH 8.1 (M-*L*-Ala), 6.8 (M-*L*-Val) and 7.3 (M-*L*-Leu); and iii)an upper plateau at pH ≥10.4 (M-*L*-Ala), pH ≥9 (M-*L*-Val) and pH ≥9.9 (M-*L*-Leu). These trends can be explained by the speciation diagrams of Figure 23. At lower pH, mostly positively charged chains may be found for each PAACs. By increasing pH, first zwitterionic and then negatively charged chains can be found in solution, due to the *tert*-amine groups deprotonation. The inflection points of the sigmoid corresponds to the half-deprotonation of the PAACs amine groups, when pH = pK_{a2}. It appeared the *tert*-amine protonation degree was the main factor governing structuring and, consequently, the shape of the CD spectrum. In addition to the positive peak, a negative peak appeared at lower wavelength. Its position kept changing with pH, shifting to lower wavelength by lowering pH.

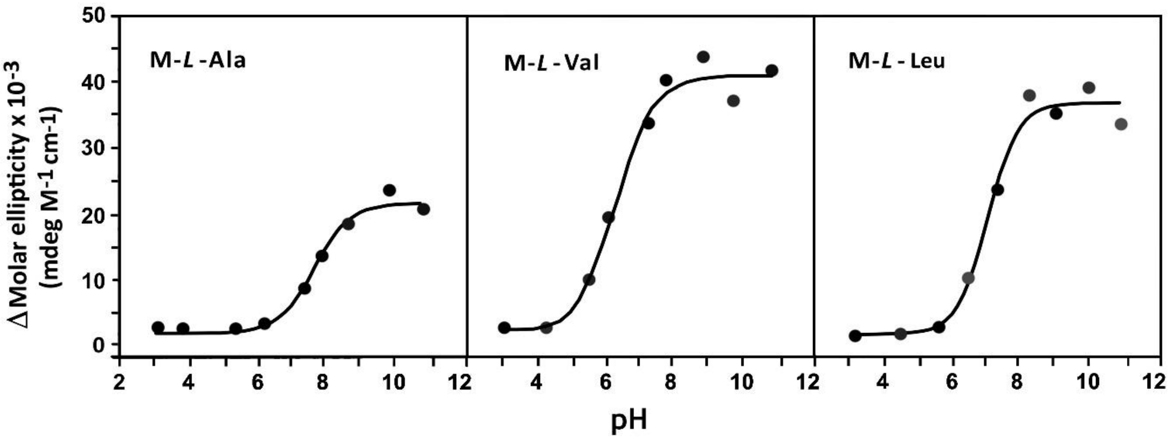

Figure 23. pH Dependence of M-*L*-Ala, M-*L*-Val and M-*L*-Leu differential molar ellipticity at 228, 234 and 231 nm, respectively. Operational conditions: 1.83 ± 0.17 mM repeating units in 0.1 M NaCl solution. Based on data points reported in Figure 20.

Circular dichroism measurements were carried out also in other conditions (Figure 24, upper row): i) at different ionic strength (0.1 M and 2 M sodium chloride) and ii) in presence of denaturating agents (2 M urea and guanidinium chloride). In all cases, spectra were only slightly affected by ionic strength and 2 M urea. Different was the case of 2 M guanidinium chloride solutions, whose interaction with the polymers changed significantly both intensity and peak maximum of all PAAC, M-*L*-Ala to a higher extent. Reversibility of each conformations toward temperature and pH was assessed as well. Results indicated that PAACs conformations were thermodynamically stable, in the 3 – 70°C interval, with only minor changes for M-*L*-Ala, whose negative peak nearly vanished (Figure 24, bottom row). The same was true for pH. M-*L*-Ala, M-*L*-Val and M-*L*-Leu self-structuring was quickly formed and showed reversibly by changing pH (Figure 24, intermediate row).

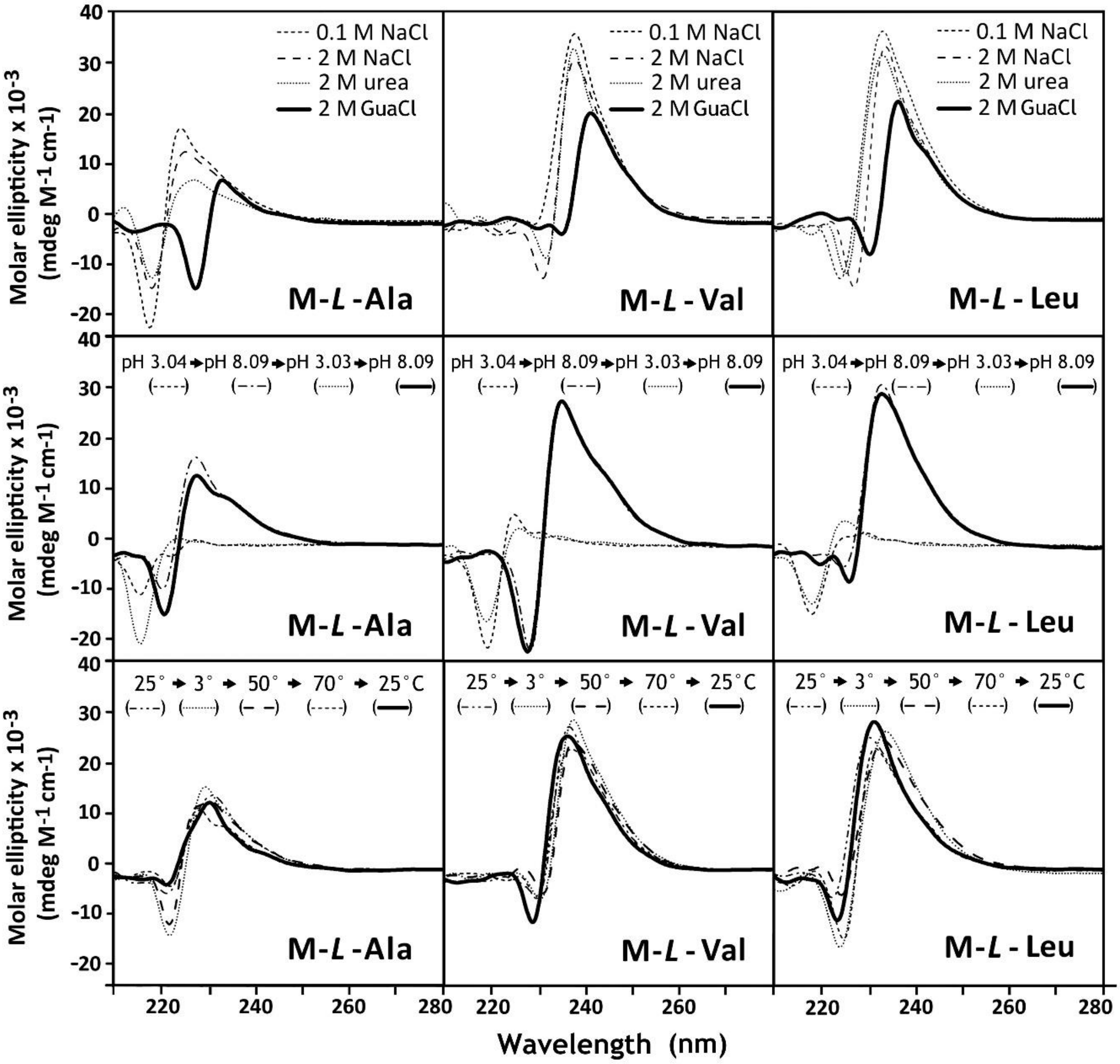

Figure 24. Dependence of PAAC CD spectra on a change of: ionic strength and presence of denaturating agents, namely urea and guanidinium chloride (GuaCl) (upper row); pH (intermediate row); temperature (bottom row). Operational conditions: 1.83 ± 0.17 mM repeating units and, where not otherwise stated, in 0.1 M NaCl solution.

2.3.4 Dynamic Light Scattering (DLS) Measurements

DLS measurements were carried out on PAACs solutions prepared in 0.1 M NaCl, as a function of pH, presence of denaturants, polymers' concentration and time. Hydrodynamic radii (R_h) of 1 mg mL^{-1} PAAC solutions did not change within the 1.5-11 pH range (Figure 25). Even increasing ionic strength or adding denaturating agents did not affect R_hs, both in acidic and basic conditions (Figure 26). The only differences were seen in water at pH 8.3, where the dimensions of M-*L*-Ala, M-*L*-Val and M-*L*-Leu resulted significantly lower, possibly due to stronger intramolecular interactions affected by the presence of salts or denaturating agents.

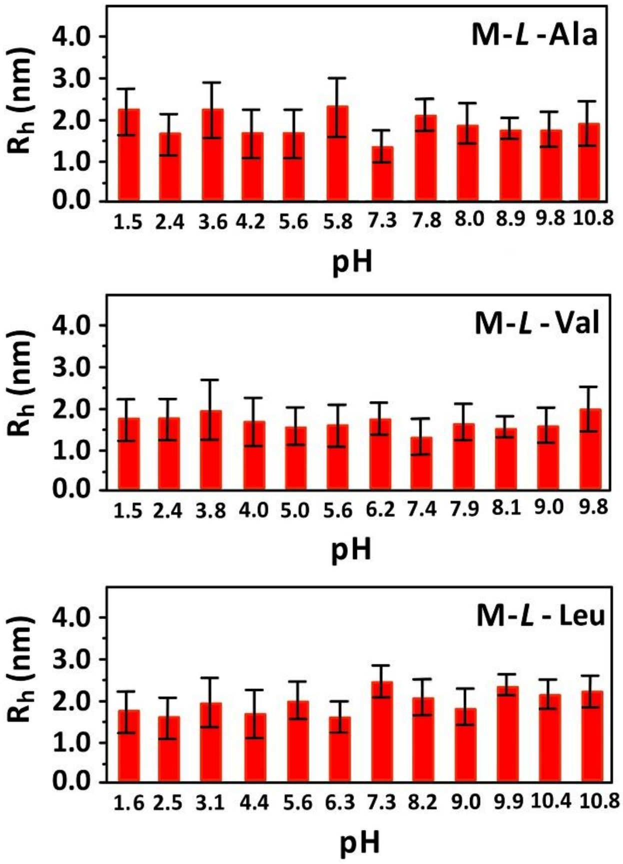

Figure 25. pH Dependence of PAAC hydrodynamic radius from DLS at 25 °C in 0.1 M aqueous NaCl. Polymer concentration 1 mg mL^{-1}.

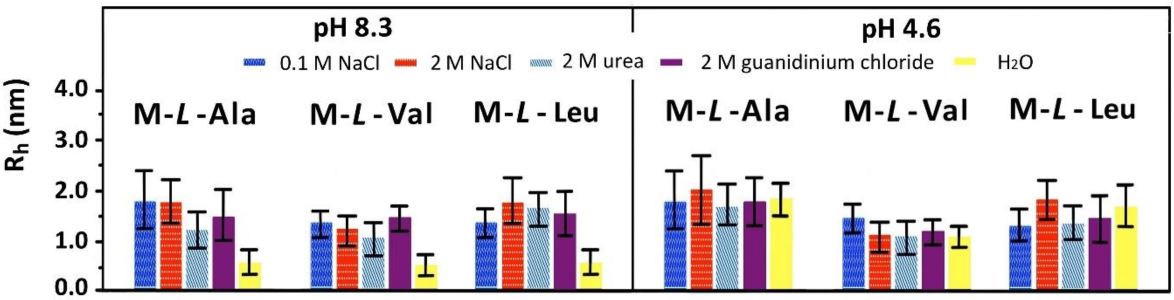

Figure 26 PAAC hydrodynamic radii from DLS in: 0.1 M and 2 M NaCl, 2 M urea, 2 M guanidinium chloride and plain water. Operational conditions: polymer concentration 1 mg mL^{-1}, 25 °C.

The particle size was studied as a function of time and concentration, as well (Figure 27). Changing concentration in the 0.5-20 mg mL^{-1} range, did not affect R_h values, ruling out formation of aggregates. Data likely suggested these polymers were able to intramolecularly self-assembled into single chain nanoparticles, whose R_h remained stable even after one month (Figure 27, dotted line).

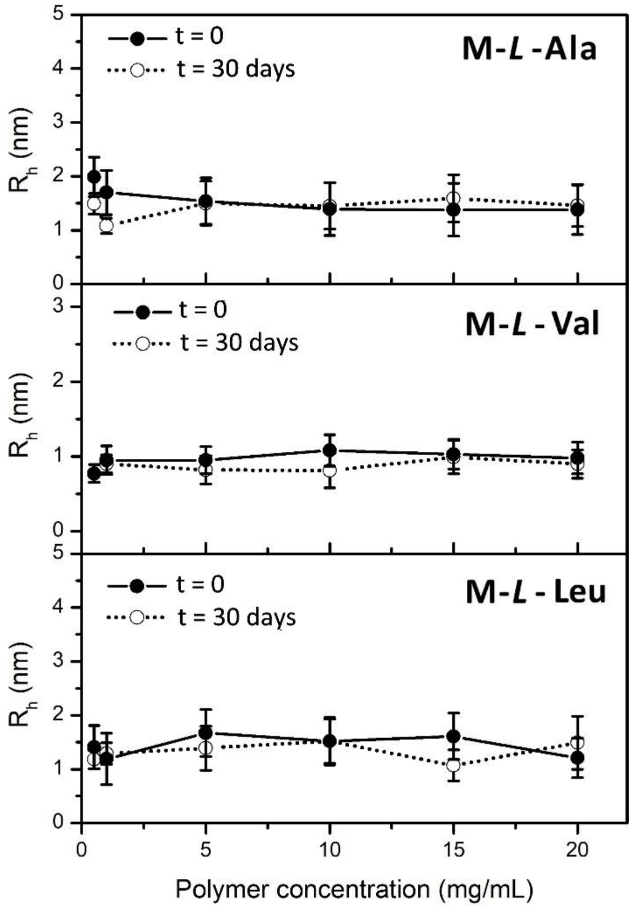

Figure 27 Concentration dependence of PAAC hydrodynamic radius in Milli-Q water, pH 4.74 ± 0.72 at 0 and 30 days.

2.3.5 Theoretical Modeling

Adopting a simulation protocol used in previous work [18-20], molecular dynamics (MD) simulations at room temperature and final energy minimizations using molecular mechanics (MM) methods were carried out for M-*L*-Ala, M-*L*-Val, M-*L*-Leu with ten repeat units (see Experimental Section). Results in water showed polymer's behavior to be rather similar to previously reported ARGO7 [16], that is, the formation of a compact conformation. Data are reported in Table 5.

In addition, M-*L*-Ala simulations were run at pH 1, initially at 500 K, then at 400 K and eventually at 300 K to check if conformations were trapped in a metastable state. In these cases, no significant differences were found for the calculated size descriptors.

Table 5. Properties of the simulated PAACs at different pH values in water at the end of the MD runs and final geometry optimization.

Polymer	pH	Charge (e)	R_g[a] (nm)	R[b] (nm)	S[c] (nm^2)	Volume[d] (nm^3)	μ[e] (D)
M-*L*-Ala	1	+10	1.07	1.57	21.1	2.35	21.8
	5	0	0.74	1.09	12.5	2.61	66.2
	11	-10	0.80	1.23	16.6	2.65	40.2
M-*L*-Val	1	+10	1.04	1.41	22.1	2.55	19.6
	5	0	0.73	1.57	13.2	2.80	20.6
	11	-10	0.85	1.46	19.9	2.66	38.1
M-*L*-Leu	1	+10	1.11	1.73	24.1	2.70	24.4
	5	0	0.85	0.84	19.9	2.95	43.0
	11	-10	0.80	1.14	16.9	3.11	28.0

[a]Gyration radius; [b]End to end Distance; [c]Surface area accessible to the solvent defined as the surface accessible to a spherical probe having a 0.14 nm radius, roughly the size of a water molecule; [d]Volume of the optimized molecule in water; [e]Dipole moment.

At both pH 5 and 11, M-*L*-Ala, M-*L*-Val and M-*L*-Leu assumed spherical conformations with lower R_g and S than pH 1. When MD were run at pH 1, chains assumed a more anisotropic shape with higher radii and S due to the presence of large cavities (Figure 29-31). All the conformations obtained at different pHs were quickly achieved in the MD runs, with small fluctuations after equilibration (Figure 28).

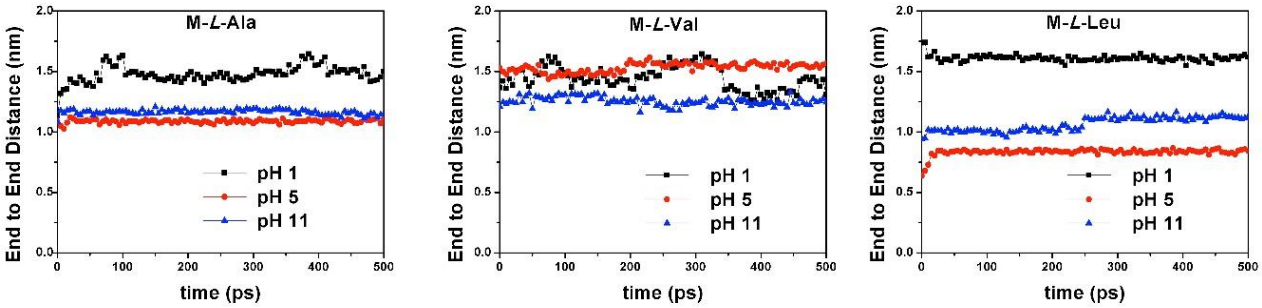

Figure 28. Time dependence of PAACs' end-to-end distance within the MD run at different pH values.

Regardless of pH, R_gs did not change much along the series, resulted unfazed by the different amino acid hydrophobic side chain. Hence, coil size was mainly dictated by the conformational properties of the backbone and, to a minor extent, by the protonation state of carboxylate and amine groups.

The variation of the overall dipole moment μ (Table 5) with pH followed the same trend shown by CD spectra (Figure 22): μ was lowest at pH 1, where all units were positively charged and many local dipole vectors mutually compensate; At pH 5, at the polymers' pI, μ was the highest for M-*L*-

Ala and M-*L*-Leu. At pH 11, where chains resulted negatively charged, μ decreased. Differently, for M-*L*-Val the highest dipole moment was obtained at pH 11, due to a favorable combination of charged groups and local dipoles.

Gyration radii were compared with hydrodynamic radii obtained from DLS measurements for polydisperse PAAC samples at the same overall charges (Table 6).

Table 6. pH Dependence of PAAC hydrodynamic radius in water.

Polymer	R_h (nm)[a] at pH 1.5	R_h (nm)[a] at pH 5.0	R_h (nm)[a] at pH 9.0
M-*L*-Ala	1.56 ± 0.52	1.54 ± 0.43	0.59 ± 0.17
M-*L*-Val	1.13 ± 0.33	0.90 ± 0.21	0.45 ± 0.17
M-*L*-Leu	1.40 ± 0.41	1.61 ± 0.49	0.67 ± 0.17

[a] Determined by DLS on polydisperse samples (see Experimental section) at 5 mg mL^{-1} concentration.

Both MD and experimental results confirmed the compactness of PAAC structures, despite the difference in molecular weight and polydispersity. Theoretical values calculated at pH 1 and 5 matched the experimental data obtained at the same pH, whereas at pH 9.0 results were not comparable. In fact, DLS measurements in basic conditions were carried out without equating the ionic strength by adding NaCl, approaching the instrument detection limits and resulting as such unreliable. As with *L*-ARGO7, a hairpin-like conformation was assumed by PAACs chains due to intramolecular interactions (Figure 29-3a). At pH 1 and 5, these conformations were characterized by a distribution of torsion angles peaked around ± 180° (transoid arrangement), less pronounced for pH 11, due to repulsive interactions among negatively charged carboxylate groups.

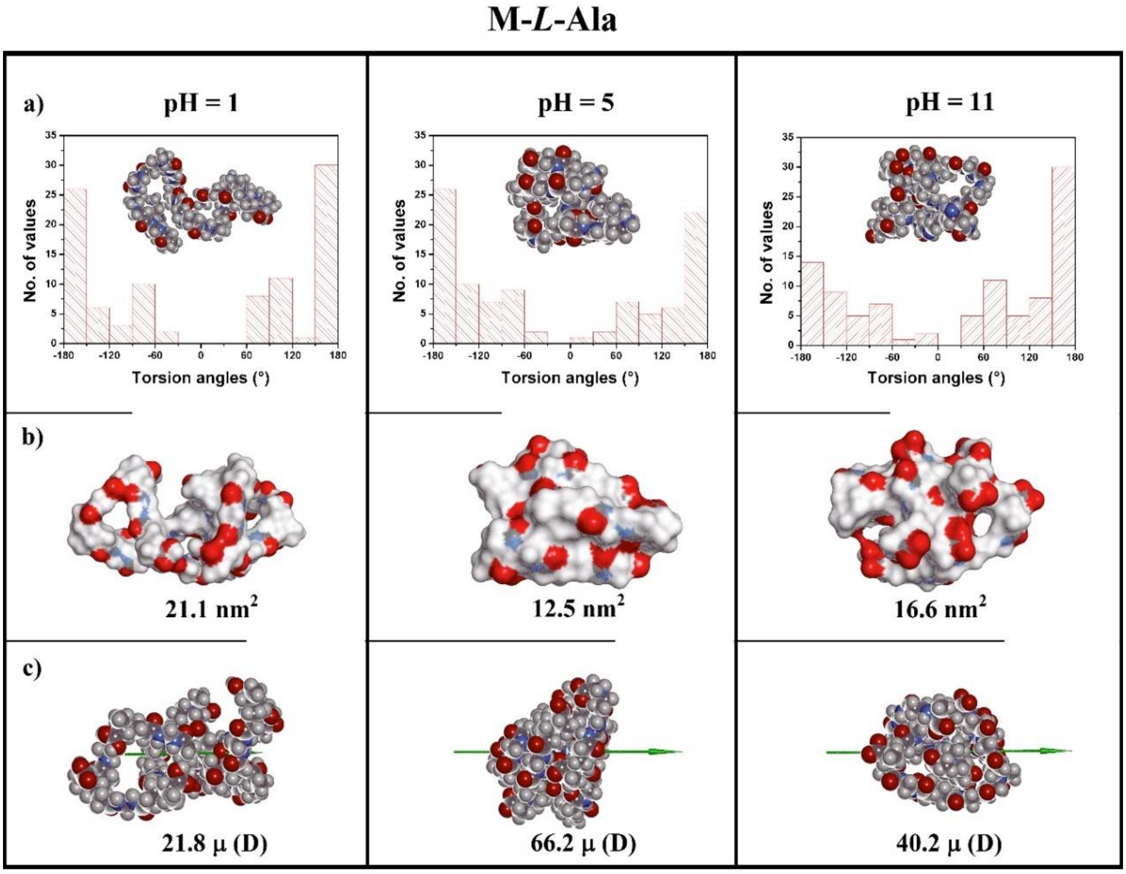

Figure 29. a) Main chain molecular conformations in water at the end of the MD runs for M-L-Ala at pH 1, 5 and 11 and torsion angle distributions around the main chain bonds: the histogram are shown with a binning of 30°. Color codes: C atoms dark grey; H atoms light gray; N atoms blue; O atoms red. b) Solvent accessible surface area in water. The surface area is in dark grey near C atoms, in light gray near H atoms, in blue near N atoms and in red near O atoms. c) Dipole moments in water. Color codes are the same as in row a).

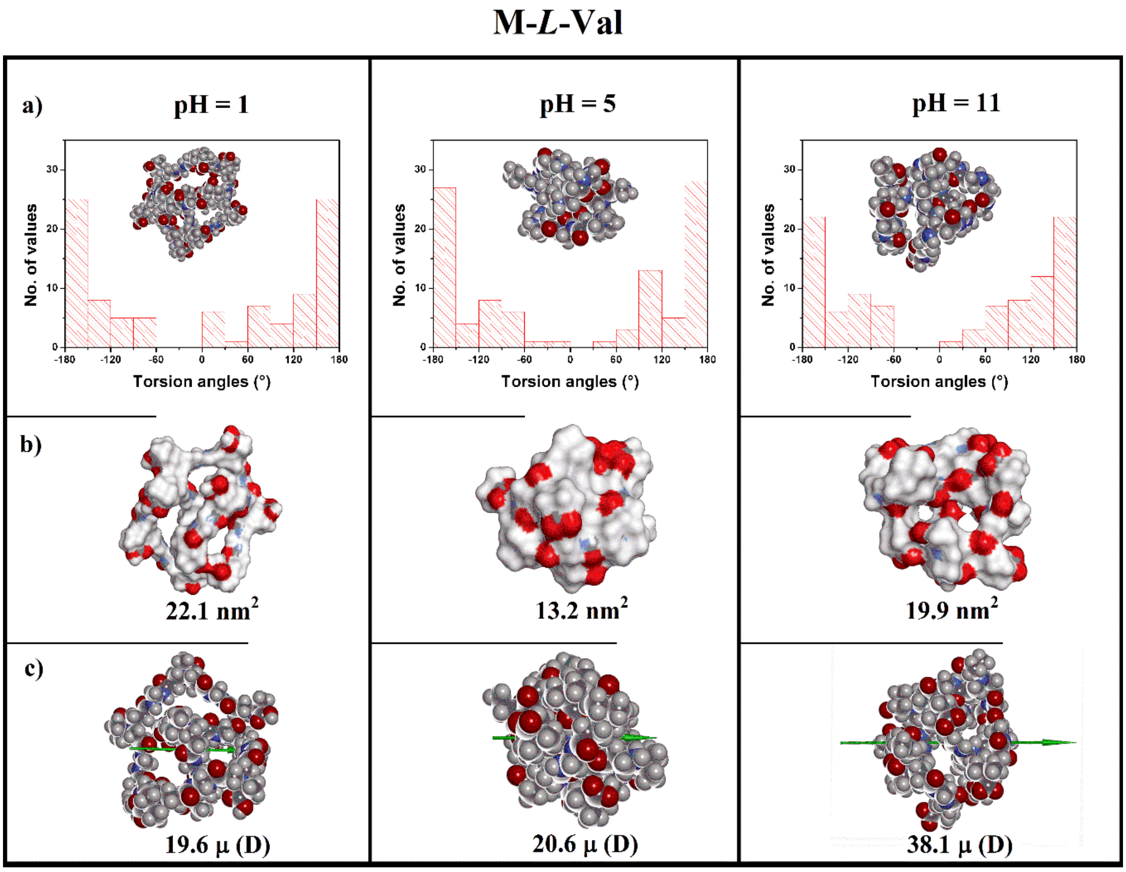

Figure 30. a) Main chain molecular conformations in water at the end of the MD runs for M-L-Val at pH 1, 5 and 11 and torsion angle distributions around the main chain bonds: the histogram are shown with a binning of 30°. Color codes: C atoms dark grey; H atoms light gray; N atoms blue; O atoms red. b) Solvent accessible surface area in water. The surface area is in dark grey near C atoms, in light gray near H atoms, in blue near N atoms and in red near O atoms. c) Dipole moments in water. Color codes are the same as in row a).

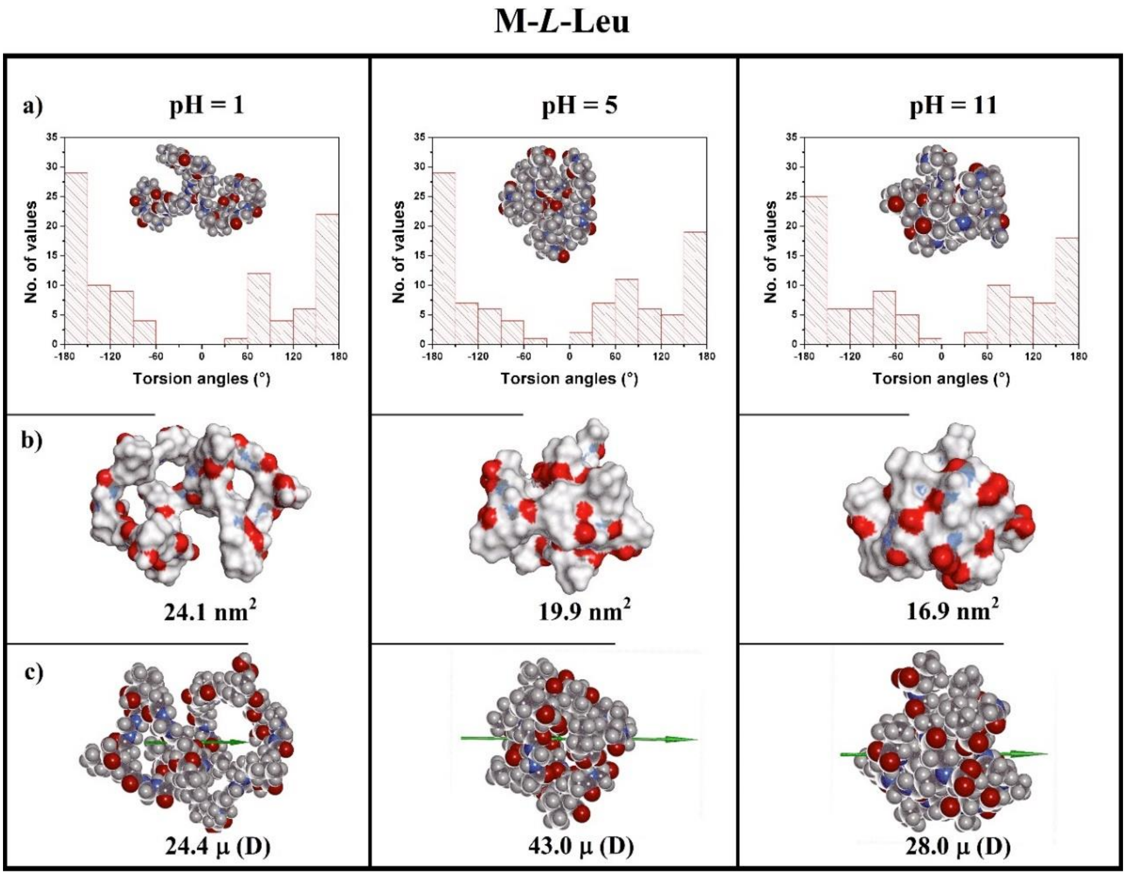

Figure 31. a) Main chain molecular conformations in water at the end of the MD runs for M-*L*-Leu at pH 1, 5 and 11 and torsion angle distributions around the main chain bonds: the histogram are shown with a binning of 30°. Color codes: C atoms dark grey; H atoms light gray; N atoms blue; O atoms red. b) Solvent accessible surface area in water. The surface area is in dark grey near C atoms, in light gray near H atoms, in blue near N atoms and in red near O atoms. c) Dipole moments in water. Color codes are the same as in row a).

GLUTAMINE-BASED POLYMER

Results obtained for *L*-ARGO7, M-*L*-Ala, M-*L*-Val and M-*L*-Leu showed that structuring and size were dictated mainly by intramolecular interactions of the polymer main chain, independently from the nature of the amino-acid side chain. Their solution properties were governed mainly by the *tert*-amine ionization degree, concluding that none of these PAACs presented a significant amount of intermolecular hydrogen bonding.

This chapter will introduce M-*L*-Gln, a glutamine-based PAACs synthesized with the same Michael polyaddition reaction. This polymer was chosen since the amino-acid *L*-glutamine is widely known in literature for its ability to associate even in dilute solutions, as a result of hydrogen bonding between side chain-side chain (CO_2HCHNH_2), backbone-backbone ($CH_2CH_2CONH_2$) and side chain-backbone interactions [28,29]. A comparison between the other PAACs and M-*L*-Gln pH dependent solution properties and ability to form intermolecular interactions, preferentially via hydrogen bonding, will be conducted.

2.3 RESULTS AND DISCUSSION

2.3.1 Synthesis of M-*L*-Gln

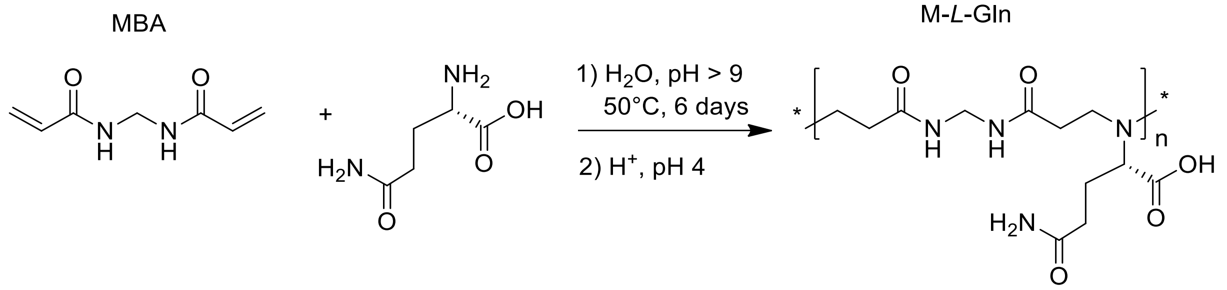

Scheme 3. Synthesis of M-L-Gln.

The reaction, a Michael type polyaddition of the amino acid *prim*-amine with *N,N'*-methylenebisacrylamide, was essentially performed as already described in the other chapters, that is, in water at 60° and pH $\geq$ 9. Molecular weights, determined by size exclusion chromatography (SEC), revealed that M-*L*-Gln had significantly higher molecular weights and polydispersity than the PAACs so far investigated (Table 7). The broader molecular weight distribution (M_w) probably pointed out to the presence of aggregates. This unique behavior was possibly associated with an increased formation, in this polymer, of intra and intermolecular hydrogen bonding, as confirmed by molecular dynamics simulations (see below, section 2.3.6).

Table 7. Comparison of PAACs molecular weights, M_w and polydispersity index, obtained from size exclusion chromatography.

Sample	M_w	**PDI**
M-*L*-Gln	21500	2.31
M-*L*-Ala	7800	1.44
M-*L*-Val	5600	1.30
M-*L*-Leu	6200	1.51

2.3.2 Acid-base properties

M-*L*-Gln carboxyl and *tert*-amine pKa values (Table 8) were determined by potentiometric titration using the modified Henderson Hasselbalch equation following the same procedure used for ARGO7 and alkyl-substituted PAACs. Both pK_as and their trend with the degree of dissociation α were in line with the results obtained for the other PAACs.

Table 8. pK_a and β values of M-L-Gln in the α range 0.2–0.8 (β_1) and 0.1–0.9 (β_2).

Sample	$^a pK_{a1}$	$^c pK_{a2}$	$^a \beta_1$	$^c \beta_2$	^{d}**IP**
M-*L*-Gln	$2.17^b \pm 0.05$	$6.80^b \pm 0.05$	$0.84^b \pm 0.09$	$1.62^b \pm 0.08$	4.5

[a] Carboxyl group. [b] Average values obtained from four forward titration experiments. [c] Amine group. [d] Isoelectric point.

The repeat units of M-*L*-Gln can exist in three ionization states, positively charged (L^+), uncharged (L^0) and negatively charged (L^-) (Figure 31b). The pH-dependent speciation curves (Figure 31a) were determined from the pK_a and β values reported in Table 8 by the method described in the Experimental Section.

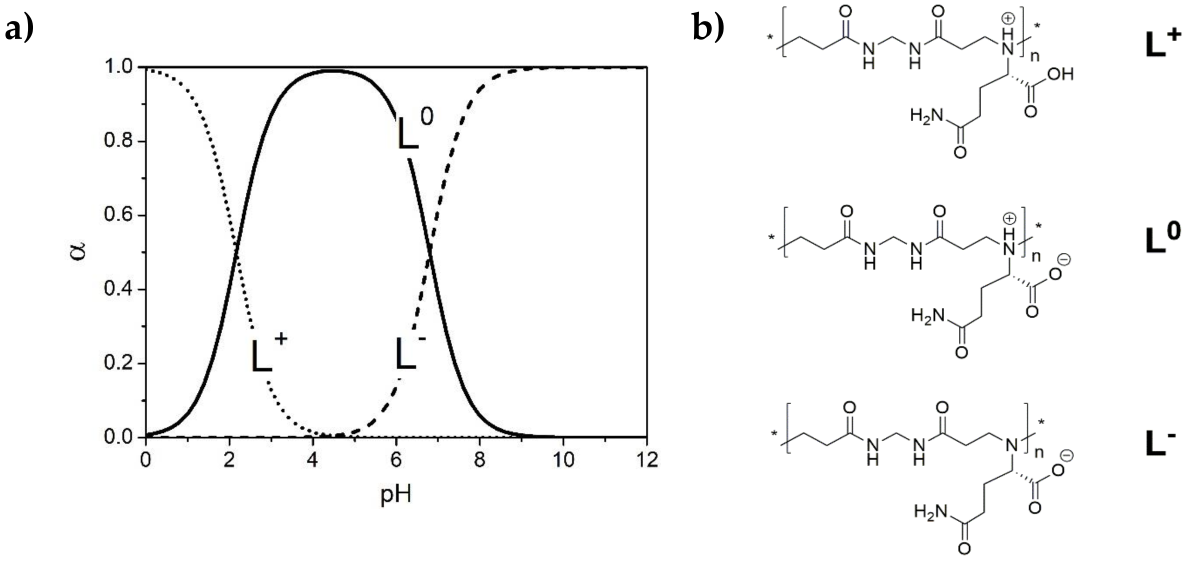

Figure 31. Speciation diagram and ionization states of M-L-Gln.

2.3.3 Circular Dichroism (CD) Analysis

CD spectra of M-*L*-Gln, obtained in 0.1 M NaCl aqueous solution in the pH range 3 – 11, were consistent with self-structuring (Figure 32). As for all PAACs so far described, also M-*L*-Gln showed pH-dependent CD patterns. However, differently from other PAACs, the M-*L*-Gln spectra obtained at acidic pH exhibited positive molar ellipticity with maxima centered at 217 nm. Only modest negative peaks were present with minima centered at 210 ÷ 215 nm. These positive peaks were mainly ascribed to the weak n → π* transition of the CONH groups [30], present both in the polymer backbone and in the glutamine side chain. Moreover, by increasing pH, the molar ellipticity maxima underwent a progressive bathochromic shift up to 227 nm at pH 9.77, with reduced intensities as well. As in the previously described PAACs, the pH-dependence of the spectral patterns was dictated by conformational changes of the polymer induced by the different ionization state of the ionizable groups.

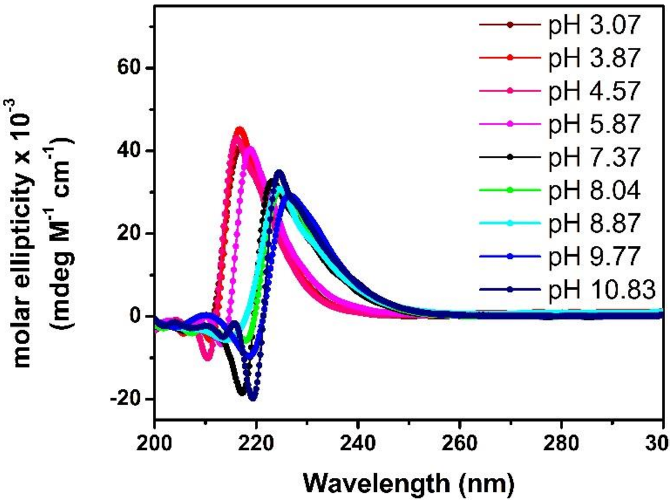

Figure 32. pH-Dependence of M-*L*-Gln CD spectra. Data were obtained in 0.1 M NaCl solution at 25 °C. The overall concentration of the repeating units was 1.66 mM.

The dependence of CD spectra on ionic strength and presence of denaturants at pH 8.0 was investigated immediately after the solution was prepared and even after 24 hrs. The spectral pattern was slightly affected by increasing ionic strength up to 2 M NaCl (Figure 33a), remaining unchanged over time (Figure 33b). By contrast, in 2 M urea it underwent a significant bathochromic shift, with a 237 nm and 243 nm maximum displacement for the negative and positive peak, respectively. Concomitantly, intensity of the positive peak decreased and increased for the negative peak. The spectral variations were more pronounced after 24 hrs (Figure 5c), suggesting the progressive breakdown of hydrogen bonds.

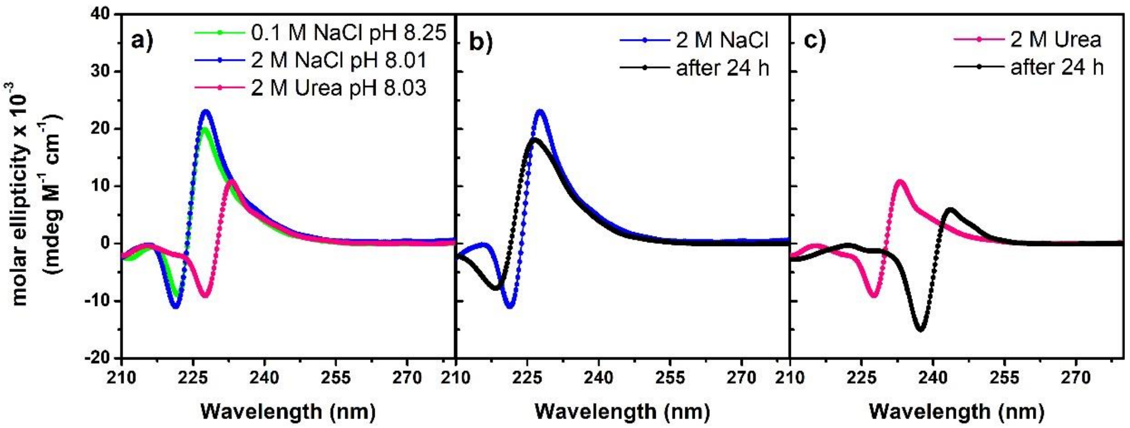

Figure 33. M-*L*-Gln CD spectra dependence on: ionic strength (blue line) and denaturating agent as 2 M urea (purple line) in panel a); time after 24 h in 2 M NaCl aqueous solution, in panel b) and time after 24 h in 2 M urea in panel c). The overall concentration of the repeating units was 1.66 mM.

2.3.4 Dynamic Light Scattering (DLS) Measurements

Dynamic light scattering analyses were carried out on 1 mg mL^{-1} solutions of M-*L*-Gln in 0.1 M aqueous NaCl at different pHs. As shown in Figure 34, R_h was ≈2.75 nm, higher than those normally recorded for the other PAACs, unaffected by pH modifications.

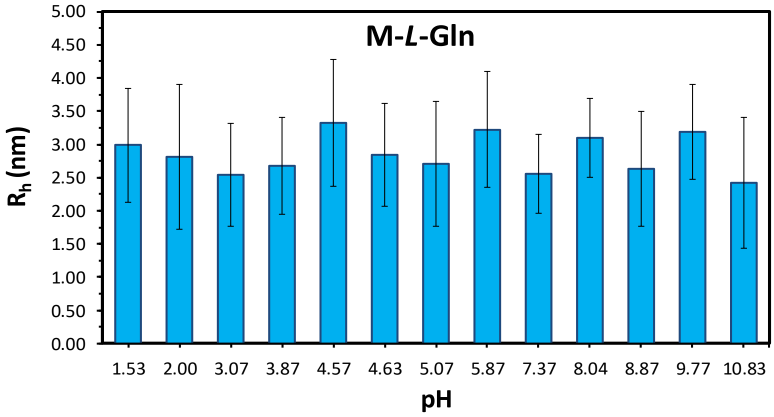

Figure 34. pH-Dependence of the hydrodynamic radius of M-L-Gln. Data were obtained in 0.1 M NaCl at 1 mg·mL^{-1} and 25 °C.

In addition, DLS was recorded at higher ionic strength (2 M NaCl) and in presence of denaturants (2 M urea and guanidinium chloride). In all cases, R_h did not change upon modifications of these parameters (Figure 35).

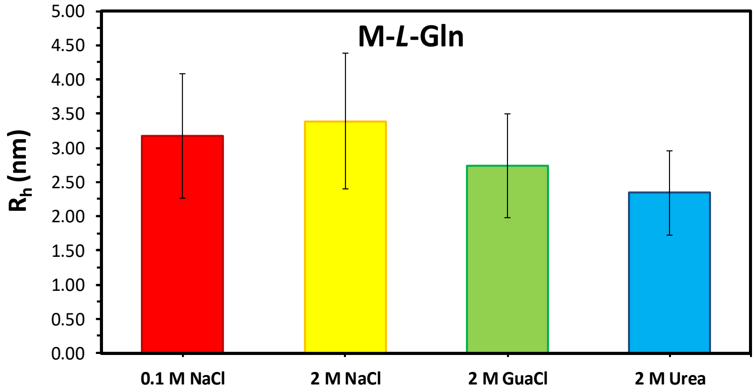

Figure 35. Dependence of the hydrodynamic radius of M-L-Gln on ionic strength (0.1 and 2 M NaCl) and presence of denaturating agents (2 M GuaCl and Urea). Data were obtained at 1 mg·mL^{-1} and 25 °C, pH = 8.

2.3.5 NMR analysis

NMR techniques like DOSY, variable-temperature NMR (VT-NMR) and NOESY were recorded for aqueous M-*L*-Gln at pH 4.5 and 25°C to obtain its structural and conformational features. Measurements were carried out at Università di Milano by Dr. Francesca Vasile. All data were compared to glycine-derived PAAC (M-Gly), the structurally simplest and less hindered polymer of all the polyamidoamino acids considered so far. M-Gly was synthesized with the same synthetic procedure mentioned above, and with comparable molecular weights.

DOSY measurements were used to calculate the diffusion coefficient and the hydrodynamic radius of the polymer. In water at pH 4.5, only one diffusion coefficient was measured, excluding as such presence of aggregates that would have apparently increased the molecular weight. Then, hydrodynamic radius was calculated using Stokes-Einstein Equation (Eq. 16). The R_h value of M-*L*-Gln was 3.53 nm, showing good agreement with DLS data. As expected, R_h resulted higher than both R_hS of all the other PAACs and of M-Gly (2.47 nm) of comparable M_w.

$$D = \frac{k_B T}{6\pi\eta r} \qquad \text{(Eq. 16)}$$

where D is the diffusion coefficient (m^2 s^{-1}), k_B the Boltzmann's constant (J K^{-1}), η is the dynamic viscosity (Pa s) and r the radius of the spherical particle.

To investigate the formation of hydrogen bonding, variable-temperature NMR (VT-NMR) experiment was performed. Attention was focused on the behavior of amide protons in water. When these protons are involved in intra- or intermolecular H-bonding formation, they experience a lower chemical shift variation (Δδ) upon temperature modification (ΔT). Comparison between amides in the glutamine side-chain and in the polymers' backbone were reported in terms of Δδ/Δt. Calculation were carried out assuming chemical shifts reflected equilibrium between conformations. The analysis of zwitterionic M-*L*-Gln (pH 4.5) revealed that the side-chain amide groups were involved in the formation of H-bonds, since their Δδ/Δt value was -4.5 ppm, whereas only a small percentage of amides of the MBA backbone did the same (Δδ/Δt value was -6.0 ppm). Even M-Gly gave the same variation of -6.0 ppm for main chain amides, demonstrating this feature to be the same in all PAACs.

By decreasing pH to 1, amides groups in M-*L*-Gln side chain still formed H-bonds but in lower amounts. Once the presence of H-bonding was established, further investigation on NOE signals were conducted to determine M-*L*-Gln chain conformations. The NOESY experiments measured two NOEs, both involving CH_2 next to the *tert*-amine and CH_2 in β and γ position of the glutamine side chain, respectively. Thus, M-*L*-Gln showed a coiled structure in which glutamine side chain moved closer to the main chain. Possibly, changing the protonation degree of the *tert*-amine will sensibly affect structural reorganization.

2.3.6 Theoretical Modeling

MD analyses were carried out with the same procedure already described for the other PAACs, considering 10 repeating units, at different pH: 1, 6 and 14. Gyration radius (R_g), surface accessible to the solvent (S) and dipole moment (μ) were reported in Table 9. Similarly to the other PAACs, M-*L*-Gln assumed a coiled structure, driven by the main-chain, with R_g between 0.8 – 1.07 nm and torsion angle distributions slightly affected by pH (Figure A5).

Table 9. Properties of simulated M-*L*-Gln at different pH values in water at the end of the molecular dynamics run.

pH	R_g (nm)	S (nm^2)[a)]	μ (D)
1	1.07	25.1	19.80
6	0.82	17.1	32.10
14	0.98	23.5	23.20

[a)] surface accessible to a 1.4 Å radius spherical probe. In all cases, SD was less than 2% of the calculated values.

The dipole moment (μ) was evaluated for the glutamine side chain and the main chain, independently. Noticeably, at pH 1 the dipole moment of glutamine side chain was almost three times higher than the overall μ of the main chain (Table 10). This peculiarity, coupled with the specific orientation of the amino-acid residues, might explain the high intensity peak shown in CD spectra (Figure 32). With increasing pH, the overall μ increased and differences between main chain and side chain were less pronounced. As expected, when M-*L*-Gln units were electrically balanced (pH 6), μ recorded its highest value.

Table 10. Calculated dipole moments among the PAACs studied so far: differences between μ of the side-chain and the main chain.

	pH 1	*pH 6*	*pH 14*
L-ARGO7			
Side chain	26.4	45.5	37.7
Main Chain	23.7	25.1	19.0
M-*L*-Ala			
Side chain	21.8	66.2	40.2
Main Chain	8.97	14.4	7.3
M-*L*-Leu			
Side chain	24.4	43.0	27.8
Main Chain	15.7	26.1	19.0
M-*L*-Val			
Side chain	19.6	20.6	38.1
Main Chain	15.1	13.6	10.3
M-*L*-Gln			
Side chain	19.8	32.1	23.2
Main Chain	6.4	28.8	20.9

Differently from the other PAACs, during the MD runs inter- and intramolecular H-bonding was formed in high quantity along the 10 repeating units. In particular, the highest amounts of H-bonds could be found at pH 6, where M-*L*-Gln was mainly in its zwitterionic form. At this pH, the overall intra- and intermolecular H-bonds along the main chain were 12, and mainly arose from carbonyl groups and *tert*-amine. Instead, considering the glutamine pendants as well, 11 were the H-bonds calculated between glutamine's amide groups, *tert*-amines and carboxylate groups. The presence of this high number of H-bonding might explain the highest M_w, since inter- and intramolecular forces stack together both glutamine monomers and the forming chains, resulting in an increase in the local concentration of the reactive amines. By decreasing or increasing pH, numbers of H-bonds drastically diminished. These data were in line with NMR measurements, showing that side-chain amide groups were the main responsible of hydrogen bonding formation.

2.4 CONCLUSIONS

In conclusion, a new family of bioinspired polymers named polyamidoamino acids (PAACs) were introduced. A small library of chiral polymers was obtained by polyaddition of natural α-aminoacids to bisacrylamides. In particular, three types of polymer were synthesized and discussed, in order: i) arginine-based PAACs obtained from *L*-arginine (*L*-ARGO7), *D*-arginine (*D*-ARGO7) and *D,L*-arginine (*D,L*-ARGO7); ii) alkyl-substituted PAACs derived from *L*-alanine (M-*L*-Ala), *L*-valine

(M-*L*-Val) and *L*-leucine (M-*L*-Leu) and iii) a glutamine-based PAAC obtained from *L*-glutamine (M-*L*-Gln). Synthesis, acid-base properties, self-structuring abilities, intermolecular interactions and size in solutions were reported. Results indicated all these polymers behave in a similar way, with minor differences owing to the amino acid side chain considered.

Syntheses were carried out at 50°C for 6 days and pH > 9, obtaining fairly high molecular weights ranging from 5600 to 7800 for all PAACs, M-*L*-Gln excluded. The latter showed higher molecular weights (M_w and M_n), associated with the presence of intra- and intermolecular hydrogen bonding, as proved by VT-NMR measurements. In no cases, traces of aggregates or side products from hydrolytic degradation were seen. Regarding acid-base properties, PAACs did not show the typical polyelectrolytes behavior: their pK_{a1s} decreased with increasing ionization degree implying the formation of inter-polyelectrolyte complexes. Thus, to release protons from ammonium groups, this complex needs to be broken down first.

In water, the PAACs considered showed CD spectra revealing, in the wavelength interval 200-280 nm, a clearly pH-dependent self-structuring. *D*- and *L*-ARGO7 showed mirror-image spectra and peak maximum centered at 228 nm with positive ellipticity. The same was true for all the other PAACs, M-*L*-Gln excluded, whose maximum was centered at 228 (M-*L*-Ala), 234 (M-*L*-Val) and 231 (M-*L*-Leu) nm respectively. These positive peaks were mainly ascribed to the weak $n \rightarrow \pi^*$ transition of the CONH groups. Their maximum value increased with increasing pH, allowing calculation of differential molar ellipticities ($\Delta\Theta$). Sigmoidal curves of $\Delta\Theta$ vs pH were then obtained with lower plateaus at acid pH, upper plateaus at basic pH, and inflection points corresponding to the half-neutralization of the *tert*-amine groups of each polymer. In the case of M-*L*-Gln, owing to the presence of $CONH_2$ groups in both the polymer backbone and in the glutamine side chain, CD spectra presented high intensity peak in the whole pH range. In acidic conditions, peak was centered at 217 nm whereas in basic conditions at 227 nm. For all PAACs, the pH induced conformational changes were quickly reversible by changing pH and temperature. Only M-*L*-Ala showed minor changes above 70°C. Conformations were little affected by ionic strength and presence of denaturating agents, with some differences: CD spectra of ARGO7 isomers did not change upon introduction of either urea or guanidinium chloride, whereas M-*L*-Ala, M-*L*-Val and M-*L*-Leu conformations changed with the introduction of guanidinium chloride. The most affected of all resulted M-*L*-Ala. Instead, CD spectra of glutamine derived PAAC resulted sensitive to the presence of urea, with time dependent spectral variations.

DLS measurements in 0.1 M NaCl gave hydrodynamic radii stable at 25 °C for at least 1 month and unaffected by pH, ionic strength and presence of denaturants. In addition, R_hs were not affected by increasing concentration in the 0.5-20 mg mL^{-1} range, suggesting that PAACs may intramolecularly self-assembled into single chain nanoparticles. Noticeably, M-*L*-Gln showed the highest R_h values of all PAACs so far considered.

Molecular dynamics studies on *L*-ARGO7, M-*L*-Ala, M-*L*-Val, M-*L*-Leu and M-*L*-Gln revealed that all of them have in water a compact structure, with R_g in the range 0.8-1.11 nm and a main chain organized into a transoid arrangement, hairpin-like conformation, due to intramolecular interactions. For all of them except M-*L*-Gln, these were principally of electrostatic nature, due to the local dipoles, and to a few intramolecular hydrogen bonds within main chain, side groups and among them. Structuring and size were dictated mainly by intramolecular interactions in the polymer main chain, with minor dependence from the amino acids side chain. Notwithstanding their compact structure, a very efficient hydration was still granted by the large cavities presented in the modeled structures. Differently from the other PAACs, MD runs of M-*L*-Gln showed a higher number of H-bonding, both along the main chain and the glutamine residues. In particular, VT-NMR and MD showed that the main responsible of H-bonding in M-*L*-Gln were side-chain amides groups. Consequently, the polymers' coiled conformation was possibly held together by these interactions as well.

2.5 REFERENCES

1. Bauri, K.; Ghosh Roy, S.; De, P. Side-Chain Amino-Acid-Derived Cationic Chiral Polymers by Controlled Radical Polymerization. *Macromol. Chem. Phys.* **2016**, *217*, 365-379, DOI: 10.1002/macp.201500271.

2. Sanda, F.; Nakamura, M.; Endo T. Syntheses and Radical Copolymerization Behavior of Optically Active Methacrylamides Having L- and D-Leucine Moieties. Interaction between L- and D-Forms. *Macromolecules* **1996**, *29*, 8064-8068, DOI: 10.1021/ma960906i.

3. Casolaro, M.; Casolaro, I. Stimuli-Responsive Hydrogels Bearing α-Amino Acid Residues: A Potential Platform for Future Therapies. *J. Biomed. Eng. Med. Devic.* **2016**, *1*, 111.

4. Mori, H.; Kato, I.; Endo, T. Dual-Stimuli-Responsive Block Copolymers Derived from Proline Derivatives. *Macromolecules* **2009**, *42*, 4985-4992, DOI: 10.1021/ma900706s.

5. Roy, S. G.; De, P. pH Responsive Polymers with Amino Acids in the Side Chains and their Potential Applications. *J. Appl. Polym. Sci.* **2014**, DOI: 10.1002/app.41084.

6. Ladmiral, V.; Charlot, A.; Semsarilar, M.; Armes, S.P. Synthesis and Characterization of Poly(Amino Acid Methacrylate)-Stabilized Diblock Copolymer Nano-Objects. *Polym. Chem.* **2015**, *6*, 1805-1816, DOI: 10.1039/C4PY01556H.

7. Sugiyama, K.; Rikimaru, S.; Okada, Y.; Shiraishi, K. Preparation and Application of Chiral Recognizable Thermosensitive Polymers and Hydrogels Consisting of N-Methacryloyl-S-Phenylalanine Methyl Ester. *J. Appl. Polym. Sci.* **2001**, *82*, 228-236, DOI: 10.1002/app.1842.

8. Liu, Z.; Hu, J.; Sun, J.; He, G.; Li, Y.; Zhang, G. Preparation of Thermoresponsive Polymers Bearing Amino Acid Diamide Derivatives via RAFT Polymerization. *J. Polym. Sci., Part A: Polym. Chem.* **2010**, *48*, 3573-3586, DOI: 10.1002/pola.24137.

9. Cheuk, K. K. L.; Li, B. S.; Lam, J. W. Y.; Xie, Y.; Tang, B. Z. Synthesis, Chain Helicity, Assembling Structure, and Biological Compatibility of Poly(Phenylacetylene)s Containing L-Alanine Moieties. *Macromolecules* **2008**, *41*, 5997-6005, DOI: 10.1021/ma800976e.

10. Hopkins, T. E.; Pawlow, J. H.; Koren, D. L.; Deters, K. S.; Solivan, S. M.; Davis, J. A.; Gómez, F. J.; Wagener, K. B. Chiral Polyolefins Bearing Amino Acids. *Macromolecules* **2001**, *34*, 7920-7922, DOI: 10.1021/ma010930i.

11. Cheng, R.; Liu, J.; Xie, P.; Wu, Y.; Deng, J. Chiral, pH-Sensitive Polyacrylamide Hydrogels: Preparation and Enantio-Differentiating Release Ability. *Polymer* **2015**, *68*, 246-252, DOI: 10.1016/j.polymer.2015.05.034.

12. Sanda, S.; Endo, T. Synthesis and Cationic Polymerization of A Novel Optically Active Vinyl Ether with L-Proline Structure. *Macromol. Chem. Phys.* **1997**, *198*, 1209-1216, DOI: 10.1002/macp.1997.021980422.

13. Wang, X.; Gan, H.; Sun, T.; Su, B.; Fuchs, H.; Vestweber, D.; Butz, S. Stereochemistry Triggered Differential Cell Behaviours on Chiral Polymer Surfaces. *Soft Matter* **2010**, *6*, 3851-3855, DOI: 10.1039/C0SM00151A.

14. Ferruti, P.; Mauro, N.; Falciola, L.; Pifferi, V.; Bartoli, C.; Gazzarri, M.; Chiellini, F.; Ranucci, E. Amphoteric, Prevailingly Cationic L-Arginine Polymers of Poly(amidoamino acid) Structure: Synthesis, Acid/Base Properties and Preliminary Cytocompatibility and Cell- Permeating Characterizations. *Macromol. Biosci.* **2014**, *14*, 390-400, DOI: 10.1002/mabi.201300387.

15. Manfredi, A.; Mauro, N.; Terenzi, A.; Alongi, J.; Lazzari, F.; Ganazzoli, F.; Raffaini, G.; Ranucci, E.; Ferruti, P. Self-Ordering Secondary Structure of D- and L-Arginine-Derived Polyamidoamino Acids. *ACS Macro Lett.* **2017**, *6*, 987-991, DOI: 10.1021/acsmacrolett.7b00492.

16. Lazzari, F.; Manfredi, A.; Alongi, J.; Mendichi, R.; Ganazzoli, F.; Raffaini, G.; Ferruti, P.; Ranucci, E. Self-structuring in water of polyamidoamino acids with hydrophobic side chains deriving from natural α-amino acids. *Polymers* **2018**, *10*, 1261, doi:10.3390/polym10111261.

17. De Levie, R. How to Use ExcelW in Analytical Chemistry and in General Scientific Data Analysis; Cambridge University Press: Cambridge, 2001.

18. Mele, A.; Raffaini, G.; Ganazzoli, F.; Juza, M.; Schurig, V. Macrocycle Conformation And Self-Inclusion Phenomena in Octakis(3-O-butanoyl-2,6-di-O-pentyl)-γ-cyclodextrin (Lipodex E) by NMR spectroscopy and molecular dynamics. *Carbohydr. Res.* **2003**, *338*, 625–635. DOI: 10.1016/S0008-6215(02)00493-7.

19. Raffaini, G.; Ganazzoli, F. Surface Hydration of Polymeric (bio)materials: A Molecular Dynamics Simulation Study. *J. Biomed. Mater. Res., Part A* **2010**, *92*, 1382–1391. DOI: 10.1002/jbm.a.32483.

20. Raffaini, G.; Ganazzoli, F. Protein Adsorption On Biomaterial And Nanomaterial Surfaces: A Molecular Modeling Approach to Study Non-Covalent Interactions. *J. Appl. Biomater. Biomech.* **2010**, *8*, 135– 145. https://doi.org/10.5301/JABB.2010.6093.

21. Dauber-Osguthorpe, P.; Roberts, V.A.; Osguthorpe, D.J.; Wolff, J.; Genest, M.; Hagler, A.T. Strucutre and energetics of ligand binding to proteins: Escherichia coli dihydrofolate reductase-trimethoprim, a drug-receptor system. *Proteins: Struct. Funct. Genet.* **1988**, *4*, 31–47.

22. Katchalsky, A.; Spitnik, P. Potentiometric titrations of polymethacrylic acid. *J. Polym. Sci.* **1947**, 2, 432-446, DOI: 10.1002/pol.1947.120020409.

23. De Alba, E.; Jiménez, M. A.; Rico, M. Turn Residue Sequence Determines β-Hairpin Conformation in Designed Peptides. *J. Am. Chem. Soc.* **1997**, *119*, 175–183. https://doi.org/10.1021/ja962325e

24. Mei, C. G.; Jahr, N.; Singer, D.; Berger, S. Hairpin Conformation of An 11-mer Peptide. *Bioorg. Med. Chem.* **2011**, *19*, 3497–3501. https://doi.org/10.1016/j.bmc.2011.04.020

25. Mondal, S.; Varenik, M.; Bloch, D. N.; Atsmon-Raz, Y.; Jacoby, G.; Adler-Abramovich, L.; Shimon, L. J. W.; Beck, R.; Miller, Y.; Regev, O.; Gazit, E. A Minimal Length Rigid Helical Peptide Motif Allows Rational Design of Modular Surfactants. *Nat. Commun.* **2017**, *8*, 14018. doi: 10.1038/ncomms14018

26. Wagner, H. L.; Long, F. A. Properties of an Amphoteric Polymer of Vinylpyridine and Acrylic Acid. *J. Phys. Chem.* **1951**, *55*, 1512-1526, DOI: 10.1021/j150492a011.

27. Lappan, U.; Geißler, U.; Oelmann, M.; Schwarz S. Apparent Dissociation Constants of Polycarboxylic Acids in Presence of Polycations. *Colloid. Polym. Sci.* **2012**, *290*, 1665-1670, DOI: 10.1007/s00396-012-2702-2.

28. Rhys, N. H.; Soper, A. K.; Dougan, L. The hydrogen-bonding ability of the amino acid glutamine revealed by neutron diffraction scattering experiments. *J. Phys. Chem. B* **2012**, *116*, 13308-13319, doi:10.1021/jp307442f.

29. Rhys, N. H.; Dougan, L. The emerging role of hydrogen bond interactions in polyglutamine structure, stability and association. *Soft Matter* **2013**, *9*, 2359-2364, doi:10.1039/C2SM27565A.

30. Kelly, S.M.; Price, N.C. The use of circular dichroism in the investigation of protein structure and function. *Curr. Protein Pept. Sci.* **2000**, *1*, 349–384, doi:10.2174/1389203003381315.

2.6 APPENDIX

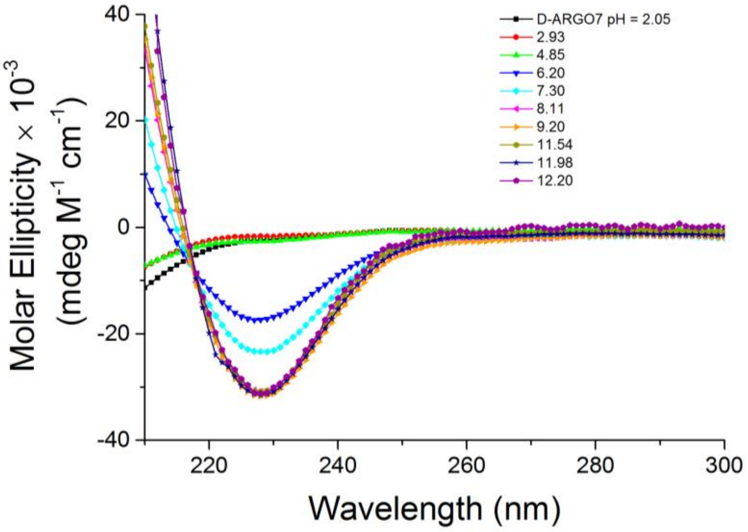

Figure A1. pH dependence of D-ARGO7 CD spectra, at 25°C.

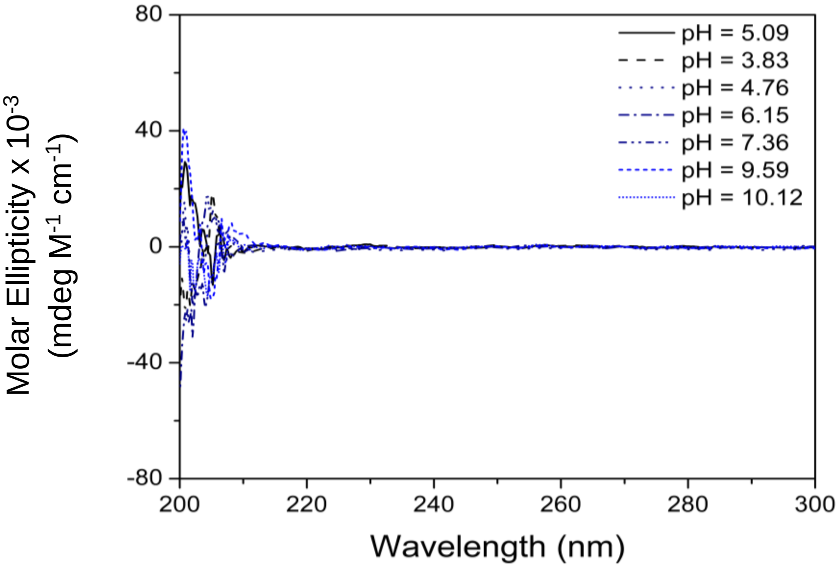

Figure A2. pH dependence of *D,L*-ARGO7 CD spectra, at 25°C.

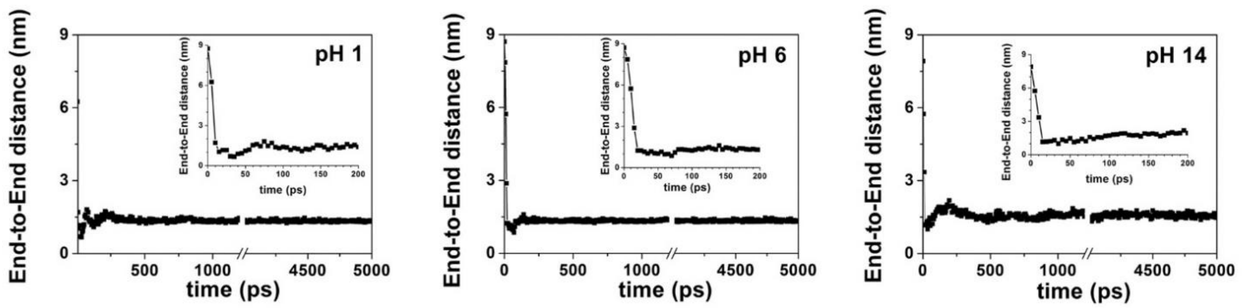

Figure A3. The end-to-end distance plotted vs the simulation time for the simulated chain at pH 1, 6, 14 in the effective dielectric medium. The inset shows an expanded view of the initial 200 ps.

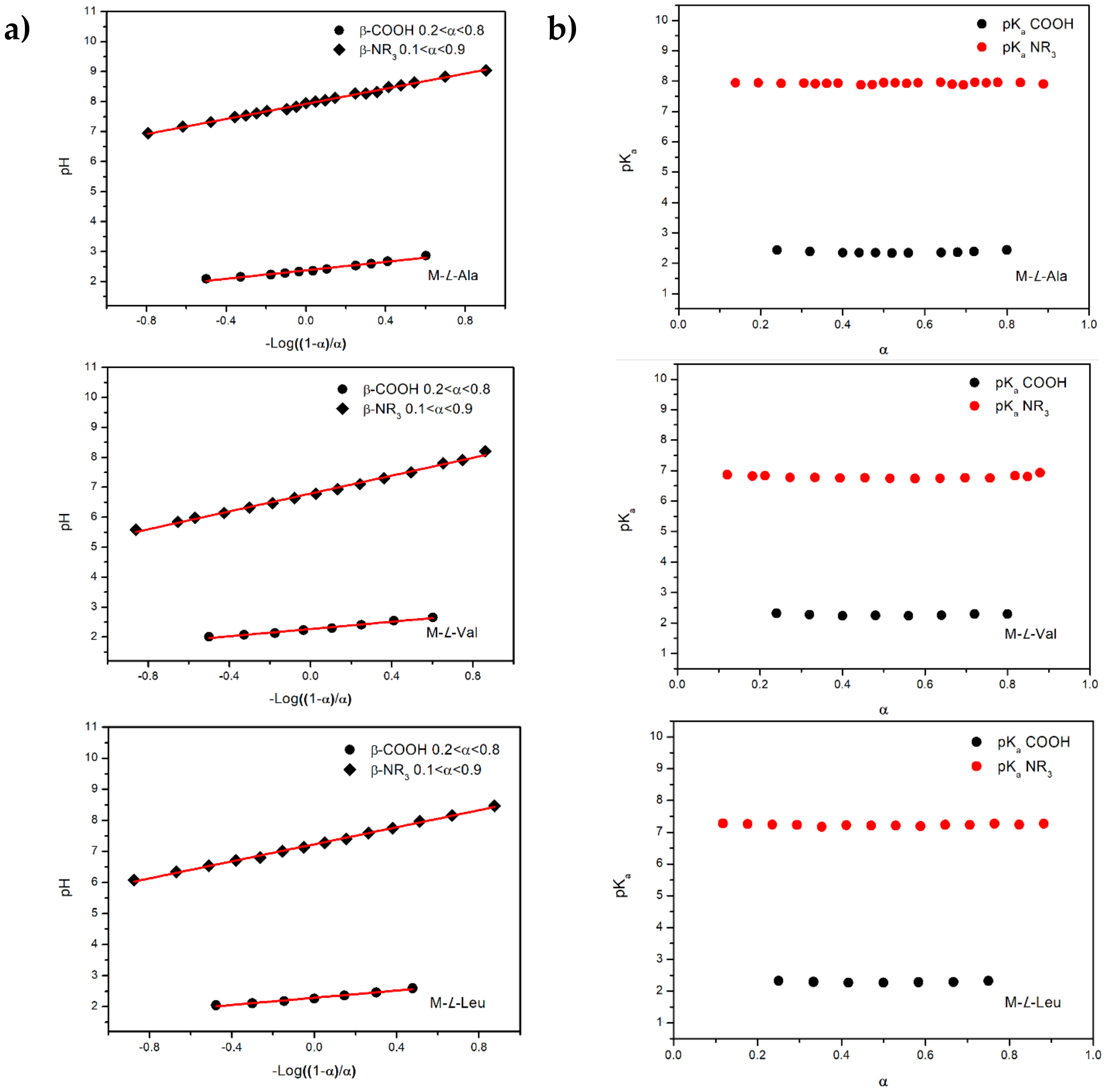

Figure A4. Determination of β parameters for side –COOH and chain tert-amine of M-*L*-Ala, M-*L*-Val and M-*L*-Leu referred to the 1st experiment of Table A2: a) calculation of β values from Eq. 1b and b) trend of the β-corrected pK_a values versus α according to Eq. 1a.

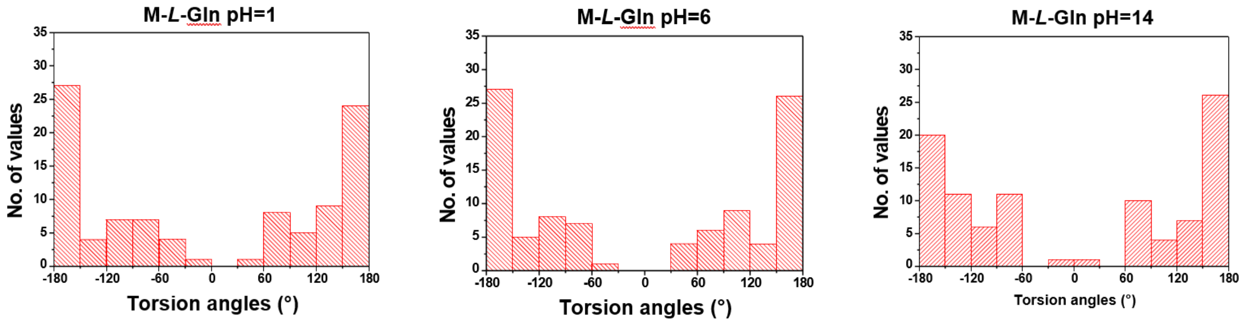

Figure A5. Torsion angle distributions around the main chain bonds of M-*L*-Gln at pH 1, 6 and 14: the histograms are shown with a binning of 30°.

Table A1. Titration data of ARGO7 isomers.

						***L*-ARGO7**
Forward	1st		2nd		3rd	
	-COOH	-NR$_3$	-COOH	-NR$_3$	-COOH	-NR$_3$
pK_a	2.31	6.48	2.29	6.37	2.33	6.44
Backward	1st		2nd		3rd	
	-COOH	-NR$_3$	-COOH	-NR$_3$		
pK_a	2.35	6.35	2.43	6.36		
						***D*-ARGO7**
Forward	1st		2nd		3rd	
	-COOH	-NR$_3$	-COOH	-NR$_3$	-COOH	-NR$_3$
pK_a	2.24	6.37	2.15	6.38	2.34	6.49
Backward	1st		2nd		3rd	
	-COOH	-NR$_3$	-COOH	-NR$_3$		
pK_a	2.37	6.51	2.40	6.37		
						***D,L*-ARGO7**
Forward	1st		2nd		3rd	
	-COOH	-NR$_3$	-COOH	-NR$_3$	-COOH	-NR$_3$
pK_a	2.27	6.40	2.36	6.39	2.39	6.37
Backward	1st		2nd		3rd	
	-COOH	-NR$_3$	-COOH	-NR$_3$		

pK$_a$	2.40	6.41	2.40	6.36

Table A2. PAAC *pK$_a$* values from forward and backward titration data.

								M-*L*-Ala
Forward	**1st**		**2nd**		**3rd**		**4th**	
	-COOH	-NR$_3$	-COOH	-NR$_3$	-COOH	-NR$_3$	-COOH	-NR$_3$
pK$_a$	2.07	7.90	2.15	8.27	2.13	8.15	2.13	8.24
Backward	**1st**		**2nd**		**3rd**		**4th**	
	-COOH	-NR$_3$	-COOH	-NR$_3$	-COOH	-NR$_3$	-COOH	-NR$_3$
pK$_a$	2.37	7.77	2.36	8.22	2.35	8.18	2.37	8.22
								M-*L*-Val
Forward	**1st**		**2nd**		**3rd**		**4th**	
	-COOH	-NR$_3$	-COOH	-NR$_3$	-COOH	-NR$_3$	-COOH	-NR$_3$
pK$_a$	2.12	6.78	1.98	6.74	2.11	6.77	2.10	6.82
Backward	**1st**		**2nd**		**3rd**		**4th**	
	-COOH	-NR$_3$	-COOH	-NR$_3$	-COOH	-NR$_3$	-COOH	-NR$_3$
pK$_a$	2.37	6.86	2.22	6.78	2.35	6.79	2.41	6.92
								M-*L*-Leu
Forward	**1st**		**2nd**		**3rd**		**4th**	
	-COOH	-NR$_3$	-COOH	-NR$_3$	-COOH	-NR$_3$	-COOH	-NR$_3$
pK$_a$	2.14	7.23	2.13	7.45	2.09	7.24	2.10	7.55
Backward	**1st**		**2nd**		**3rd**		**4th**	
	-COOH	-NR$_3$	-COOH	-NR$_3$	-COOH	-NR$_3$	-COOH	-NR$_3$
pK$_a$	2.37	7.16	2.42	7.28	7.28	2.40	7.23	2.68

3

Fluorescent properties and pH dependent self-organization of *D*-, *L*- and *D,L*-Tryptophan based polyamidoamino acids

> *"Se ti dico che la città a cui tende il mio viaggio è discontinua nello spazio e nel tempo, ora più rada ora più densa, tu non devi credere che si possa smettere di cercarla"*
>
> *(Calvino, Le città Invisibili)*

Lazzari, F.; Manfredi, A.; Alongi, J.; Marinotto, D.; Ferruti, P.; Ranucci, E. *Polymers* **2019**, 11, 543, doi:10.3390/polym11030543.

3.1 INTRODUCTION

Bioinspired homo- and copolymers synthesized from α-amino acids and bearing side-chain chirality have gained much attention in recent years due to their widespread applications as stimuli-responsive materials [1] with tunable pH- [2] and thermoreversible [3] solubility, chirality-dependent self-assembling via non-covalent forces [4,5] and chiral recognition [6] abilities. Among the synthetic side-chain chiral polymers, tryptophan-derived polymers are inherently fluorescent, and as such they may be of interest in cellular and molecular imaging [7]. In proteins, the fluorescence decay of *L*-tryptophan residues is used as a diagnostic tool to study their conformation [8]. Moreover, it has been shown that *L*-tryptophan-rich peptides have a critical role on the cellular uptake and membrane interaction of arginine-rich cell penetrating peptides [9]. In this case, the hydrophobicity of the indole moieties undoubtably plays a major role, whereas the hydrophobicity of other amino acids, such as *L*-phenylalanine [9], was reported to be much less effective in this respect. Several examples of tryptophan-derived polymers have been studied. For instance, poly-*N*-acryloyltryptophan was chosen as a model to study the chiral interactions with 1,1-bis-2-naphthol [10], while copolymers of *N*-acryloyltryptophan with other acrylamides [11] were employed in recognition studies [12–14]. In other cases, the interaction between copolymeric poly-*N*-methacryloyltryptophan and β-cyclodextrin was investigated [15]. Also, the tryptophan ester of polyhydroxyethylmethacrylate was synthesized, and its pH-dependent chiro-optical and fluorescence properties studied [16].

This chapter reports on the synthesis and characterization of homo- and copolymeric PAACs bearing tryptophan and tryptophan/glycine units as side chains. Tryptophan-based homopolymers were obtained by polyaddition of *D*-, *L*- and *D,L*-tryptophan to *N,N′*-methylenebisacrylamide, using the same reaction procedure reported in Chapter 2, Experimental Section p. 45. Polymers were named M-*D*-Trp, M-*L*-Trp and M-*D,L*-Trp respectively. Copolymers were synthesized starting from mixtures of *L*-tryptophan/glycine at different ratio, to obtain M-G-*L*-Trp_5, M-G-*L*-Trp_{10}, M-G-*L*-Trp_{20} and M-G-*L*-Trp_{40}. Their acid-base properties, structuring ability, pH dependent solubility, chiro-optical and fluorescence properties were determined as well.

3.2 EXPERIMENTAL SECTION

3.2.1 Materials

Solvents and reagents, unless otherwise indicated, were analytical-grade commercial products and used as received. *D*-, *L*-, *D,L*-tryptophan (≥ 98%, 97% and 98% respectively) and glycine (≥ 99%) were purchased from Sigma-Aldrich (Milano, Italy). *N,N′*-Methylenebisacrylamide (MBA, 96%) purchased from Acros Organics (Milano, Italy) and LiOH monohydrate (≥ 98%) was supplied by Honeywell Fluka (Steinheim, Westphalia, Germany). HCl and NaOH volumetric standard solutions were purchased from Fluka analytics (Milano, Italy), while ethanol (≥ 98%) from Riedel-de-Haën (Seelze, Hannover, Germany). Ultrapure water (18 $M\Omega \cdot cm^{-1}$), produced with a Millipore Milli-Q® apparatus (Darmstadt, Hesse, Germany), was used to prepare solutions.

3.2.2 Instruments and methods

^{1}H and ^{13}C NMR spectra were recorded in D_2O at 25 °C using a Bruker Avance DPX-400 NMR operating (Bruker, Milano, Italy) at 400.13 MHz (d1 = 10 s) and 100.40 MHz, respectively. Prior to the analysis, polymers were dissolved in water and basified with 0.1 M NaOH until pH 10. The final product was freeze-dried and dissolved in D_2O.

Fourier-Transform Infrared spectroscopy was recorded as described in Chapter 2, Experimental Section p. 39.

Size exclusion chromatography (SEC) traces were obtained as described in Chapter 2, Experimental Section p. 39.

Dynamic light scattering (DLS) analyses were carried out on 1 mg mL^{-1} polymer solutions using the instrument and procedure reported in Chapter 2, Experimental Section p. 39.

Circular dichroism (CD) spectra were obtained using the same instrument and procedure of Chapter 2, Experimental Section p. 40 reported for M-*L*-Ala, M-*L*-Val and M-*L*-Leu.

Solubility tests were performed in aqueous media at different pH's by recording the transmittance at 450 nm with a Perkin-Elmer Lambda 35 spectrometer using plastic cuvettes with 1 cm path length. Solutions were prepared by dissolving 20 mg polymer in 0.1 M NaOH (2.7 mL), adjusting the pH with 0.1 M or 0.01 M HCl aqueous solutions, and finally diluting with ultrapure water to 1 $mg \cdot mL^{-1}$

concentration. The solutions were thermostated for 90 min at 30 °C before measurements. Each analysis was performed in triplicate. The scattering of a polarized IR beam in ultrapure water at different pH's was used to detect the presence of aggregates, if any.

Acid-base properties, pKa and β parameter determination were determined using the procedure reported in Chapter 2, Experimental Section p. 40 with the following quantities: samples were dissolved in a 0.1 M NaCl aqueous solution (10 mL) to obtain a 0.05 M repeating unit solution. All solutions were adjusted to pH 1.2-1.3 using 1 M HCl (0.7 mL). Due to solubility limits, M-G-*L*-Trp$_{40}$ was back titrated with 0.1 M HCl starting from pH 12.3-12.4 adjusted with 0.1 M NaOH (0.7 mL).

Determination of simulated titration curves. Simulated titration curves were determined following the De Levie approach [17], already reported in Chapter 2, Experimental Section p.41, to iteratively refine *pKa* and *β* values achieving the best fitting to the experimental data. For tryptophan-based copolymers the equations considered were the same as M-*L*-Ala, M-*L*-Val and M-*L*-Leu:

- <u>Initial conditions:</u>

V_0 = initial solution volume
c_0 = initial PAACs concentration expressed as molarity of the repeat unit
c_S = initial concentration of ionic strength stabilizer
c_t = titrant concentration (strong base in forward titration or acid in backward titration)
V_t = volume of the titrant added (strong base in forward titration or acid in backward titration)
c_A or c_B = acid concentration (or base in backward titration) used to correct pH
N = moles of strong acid possibly present as residual from the synthetic process or PAACs pretreatments

- *<u>Mass balance:</u>*

$$C_{PAACS} = C_{L^+} + C_{L^0} + C_{L^-} = \frac{C_0 V_0}{V_0 + V_t} \qquad \text{(Eq. 1)}$$

- *<u>Equilibrium constants</u>* (Eq. 2a-c):

$$K_{a1} = \frac{C_{L^0} C_{H^+}}{C_{L^+}} \text{ (a)}; \qquad K_{a2} = \frac{C_{L^-} C_{H^+} y^2}{C_{L^0}} \text{ (b)}; \quad K_w = C_{H^+} C_{OH^-} y^2 \text{ (c)};$$

- *<u>Concentration fractions</u>* (Eq. 3a-c):

$$\alpha_2 = \frac{C_{L^+}}{C} = \frac{C_{H^+}^2}{D} \text{ (a)}; \qquad \alpha_1 = \frac{C_{L^0}}{C} = \frac{C_{H^+}y^2K_{a1}}{D} \text{ (b)}; \quad \alpha_0 = \frac{C_{L^-}}{C} = \frac{K_{a1}K_{a2}}{D} \text{ (c)};$$

with:

$$\mathrm{D} = \mathrm{C}_{\mathrm{H}^+}^2 + \mathrm{C}_{\mathrm{H}^+}\mathrm{K}_{\mathrm{a1}} + \mathrm{K}_{\mathrm{a1}}\mathrm{K}_{\mathrm{a2}} \qquad \text{(Eq. 4)}$$

The activity coefficients (Davies equation):

$$y = 10^{-0.5\left[\frac{\sqrt{I}}{1+\sqrt{I}}-0.3I\right]} \qquad \text{(Eq. 5)}$$

Ionic strength:

$$I = \frac{1}{2}\left(C_{H^+} + C_{OH^-} + C_{Na^+} + C_{Cl^-} + C_{L^+} + C_{L^-}\right) \quad \text{(Eq. 6)}$$

- <u>*Charge balance*</u>:

$$H^+ + Na^+ + L^+ = L^- + OH^- + Cl^- \qquad \text{(Eq. 7)}$$

where (Eq. 8a-e):

$$C_{Na^+} = \frac{C_TV_T+C_SV_0}{V_0+V_T} \text{ (a)}; \qquad C_{Cl^-} = \frac{C_SV_0+C_AV_A+N}{V_0+V_T} \text{ (b)}; \qquad C_{L^+} = \frac{\alpha_2C_0V_0}{V_0+V_T} \text{ (c)};$$

$$C_{L^-} = \frac{\alpha_0C_0V_0}{V_0+V_T} \text{ (d)}; \qquad C_{OH^-} = \frac{K_W}{C_{H^+}y^2} \text{ (e)};$$

Combining all former conditions, the following solving equation, representing the whole forward titration curve, was obtained in terms of V_T as a function of pH:

$$V_T = \frac{V_0[C_0(\alpha_0-\alpha_2)+C_A-\Delta]+N}{\Delta+C_T} \qquad \text{(Eq. 9)}$$

where:

$$\Delta = H^+ - OH^- = H^+ - {}^{K_W}\!/_{H^+y^2} \qquad \text{(Eq. 10)}$$

The whole backward titration is expressed in terms of *V_T* as a function of pH:

$$V_T = \frac{V_0[C_0(\alpha_0-\alpha_2)+C_A-\Delta]+N-(\Delta+C_B)V_B}{\Delta-C_T} \qquad \text{(Eq. 11)}$$

Simulated titration curves were obtained from Eq. 9-11 with the same calculation reported in Chapter 2, Experimental Section p. 41. The same was applied to *determine speciation diagrams.*

Absolute photoluminescence quantum yield, Φ, was measured using a C11347 Quantaurus Hamamatsu Photonics K.K spectrometer (Hamamatsu City, Shizuoka, Japan), equipped with a 150 W Xenon lamp, an integrating sphere and a multichannel detector. Φ was calculated using Eq. 12:

$$\Phi = \frac{PN(em)}{PN(abs)} = \frac{\int \frac{\lambda}{hc}\left[I_{em}^{sample}(\lambda) - I_{em}^{reference}(\lambda)\right]d\lambda}{\int \frac{\lambda}{hc}\left[I_{exc}^{reference}(\lambda) - I_{exc}^{sample}(\lambda)\right]d\lambda} \qquad \text{(Eq. 12)}$$

where PN(em) is the number of emitted photons, PN(abs) the number of absorbed photons, λ the wavelength, *h* the Planck's constant, *c* the speed of light, I_{em}^{sample} and $I_{em}^{reference}$ the photoluminescence intensities of the sample solution in ultrapure water and of water, respectively, I_{exc}^{sample} and $I_{exc}^{reference}$ the excitation light intensities of the sample solution in ultrapure water and of water, respectively. The error made was estimated to be around 5%.

Steady state and time-resolved fluorescence data were obtained using a FLS980 spectrofluorimeter (Edinburgh Instrument Ltd, Livingston, Scotland, UK). Emission spectra were recorded exciting at 279 nm, corrected for background intensity and quantum efficiency of the photomultiplier tube. Excitation spectra were carried out at the maximum of the emission spectrum and corrected for the intensity fluctuation of a 450 W Xenon arc lamp.

Time-resolved fluorescence measurements were performed through the time-correlated single photon counting technique with an Edinburgh Picosecond Pulsed Diode Laser EPLED-300 (Livingston, Scotland, UK): emitted wavelength 301 nm, temporal pulse width (FWHM) 857 ps. A Ludox solution was used as scatter to determine the instrument response function (IRF). Time-resolved fluorescence curves were reconvoluted using the IRF and a multi-exponential impulse response function (Eq. 13):

$$I(\lambda, t) = \sum_{i=1}^{n} \alpha_{\mathrm{i}}(\lambda) \exp\left(\frac{-t}{\tau_{\mathrm{i}}}\right) \quad \text{(Eq. 13)}$$

where n is the number of exponentials, α_i (λ) is the amplitude at wavelength λ and τ_i is the lifetime of the component i. Quality of the fit was evaluated through the reduced χ^2 values. Two different sets of 1 cm path-length quartz cells were employed for the photoluminescence analysis: the first ones were classic fluorescent cuvettes for non-degassed solutions, the second ones were built specifically to perform freeze-pump-thaw cycles to remove dissolved oxygen into the solution. To degas the solution as much as possible, three freeze-pump-thaw cycles were executed using a turbomolecular pump.

Steady-state, time-resolved and quantum yields measurements were carried out at room temperature on *L*-tryptophan, M-*L*-Trp and M-G-*L*-Trp$_5$, M-G-*L*-Trp$_{10}$, M-G-*L*-Trp$_{20}$ and M-G-*L*-Trp$_{40}$ at pH 11, 7-8 and 1.5-2, considering the solubility limits. The pH was adjusted using 0.1 M HCl or 0.1 M NaOH aqueous solutions and measured by a combined Metrohm microelectrode.

3.2.3 Synthesis of *L*-tryptophan based homo- and copolymers

M-*L*-Trp. Thermostated and deaerated ultrapure water (4 mL) was added to a mixture of L-tryptophan (3.54 g, 17.33 mmol) and MBA (2.79 g, 18.01 mmol) at 50 °C under magnetic stirring. After 5 min, a thermostated and deaerated LiOH monohydrate aqueous solution (0.36 g; 8.60 mmol; 2 mL) was added to the mixture. After 2 h, a second portion of LiOH solution (0.36 g; 8.60 mmol; 2 mL) was introduced. The reaction mixture was kept at 50 °C for 6 days under nitrogen atmosphere. After this time, the solution was acidified to pH 3.5 with 6 M HCl, inducing separation of crude M-*L*-Trp in form of a brown oily liquid. The product was extracted five times with ethanol (20 mL) until the formation of a brown powder. The polymer was further dried under vacuum until constant weight (yield: 92%). Subsequently, 2 g were solubilized in H_2O at pH 9 and ultrafiltered through membranes with 100000 and then 5000 as nominal molecular weight cut-off. The solution passed through the former and retained by the latter was freeze-dried recovering the product as a yellowish powder.

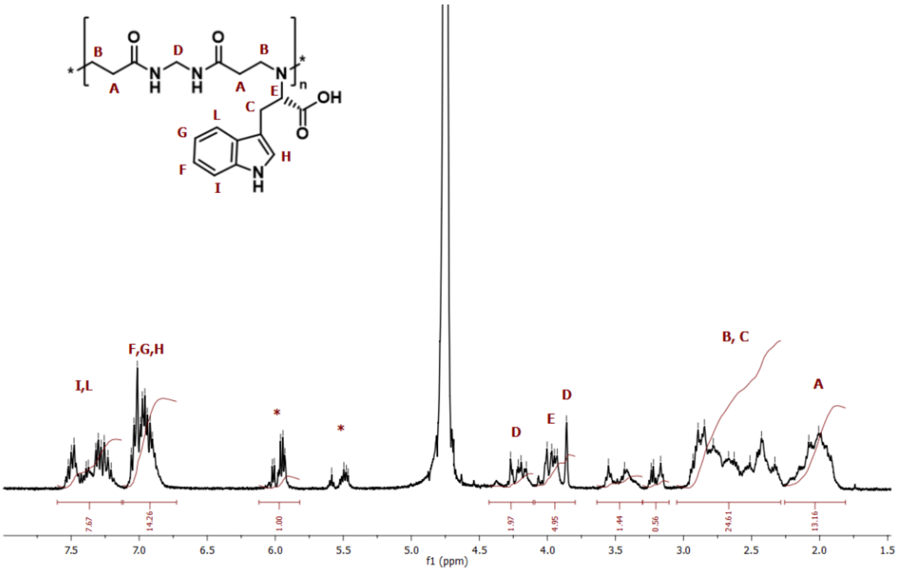

Figure 1. ^1H NMR spectra of M-*L*-Trp in D_2O at pH 10. Asterisks represent the signals of methylene and double bond protons of the terminal acrylamide.

^1H NMR (D_2O, 400.132 MHz, ppm): δ 2.01–2.08 (m, 4H, $CO\mathbf{CH_2}CH_2N$) 2.33–2.93 (m, 6H, $COCH_2\mathbf{CH_2}N$ and $\mathbf{CH_2}CHCOO^-$), 3.86 and 4.16–4.27 (m, 2H, $NH\mathbf{CH_2}NH$), 3.93–4.00 (m, 1H, $CH_2\mathbf{CH}COO^-$), 5.68–5.71 and 6.13–6.15 ppm (m, 3H, $\mathbf{H_2}C{=}C\mathbf{H}$ of terminal acrylamide), 6.90–7.06 (m, 3H, $\mathbf{H_F}$, $\mathbf{H_G}$, $\mathbf{H_H}$ of L-tryptophan), 7.21–7.52 (m, 2H, $\mathbf{H_I}$, $\mathbf{H_L}$ of L-tryptophan) (Figure 1). ^{13}C NMR (D_2O, 100.623, ppm): δ 16.99, 26.10, 28.69, 33.42, 42.97, 43.73, 46.40, 57.40, 63.85, 64.86, 65.83, 110.79, 111.76, 118.51, 118.72, 119.03, 121.68, 123.65, 124.04, 127.05, 128.05, 136.14, 174.13, 179.54, 181.62.

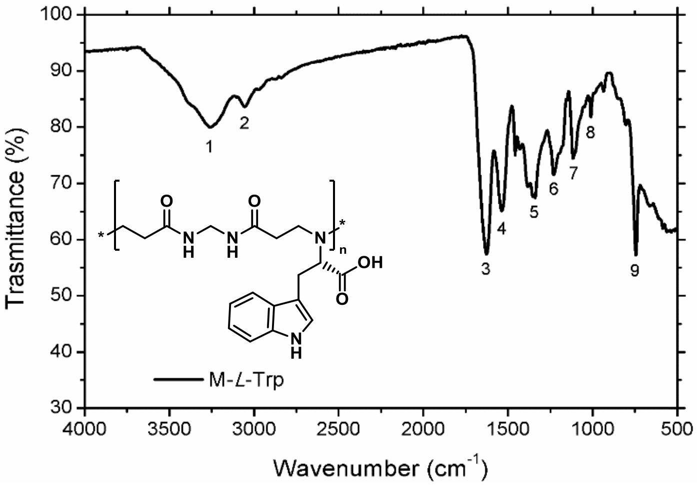

Figure 2. FTIR-ATR spectra of M-*L*-Trp powder.

Peak assignment for M-*L*-Trp are (Figure 2): 3252-3257 cm^{-1} (signal 1, N-H stretching); 3057-3059 cm^{-1} (signal 2, C-H stretching); 1629-1635 cm^{-1} (signal 3, C=O stretching); 1533-1542 cm^{-1} (signal 4, N-H bending); 1338-1342 cm^{-1} (signal 5, O-H bending); 1225-1228 cm^{-1} (signal 6, C-N stretching); 1190-1193 cm^{-1} (signal 7, C-O stretching); 1041-1047 cm^{-1} (signal 8, C-C stretching); 744 cm^{-1} (signal 9, C-H vibrations out of the plane of aromatic rings in L-tryptophan).

M-*D*-Trp and **M-*D,L*-Trp** were prepared as M-*L*-Trp by substituting D-Trp and D,L-Trp for L-Trp. Yields 94% and 98%.

M-G-*L*-Trp$_5$. Thermostated and deaerated ultrapure water (5 mL) was added to a mixture of L-tryptophan (0.53 g, 2.60 mmol), glycine (3.59 g, 47.80 mmol) and MBA (8.09 g, 52.50 mmol) at 50 °C under magnetic stirring. After 5 min, thermostated and deaerated LiOH monohydrate solution (1.07 g, 25.50 mmol, 5 mL) was added to the mixture. After 2 h, a second portion of LiOH (0.36 g, 8.60 mmol, 2 mL) was introduced. The reaction mixture was maintained at 50 °C for 6 days under nitrogen atmosphere. After this time, the solution was acidified to pH 3.5 with 6 M HCl and ultrafiltered as in the case of M-*L*-Trp. Yield: 90 %. M_w=13000; $M_\mathrm{w}/M_\mathrm{n}$=1.44.

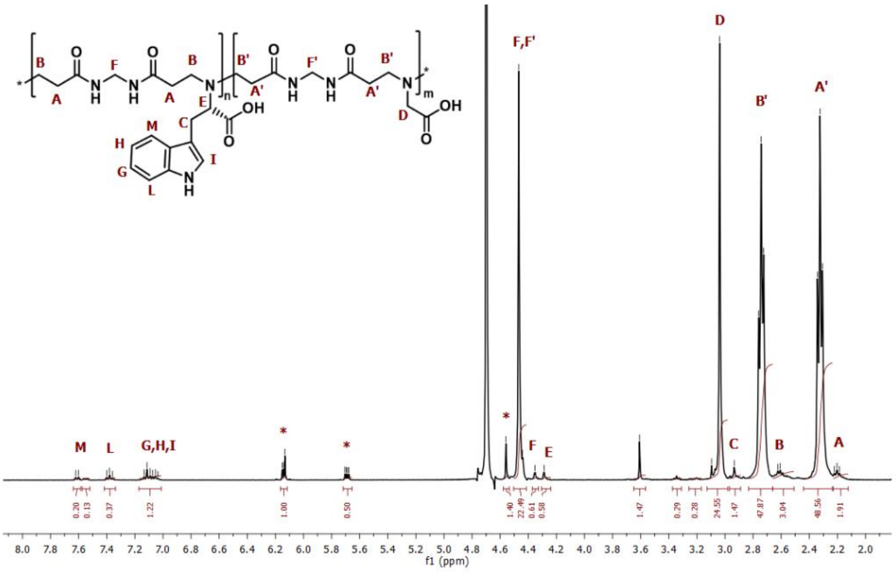

Figure 3. ^1H NMR spectrum of M-G-*L*-Trp$_5$ recorded in D_2O, at pH 10 and 25°C. Asterisks represent the signals of methylene and double bond protons of the terminal acrylamide.

^1H NMR (D_2O, 400.132 MHz, ppm): δ 2.19–2.22 (m, 4H, CO**CH$_2$**CH$_2$N of L-tryptophan bearing units), 2.32 (t, 4H, CO**CH$_2$**CH$_2$N of glycine bearing units), 2.61-2.62 (m, 4H, COCH$_2$**CH$_2$**N of L-tryptophan bearing units), 2.73–2.76 (m, 4H, COCH$_2$**CH$_2$**N of glycine bearing units), 2.93 (s, 2H, **CH$_2$**CHCOO− of L-tryptophan), 3.04 (s, 2H, **CH**COO− of glycine), 4.29 (s, 1H, **CH**COO− of L-tryptophan), 4.35 (s, 1H, NH**CH$_2$**NH of L-tryptophan bearing units), 4.44–4.47 (m, 3H, NH**CH$_2$**NH of both L-tryptophan and glycine bearing units), 4.56 (s, 2H, NH**CH$_2$**NH of terminal acrylamide), 5.68–5.71 and 6.13–6.15

ppm (m, 3H, **H_2C=CH** of terminal acrylamide), 7.04–7.13 (m, 3H, **H_G**, **H_H**, **H_I** of L-tryptophan), 7.36–7.40 (m, 1H, **H_L** of L-tryptophan), 7.60–7.62 (m, 1H, **H_M** of L-tryptophan) (Figure 3). ^{13}C NMR (D_2O, 100.623, ppm): δ 32.87, 44.34, 49.33, 57.33, 175.32, 178.83. Content of L-tryptophan-bearing units by ^{1}H NMR = 4.53%.

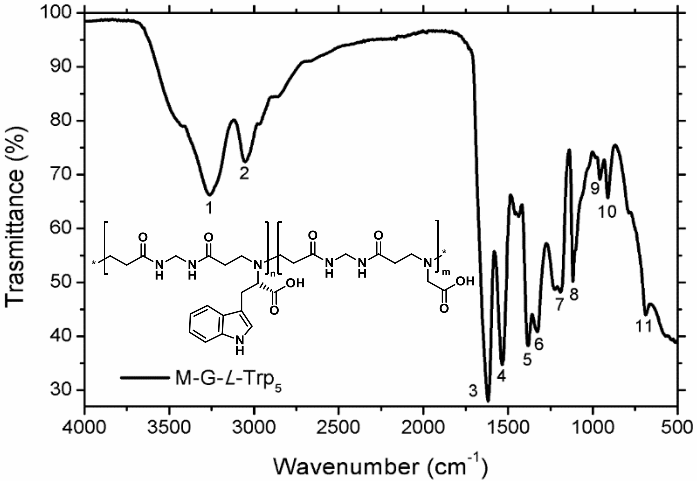

Figure 4. FTIR-ATR spectra of M-G-*L*-Trp$_5$ powder.

Peak assignment for M-G-*L*-Trp$_5$ are (Figure 4): 3247-3260 cm^{-1} (signal 1, N-H stretching); 3045-3057 cm^{-1} (signal 2, C-H stretching); 1617-1625 cm^{-1} (signal 3, C=O stretching); 1533-1537 cm^{-1} (signal 4, N-H bending); 1382-1387 cm^{-1} (signal 5, O-H bending); 1328-1343 cm^{-1} (signal 6, C-H bending); 1224-1229 (signal 7, C-N stretching); 1185-1190 cm^{-1} (signal 8, C-O stretching); 1114-1118 cm^{-1} (signal 9, C-C stretching); 955-958 and 908-914 cm^{-1} (signal 10,11 C-H vibrations out of the plane in Gly).

M-G-*L*-Trp$_{10}$ was prepared as *M-G-L-Trp$_5$* using a different L-tryptophan/glycine ratio (1.04 g, 5.10 mmol for L-tryptophan and 3.41 g, 45.40 mmol for glycine). Yield 72%. M_w=11400; M_w/M_n=1.30.

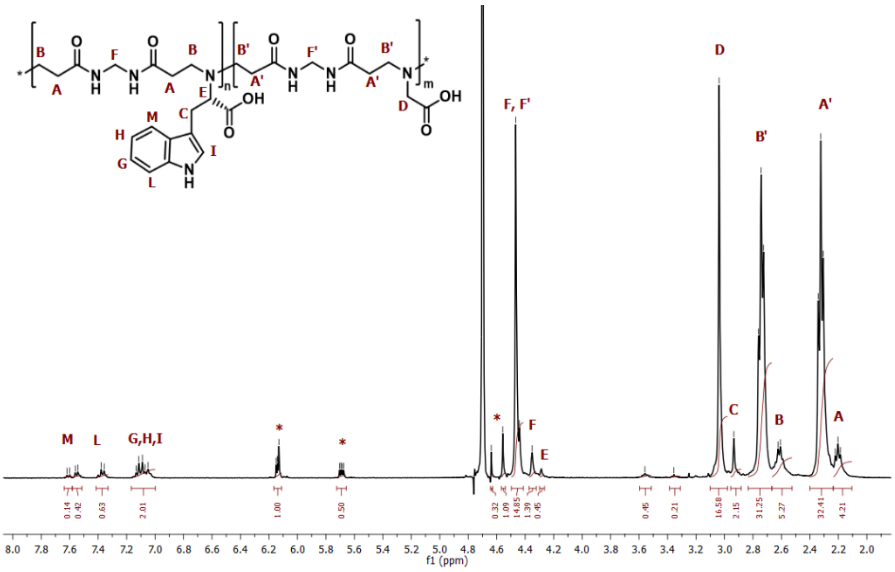

Figure 5. ^{1}H NMR spectrum of M-G-*L*-Trp$_{10}$ recorded in D_2O, at pH 10 and 25°C. Asterisks represent the signals of methylene and double bond protons of the terminal acrylamide.

^{1}H NMR (D_2O, 400.132 MHz, ppm): δ 2.19–2.22 (m, 4H, CO**CH$_2$**CH$_2$N of L-tryptophan bearing units), 2.31–2.34 (m, 4H, CO**CH$_2$**CH$_2$N of glycine bearing units), 2.61–2.62 (m, 4H, COCH$_2$**CH$_2$**N of L-tryptophan bearing units), 2.73-2.76 (m, 4H, COCH$_2$**CH$_2$**N of glycine bearing units), 2.93 (s, 3H, **CH$_2$**CHCOO−), 3.04 (s, 2H, **CH**COO− of glycine), 4.29 (s, 1H, **CH**COO− of L-tryptophan), 4.35 (s, 1H, NH**CH$_2$**NH of L-tryptophan bearing units), 4.44–4.47 (s, 2H, NH**CH$_2$**NH of both L-tryptophan and glycine bearing units), 4.56 (s, 2H, NH**CH$_2$**NH of terminal acrylamide), 5.68–5.70 and 6.13–6.15 ppm (m, 3H, **H$_2$**C=CH of terminal acrylamide), 7.05–7.13 (m, 3H, **H$_G$**, **H$_H$**, **H$_I$** of L-tryptophan), 7.36-7.38 (m, 1H, **H$_L$** of L-tryptophan), 7.54–7.62 (m, 1H, **H$_M$** of L-tryptophan) (Figure 5). ^{13}C NMR (D_2O, 100.623, ppm): δ 32.85, 44.32, 49.30, 51.94, 57.32, 118.52, 121.68, 123.67, 127.03, 136.14, 168.44, 175.21, 178.81. Content of L-tryptophan bearing units from ^{1}H NMR = 9.70%.

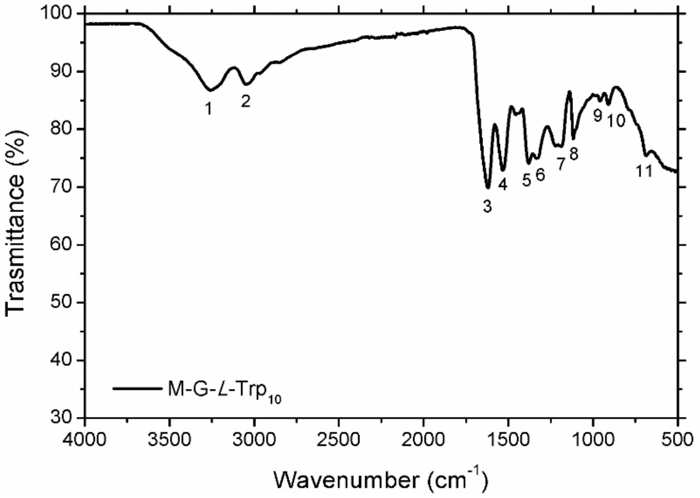

Figure 6. FTIR-ATR spectra of M-G-*L*-Trp$_{10}$ powder.

Peak assignment for M-G-*L*-Trp$_{10}$ are (Figure 6): 3247-3260 cm^{-1} (signal 1, N-H stretching); 3045-3057 cm^{-1} (signal 2, C-H stretching); 1617-1625 cm^{-1} (signal 3, C=O stretching); 1533-1537 cm^{-1} (signal 4, N-H bending); 1382-1387 cm^{-1} (signal 5, O-H bending); 1328-1343 cm^{-1} (signal 6, C-H bending); 1224-1229 (signal 7, C-N stretching); 1185-1190 cm^{-1} (signal 8, C-O stretching); 1114-1118 cm^{-1} (signal 9, C-C stretching); 955-958 and 908-914 cm^{-1} (signal 10,11 C-H vibrations out of the plane in Gly).

M-G-*L*-Trp$_{20}$ was prepared as *M-G-L-Trp$_5$* using a different L-tryptophan/glycine ratio (2.08 g, 10.20 mmol for L-tryptophan and 3.03 g, 40.40 mmol for glycine). Yield 72%. M_w=11200; $M_\mathrm{w}/M_\mathrm{n}$=1.30.

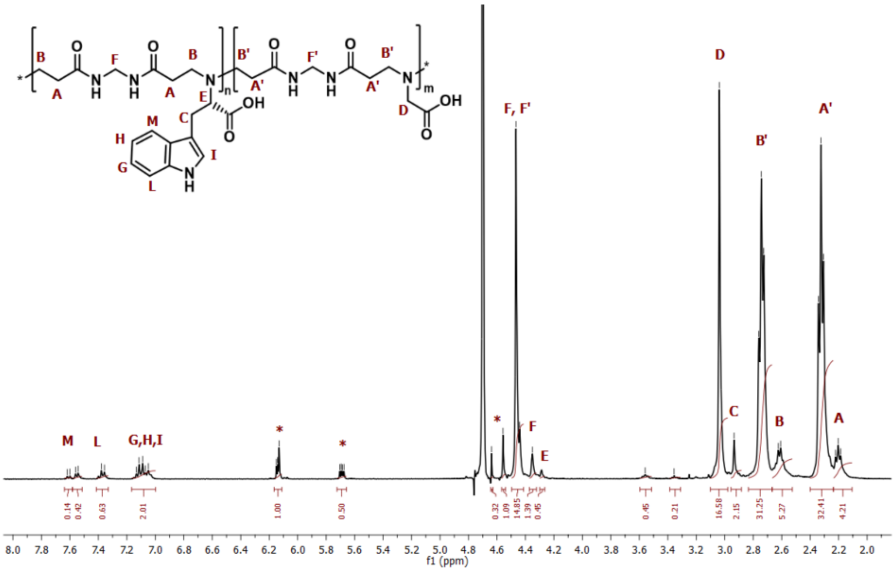

Figure 7. ^{1}H NMR spectrum of M-G-*L*-Trp$_{20}$ recorded in D_2O, at pH 10 and 25°C. Asterisks represent the signals of methylene and double bond protons of the terminal acrylamide.

^{1}H NMR (D_2O, 400.132 MHz, ppm): δ 2.19–2.22 (m, 4H, CO$\mathbf{CH_2}$$CH_2$N of L-tryptophan bearing units), 2.30–2.34 (m, 4H, CO$\mathbf{CH_2}$$CH_2$N of glycine bearing units), 2.59–2.62 (m, 4H, COCH$_2$$\mathbf{CH_2}$N of L-tryptophan bearing units), 2.72–2.74 (m, 4H, COCH$_2$$\mathbf{CH_2}$N of glycine bearing units), 2.93 (s, 3H, $\mathbf{CH_2}$CHCOO–), 3.04 (s, 2H, **CH**COO– of glycine), 4.29 (s, 1H, **CH**COO– of L-tryptophan), 4.35 (s, 1H, NH$\mathbf{CH_2}$NH of L-tryptophan bearing units), 4.44–4.47 (s, 2H, NH$\mathbf{CH_2}$NH of both L-tryptophan and glycine bearing units), 4.56 (s, 2H, NH$\mathbf{CH_2}$NH of terminal acrylamide), 5.67–5.70 and 6.12–6.15 ppm (m, 3H, $\mathbf{H_2C{=}CH}$ of terminal acrylamide), 7.05–7.13 (m, 3H, $\mathbf{H_G}$, $\mathbf{H_H}$, $\mathbf{H_I}$ of L-tryptophan), 7.36-7.38 (m, 1H, $\mathbf{H_L}$ of L-tryptophan), 7.54–7.60 (m, 1H, $\mathbf{H_M}$ of L-tryptophan) (Figure 7). ^{13}C NMR (D_2O, 100.623, ppm): δ 32.85, 44.32, 49.30, 51.94, 57.32, 118.52, 121.68, 123.67, 127.03, 136.14, 168.44, 175.21, 178.81. Content of L-tryptophan bearing units from ^{1}H NMR from 1H NMR = 17.40%.

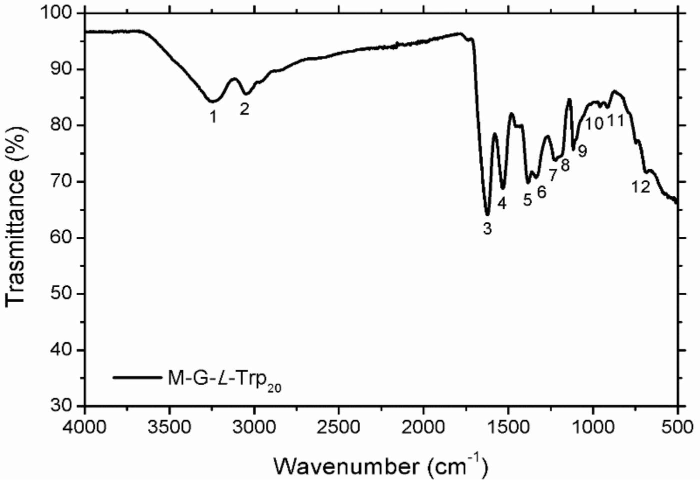

Figure 8. FTIR-ATR spectra of M-G-*L*-Trp$_{20}$ powder.

Peak assignment for M-G-*L*-Trp$_{10}$ are (Figure 8): 3247-3260 cm^{-1} (signal 1, N-H stretching); 3045-3057 cm^{-1} (signal 2, C-H stretching); 1617-1625 cm^{-1} (signal 3, C=O stretching); 1533-1537 cm^{-1} (signal 4, N-H bending); 1382-1387 cm^{-1} (signal 5, O-H bending); 1328-1343 cm^{-1} (signal 6, C-H bending); 1224-1229 (signal 7, C-N stretching); 1185-1190 cm^{-1} (signal 8, C-O stretching); 1114-1118 cm^{-1} (signal 9, C-C stretching); 955-958 and 908-914 cm^{-1} (signal 10,11 C-H vibrations out of the plane in Gly); 742-744 cm^{-1} (signal 12, C-H vibrations out of the plane of aromatic rings in L-tryptohan).

M-G-*L*-Trp$_{40}$ was prepared as M-*L*-Trp by substituting an L-tryptophan/glycine mixture (L-tryptophan 34.17 g, 20.42 mmol; glycine 2.27 g, 30.24 mmol) for L-tryptophan. The product was extracted five times with EtOH (20 mL) until the formation of a brown powder, then dried under vacuum until constant weight (yield: 41%). M_w=20300; $M_\mathrm{w}/M_\mathrm{n}$=2.45.

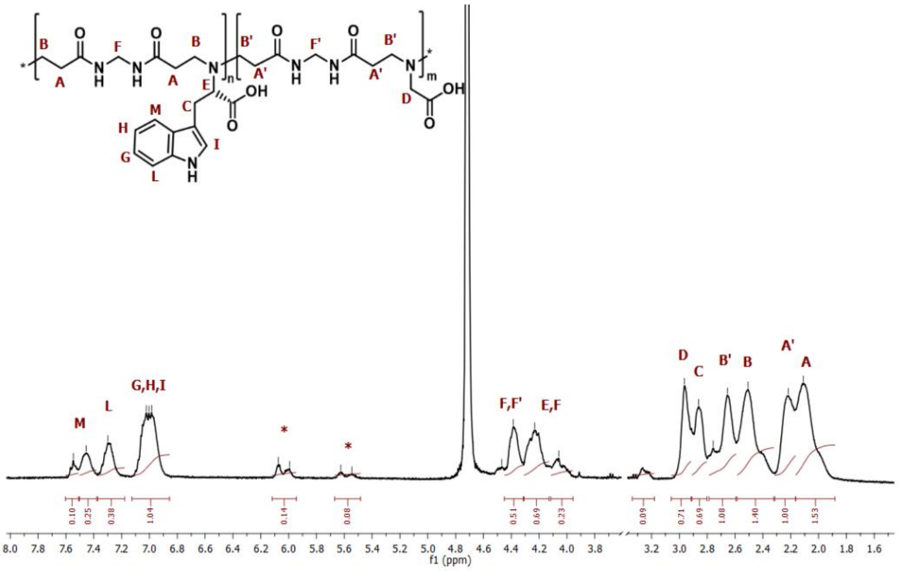

Figure 9. ^{1}H NMR spectrum of M-G-*L*-Trp$_{40}$ recorded in D$_2$O, at pH 10 and 25°C. Asterisks represent the signals of methylene and double bond protons of the terminal acrylamide.

^{1}H NMR (D$_2$O, 400.132 MHz, ppm): δ 2.11 (s, 4H, CO**CH$_2$**CH$_2$N of L-tryptophan bearing units), 2.22 (s, 4H, CO**CH$_2$**CH$_2$N of glycine bearing units), 2.51 (m, 4H, COCH$_2$**CH$_2$**N of L-tryptophan bearing units), 2.65 (m, 4H, COCH$_2$**CH$_2$**N of glycine bearing units), 2.86 (s, 2H, **CH$_2$**CHCOO–), 2.96 (s, 2H, **CH**COO– of glycine), 4.06–4.23 (m, 3H, **CH**COO- and NH**CH$_2$**NH of L-tryptophan bearing units), 4.39–4.47 (m, 3H, NH**CH$_2$**NH of both L-tryptophan and glycine bearing units), 5.55–5.63 and 5.99–6.07 ppm (m, 3H, **H$_2$**C=**CH** of terminal acrylamide), 6.98–7.02 (m, 3H, **H$_G$**, **H$_H$**, **H$_I$** of L-tryptophan), 7.30 (m, 1H, **H$_L$** of L-tryptophan), 7.45–7.55 (m, 1H, **H$_M$** of L-tryptophan) (Figure 9). ^{13}C NMR (D$_2$O, 100.623, ppm): δ 32.67, 33.76, 35.08, 44.04, 46.52, 49.19, 57.36, 63.91, 65.78, 111.64, 118.59, 119.02, 121.68, 122.40, 123.99, 127.04, 136.13, 175.21, 178.74, 179.44, 181.65. Content of L-tryptophan bearing units from ^{1}H NMR = 40.5%.

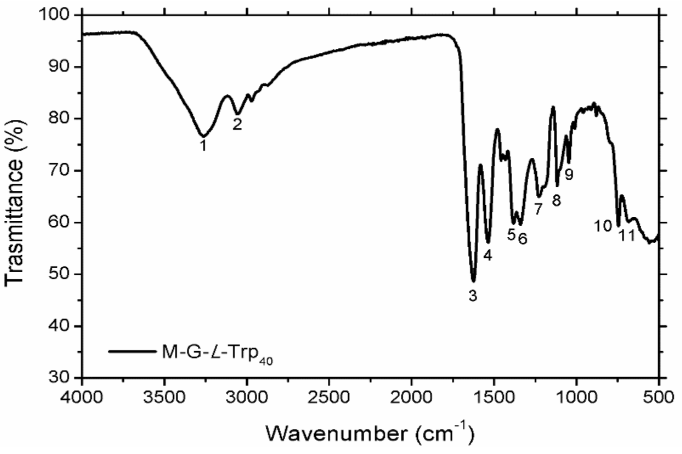

Figure 10. FTIR-ATR spectra of M-G-*L*-Trp$_{20}$ powder.

Peak assignment for M-G-*L*-Trp$_{10}$ are (Figure 10): 3247-3260 cm^{-1} (signal 1, N-H stretching); 3045-3057 cm^{-1} (signal 2, C-H stretching); 1617-1625 cm^{-1} (signal 3, C=O stretching); 1533-1537 cm^{-1} (signal 4, N-H bending); 1382-1387 cm^{-1} (signal 5, O-H bending); 1328-1343 cm^{-1} (signal 6, C-H bending); 1224-1229 (signal 7, C-N stretching); 1185-1190 cm^{-1} (signal 8, C-O stretching); 1114-1118 cm^{-1} (signal 9, C-C stretching); 955-958 and 908-914 cm^{-1} (signal 10,11 C-H vibrations out of the plane in Gly).

3.3 RESULTS AND DISCUSSION

3.3.1 Synthesis of M-*L*-Trp and M-G-*L*-Copolymers

D-, L- and D,L-tryptophan polyamidoamino acids were synthesized by polyaddition of L-, D-, and D,L-tryptophan to *N,N'*-methylenebisacrylamide (MBA) according to Scheme 1. The reaction was carried out in aqueous solution, at 50 °C and pH > 9 for 6 days, following the same procedure reported for all PAACs (Chapter 2, Experimental Section p. 45). Glycine copolymers were obtained in the same way but starting from different glycine/tryptophan mixtures. In the recipe of these copolymers, tryptophan was partly added in place of glycine according to the composition reported in Table 1.

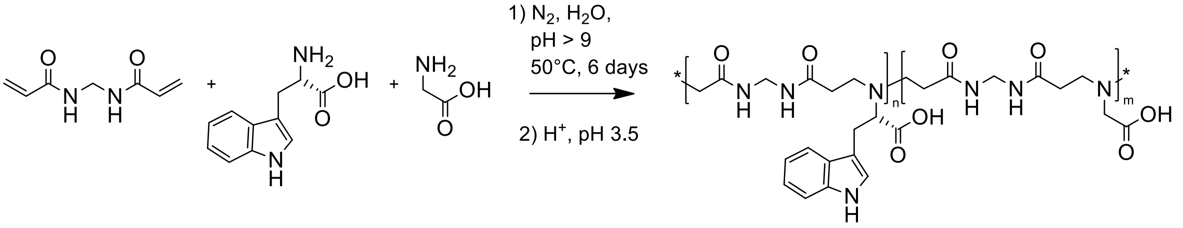

m = 0, M-*L*-Trp
m = 0.95 n= 0.05, M-G-*L*-Trp$_5$
m = 0.90 n= 0.10, M-G-*L*-Trp$_{10}$
m = 0.80 n= 0.20, M-G-*L*-Trp$_{20}$
m = 0.60 n= 0.40, M-G-*L*-Trp$_{40}$

Scheme 1. Synthesis of L-tryptophan based homo- and copolymers.

This synthesis was similar to that previously described for MBA-arginine (ARGO7) [18], MBA-*L*-alanine (M-L-Ala), MBA-L-valine (M-L-Val) and MBA-L-leucine (M-L-Leu) [19], albeit with some differences. Generally, in the polyadditions of acid- or neutral α-amino acids with bisacrylamides, including alanine, valine, leucine and arginine mentioned above, the base is added at the beginning of the reaction, to de-protonate the amine groups. Its amount is equivalent to the carboxyl group of the starting monomer. However, in the case of tryptophan, additional expedients need to be adopted, due to the tryptophan's high sensitivity to O_2-mediated oxidation in basic environment [20,21]. As such, the reaction mixture was flushed with ultrapure nitrogen and the base, $LiOH_2$ aqueous solution, was slowly added to the mixture. This resulted in the presence of limited amounts of tryptophan salt in an excess of free tryptophan. Only the molar equivalent of salified tryptophan, formed at each base addition, reacted. Noticeably, no more solution blackening due to oxidation was observed after the tryptophan amine groups reacted with the MBA double bonds. Probably, when the base was added in portion to the tryptophan/MBA reacting mixture, the resultant *tert*-amine groups, due to the carbonyl groups in β-position, were not basic enough to de-protonate the indole ring. Hence, the amino acid *prim*-amine groups were stepwise activated by deprotonation at a rate roughly matching the rate of the addition reaction.

L-Tryptophan/glycine copolymers were prepared in the same way, starting from a mixture of *L*-tryptophan and glycine, with the tryptophan molar content ranging from 5% to 40%. The amount of tryptophan is indicated by the subscripts of the copolymer's acronyms, namely M-G-*L*-Trp_5, M-G-*L*-Trp_{10}, M-G-*L*-Trp_{20} and M-G-*L*-Trp_{40}. The structure of homo- and copolymers was confirmed by ^1H and ^{13}C NMR, and FTIR-ATR analyses (see Experimental Section). In the ^1H NMR spectra, the presence of the peaks of terminal acrylamide groups were visible. Moreover, peaks assigned to the tryptophan M hydrogen were split, probably due to conformational effects. The molar ratios in the reaction recipes were comparable to those calculated from ^1H NMR in the resultant copolymers (Table 1).

Table 1. Comparison of copolymers tryptophan content from reaction recipes and ^1H NMR.

Sample	**Tryptophan content in the feed**[a]	**Tryptophan content from ^1H NMR**[a]
M-G-*L*-Trp_5	5	4.53
M-G-*L*-Trp_{10}	10	9.70
M-G-*L*-Trp_{20}	20	17.4
M-G-*L*-Trp_{40}	40	40.5

[a] Expressed as mole %.

Normally, in PAAs and PAACs SEC analyses, the mobile phase is a TRIS buffer solution at pH 8, with 0.2 M sodium chloride. However, the poor solubility of M-*D*-Trp, M-*L*-Trp and M-*D,L*-Trp in this solvent, discouraged the use of this technique for determining their molecular weights. Then, the number-average molecular weights (M_n) were estimated in the range 3500–5000 by end-group counting in their ^1H NMR spectra, choosing as end-groups the easily determined terminal double bonds. Two cases were considered: 1) polymeric chains bear acrylamide double bonds at both ends; 2) polymers bear statistically only one terminal acrylamide double bond per macromolecule. Whenever possible, as in the case of copolymers, the results were compared with those of SEC. In both cases, the trend was decreasing M_n by increasing tryptophan content (Table 2). To note, the M_n values obtained by SEC were in better agreement with those calculated from ^{1}H NMR if two terminals acrylamide units per macromolecule were assumed.

Table 2. NMR and SEC M_n evaluation of homo- and copolymers: comparison between calculated and experimental M_n values.

Sample	M_n from ^{1}H NMR[a]	M_n from ^{1}H NMR[b]	M_n from SEC
M-G-*L*-Trp_5	12000	6000	9000
M-G-*L*-Trp_{10}	8800	4400	8800
M-G-*L*-Trp_{20}	7600	3800	8600
M-G-*L*-Trp_{40}	5700	2850	8300
M-*L*-Trp	5400	2700	-- [c]

[a] calculated assuming terminal acrylamide units at both chain ends, [b] calculated assuming terminal acrylamide units at one chain end. [c] Analyses were not carried out due to solubility limits.

Weight- (M_w) and number-average (M_n) molecular weights of the tryptophan-based copolymers were determined by SEC employing a right and small angle light scattering detectors with a 670 nm laser (Figure 11). Since tryptophan excitation maximum is 280 nm [22], any interference from tryptophan fluorescence was excluded.

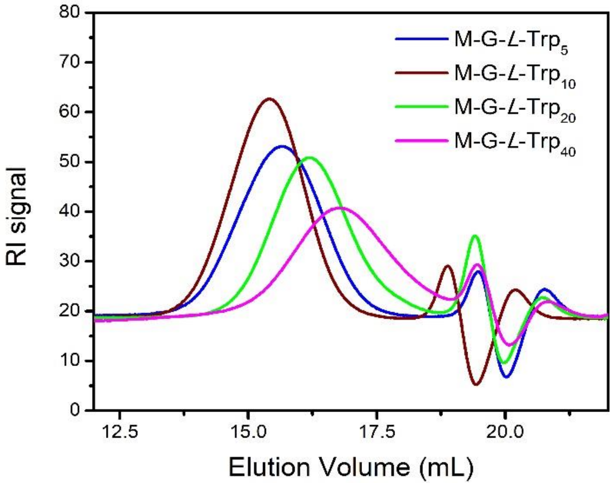

Figure 11. Size exclusion chromatography (refractive index signal) of *L*-tryptophan based copolymers in 0.1 M TRIS buffer (pH 8.00 ± 0.05) solution with 0.2 M sodium chloride.

3.3.2 Acid-Base Properties

Acid-base properties of tryptophan-derived PAACs were determined by potentiometric titration using the Henderson-Hasselbalch equation and procedure described in Experimental Section. The titration curves (Figure 12) presented only two inflection points and two buffer regions. Hence, in all these copolymers, units bearing glycine and *L*-tryptophan presented similar acid-base properties. This result may be confirmed observing that the parent amino acids have almost the same pK_a values, respectively 2.34 (carboxyl group) and 9.6 (amine group) for glycine and 2.83 and 9.30 for tryptophan.

Table 3. pK_a and β values of M-G-*L*-Trp copolymers in the α range 0.2–0.8 (β_1) and 0.1–0.9 (β_2).

Sample	pK_{a1}[a,b]	pK_{a2}[b,c]	β_1[a,b]	β_2[b,c]	**IP**[d]
M-G-*L*-Trp$_5$	2.05 ± 0.15	7.78 ± 0.12	0.61 ± 0.08	1.39 ± 0.03	4.9
M-G-*L*-Trp$_{10}$	2.06 ± 0.18	7.75 ± 0.18	0.61 ± 0.06	1.36 ± 0.06	4.9
M-G-*L*-Trp$_{20}$	2.04 ± 0.19	7.74 ± 0.13	0.57 ± 0.05	1.60 ± 0.11	4.9
M-G-*L*-Trp$_{40}$	-	7.77 ± 0.02[e]	-	1.51 ± 0.07[e]	-

[a] Carboxyl group. [b] Average values obtained from four forward titration experiments. [c] Amine group. [d] Isoelectric point. [e] Calculated from the simulated titration curves by the De Levie approach.

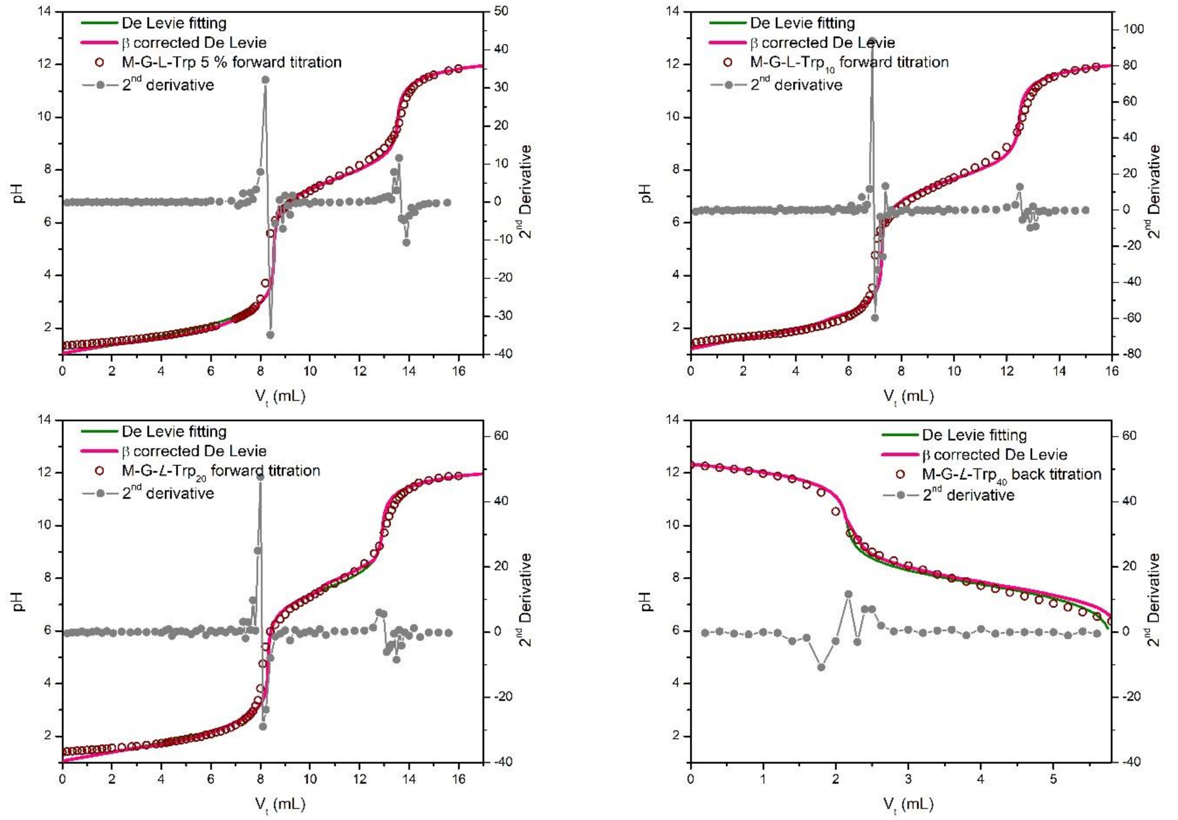

Figure 12. Titrations of M-G-*L*-Trp$_5$, M-G-*L*-Trp$_{10}$, M-G-*L*-Trp$_{20}$ and M-G-*L*-Trp$_{40}$: experimental, simulated and β corrected curves. Due to solubility limits, for M-G-*L*-Trp$_{40}$ only the backward titration is reported.

The Katchalsky and Spitnik parameter β were calculated considering α in the range, respectively, 0.2–0.8 for β_1 and 0.1–0.9 for β_2, to exclude values that clearly deviates from the trend. The average values are in line with the ones calculated for the other polymers of the PAAC family (Table 3).

Glycine and L-tryptophan repeat units in the M-G-L-Trp copolymers can exist in three ionization states (Figure 13). The pH-dependent speciation curves (Figure 13) were determined from the pK_a and β values reported in Table 3, following methods described in Experimental Section.

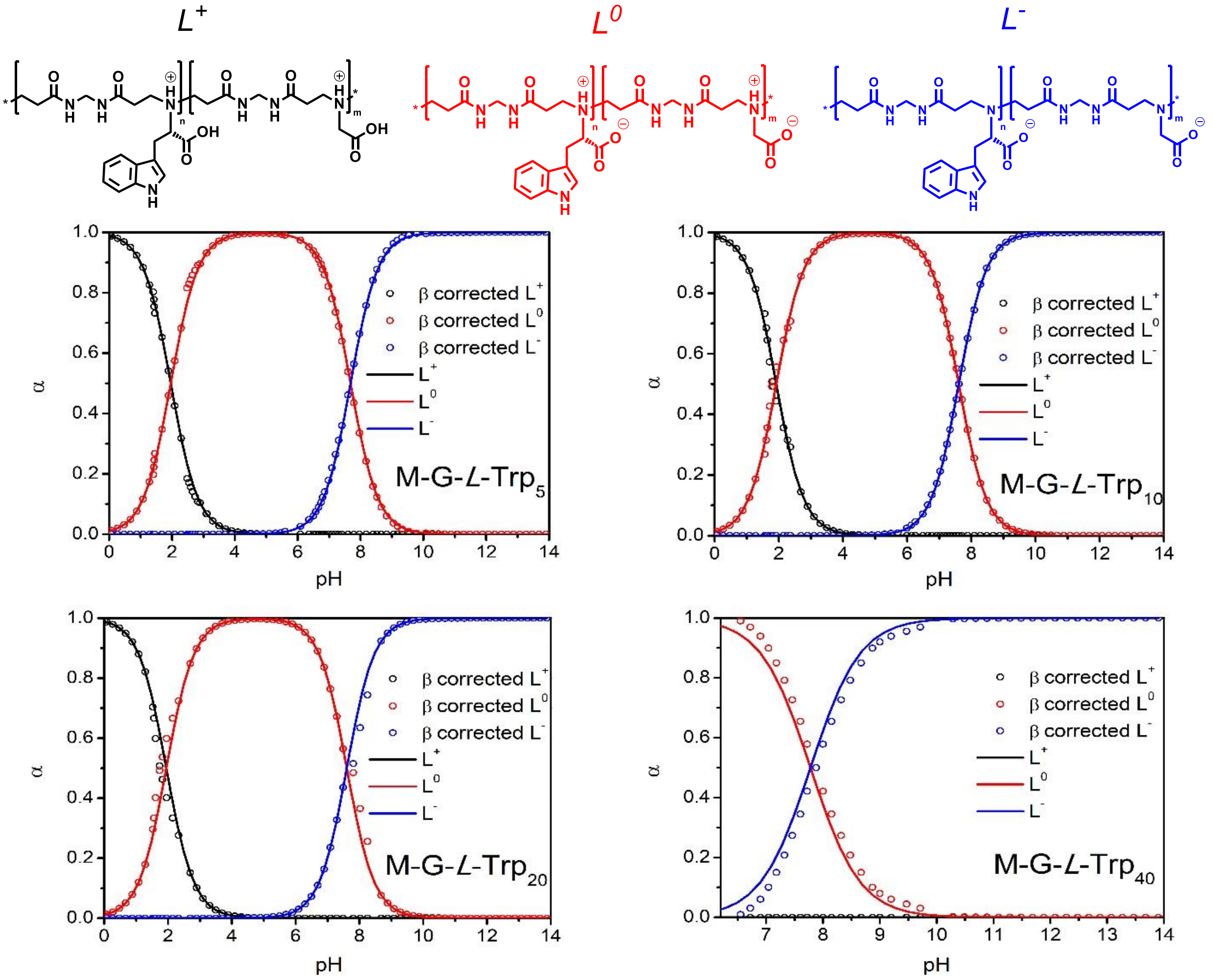

Figure 13. Distribution of charged species referred to the 1st titration of M-G-L-Trp$_5$, M-G-L-Trp$_{10}$, M-G-L-Trp$_{20}$ and M-G-L-Trp$_{40}$: ionization states (above); simulated and β corrected speciation curves (below). The speciation curve of M-G-L-Trp$_{40}$ is calculated assuming $pKa_1 = 2.00$.

3.3.3 Solubility Properties

UV–Vis measurements (Figure 14A) and scattering of polarized IR beam (Figure 14B) tests were carried out on 1 mg·mL^{-1} polymer solutions at different pHs. Light transmittance measurements were recorded at 480 nm, outside PAACs' absorption wavelength range. Both analyses indicated composition and pH-dependent solubility of all homo- and copolymers. Copolymers with lowest tryptophan content, namely M-G-*L*-Trp$_5$, M-G-*L*-Trp$_{10}$ and M-G-*L*-Trp$_{20}$, resulted completely soluble in the whole 2–12 pH range. Differently, M-G-*L*-Trp$_{40}$ showed a solubility gap centered at pH 4.5, close to the polymer IP, whereas M-*L*-Trp proved soluble only at pH > 7. The polarized IR beam scattering tests were in line with the UV-vis measurements.

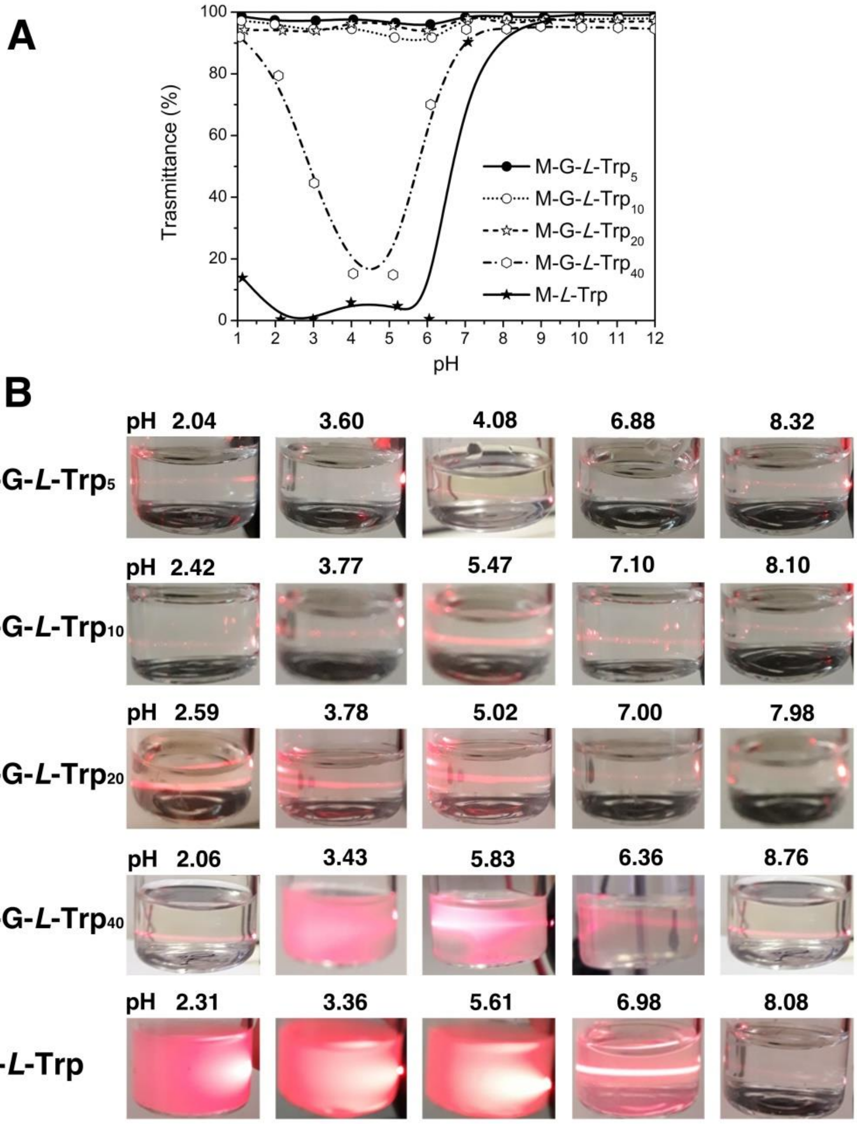

Figure 14. Solubility of M-G-*L*-Trp copolymers in water. **A**) pH-dependence of transmittance at 480 nm; **B**) scattering of a polarized IR beam. Measurements were performed on 1 mg mL^{-1} solutions at 25 °C.

3.3.4 Dynamic Light Scattering (DLS) Measurements

To evaluate the pH-dependence of R_h of tryptophan-based PAACs, DLS measurements were carried out in 0.1 M NaCl solution at 1 mg mL^{-1}. Data were collected within the pH range 2-11 for M-G-*L*-Trp$_5$, M-G-*L*-Trp$_{10}$ and M-G-*L*-Trp$_{20}$, and within the pH range 7–11 for M-G-*L*-Trp$_{40}$, M-*L*-Trp, M-*D*,*L*-Trp and M-*D*-Trp. In all cases, monomodal volumetric distributions were observed. Similarly to the other PAACs [19], R_h values did not significantly change across their solubility pH range (Figure 15).

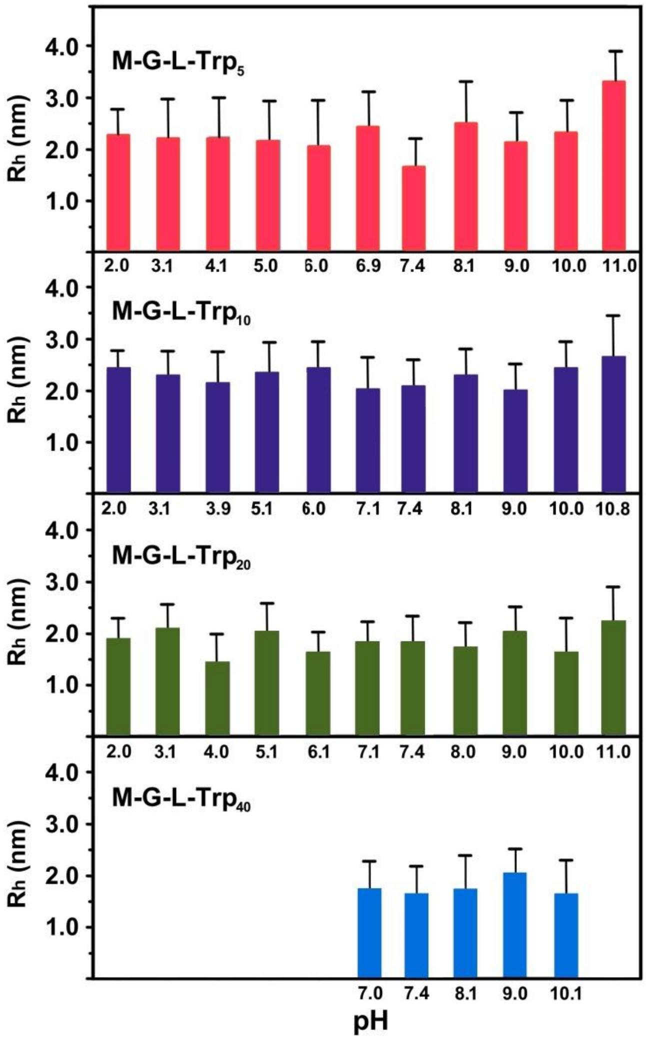

Figure 15. pH-dependence of the hydrodynamic radius of M-G-*L*-Trp copolymers. Data were obtained in 0.1 M NaCl at 1 mg·mL^{-1} and 25 °C.

The stability over time was assessed for all M-G-*L*-Trp copolymers by recording DLS, at pH 2 and 8, on the same solution kept at room temperature for one month (Figure 16). Measurements did not show any significant variation of R_h.

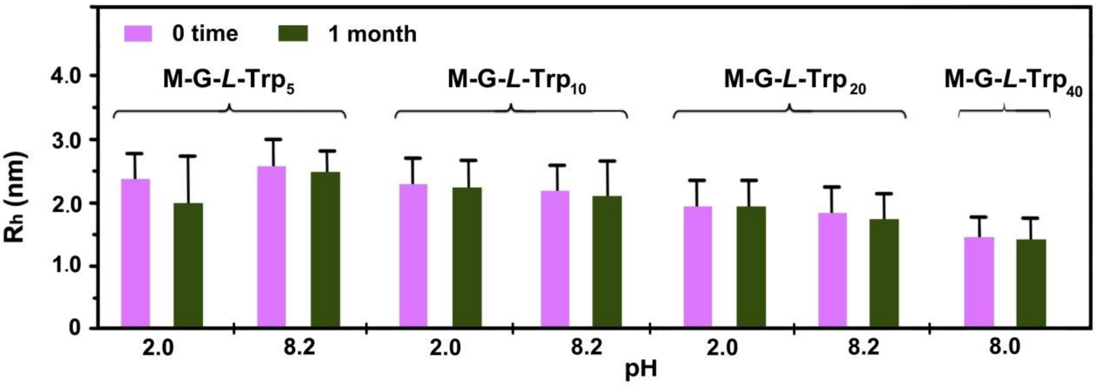

Figure 16. Hydrodynamic radius of M-G-L-Trp copolymers at 0 and 1 month. Data were recorded in 0.1 M NaCl at 1 mg·mL^{-1} and 25 °C.

The R_h dependence on concentration was assessed for both homo- and copolymers. For M-G-L-Trp copolymers, by decreasing concentration R_h increased (Figure 17). This trend suggested that a polyelectrolyte effect occurred, that is, when in dilute solutions charges resulted less shielded causing, as such, coil expansion. In contrast, homopolymers' R_h was little affected by changing concentration in the 1–30 mg mL^{-1} range. Variations may be overshadowed by a more rigid conformation probably induced by the superior bundling ability of the bulky, hydrophobic indole substituents.

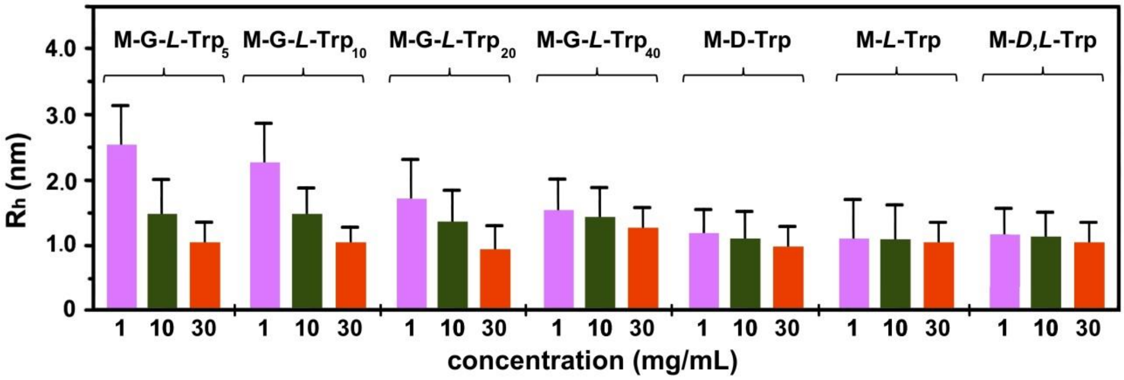

Figure 17. Hydrodynamic radius of M-G-L-Trp copolymers in the 1–30 mg mL^{-1} range. Data were recorded in 0.1 M NaCl at pH 8 and 25 °C.

3.3.5 Circular Dichroism Analysis

The CD spectra of M-L-Trp and M-G-L-Trp in 0.1 M NaCl at pH 2, 7–8 and 11 are shown in Figure 18, where curves were normalized based on the molar concentration of the tryptophan units. These spectra proved that all polymers self-structure into stable conformations, whose CD pattern were highly affected by pH and tryptophan content. The dependence over pH may be considered a general feature of PAACs' CD spectra, independent by the nature of the amino acid residue, as already shown by MBA-arginine (ARGO7) [18], bearing cationic residues, MBA-*L*-alanine (M-*L*-Ala), MBA-*L*-valine (M-*L*-Val) and MBA-*L*-leucine (M-*L*-Leu), bearing alkyl residues [19].

Among the CD spectra of homo- and copolymers, M-G-*L*-Trp$_5$ resulted the most intense and most affected by pH of all. At pH 2.0, the negative band centered at 222 nm was mainly associated to the weak n → π^* transition of the CONH groups [22]. Hence, the CONH absorption most probably masked the high-energy $\pi \rightarrow \pi^*$ transition of indole [23,24], named B_b, reported in literature as a positive band at 220 nm. The high intensity of M-G-*L*-Trp$_5$ CD spectrum was associated to a strong dipole moment, possibly caused by the specific conformations assumed by the large excess of glycine-bearing repeat units. When pH is increased from 2 to 7, the CD spectra reported a 2 nm shift, possibly ascribed to the modification of the macromolecule average ionization degree. As expected from M-G-*L*-Trp$_5$ speciation curves, at pH 7, 22% of the main chain *tert*-amine groups were deprotonated and the average net charge per repeat unit was −0.14. The same hold true in basic conditions. At pH 11.0, all *tert*-amine groups were deprotonated, and the net charge per repeat unit was −1. In the CD spectrum, this resulted in changes of both intensities and wavelength at which maxima were found. In particular, the negative peak centered at 226 nm decreased in intensity, whereas a the positive peak increased. Apparently, as for the other PAACs studied so far, the protonation degree of the *tert*-amine in the main chain was considered the major responsible of the CD spectra modification and, as such, was recognized fundamental for structuring.

The remaining polymers, M-G-*L*-Trp$_{10}$, M-G-*L*-Trp$_{20}$ and M-G-*L*-Trp$_{40}$ proved to be less pH-responsive. This difference might be associated to the increasing tryptophan content, whose dipole moment and B_b transition canceled out those of glycine repeating units, causing as such lower intensities. Apart from the trend observed with *L*-tryptophan content, M-G-*L*-Trp$_{10}$, M-G-*L*-Trp$_{20}$ and M-G-*L*-Trp$_{40}$ showed the same variation with pH of the wavelength at which the molar ellipticity maxima occurred. Finally, M-G-*L*-Trp$_{20}$ and M-G-*L*-Trp$_{40}$ spectra, at pH 8 and 11, corresponding, respectively, to 67% and 100% *tert*-amine deprotonation, were comparable to those of M-*L*-Trp. They both presented a positive peak with equal or higher intensity than the negative one and seemed rather unaffected by pH. Overall, an increase in *L*-tryptophan content, from M-G-*L*-Trp$_5$ to M-*L*-Trp, caused negative peaks, at the same pH, to shift of 10 nm toward higher wavelengths, with reduced intensities as well due to the balancing of the dipole moments. In contrast, the UV–Vis absorption spectra remained unmodified (Figure 19). The CD dependence over the amount of tryptophan suggested chromophores might establish intramolecular interactions between each other. On the other hand, the positive peaks showed only intensity differences. In fact, as the content of tryptophan became higher, the major contribution was associated with the consequently predominant indole B_b transition. The CD spectral pattern of M-*L*-Trp, with the highest tryptophan content, was similar to that of *L*-tryptophan, whose aromatic side chain generated only one strong positive transition at pH 7.0 [25].

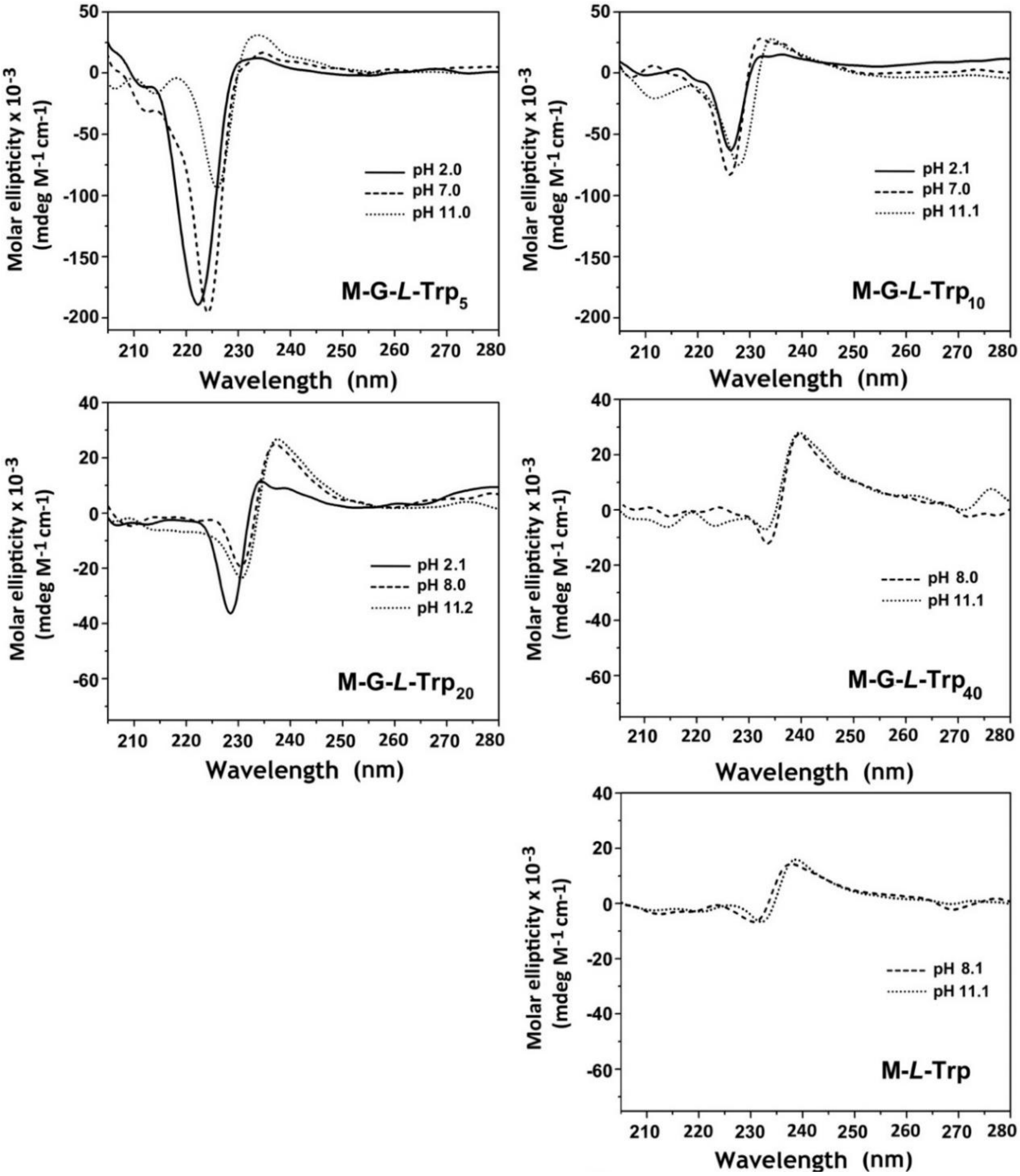

Figure 18. pH-Dependence of M-G-*L*-Trp CD spectra. Data were obtained in 0.1 M NaCl solution at 25 °C. The overall concentration of the repeating units was 1.81 ± 0.25 mM. The curves were normalized accounting for the molar concentration of tryptophan units.

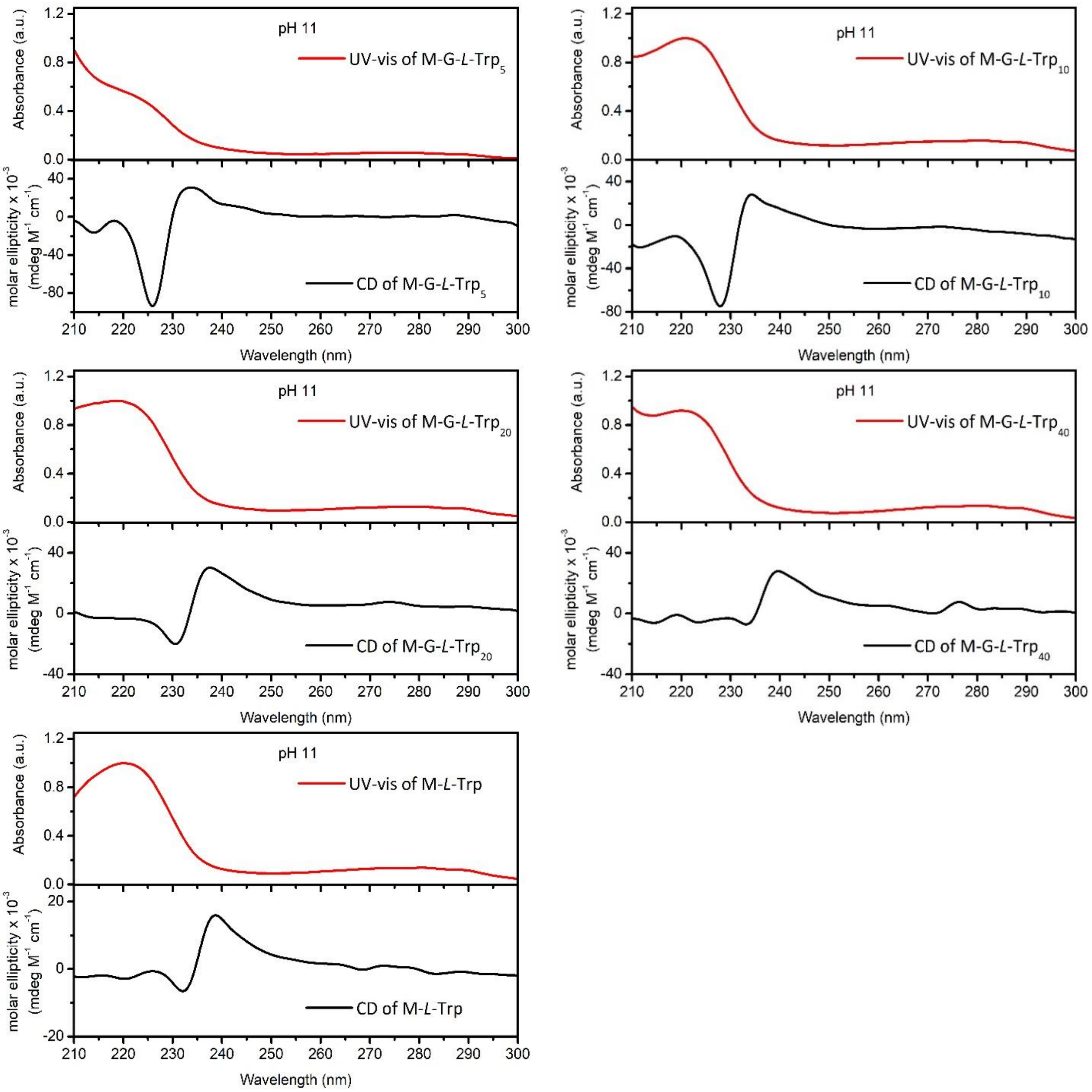

Figure 19. Circular dichroism and UV-vis absorption spectra of *L*-tryptophan derived homo- and copolymers, at pH 11.

3.3.6 Photoluminescence Analysis

Generally, the fluorescent properties of *L*-tryptophan are exploited to probe conformational dynamics and the microenvironment of proteins and peptides [26]. These properties originate from the two low-energy indole excited states, namely ^1L_a and ^1L_b [27–31]. The dipole moment of ^1L_b is small and very close to the value of the ground state (1.86 D), whereas the dipole moment of ^1L_a is large (5.86 D), imparting *L*-tryptophan fluorescence high sensitivity to changes in the micro-environment [32]. In water, *L*-tryptophan exists in three ionization states. All of them are fluorescent

[33,34], and their emission spectra are pH- [34] and solvent [35] sensitive. In the present work, preliminary photoluminescence studies were carried out to assess the pH-dependence of *L*-tryptophan emission spectra and quantum yields. Collected data resulted comparable to those reported in literature, both showing that *L*-tryptophan emission spectra shifted to higher wavelength with increasing pH (Figure 20 and Table 4), due to changes in the local electrostatic environment of the indole side group [36].

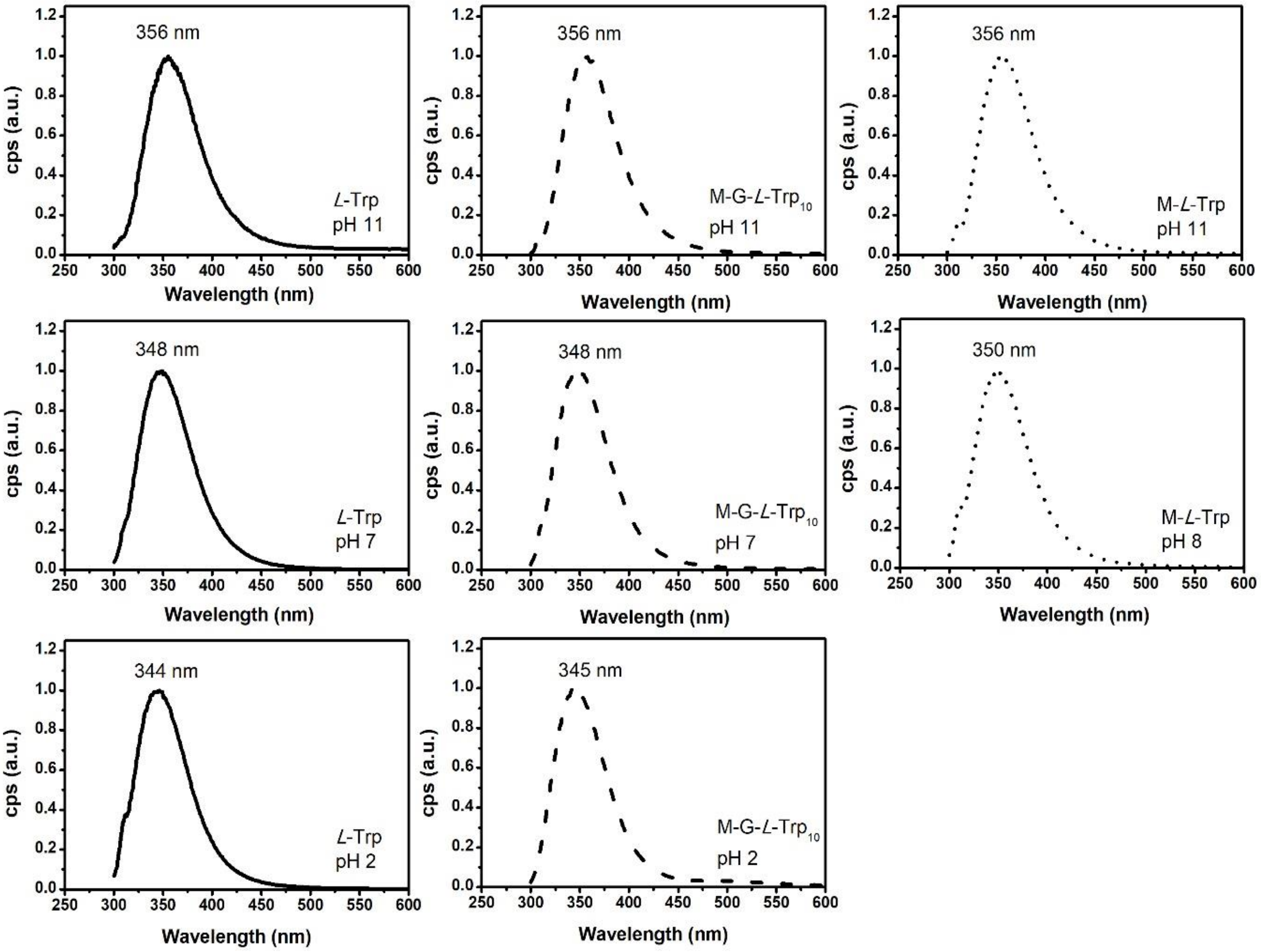

Figure 20. pH-dependence of the emission spectra of M-*L*-Trp and M-G-*L*-Trp$_{10}$ compared with those of *L*-tryptophan at λ_{ex} = 279 nm. For the sake of clarity, some curves have been omitted.

Table 4. *L*-Tryptophan, homo- and copolymers emission maximum recorded by steady-state fluorescence measurements of non-degassed solutions in distilled water versus pH at λ_{ex} = 279 nm.

pH	***L*-Trp λ_{em} (nm)**	**M-G-*L*-Trp$_5$ λ_{em} (nm)**	**M-G-*L*-Trp$_{10}$ λ_{em} (nm)**	**M-G-*L*-Trp$_{20}$ λ_{em} (nm)**	**M-G-*L*-Trp$_{40}$ λ_{em} (nm)**	**M-*L*-Trp λ_{em} (nm)**
11	356	356	356	355	356	356
7	348	347	348	348	351[a]	350[a]
2	344	345	345	345	343[a]	

[a] Analyses carried out at pH 1.5-8, instead of 2 and 7, due to solubility limits.

Quantum yields (QY) measurements (Table 5) resulted dependent on pH. In particular, the highest value was reached at pH 11, for *L*-tryptophan anionic form (22.1%), followed by the zwitterionic form (11.7%) at pH 7, and by the cationic form (4.2%) at pH 2. Differences were ascribed to various intramolecular quenching processes affecting the indole excited states, represented by the positively-charged ammonium group and the carboxyl group. In agreement with literature [37], time-resolved fluorescence measurements showed biexponential decays, from which two lifetimes were determined (Table 6). The trend with pH of those lifetimes was the same as for quantum yields. Lifetimes are normally interpreted by the rotamer model [37–39]. This model implies that, as the interconversion between rotamers is slower (ms) than the fluorescence time scale (ns), the fluorescence decay is multiexponential with relative amplitudes proportional to the rotamer populations. The different lifetimes of the *L*-tryptophan rotamers arise from the different distances of the quenching functional groups from the indole moiety. For example, at pH 7 the calculated lifetimes were 0.2 and 2.79 ns. The former was attributed to the rotamer whose ammonium group resulted closer to the indole ring, whereas the latter was ascribed to rotamers whose carboxylate groups, a less efficient quencher, were closer to the indole ring [38]. Considering *L*-tryptophan ionization degree, similar considerations were made to explain lifetimes recorded at pH 2 and 11, and the decrease, by decreasing pH, of their values (Table 6). In air, also O_2-collisional quenching processes may occur [40,41]. To study the efficiency of O_2 as a *L*-tryptophan quencher, QYs of degassed and non-degassed solutions at pH 11 were recorded (Table 5). According to literature [40,41], higher QY was recorded for degassed solutions.

Table 5. Quantum yields of *L*-tryptophan, M-G-*L*-Trp and M-*L*-Trp copolymers at different pH's. All values should be considered with a ± 5% S.D.

pH	***L*-tryptophan**	**M-G-*L*-Trp$_5$**	**M-G-*L*-Trp$_{10}$**	**M-G-*L*-Trp$_{20}$**	**M-G-*L*-Trp$_{40}$**	**M-*L*-Trp**
11	23.0	14.3	9.5	7.6	7.2	6.3
	28.4^a	15.2^a	11.0^a	7.8^a	7.5^a	6.1^a
7	11.7	8.5	6.4	5.7	4.9^b	4.0^b
2	4.9	5.6	4.7	4.9	2.0^b	-

^{a} Analyses carried out after three freeze-pump-thaw cycles, in O_2 free environment. ^{b} Analyses carried out at pH 1.5–8, instead of 2 and 7, due to solubility limits.

In the present work, the fluorescence properties of M-*L*-Trp and M-G-*L*-Trp copolymers were studied at 2×10^{-4} M concentration, referred to the repeat units, in non-degassed ultrapure water at different pH's. The chosen pH values were different for different tryptophan contents in the polymers, since M-*L*-Trp and M-G-*L*-Trp$_{40}$ showed solubility only at pH > 8. Excitation spectra were carried out at the polymer emission maxima, whose values are reported in Table 4. The UV–Vis and excitation spectra of all tryptophan-based PAACs were superimposable to that of *L*-tryptophan, irrespective of tryptophan content (Figure 21a) and pH (Figure 21b).

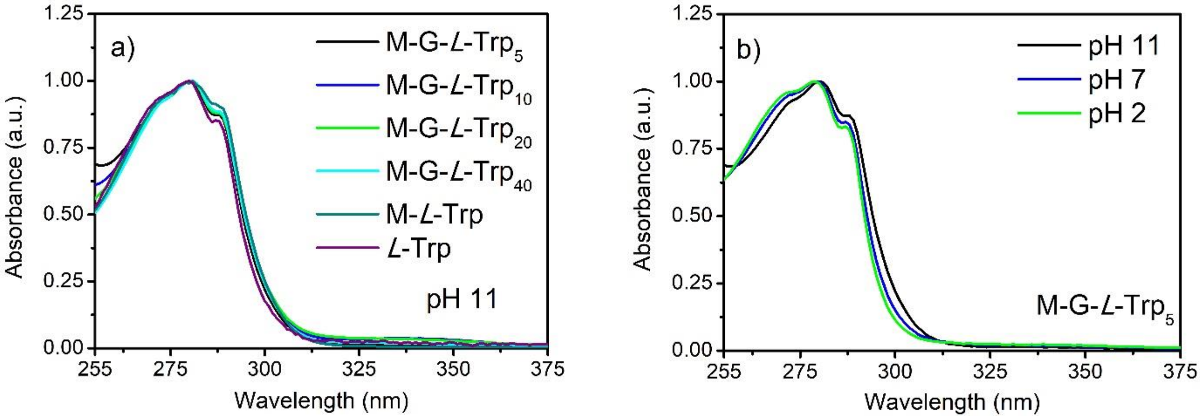

Figure 21. UV-Vis absorption spectra of: a) *L*-tryptophan-based homo- and copolymers spectra recorded at pH 11; b) M-G-*L*-Trp$_5$ recorded at different pHs. *L*-Tryptophan is reported for comparison purposes as well.

The emission spectra (Figure 20) were recorded at 279 nm, resulted unstructured and, at the same pH, almost superimposable to that of *L*-tryptophan. This provided solid evidence that the photoluminescence properties of all tryptophan derived polymers were governed solely by tryptophan. As in case of the amino-acid, in M-*L*-Trp and M-G-*L*-Trp copolymers an increase in pH induced a slight increase of the emission wavelength maximum (λ_{em}) (Table 4), associated with the different ionization degree of the microenvironment surrounding the indole ring.

Absolute photoluminescence quantum yield measurements (Table 5) showed that QY values decreased with decreasing pH. This dependence was attributed to intramolecular quenching processes involving the excited state of indole. As hypothesized for peptides, in tryptophan-based polymers three possible quenchers of indole fluorescence were identified: main chain amide groups, protonated amines and carboxyl group [42–45]. At higher pH's, higher QYs were observed, considering the electron transfer from the indole to the carboxylate quenching groups was less efficient than, at lower pH's, the transfer to both COOH and ammonium groups [37,41]. To notice, at all pH values, by increasing *L*-tryptophan content, a significant decrease in QY was recorded, reaching the lowest value in the case of M-*L*-Trp. In addition, these values resulted significantly lower than those of *L*-tryptophan, even in the case of M-G-*L*-Trp$_5$, the copolymer with the lowest tryptophan content. Probably, at higher tryptophan contents, the proximity among *L*-tryptophan moieties maximized the quenching due to tryptophan-to-tryptophan homotransfer (resonance energy transfer) [46–48].

To assess the efficiency of O_2 as a quencher, the absolute QYs of degassed and non-degassed M-*L*-Trp and M-G-*L*-Trp solutions were compared at pH 11 (Table 5). Unexpectedly, in contrast to what observed with *L*-tryptophan, no significant differences were detected. This might be ascribed to the low accessibility of O_2 to *L*-tryptophan bearing units for conformational reasons [49].

To evaluate intermolecular tryptophan quenching by approaching chains, solutions at different concentration were tested. Non-degassed solutions of M-*L*-Trp and M-G-*L*-Trp_{10} were studied at pH 11 in the 1×10^{-3}–1×10^{-5} M concentration range of the repeat units (Figure 22). As expected, the two curves exhibited different absolute QY values but, more importantly, their trends were similar. In both cases, the QY values decreased with increasing concentration, suggesting quenching mechanisms related to intermolecular interactions.

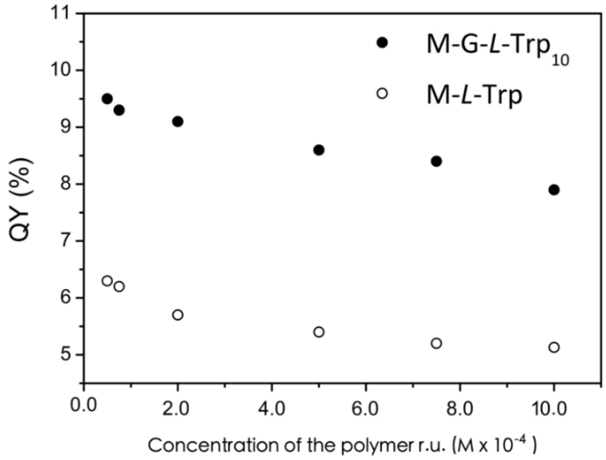

Figure 22. Quantum yields of M-*L*-Trp and M-G-*L*-Trp_{10} recorded at pH 11 and increasing concentration of the polymer repeat units (r.u.).

Time-resolved fluorescence measurements were performed on M-*L*-Trp and M-G-*L*-Trp copolymers as a function of pH, at 2×10^{-4} M concentration referred to the repeat units and $\lambda_{ex} = 301$ nm (Figure 23). As previously reported for *L*-tryptophan, two lifetimes—a short (0.8–1.2 ns) and a long one (3.62–6.13 ns)—were calculated. Both lifetimes decreased with decreasing pH and increasing tryptophan content of the polymer samples (Table 6).

Table 6. *L*-tryptophan, homo- and copolymers time-resolved fluorescence measurements of non-degassed solutions in distilled water versus pH. In brackets % of *L*-tryptophan populations that decay at the calculated τ time. λ_{ex} = 301 nm.

pH	*L*-Trp τ (ns); %	M-G-*L*-Trp$_5$ τ (ns); %	M-G-*L*-Trp$_{10}$ τ (ns); %	M-G-*L*-Trp$_{20}$ τ (ns); %	M-G-*L*-Trp$_{40}$ τ (ns); %	M-*L*-Trp τ (ns); %
11	τ_1 = 0.30 (0.59) τ_2 = 6.89 (99.41)	τ_1 = 1.07 (14.63) τ_2 = 6.13 (85.37)	τ_1 = 1.07 (32.16) τ_2 = 5.54 (67.84)	τ_1 = 1.21 (37.56) τ_2 = 5.66 (62.44)	τ_1 = 1.01 (37.74) τ_2 = 4.63 (62.26)	τ_1 = 0.87 (34.77) τ_2 = 3.62 (65.23)
7	τ_1 = 0.20 (9.66) τ_2 = 2.79 (90.34)	τ_1 = 0.79 (30.11) τ_2 = 3.41 (69.89)	τ_1 = 0.88 (32.28) τ_2 = 3.40 (67.72)	τ_1 = 0.80 (32.74) τ_2 = 3.14 (67.26)	τ_1 = 0.94[a] (41.96) τ_2 = 3.14[a] (58.04)	τ_1 = 0.81[a] (42.26) τ_2 = 3.49[a] (57.74)
2	τ_1 = 0.05 (27.50) τ_2 = 1.34 (72.50)	τ_1 = 0.41 (22.88) τ_2 = 2.35 (77.12)	τ_1 = 0.50 (22.70) τ_2 = 2.30 (77.30)	τ_1 = 0.56 (21.00) τ_2 = 2.25 (79.00)	τ_1 = 0.27[a] (30.10) τ_2 = 1.11[a] (69.90)	

[a] Analyses carried out at pH 1.5-8, instead of 2 and 7, due to solubility limits.

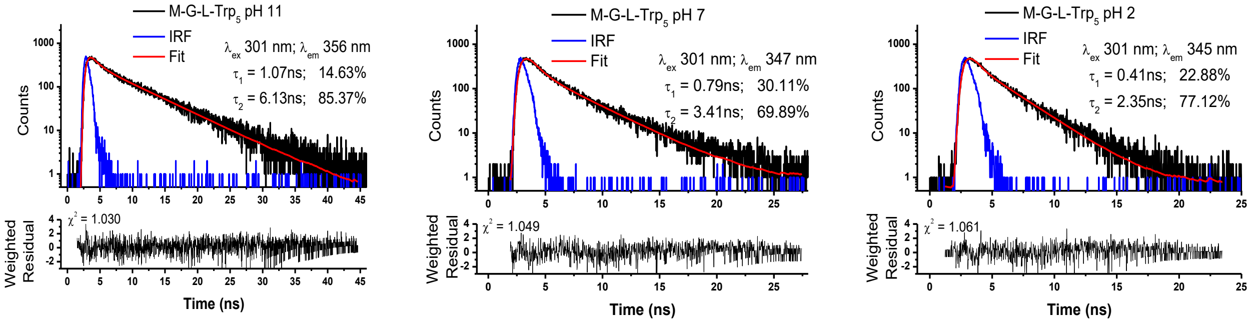

Figure 23. Emission decay of M-G-*L*-Trp$_5$ vs pH at λ_{ex} 301 nm: data (black line), IRF (blue line) and convolution fit (red line). Weighted residuals are shown under the decay curves.

3.4 CONCLUSIONS

New polymers belonging to the PAACs family were synthesized by Michael-type polyaddition of MBA with *L*-tryptophan, its isomer, and different molar ratio of *L*-tryptophan/glycine mixtures. Differently from the other PAACs, tryptophan-based homo- and copolymer were synthesized under nitrogen flux and by portion wise addition of the base to avoid indole oxidation. Firstly, acid-base properties were evaluated, to assess their polyelectrolyte behavior. Then size, self-structuring ability and fluorescent properties were studied. All of them showed composition- and pH-dependent solubility, as ascertained from UV–Vis absorption and scattering of polarized IR beam tests. Hydrodynamic radii were measured by DLS in 0.1 M NaCl. Results indicated that R_h were stable for at least 1 month, and unaffected by pH in the range 1–11 for M-G-*L*-Trp$_5$, M-G-*L*-Trp$_{10}$ and M-G-*L*-

Trp$_{20}$ but only in pH range 7–11 for M-G-*L*-Trp$_{40}$ and M-*L*-Trp homopolymers. Instead, they were, to some extent, sensitive to concentration in the range 1–30 mg·mL^{-1}. Similarly to the other PAACs, all MBA-tryptophan aqueous solution gave rise to pH dependent CD spectra, revealing self-structuring dictated by the polymer main chain and its average ionization degree. Photoluminescence analyses, quantum yields, steady state and time-resolved fluorescence measurements, resulted governed solely by tryptophan photo physics. All polymers exhibited pH-dependent quantum yields, lifetimes and emission maximum. Interestingly, fluorescence studies conducted on oxygen-free solution gave comparable results, indicating compact conformations where L-tryptophan moieties were not accessible to the quencher. Also, intermolecular quenching by approaching chains was studied and observed in M-*L*-Trp and M-G-*L*-Trp$_{10}$.

It can be reasonably concluded that tryptophan-containing PAACs, combining chirality, multifunctionality, pH-dependent water solubility, self-structuring in water, chiro-optical and fluorescence properties, represent singular examples of synthetic bioinspired chiral polymers and can open an interesting field of investigation because of their selective interactions with chiral structures, including biological structures.

3.5 REFERENCES

1. Sanda, F.; Endo, T. Syntheses and functions of polymers based on amino acids. *Macromol. Chem. Phys*. **1999**, *200*, 2651–2661, doi:10.1002/(SICI)1521-3935(19991201)200:12<2651::AID-MACP2651>3.0.CO;2-P.

2. Roy, S.G.; De, P. pH responsive polymers with amino acids in the side chains and their potential applications. *J. Appl. Polym. Sci.* **2014**, *131*, 41084, doi:10.1002/APP.41084.

3. Liu, Z.; Hu, J.; Sun, J.; He, G.; Li, Y.; Zhang, G. Preparation of thermoresponsive polymers bearing amino acid diamide derivatives via RAFT polymerization. *J. Polym. Sci. Part A* **2010**, *48*, 3573–3586, doi:10.1002/pola.24137.

4. Bauri, K.; Ghosh Roy, S.; De, P. Side-chain amino-acid-derived cationic chiral polymers by controlled radical polymerization. *Macromol. Chem. Phys*. **2016**, *217*, 365–379, doi:10.1002/macp.201500271.

5. Wang, X.; Gan, H.; Sun, T.; Su, B.; Fuchs, H.; Vestweber, D.; Butz, S. Stereochemistry triggered differential cell behaviours on chiral polymer surfaces. *Soft Matter* **2010**, *6*, 3851–3855, doi:10.1039/C0SM00151A.

6. Cheng, R.; Liu, J.; Xie, P.; Wu, Y.; Deng, J. Chiral, pH-sensitive polyacrylamide hydrogels: Preparation and enantio-differentiating release ability. *Polymer* **2015**, 68, 246e252, doi:10.1016/j.polymer.2015.05.034.

7. Walling, M.A.; Novak, J.A.; Shepard, J.R.E. Quantum dots for live cell and in vivo imaging. *Int. J. Mol. Sci.* **2009**, *10*, 441–491, doi:10.3390/ijms10020441.

8. Shimazaki, Y.; Yajima, T.; Takani, M.; Yamauchi, O. Metal complexes involving indole rings: Structures and effects of metal–indole interactions. *Coord. Chem. Rev.* **2009**, *253*, 479–492, doi:10.1016/j.ccr.2008.04.012.

9. Jobin, M.-L.; Blanchet, M.; Henry, S.; Chaignepain, S.; Manigand, C.; Castano, S.; Lecomte, S.; Burlina, F.; Sagan, S.; Alves, I.D. The role of tryptophans on the cellular uptake and membrane interaction of arginine-rich cell penetrating peptides. *Biochim. Biophys. Acta Biomembr*. **2015**, *1848*, 593–602, doi:10.1016/j.bbamem.2014.11.013.

10. Moore, B.L.; O'Reilly, R.K. Preparation of chiral amino acid materials and the study of their interactions with 1,1-bi-2-naphthol. *J. Polym. Sci. Part A* **2012**, *50*, 3567–3574, doi:10.1002/pola.26141.

11. Nechifor, M.; Podasca, V.E.; Buruiana, E.C. Synthesis and fluorescence properties of some tryptophan-containing polyacrylates. *Rev. Roum. Chim*. **2016**, *61*, 363–369.

12. Hiruta, Y.; Kanazashi, R.; Ayano, E.; Teruo Okano, T.; Kanazawa, H. Temperature-responsive molecular recognition chromatography using phenylalanine and tryptophan derived polymer modified silica beads. *Analyst* **2016**, *141*, 910–917, doi:10.1039/c5an01996f.

13. Gingter, S.; Bezdushna, E.; Ritter, H. Chiral recognition of poly(*N*-isopropylacrylamideco-(D or L)-*N*-tryptophan-acrylamide) with methylated β-cyclodextrin. *Macromolecules* **2010**, *43*, 3128–3131, doi:10.1021/ma9025527.

14. Mori, H.; Eri Takahashi, E.; Ishizuki, A.; Nakabayashi, K. Tryptophan-containing block copolymers prepared by raft polymerization: Synthesis, self-assembly, and chiroptical and sensing properties. *Macromolecules* **2013**, *46*, 6451–6465, doi:10.1021/ma400596r.

15. Hashidzume, A.; Harada, A. Macromolecular recognition by cyclodextrins. Interaction of cyclodextrinswith polymethacrylamides bearing hydrophobic amino acid residues. *Polymer* **2006**, *47*, 3448–3454, doi:10.1016/j.polymer.2006.03.040.

16. Roy, S.G.; Acharya, R.; Chatterji, U.; De, P. RAFT polymerization of methacrylates containing a tryptophan moiety: Controlled synthesis of biocompatible fluorescent cationic chiral polymers with smart pH-responsiveness. *Polym. Chem.* **2013**, *4*, 1141–1152, doi:10.1039/c2py20821k.

17. De Levie, R. How to Use ExcelW in Analytical Chemistry and in General Scientific Data Analysis; Cambridge University Press: Cambridge, 2001.

18. Manfredi, A.; Mauro, N.; Terenzi, A.; Alongi, J.; Lazzari, F.; Ganazzoli, F.; Raffaini, G.; Ranucci, E.; Ferruti, P. Self-ordering secondary structure of D- and L-arginine-derived polyamidoamino acids. *ACS Macro Lett.* **2017**, *6*, 987–991, doi:10.1021/acsmacrolett.7b00492.

19. Lazzari, F.; Manfredi, A.; Alongi, J.; Mendichi, R.; Ganazzoli, F.; Raffaini, G.; Ferruti, P.; Ranucci, E. Self-structuring in water of polyamidoamino acids with hydrophobic side chains deriving from natural α-amino acids. *Polymers* **2018**, *10*, 1261, doi:10.3390/polym10111261.

20. Ronsein, G.E.; Oliveira, M.C.B.; Miyamoto, S.; Medeiros, M.H.G.; Di Mascio, P. Tryptophan oxidation by singlet molecular oxygen [O_2 ($^1\Delta_g$)]: Mechanistic studies using ^{18}O-labeled hydroperoxides, mass spectrometry, and light emission measurements. *Chem. Res. Toxicol.* **2008**, *21*, 1271–1283, doi:10.1021/tx800026g.

21. Davies, M.J. The oxidative environment and protein damage. *Biochim. Biophys. Acta* **2005**, *1703*, 93–109, doi:10.1016/j.bbapap.2004.08.007.

22. Kelly, S.M.; Price, N.C. The use of circular dichroism in the investigation of protein structure and function. *Curr. Protein Pept. Sci.* **2000**, *1*, 349–384, doi:10.2174/1389203003381315.

23. Myer, P.Y.; MacDonald, L.H. Circular dichroism of L-tryptophan by an improved dichrograph. *J. Am. Chem. Soc.* **1967**, *89*, 7142–7144, doi:10.1021/ja01002a071.

24. Woody, W.R. Contributions of tryptophan side chains to the far-ultraviolet circular dichroism of proteins. *Eur. Biophys. J.* **1994**, *23*, 253–262, doi:10.1007/BF00213575.

25. Buczkowski, A.; Urbaniak, P.; Belica, S.; Sekowski, S.; Bryszewska, M.; Palecz, B. Formation of complexes between PAMAM-NH_2 G4 dendrimer and L-α-tryptophan and L-α-tyrosine in water. *Spectrochim. Acta A* **2014**, *128*, 647–652, doi:10.1016/j.saa.2014.02.174.

26. Ghisaidoobe, A.B.; Chung, S.J. Intrinsic tryptophan fluorescence in the detection and analysis of proteins: A focus on Förster resonance energy transfer techniques. *Int. J. Mol. Sci.* **2014**, *15*, 22518-22538, doi:10.3390/ijms151222518.

27. Creed, D. The photophysics and photochemistry of the near-UV absorbing amino acids-I. Tryptophan and its simple derivatives. *Photochem. Photobiol.* **1984**, *39*, 537-562, doi:10.1111/j.1751-1097.1984.tb03890.x.

28. Song, P.-S.; Kurtin, W.E. A spectroscopic study of the polarized luminescence of indole. *J. Am. Chem. Soc.* **1969**, *91*, 4892–4906.

29. Albinsson, B.; Kubista, M.; Norden, B.; Thulstrup, E.W. Near-ultraviolet electronic transitions of the tryptophan chromophore: Linear dichroism, fluorescence anisotropy, and magnetic circular dichroism spectra of some indole derivatives. *J. Phys. Chem.* **1989**, *93*, 6646–6655, doi:10.1021/j100355a016.

30. Albinsson, B.; Norden, B. Excited-state properties of the indole chromophore: Electronic transition moment directions from linear dichroism measurements-effect of methyl and methoxy substituents. *J. Phys. Chem.* **1992**, *96*, 6204–6212, doi:10.1021/j100194a023.

31. Callis, P.R. ^1L_a and ^1L_b transitions of tryptophan: Applications of theory and experimental observations to fluorescence of proteins. *Methods Enzymol.* **1997**, *278*, 113–150, doi:10.1016/S0076-6879(97)78009-1.

32. Pierce, D.W.; Boxer, S.G. Stark effect spectroscopy of tryptophan. *Biophys. J.* **1995**, *68*, 1583–1591, doi:10.1016/S0006-3495(95)80331-0.

33. De Lauder, W.B.; Wahl, P. pH dependence of the fluorescence decay of tryptophan. *Biochemistry* **1970**, *9*, 275–2754, doi:10.1021/bi00815a025.

34. Cowgill, R.W. Fluorescence and the structure of proteins II. Fluorescence of peptides containing tryptophan or tyrosine. *Biochim. Biophys. Acta* **1963**, *75*, 272–273.

35. Gryczynski, I.; Wiczk, W.; Johnson, M.L.; Lakowicz, J.R. Lifetime distributions and anisotropy decays of indole fluorescence in cyclohexane/ethanol mixtures by frequency-domain fluorometry. *Biophys. Chem*. **1988**, *32*, 173–185, doi:10.1016/0301-4622(88)87005-4.

36. Albani, J.R. Origin of tryptophan fluorescence lifetimes Part 1 fluorescence lifetimes origin of tryptophan free in solution. *J. Fluoresc*. **2014**, *24*, 93–104, doi:10.1007/s10895-013-1277-8.

37. Szabo, A.G.; Rayner, D.M. Fluorescence decay of tryptophan conformers in aqueous solution. *J. Am. Chem. Soc.* **1980**, *102*, 554–563, doi:10.1021/ja00522a020.

38. Donzel, B.; Gauduchon, P.; Wahl, P. Conformation in the excited state of two tryptophanyl diketopiperazines. *J. Am. Chem. Soc.* **1974**, *96*, 801–808, doi:10.1021/ja00810a027.

39. Eftink, M.R.; Jia, J.; Hu, D.; Ghiron, C.A. Fluorescence studies with tryptophan analogues: Excited state interactions involving the side chain amino group. *J. Phys. Chem.* **1995**, *99*, 5713–5723, doi:10.1021/j100015a064.

40. Lehrer, S.S. Solute perturbation of protein fluorescence. Quenching of the tryptophyl fluorescence of model compounds and of lysozyme by iodide ion. *Biochemistry* **1971**, *10*, 3254–3263, doi:10.1021/bi00793a015.

41. Lakowicz, J.R.; Weber, G. Quenching of fluorescence by oxygen: A probe for structural fluctuation in macromolecule. *Biochemistry* **1973**, *12*, 4161–4170, doi:10.1021/bi00745a020.

42. Osysko, A.P.; Muíño, P.L. Fluorescence quenching of tryptophan and tryptophanyl dipeptides in solution. *J. Biophys. Chem.* **2011**, *2*, 316–321, doi:10.4236/jbpc.2011.23036.

43. Callis, F.R.; Liu, T. Quantitative prediction of fluorescence quantum yields for tryptophan in proteins. *J. Phys. Chem. B* **2004**, *108*, 4248–4259, doi:10.1021/jp0310551.

44. Adams, P.D.; Chen, Y.; Ma, K.; Zagorski, M.; Sonnichsen, F.D.; McLaughlin, M.L.; Barkley, M.D. Intramolecular quenching of tryptophan fluorescence by the peptide bond in cyclic hexapeptides. *J. Am. Chem. Soc.* **2002**, *124*, 9278–9286, doi:10.1021/ja0167710.

45. Chen, Y.; Liu, B.; Yu, H.T.; Barkley, M.D. The peptide bond quenches indole fluorescence. *J. Am. Chem. Soc.* **1996**, *118*, 9271–9278, doi:10.1021/ja961307u.

46. Moens, P.D.J.; Helms, M.; Jameson, D.M. Detection of tryptophan to tryptophan energy transfer in proteins. *Protein J.* **2004**, *23*, 79–83, doi:10.1023/B:JOPC.0000016261.97474.2e.

47. Weber, G. Fluorescence-polarization spectrum and electronic-energy transfer in tyrosine, tryptophan and related compound. *Biochem. J.* **1960**, *75*, 335–345.

48. Lakowicz, J.R. *Principles of Fluorescence Spectroscopy*, 3rd ed.; Springer publishing: Berlin, Germany, 2006; pp. 529–575.

49. Eftink, M.R.; Ghiron, C.A. Exposure of tryptophanyl residues in proteins. Quantitative determination by fluorescence quenching studies. *Biochemistry* **1976**, *15*, 672–680, doi:10.1021/bi00648a035.

4

Chiral recognition of *D*- and *L*-Arginine derived polyamidoamino acids with pH dependent self-assembled sodium deoxycholate

4.1 INTRODUCTION

Bile salts are a complex mixture of several cholic acid derivatives, composed by a rigid, slightly bent steroid structure and a short aliphatic side chain. Physiologically, their main function lies in the formation of mixed micelles able to solubilize lipids and fat-based compounds [1]. As well, cholic acids and cholate-derived compounds are exploited in the absorption of low-solubility drugs [2,3] and membrane chemistry [4]. Bile salts are ionic facial amphipiles, i.e. when hydrophilic and hydrophobic groups are located on two opposite faces. The steroid backbone is composed of a convex methyl rich hydrophobic face and a concave hydroxyl rich hydrophilic side. Upon increasing concentration in aqueous solutions, bile salts are able to self-assemble into different chiral micelles [5-8], whose chirality may arise from both the stereogenic centers present in their structures and from the twisted conformation. To describe micelles formation, the most known and accepted model, is a two-step mechanism. Firstly, hydrophobic forces drive the back-to-back formation of primary aggregates, secondly, by further increasing concentration, aggregates are held together by hydrogen bonding and generate elongated secondary micelles [9]. Taking into account both steps, cholate-derived micelles appear polydisperse [10]. Small angle neutron scattering (SANS) reported rod-like structures with various aggregation numbers, highly affected by concentration [11,12], ionic strength and pH [13]. Upon decreasing pH, these rods became more and more elongated until a thixotropic gel is formed [14]. The supramolecular complex resulted by the micelles entanglement [15] assumed a helical structure [14].

Among bile salts, sodium deoxycholate (NaDC) is one of the most familiar gelators. Whereas NaDC pH dependent behaviour is widely studied, albeit poorly understood, very little is known on its ability to interact with chiral molecules or polymers and to show enantiomeric selection. NaDC is known to separate chiral drugs or organic compounds in micellar electrokinetic capillary chromatography (MECC) [16-18], with advantages like reduction of retention factor values and possible extension of the elution range [19]. Foreseeing its behaviour, i.e. the driving forces behind the chiral recognition, is of paramount importance in predicting the results of specific chiral interactions in more complex systems, and hence to be exploited in techniques like MECC or as smart delivery vehicles. Enantio-preference release from NaDC/Tris(hydroxymethyl)aminomethane hydrogel was recorded for *D*-tryptophan and (*R*)-ibuprofen, starting from the racemic mixtures [20]. Additionally, isothermal titration calorimetry (ITC) studies showed NaDC is capable of bind more tightly the (*S*)-atropisomer of 1,1′-binaphthyl-2,2′-diylhydrogenphosphate (BNDHP), resulting in a chiral guest-host recognition [21]. Nonetheless, regarding synthetic biobased chiral polymers literature remains scarce [22-24].

Due to the ability of *D*- and *L*-ARGO7, the first polymers of the PAACs family, to self-assemble in solution forming mirror-image chiral structures, chirality-dependent interaction with chiral surfaces or biomolecules may be shown. The aim of this chapter is to report how the enantiomeric forms of the chiral arginine-based polymers (*D*- and *L*-ARGO7) might interact with the different pH dependent self-assembled structures of NaDC micelles.

4.2 EXPERIMENTAL SECTION

4.2.1 Materials

Solvents and reagents, unless otherwise indicated, were analytical-grade commercial products and used as received. *L*-arginine (≥ 98.5%), *D*-arginine (≥ 99%,) and *D,L*-.arginine (≥ 98.5%), sodium deoxycholate (≥ 97%), deuterium oxide (D_2O, 99.9%), deuterium chloride (DCl, 99%) and sodium deuteroxide (NaOD, 40 wt.-% in D_2O) were purchased from Sigma-Aldrich (Milano, Italy), while *N,N′*-methylenebisacrylamide (MBA, 96%) from Acros Organics (Milano, Italy). 0.3 M HCl and 0.3 M NaOH volumetric standard solutions were purchased from Fluka analytics (Milano, Italy). Ultrapure water (18 $M\Omega \cdot cm^{-1}$), produced with a Millipore Milli-Q® apparatus (Darmstadt, Hesse, Germany), was used to prepare all solutions.

4.2.2 Instruments and methods

Pulsed-gradient spin-echo nuclear magnetic resonance (PGSE-NMR) and *^1H NMR* were carried out in D_2O at 25 °C using a 400 MHz Bruker FT NMR spectrometer operating at 400.13 MHz, employing a 5 mm diffusion probe. Spectra were recorded at different pD (pH of the D_2O solution), using diluted NaOD and DCl solutions. In PGSE-NMR, parameters used for the stimulated echo sequence were the followings: diffusion time (*D*) was set to 150 ms, the duration of the gradient pulses (*d*) was held constant at 1 ms and their intensity (*G*) varied from 5 to 300 G cm^{-1}. The number of scans was set to 16, accumulated over 32 gradient steps. Typically, self-diffusion coefficients (D_s) were calculated with CORE software [25]. In some cases, where specified, D_s were extracted by fitting peak intensities (I) to the simplified Stejskal-Tanner equation (Eq. (1)), obtained when the total echo time 2τ is held constant and the gradient strength G varied.

$$I = I_0 e^{-D_s \gamma^2 G^2 \delta^2 (\Delta - \frac{\delta}{3})} \qquad \text{Eq. (1)}$$

where I_0 is the signal intensity in the absence of gradient pulses and γ the gyromagnetic ratio of protons [26].

Size exclusion chromatography (SEC) traces were obtained for ARGO7 isomers following the procedure described in Chapter 2, Experimental Section p. 40.

Surface tension measurements were carried out using a maximum bubble pressure tensiometer, model SITA Science line t60 (SITA Messtechnik GmbH, UK), calibrated with 0.1 M NaCl solution. The surface tension of NaDC and NaDC/*L*-ARGO7 aqueous mixtures, at different pHs and concentrations, was measured in triplicate at 25°C. A bubble lifetime of 15 s was used to ensure full equilibration.

Dynamic light scattering (DLS) analyses were carried out on i) ARGO7, ii) NaDC and iii) their mixtures at difference concentration and pHs, in the solubility range. Solutions were prepared using 0.1 M NaCl and analysed by a Malvern Zetasizer NanoZS instrument (Malvern, Worcestershire, UK), equipped with a laser fitted at 532 nm and fixed 173° scattering angle. Before analyses, samples were filtered through a 0.2 μm syringe Whatman filter. The solution pH was adjusted to the selected value by the MPT-2 autotitrator (Malvern, Worcestershire, UK), using 0.3 M HCl or 0.3 M NaOH aqueous solutions. Typically, measurements were performed in triplicate and each value reported as the average of 10 runs.

Zeta potentials (ZP) was measured in 0.5 mm folded capillary cells on the same NaDC and ARGO7 solutions employed for DLS measurements. Solution pH was adjusted by the MPT-2 accessory mentioned above. Before each measurement, samples were filtered through a 0.2 μm syringe Whatman filter. Data were collected after the stability of the ZP was reached, in monomodal mode and were reported as an average of 6 runs.

Circular Dichroism (CD) spectra were recorded using a Chirascan spectrophotometer (Applied Photophysics Ltd., Surrey, UK) equipped with a Peltier temperature control system. Typically, CD signals were acquired at 25°C by scanning in the 190 - 280 nm range, in rectangular quartz cells with 1 mm path-length at various pHs. Each spectrum was the average of 4 measurements at 2.5 s time-per-point. Samples of NaDC, *D*- and *L*-ARGO7 and NaDC/ARGO7 mixtures were prepared in 0.1 M NaCl solution using D_2O. The pH was adjusted with 0.1 M DCl or 0.1 M NaOD aqueous solutions and measured by a combined Metrohm microelectrode (Metrohm, Cheshire, UK). At pH 7.3, when NaDC/ARGO7 systems formed gels, measurements were performed after 2 hrs. After this time, it was observed that CD measurements resulted stable and reproducible (see for example NaDC spectra in Figure A1 in Appendix).

Small-angle neutron scattering (SANS) experiments were performed on the fixed-geometry, time-of flight LOQ diffractometer at the ISIS Spallation Neutron Source, Rutherford Appleton Laboratory, Didcot, UK. A range defined by $Q = (4\pi/\lambda) \sin(\theta/2)$ between 0.009 and 0.67 $Å^{-1}$ was obtained by using neutron wavelengths (λ) spanning from 2.2 to 10 Å with a fixed sample-detector distance of 4.1 m. The samples were contained in either 1- or 2-mm path length, UV-spectrophotometer grade~~,~~ quartz cuvettes (Hellma, GmBh) and mounted in aluminum holders on top of an enclosed, computer-controlled, sample chamber. All experiments were conducted at 25°C and different pD (pH of the D_2O solution). Experimental measuring times were approximately 50 – 60 min. All scattering data were i) normalized for the sample transmission, ii) background corrected using a quartz cell filled with D_2O, and iii) corrected for the linearity and efficiency of the detector response using the instrument specific software package.

4.2.3 Synthesis of ARGO7 isomers

The synthesis of *L*-, *D*- and *D,L*-ARGO7 isomers was carried out as previously described in Chapter 2, Experimental Section page 46. SEC and ^1H NMR were reported in the same chapter at pages 46-47.

4.2.4 Structure and ^{1}H NMR of NaDC

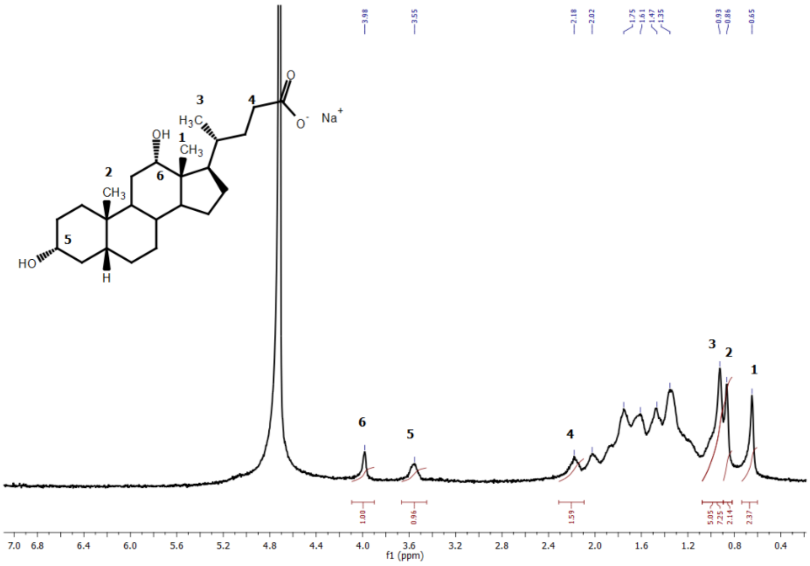

Figure 1. ^{1}H NMR spectra of NaDC in D_2O at pH 8.50.

^{1}H NMR (D_2O, 400.132 MHz, ppm): δ 0.65 (s, 3H, -C**H$_3$** **1**), 0.86-0.93 (m, 6H, -CH_3 **1 and 3**), 2.18 (m, 2H, -C**H$_2$**COO-), 3.55 (m, 1H, -C**H** **5**), 3.98 (m, 1H, -CH **6**) (Figure 2).

4.3 RESULTS AND DISCUSSION

4.3.1 Synthesis of ARGO7 isomers

D-, *L*- and *D,L*-ARGO7 were obtained following the synthesis described previously (Chapter 2, Experimental Section page 47). Molecular weights were measured by size exclusion chromatography in TRIS buffer solutions at pH 8.00. Number-average molecular weights M_n did not show any differences between the three isomers. All the stereoisomers were also characterized by ^{1}H NMR spectra and FT-IR/ATR and resulted the same.

4.3.2 Phase behavior of NaDC/water mixtures

It is widely known that NaDC/water mixtures showed a pH- [27] and concentration [9] dependent behaviour. In order to identify the phase-stability boundaries of the chosen model system NaDC, 0.5 – 50 mg mL^{-1} NaDC/water mixtures in 0.1 M NaCl and at different pHs, were studied. When NaDC concentration was higher than 2.5 mg mL^{-1}, NaDC/water showed three different phases

(Figure 2): transparent homogenous liquids (pH ≥ 7.50), transparent gels (pH 7.0 – 7.5), precipitate (pH ≤ 7.00) (Figure 2). When NaDC concentration was lower than 2.5 mg mL^{-1}, only two phases were seen: transparent homogenous liquids (pH ≥ 6.50) and precipitate (pH 6.00) (Figure 2).

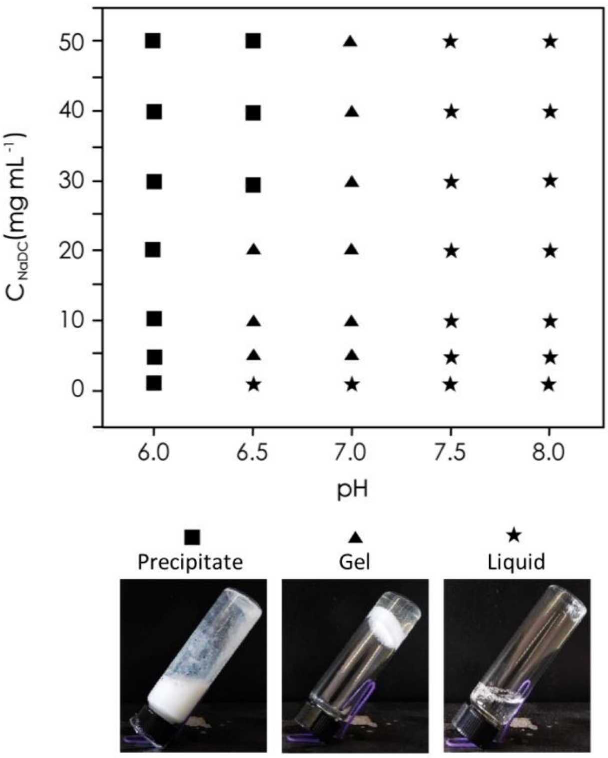

Figure 2. Phase behaviour of NaDC/water mixture as a function of pH and concentration. ☆: transparent homogeneous liquid; △: transparent gel; □: precipitate.

4.3.3 Phase behavior of NaDC/water/ARGO7 mixtures

In Chapter 2, the acid-base properties of ARGO7 isomers were reported and showed isoelectric points of 9.7. Therefore, *D*-, *L*- or *D,L*-ARGO7 resulted mainly positively charged when pH < 9.0. Being NaDC negative charged until -COOH neutralization, it is expected that NaDC/water/ARGO7 mixtures have some form of pH dependent electrostatic interactions that may alter the phase transitions observed for the NaDC/water system. On the other hand, since *D*- and *L*-ARGO7, but not *D,L*-ARGO7, and NaDC are chiral, modification of the phase transitions may occur also due to some chirality dependent interactions. To ascertain this point, mixtures containing 0.5 wt % of either *D*-, or *L*- or *D,L*-ARGO7 and 5 mg mL^{-1} NaDC in 0.1 M NaCl were tested.

Differences were observed for the gel phase and at the onset of flocculation. In particular, for NaDC/water/*L*-ARGO7 mixtures, transparent gel was formed at pH 7.60. Interestingly, the gel formation took a longer time, and produced a soft opaque gel compared with that obtained in the absence of the polymer. NaDC/water/*D*-ARGO7 mixtures gave a transparent gel at pH 7.50, whereas *D,L*-ARGO7 formed a transparent and harder gel at pH 7.25. Additionally, when the polymer was present in the mixtures, precipitation occurred at higher pH than in the binary NaDC/water system (pH 6.90 vs pH 6.70).

4.3.4 Surface tension of NaDC/water/ARGO7 mixtures

In the literature the critical micellar concentration (CMC) of NaDC is extensively studied under various conditions of pH, ionic strength and temperature [28-30]. It is known that the transition region is broader than that of classical amphiphiles and may present two CMCs [31], the first associated with the formation of small aggregates and the second to the presence of stable micelles [31]. In this chapter, surface tension measurements were performed on NaDC/water and NaDC/water/*L*-ARGO7 systems at various concentrations and at set ionic strength, in 0.1 M NaCl. This was done for determining the CMC value of NaDC and assessing the possible variations in micelle formation due to the presence of *L*-ARGO7.

The concentration dependence of the surface tension of NaDC/water mixtures was studied at pH 8.63 ± 0.47 and 24.7 ± 0.4 °C, and showed decreasing values with increasing concentration, reaching initially a minimum and then a plateau. The CMC of NaDC value was determined by linear fitting, taking into account the intersection of two drawn lines with respect to the log-concentration of NaDC (Figure 3). NaDC showed a CMC of 0.802 mg mL^{-1} in 0.1 M NaCl in accordance with the literature data [9]. The addition of 0.5 wt % of *L*-ARGO7 did not affect the surface tension of NaDC/water system (gray dots in Figure 3). This may be ascribed by the fact that the water-soluble *L*-ARGO7 remained in the aqueous phase and therefore did not interfere with the water/air interphase.

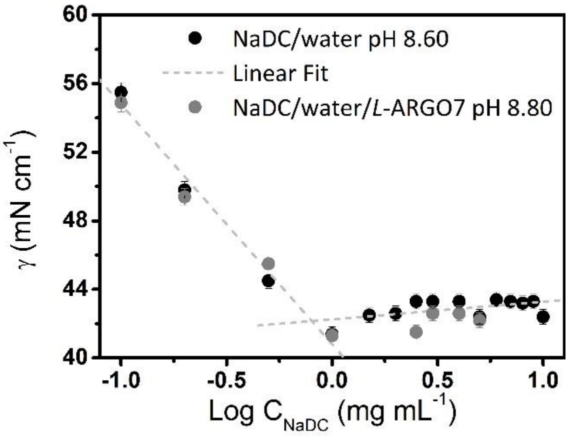

Figure 3. Surface tension trend with increasing NaDC concentration in 0.1 M NaCl, at pH 8.63 ± 0.47 and temperature of 24.7 ± 0.4 °C (black dots) before and after the addition of 0.5 wt % *L*-ARGO7 (gray dots).

4.3.5 Dynamic light scattering and ζ-potential measurements

Dynamic light scattering and ζ-potential measurements were performed to evaluate electrostatic interactions in several conditions of pH, NaDC concentration and NaDC/*L*-ARGO7 ratio. This was done to select the right conditions to use later to detect chiral interactions.

The pH-dependence of the ζ-potential of both NaDC/water and NaDC/water/*L*-ARGO7 mixtures was studied in the pH interval 6.5 – 9.5, at 0.1 M NaCl. Along this pH interval, both mixtures changed their phase (see phase behavior of binary mixtures in Figure 2). As already shown, the presence of *L*-ARGO7 did not substantially alter this pattern. The ζ-values recorded for NaDC were always negative, irrespective of pH and concentration (Figure 4 and Figure A2 in Appendix). Also in the case of 0.5 mg mL^{-1} *L*-ARGO7 solution, ζ-values resulted negative, notwithstanding ARGO7 isoelectric point of 9.7 (Figure 4). This might be explained by the molecular dynamics simulations carried out on ARGO7 solutions (see Chapter 2, page 60). Results indicated carboxylate groups were prevailingly exposed on the outer surface of the ARGO7 compact conformation, as such resulting in negative ζ-potential values.

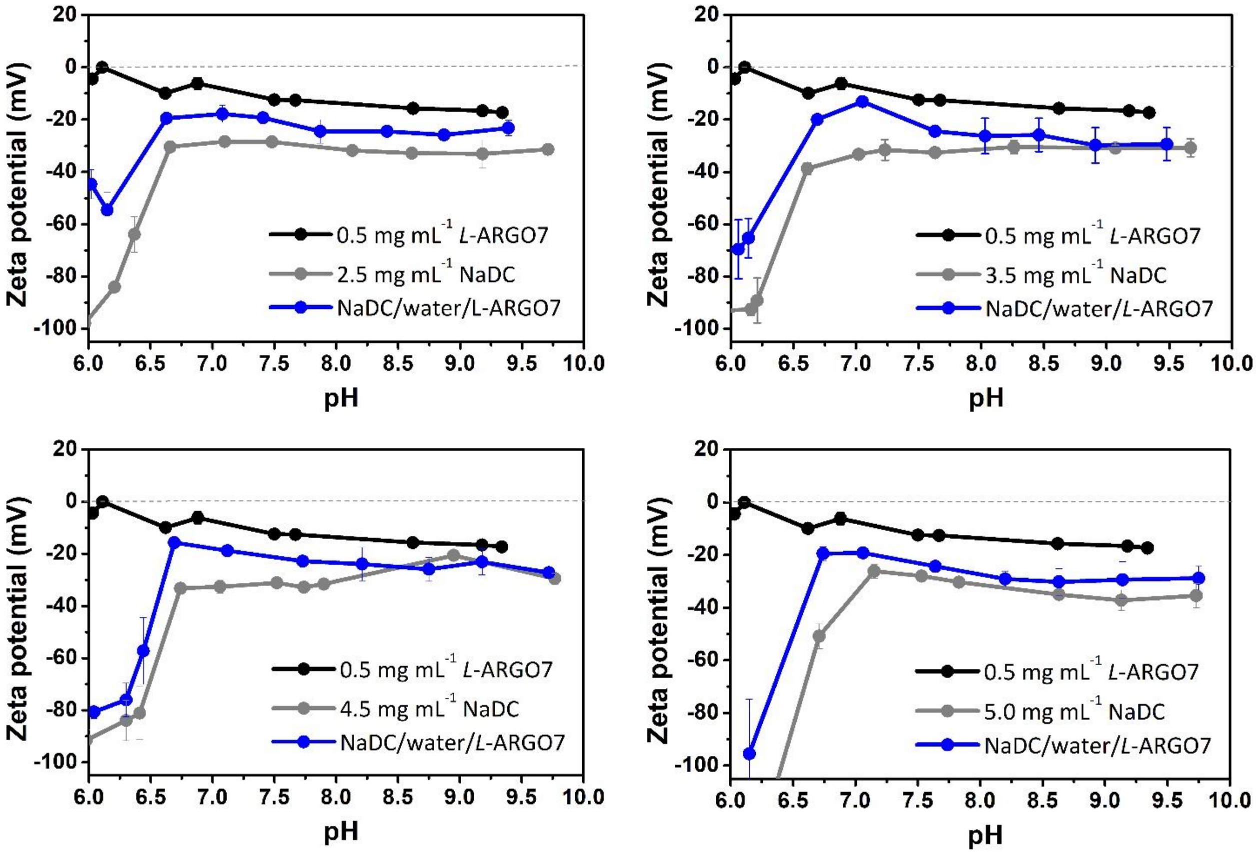

Figure 4. pH-Dependence of ζ-potentials values ofL-ARGO7 (black line), NaDC (gray line) and NaDC/water/*L*-ARGO7 mixtures (blue line) at various NaDC concentration, above the CMC. The concentration of *L*-ARGO7 is 0.5 mg mL^{-1}.

The ζ-values of NaDC/water/*L*-ARGO7 mixtures were recorded at different NaDC concentration and pHs (blue line in Figure 4). At NaDC concentration ≤ CMC, ζ-potential curves showed the same trend of plain *L*-ARGO7 solution, albeit with more negative ζ-values (Figure A2 in Appendix). At NaDC concentration > CMC, curves showed a pH dependence trend similar to that of pure NaDC solutions (Figure 4). Differences in ζ-values were observed between pH 6.7 – 7.5, possibly caused by the protonation of the *tert*-amine groups of the *L*-ARGO7 main chain. In fact, speciation curves reported in Chapter 2 page 56 showed that 10% of these groups were protonated. From the ζ-potential trends it seemed the NaDC/*L*-ARGO7 ratio of 10:1 was the best in minimizing electrostatic interactions.

DLS measurements were carried out on both NaDC/water and NaDC/water/*L*-ARGO7 mixtures in 0.1 M NaCl and pH ≥ 7.50, according to NaDC solubility. In all cases hydrodynamic radii (R_h) of NaDC did not change upon changing concentration or pH (Table 1). Even in the NaDC/water/*L*-ARGO7 mixtures, R_h values resulted comparable with NaDC/water systems. The volumetric size recorded for *L*-ARGO7 alone was in line with the data obtained in Chapter 2 page 57, associated with a compact structure.

Table 1. Hydrodynamic radii of NaDC before and after adding *L*-ARGO7 from DLS volume size distribution.

	NaDC/water	**NaDC/water/*L*-ARGO7***
C_{NaDC} **(mg mL^{-1})**	R_h **NaDC (nm) at pH 8.50**	R_h **NaDC (nm) at pH 8.50**
2.5	1.32 ± 0.29	1.83 ± 0.49
3.5	1.70 ± 0.45	1.63 ± 0.46
4.5	1.39 ± 0.41	1.50 ± 0.40
5.0	1.63 ± 0.37	1.57 ± 0.46

* In all cases, the concentration of *L*-ARGO7 was 0.5 mg mL^{-1} and its size 2.05 ± 0.53 nm, at pH 7.5.

4.3.6 Self-diffusion coefficients (D_s) in NaDC/water/ARGO7 mixtures

Pulsed-gradient spin echo (PGSE) NMR sequence is generally employed to measure the self-diffusion coefficients (D_s) of different species in a multicomponent solution [32]. PGSE-NMR was employed to record D_s values of ARGO7 isomers, NaDC and NaDC/water/ARGO7 mixtures. Measurements were carried out in D_2O containing 0.1 M NaCl at different concentration, pH and ionic strength. Data are reported with their pD, that is the pH measured in D_2O.

For ARGO7 isomers, it may be observed that all peaks decayed mono-exponentially, demonstrating that the molecular dimensions of the polymers were homogeneous. The hydrodynamic radii (R_h) were obtained from the D_s values using the Stokes-Einstein equation (Eq. 2).

$$D = \frac{k_B T}{6\pi\eta r} \qquad \text{Eq. (2)}$$

where k_B is Boltzmann's constant, T is the absolute temperature, η is solution viscosity, and r is the hydrodynamic radius of the particle. For *L*- and *D*-ARGO7 the concentration dependence of the D_s values was determined at pD 9.0 in the concentration range 5 – 30 mg mL^{-1} (Table 1), whereas the pH dependence was determined at pD 2, 5, 7 and 11 with 10 mg mL^{-1} ARGO7 solutions (Table 2). The R_h values were around 2 nm and did not significantly vary with concentration. As for pH, they only moderately varied even at very high pH. The values reported were in line with those previously obtained by dynamic light scattering.

Table 1: Concentration dependence (C) of *L*- and *D*-ARGO7 self-diffusion coefficients and hydrodynamic radii, at pD 9.0.

	***D*-ARGO7**		***L*-ARGO7**	
C (mg mL^{-1})	**D_s (m^2 s^{-1} x 10^{-10})**	**R_h (nm)**	**D_s (m^2 s^{-1} x 10^{-10})**	**R_h (nm)**
5	1.06 ± 0.03	2.03 ± 0.12	1.11 ± 0.02	1.93 ± 0.07
10	1.08 ± 0.02	1.99 ± 0.08	0.876 ± 0.04	2.45 ± 0.16
15	1.04 ± 0.04	2.06 ± 0.16	0.942 ± 0.02	2.28 ± 0.08
20	1.11 ± 0.02	1.93 ± 0.07	0.827 ± 0.04	2.60 ± 0.16
30	0.945 ± 0.01	2.27 ± 0.01	0.872 ± 0.03	2.46 ± 0.12

Table 2: pH dependence of the *D*- and *L*-ARGO7 self-diffusion coefficients and hydrodynamic radii.

	***D*-ARGO7**		***L*-ARGO7**	
pD	**D_s (m^2 s^{-1} x 10^{-10})**	**R_h (nm)**	**D_s (m^2 s^{-1} x 10^{-10})**	**R_h (nm)**
2.0 ± 0.1*	0.884 ± 0.03	2.43 ± 0.02	0.757 ± 0.04	2.84 ± 0.03
5.0 ± 0.4	1.13 ± 0.08	1.90 ± 0.28	0.899 ± 0.10	2.39 ± 0.12
7.0 ± 0.2*	1.19 ± 0.10	1.80 ± 0.03	1.38 ± 0.09	1.56 ± 0.19
11.0 ± 0.8	1.23 ± 0.08	1.75 ± 0.26	1.18 ± 0.09	1.82 ± 0.18

* Self-diffusion coefficients were extracted from the simplified Stejskal-Tanner equation (Eq. (1)) due to the small intensity of each proton signal.

For NaDC/water system, the PGSE NMR spectra showed that all peaks decayed monoexponentially, confirming the presence in solution of only one component. The D_s values were recorded at pD 8.86 ± 0.56 in the 0.5 – 50 mg mL^{-1} concentration range (black line in Figure 5a) and showed that the CMC of NaDC was equal 1 mg mL^{-1} as already calculated from surface tension measurements.

The same technique was adopted to study the dependence, in the NaDC/water/ARGO7 mixtures, of the D_s of both NaDC and ARGO7 isomers on the NaDC/ARGO7 ratio at two different pH's, namely pD 9.0 (gray line in Figure 5a), where the system was a homogeneous liquid, and pD 7-8 (gray line in Figure 6a), where the system was a transparent homogeneous gel. At pD 9.0, the D_s of NaDC was significantly affected by the presence of *L*-ARGO7 for NaDC concentrations in the 1-5 mg mL^{-1} range, that is, up to a 1:1 NaDC/ARGO7 ratio (Figure 5a). Instead, at NaDC/ARGO7 ratios > 1 the D_s of NaDC in the mixture was very close to that of plain NaDC (Figure 5a). The D_s of ARGO7 in the mixtures decreased with increasing NaDC/ARGO7 ratio with respect to the obtained values for plain *L*-ARGO7 solution (Figure 5b).

It should be observed that whereas all the NaDC peaks always decayed monoexponentially, even after the addition of the polymer, peaks of *L*-ARGO7 decayed monoexponentially only at

NaDC/ARGO7 ratios >1. When NaDC/ARGO7 ratio < 1, biexponential decays were seen, ascribed to the free and NaDC-bound ARGO7 respectively.

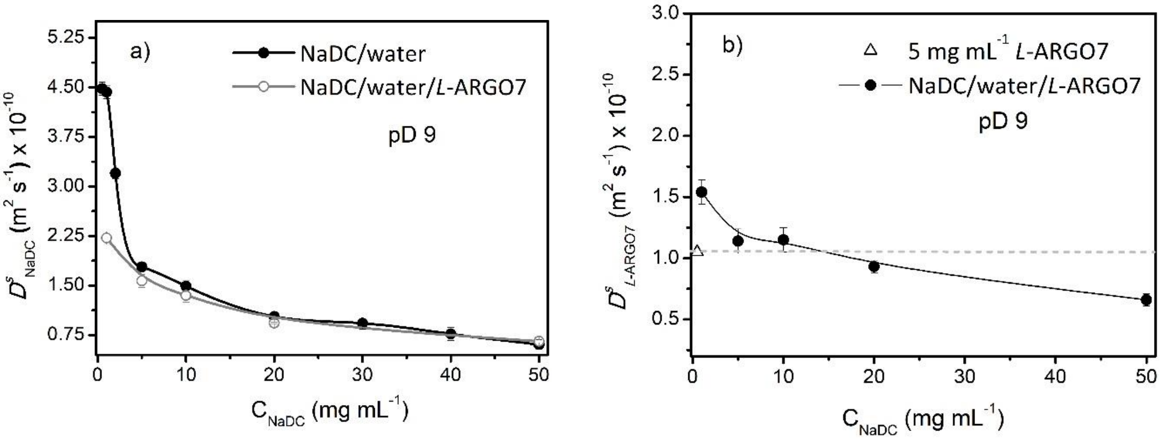

Figure 5. Self-diffusion coefficients (D_s) at pD 9.0 of: a) NaDC/water and NaDC/water/*L*-ARGO7 systems and b) *L*-ARGO7 in the same mixtures. In this case, for comparison purposes, also 5 mg mL^{-1} D_s of plain *L*-ARGO7 was reported (pale gray dotted line).

Table 3: Hydrodynamic radii of NaDC alone and in presence of *L*-ARGO7, at pD 9, obtained from PGSE-NMR applying Stokes-Einstein equation.

	NaDC/water	**NaDC/water/*L*-ARGO7**	**NaDC/water/*L*-ARGO7**
C_{NaDC} (mg mL^{-1})	**R_h NaDC (nm)**	**R_h NaDC (nm)**	**R_h *L*-ARGO7 (nm)**
0.5	0.480 ± 0.20	--	--
1	0.484 ± 0.09	0.970 ± 0.18	1.40 ± 0.20
2	0.671 ± 0.12	--	--
5	1.20 ± 0.35	1.37 ± 0.18	1.89 ± 0.33
10	1.44 ± 0.21	1.59 ± 0.15	1.87 ± 0.28
20	2.08 ± 0.32	2.31 ± 0.30	2.35 ± 0.36
30	2.31 ± 0.33	--	--
40	2.80 ± 0.39	--	--
50	3.53 ± 0.27	3.28 ± 0.44	3.26 ± 0.33

At pD 7-8, when NaDC/water/*L*-ARGO7 mixtures appeared as transparent gels, NaDC peaks still decayed monoexponentially, exhibiting D_s very close to those determined at pD 9.0 (Figure 6a). In these conditions, whereas D_s values of NaDC recorded in absence and presence of *L*-ARGO7 were almost the same, D_s of *L*-ARGO7 observed in the mixtures kept decreasing with increasing NaDC/ARGO7 ratio (Figure 6b).

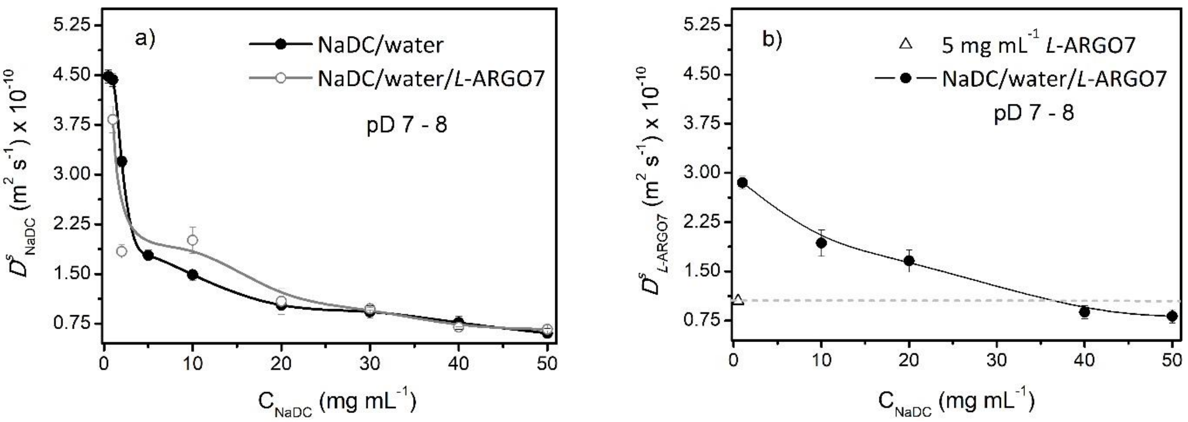

Figure 6. Self-diffusion coefficients (D_s) at pD 7-8 of: a) NaDC/water and NaDC/water/*L*-ARGO7 systems and b) *L*-ARGO7 in the same mixtures. In this case, for comparison purposes, also 5 mg mL^{-1} D_s of plain *L*-ARGO7 was reported (pale gray dotted line).

Table 4: Hydrodynamic radii of NaDC alone and in presence of *L*-ARGO7, at pD 7-8, obtained from PGSE-NMR applying Stokes-Einstein equation.

	NaDC/water	**NaDC/water/*L*-ARGO7**	**NaDC/water/*L*-ARGO7**
C_{NaDC} (mg mL^{-1})	**R_h NaDC (nm)**	**R_h NaDC (nm)**	**R_h *L*-ARGO7 (nm)**
0.5	0.480 ± 0.20	--	--
1	0.484 ± 0.09	0.560 ± 0.12	0.75 ± 0.19
2	0.671 ± 0.12	--	--*
5	1.20 ± 0.35	0.99 ± 0.21	--*
10	1.44 ± 0.21	1.07 ± 0.20	1.11 ± 0.17
20	2.08 ± 0.32	1.97 ± 0.33	1.29 ± 0.21
30	2.31 ± 0.33	2.20 ± 0.27	--*
40	2.80 ± 0.39	3.08 ± 0.36	2.44 ± 0.33
50	3.53 ± 0.27	3.22 ± 0.32	2.63 ± 0.29

* In this cases CORE software gave only one *Ds* value associated to either NaDC, *L*-ARGO7 or both. In no case two distinct values of *Ds*, for NaDC and *L*-ARGO7, were obtained.

4.3.7 Circular dichroism of NaDC/water/ARGO7 stereoisomer mixtures

NaDC conformational changes induced by pH-dependent chiral interactions with ARGO7 stereoisomer were studied by means of circular dichroism (CD) spectroscopy in 0.1 M NaCl at two different pH's, namely 9.0, in which NaDC is completely water soluble, and 7.30, where the NaDC/water system is a transparent, homogeneous gel. Since it is known from the literature that NaDC micelles may show chiral discrimination [16-18, 20,21], interactions were studied only between NaDC above its CMC, when it formed micelles, and ARGO7 stereoisomers. The CD spectra of NaDC and NaDC/water/*L*-ARGO7 mixtures were first carried out at pD 9.06 in the NaDC concentration range of 2.5 – 5.0 mg mL^{-1}. This to identify the best experimental conditions necessary for CD measurements, keeping in mind that the NaDC/*L*-ARGO7 ratio of 10:1 best minimized electrostatic interactions. In all cases, the UV-vis spectra of NaDC/water systems showed absorbance lower than 1.0 in the 200 -270 nm (Figure A3a). CD spectra resulted superimposable, with a low intensity minimum at 211 nm. The major absorption, probably due to C=O groups, fell below 200 nm (Figure A3b). The NaDC selected concentration was 5 mg mL^{-1}. Consequently, *L*- and *D*-ARGO7 concentration was set to 0.5 mg mL^{-1}. Confirming previously reported data (Chapter 2, page 53), the *L*- and *D*-ARGO7 spectra were in mirror-image relationship. At pD 7.30, the 5 mg mL^{-1} NaDC/water system appeared as a homogeneous gel and showed a different CD pattern, suggesting NaDC ability to self-assemble into stable pH-dependent structures (Figure 7).

The CD spectra of the NaDC/water/*D*-ARGO7 and NaDC/ water/*L*-ARGO7 systems carried out at pD 9.06 and pD 7.30, NaDC concentration 5 mg mL^{-1} and ARGO7 concentration 0.5 mg mL^{-1} are reported in Figure 7.

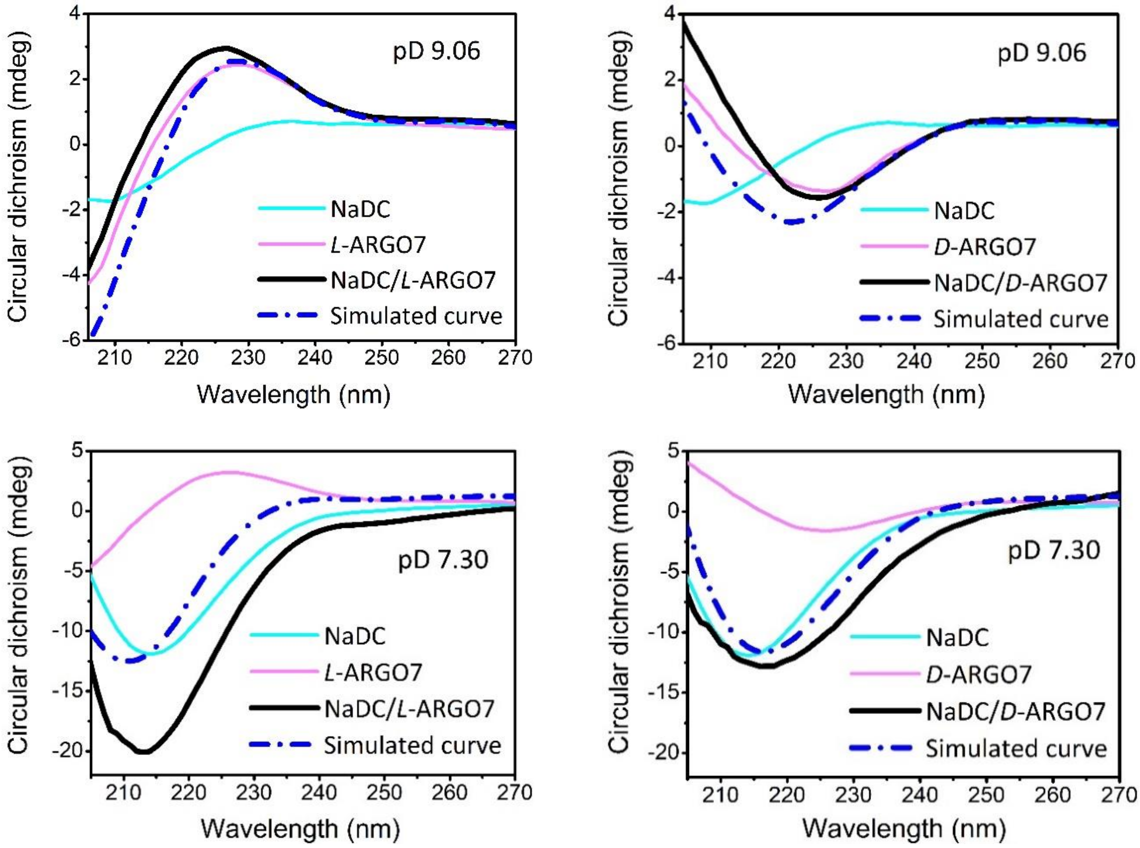

Figure 7. CD spectra of NaDC, *D*- and *L*-ARGO7 and NaDC/water/ARGO7 stereoisomers mixtures at different pH's. Experimental conditions: NaDC concentration 5 mg mL^{-1}; ARGO7 concentration 0.5 mg mL^{-1}; temperature 25°C; optical path 1 mm.

It can be noticed that at pD 9.06, that is, when the NaDC/water/ARGO7 mixtures are homogeneous transparent liquids, no significant differences can be observed between the spectra of *L*-ARGO7 and *D*-ARGO7 and those of their mixtures with NaDC (Figures 7a and 7b). Simulated traces of NaDC/ARGO7 mixtures were calculated as the sum of the CD traces of the two components alone (dotted blue line in Figures 7a and 7b). They showed a significant difference with the experimental traces. However, for the two isomers, both traces were still in a mirror-image relationship, showing that in these conditions no traces of chiral-dependent interactions were detected. Chiral-dependent interactions existed at pD 7.30, that is, when the NaDC/ARGO7 mixtures appeared as transparent, homogeneous gels. In fact, the experimental CD trace of the NaDC/*L*-ARGO7 mixture differed much more significantly from the simulated curve compared to the NaDC/*D*-ARGO7 mixture. In addition, whereas the spectrum of the NaDC/*D*-ARGO7 mixture retains its shape, the spectrum of the NaDC/*L*-ARGO7 mixture changes both shape and intensity.

4.3.8 Small-angle neutron scattering (SANS) measurements

4.3.8.1 NaDC/water system

An in-depth understanding of the conformational changes of the structure of NaDC micelles upon chiral interactions with ARGO7 stereoisomers, was carried out by means of small-angle neutron scattering (SANS) experiments. Analyses were recorded as a function of NaDC concentration and pH and reported as scattering intensity vs scattering vector (Q) with their pD, that is the pH measured in D_2O.

At pD 8.5 – 8.8, scattering data collected in the NaDC concentration range of 5 – 100 mg mL^{-1}, showed curves consistent with the presence of micellar structures (Figure 8a). In order to determine their shape, all curves were fitted with the theoretical scattering function of prolate ellipsoids with polar radius of 22 – 28 Å and equatorial radius of 7 – 10 Å. To account for interparticle interactions of charged spheroidal objects, the Hayter-Penfold Rescaled Mean Spherical Approximation (RMSA) structure factor was introduced for all data. Results about radii, scattering light density (SLD) and charge values were reported in Table A1 in Appendix and were in all cases comparable (Figure 8a). To note, above 35 mg mL^{-1}, a small shoulder at 0.1 A^{-1} appeared suggesting changes in interparticle interactions due to different electrostatic charges.

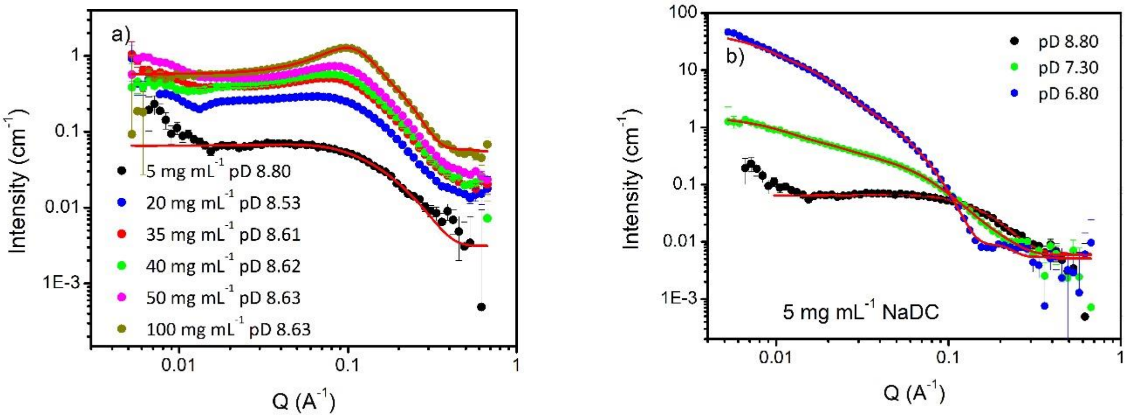

Figure 8. Small angle-neutron scattering data of NaDC as a function of: a) concentration, at pD 8.5 – 8.8 and b) pH, at 5 mg mL^{-1} concentration. The mathematical fittings are reported in the graph as red line.

Upon decreasing pH, the structure of 5 mg mL^{-1} NaDC micelles changed from a prolate ellipsoid (pD 8.80) to an elongated rod (pD 7.30) described by elliptical cylinders of 487.6 ± 21.2 Å length and 2.88 ± 0.19 axis ratio (Figure 8b and Table A2 in Appendix). By further decreasing pH, at the brink of NaDC aggregation and flocculation (pD 6.80), rods' dimensions increased reaching lengths of 630.5 ± 4.3 Å and axis ratio of 5.25 ± 0.012 with a concomitant reduction in SLD (Figure 8b and Table A2 in Appendix).

4.3.8.2 NaDC/water/ARGO7 liquid phase at pD 8.50-9.50

Once the shape of the micelles was assessed, 5 mg mL^{-1} of NaDC were mixed with 0.5 mg mL^{-1} solution of *D*-, or *L*-, or *D,L*-ARGO7, or an equimolar mixture obtained by mixing *L*- and *D*-isomer of the polymer (*D*-/*L*-ARGO7), to reach the total concentration of 0.5 mg mL^{-1}. Mixtures were prepared in the pD range of 8.50-9.50, conditions at which NaDC/water/ARGO7 systems resulted as transparent homogenous liquids (see phase boundaries in Figure 2, page 132). At this concentration the solutions of ARGO7 alone did not give rise to a significant scattering data, independently from the considered pH. Consequently, only modification of the NaDC behavior in the mixtures were assessed.

At pD 8.50 – 9.50, for all the stereoisomers, data resulted superimposable and were fitted with the same prolate ellipsoid model used for the NaDC/water system (Figure 9a). Thus, only small changes in the total charge and in the semi-minor and semi-major axis were seen (Table A3 in Appendix). These results confirmed the trend observed from CD measurements, that is the modest effect of the electrostatic interactions between ARGO7 stereoisomers and NaDC micelles, and the absence of chiral dependent interactions.

In order deeply investigate how the interactions in the NaDC/water/ARGO7 liquid mixtures may affect the conformation of NaDC micelles, it was chosen to change NaDC/*D*-polymer ratio (Figure 9b). When the NaDC/*D*-ARGO7 ratio reached 1:2, that is at 70 mg mL^{-1} of *D*-ARGO7 and 35 mg mL^{-1} NaDC, micelles changed from prolate to triaxial ellipsoid (Figure 9b and Table A4 in Appendix). Hence, the addition of the polymer changed the magnitude of NaDC hydrophobic forces, due to the complete charge neutralization of its carboxylate groups. At pD 8.40, ARGO7 average net charge per repeating units is slightly positive (+0.011), since the *tert*-amine groups were almost completely deprotonated and the remaining internally shielded by the carboxylate groups (see Chapter 2, page 56). The guanidine pendant remained positively charged. This coupled with the presence of carboxylate and amine groups, sources of hydrogen bonding, may unbalanced NaDC hydrophobic forces and thus change micelles structure. In conclusion, when NaDC/*D*-ARGO7 ratio reached 1:2, SANS data confirmed the existence of interactions between NaDC and *D*-ARGO7.

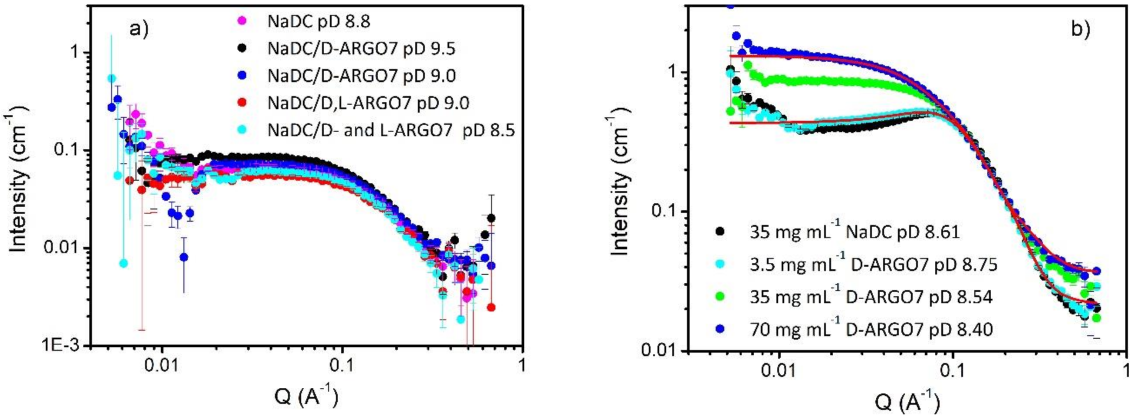

Figure 9. NaDC scattering data in presence of: a) *D*-, *L*-, *D,L*-ARGO7 and the equimolar mixture *D*-/*L*-ARGO7 and b) increasing concentration of *D*-ARGO7. Mathematical fittings were reported as red lines.

4.3.8.3 NaDC/water/ARGO7 gel phase at pD 7.30-7.50

Based on the results obtained from the CD spectra, further investigations were carried out in order to assess the possible chiral recognition by means of SANS measurements. Solutions were prepared with 5 mg mL^{-1} NaDC and 0.5 mg mL^{-1} of *D*-, *L*-, *D,L*-ARGO7 or an equimolar mixture obtained by mixing *L*- and *D*-isomer of the polymer (*D*-/*L*-ARGO7), to reach the total concentration of 0.5 mg

mL^{-1}. Mixtures were prepared in the pD range of 7.30-7.50, conditions at which NaDC/water/ARGO7 systems resulted as transparent gels (see phase boundaries in Figure 2, page 132).

SANS data confirmed that NaDC conformation was affected in different ways by the chirality of the polymer (Figure 10a). In particular, *D*-, *D,L*-ARGO7 and the equimolar mixture changed SANS pattern in the same way: they retained the rod-like structure of NaDC micelles as in the NaDC/water system, albeit with a lower axis ratio (1.51 ± 0.41) and a smaller SLD (Figure 10a and Table A5 in Appendix). Instead, in the case of NaDC/water/*L*-ARGO7 mixture, the correlation length model used to describe shape independent functions was chosen in order to fit SANS curve (Figure 10a and Table A6 in Appendix).

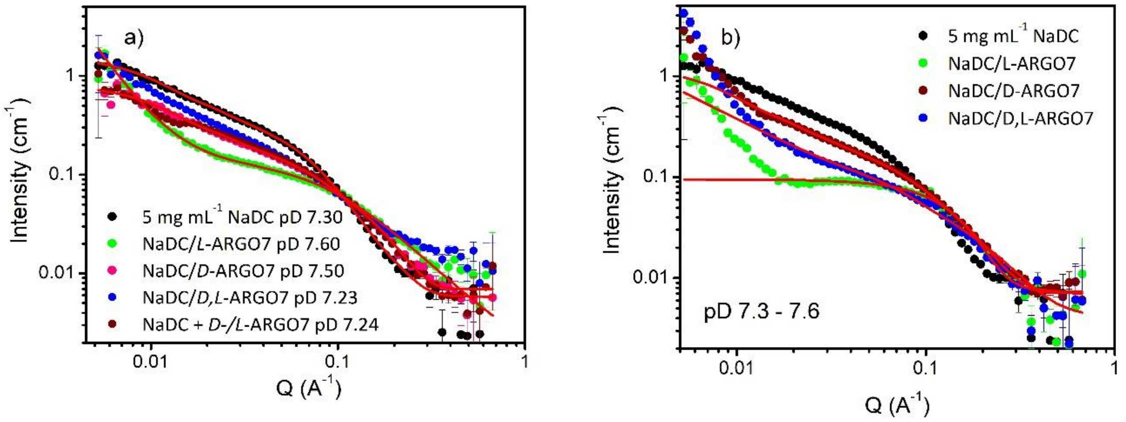

Figure 10. 5 mg mL^{-1} NaDC scattering data: a) in a mixture with 0.5 mg mL^{-1} *D*-, *L*-, *D,L*-ARGO7 and the equimolar *D*-/*L*-ARGO7 and b) in a mixture with higher M_n *D*-, *L*- and *D,L*-ARGO7. Mathematical fittings were reported as red lines.

In order to study if and how the length of the ARGO7 chains may affect the chiral-dependent NaDC self-structuring, chiral interactions were assessed in the NaDC/water/ARGO7 mixtures prepared with ARGO7 stereoisomers with higher number-average molecular weights, $M_{n\ D\text{-ARGO7}} = 8400$, $M_{n\ L\text{-ARGO7}} = 10600$ and $M_{n\ D,L\text{-ARGO7}} = 8800$ (Figure 10b and Table A7-8 in Appendix). The addition of *L*-ARGO7 triggered the conformational change of NaDC micelles from ellipsoidal cylinder to ellipsoids with 8.73 ± 1.34 Å polar radii and 17.71 ± 0.51 Å equatorial radii, and a significant low charge (Table A8 in Appendix). Instead, *D*- and *D,L*-ARGO7 retained the NaDC rod-like structures, albeit with higher dimensions and lower SLD than NaDC/water (Table A7). These results suggested that chirality and length of the polymer chain affected NaDC conformation in aqueous solution. Thus, it is possible to conclude that NaDC is a suitable model for the chiral recognition of ARGO7 stereoisomers.

SANS collected in the 5 – 100 mg mL^{-1} range on NaDC/water systems at pD 7.3-7.5 showed concentration-dependent structuring of NaDC. When NaDC concentration was lower than 35 mg mL^{-1} SANS pattern were always described by the elliptical cylinder model (Figure 11a).

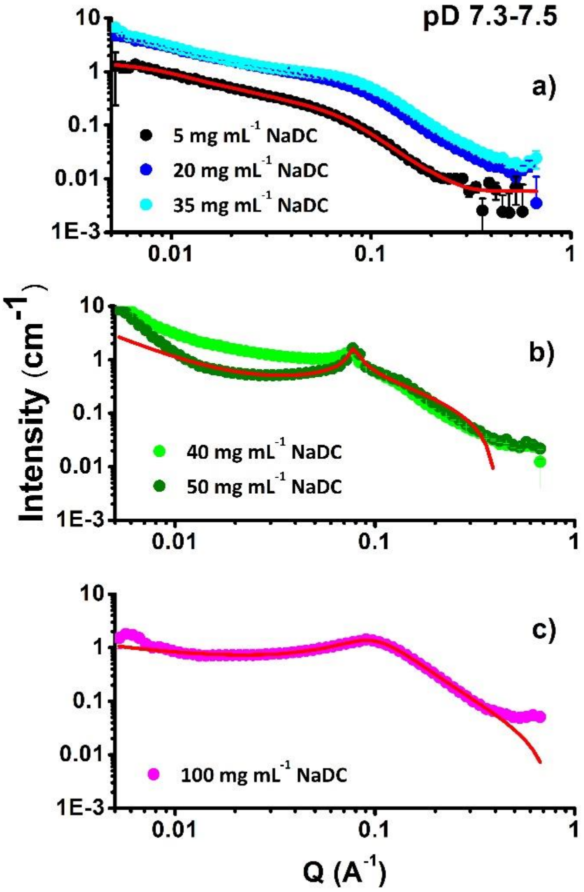

Figure 11. NaDC scattering data as a function of concentration, at pD 7.3 – 7.5. Mathematical fittings were reported as red lines.

Interestingly, when the concentration was 40 and 50 mg mL^{-1}, NaDC showed a layered structure with a peak centered at 0.07 Å^{-1} (Figure 11b). Their SANS patterns were described by the broad peak mathematical model, with a Porod's exponent of 0.9 for 40 mg mL^{-1} and 1.6 for 50 mg mL^{-1}. These values suggested a layered structure composed of stacked rigid rods. The d-spacing describing the distance between scattering centers was calculated as Q = 2π/d and resulted of 8.97 nm. The same layered structure can still be seen at 100 mg mL^{-1} (Figure 11c). However, at this concentration the sharp peak was lost suggesting a more amorphous material than the lowest concentrations. To assess the influence of ARGO7 stereoisomers on NaDC layered structure, SANS data were collected for NaDC/water/ARGO7 mixtures prepared with 5 mg mL^{-1} of *L*-, *D*-, *D,L*-ARGO7 and an equimolar mixture of *D*- and *L*-ARGO7 and 50 mg mL^{-1} NaDC solution at pD 7.5 – 7.6. SANS measurements did not show any difference (Figure 12), excluding as such interactions of any nature between ARGO7 polymers and NaDC, in these conditions.

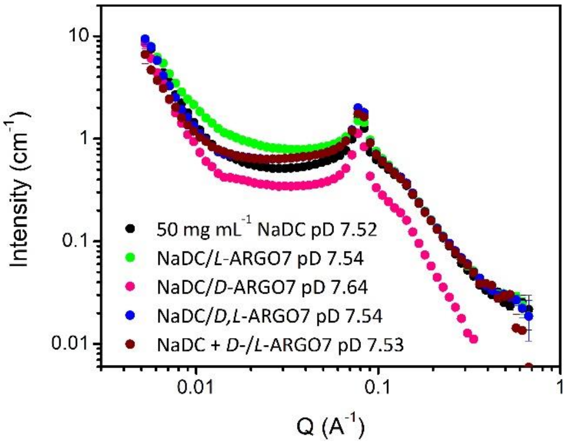

Figure 12. Scattering data recorded for 50 mg mL^{-1} NaDC solutions mixed with 5 mg mL^{-1} of *D*-, *L*-, *D,L*-ARGO7 and the equimolar mixture *D*-/*L*-ARGO7, at pD 7.5 – 7.6.

4.3.8.4 NaDC/water/ARGO7 heterogeneous phase at pD 6.40-6.90

To assess the pH-dependence of the chiral interactions, SANS measurements were carried out at pD 6.40-6.90, when NaDC/water and NaDC/water/ARGO7 systems appeared as heterogeneous mixtures (precipitate), due to NaDC flocculation (see phase boundaries in Figure 2, page 132). Samples were prepared mixing 5 mg mL^{-1} NaDC solutions and 0.5 mg mL^{-1} of *D*-, *L*-, *D,L*-ARGO7 or an equimolar mixture composed of 0.5 mg mL^{-1} *D*-ARGO7 and 0.5 mg mL^{-1} *L*-ARGO7. Diffraction pattern showed the same behaviour of NaDC/water/ARGO7 gels (Figure 12). *D*-, *D,L*-ARGO7 and the equimolar mixture gave rise to superimposable pattern, modelled by the elliptical cylinder model with higher lengths and SLD, and smaller axis ratios and charge than NaDC/water at the same pD (Figure 12 and Table A9 in Appendix). Instead, *L*-ARGO7 triggered the formation of spheroidal NaDC clusters, represented by the correlation length function used to fit the scattering data (Figure 12 and Table A10 in Appendix). In these conditions, changes induced by the presence of ARGO7 stereoisomers were linked to their chirality and the overall ionization degree of the polymer chains. At pD 6.8, 30% of ARGO7 chains resulted positively charged, while the remaining 70% were in their zwitterionic form, capable to induce H-bonding. Electrostatic interactions between ARGO7 chains and NaDC neutralized NaDC carboxylate groups at higher pH than NaDC/water alone and resulted in longer rods. Once the charge was neutralized, NaDC micelles packed together by hydrophobic forces, whose magnitude and orientation were affected by the chirality of the polymer, as stated by SANS modified pattern.

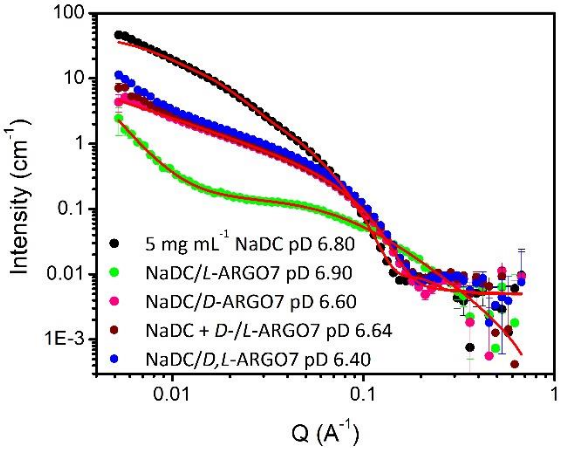

Figure 12. 5 mg mL^{-1} NaDC scattering data in presence of 0.5 mg mL^{-1} *D*-, *L*-, *D,L*-ARGO7 and the equimolar mixture *D*-/*L*-ARGO7, at pD 6.40-6.90. Mathematical fittings were reported as red lines.

4.4 CONCLUSIONS

Sodium deoxycholate (NaDC), one of the components of bile salts, was chosen as a chiral model surface to detect chiral interactions with ARGO7 stereoisomers. In order to characterize the model system and choose the optimum conditions to be used later for chirality-dependent interactions studies, surface tension, dynamic light scattering, ζ-potential, pulsed-gradient spin echo NMR measurements were first carried out on NaDC/water and NaDC/water/*L*-ARGO7 mixtures.

Results for NaDC/water systems indicated a concentration- and pH-dependent solubility in 0.1 M NaCl. At NaDC concentration > 2.5 mg mL^{-1}, NaDC showed three phases: homogenous solution (pH ≥ 7.50), gel phase (pH 7.0 – 7.5), flocculation and aggregation (pH ≤ 7.00), whereas below 2.5 mg mL^{-1} only two phases were seen: homogenous solution (pH ≥ 6.50) and precipitation (pH 6.00). The same phases were seen even in the presence of 0.5 wt % ARGO7 stereoisomers, with some differences in the pH that induced the phase transitions, likely due to the chirality of the polymer. From surface tension measurements, the CMC of NaDC/water at pH 8.63 ± 0.47 in 0.1 M NaCl resulted of 0.802 mg mL^{-1}, value that did not change in presence of 0.5 wt % of *L*-ARGO7. The ζ-potential measurements indicated the NaDC/*L*-ARGO7 ratio of 10:1 was the best in order to minimize electrostatic interactions. Hence mixtures were prepared with 5 mg mL^{-1} NaDC and 0.5 mg mL^{-1} ARGO7 polymers. DLS and PGSE-NMR recorded 1.8-2.1 nm for plain *D*- and *L*-ARGO7, regardless of concentration and pH, and increasing size from 1.20 to 3.53 nm for plain NaDC, in the concentration range 5 – 50 mg mL^{-1}. Radii of NaDC were not affected by the presence of *L*-ARGO7.

In order to study chiral recognition, measurements of circular dichroism and small-angle neutron scattering were carried out on NaDC/water and NaDC/water/ARGO7 mixtures. Circular dichroism spectra recorded at pD 9.06 did not show any sign of chiral discrimination, since the presence of NaDC did not result in any significant modification of the polymers' CD spectra, in either *L*- or *D*-form. At pD 7.30, when NaDC/water/ARGO7 mixtures appeared as gels, spectra of NaDC showed CD pattern differently affected by presence of *L*- or *D*-ARGO7, indicating that the self-reorganization of NaDC into an ordered gel triggered the chiral recognition of the different stereoisomers. Morphology of NaDC micelles in presence and absence of ARGO7 stereoisomers was deeply studied by SANS analyses. Concentration-dependent data collected for NaDC at pD 8.5 - 8.8 were consistent with the presence of micelles, described by prolate ellipsoids. By decreasing pH, NaDC micelles' conformation changed to elongated rods. Coherently with CD measurements, at pD 8.5, NaDC/water/ARGO7 stereoisomers mixtures showed superimposable curves, indicating absence of chiral discrimination, whereas at pD 7.30-7.50, NaDC conformation was differently affected by the chirality of the polymer. In particular, *D*- and *D,L*-ARGO7 changed SANS pattern in the same way, retaining the rod-like structure of NaDC micelles, whereas *L*-ARGO7 seemed able to trigger the formation of NaDC ellipsoidal clusters. The same chiral-dependent interactions were observed at pD 6.40-6.90, at the onset of flocculation, and at pD 7.50 for higher M_n ARGO7 polymers.

It can be concluded that *D*- and *L*-ARGO7 are able to selectively interact, based on their chirality, with NaDC micelles. This coupled with their already proved cytobiocompatibility and cell-internalization, may open the way for intracellular selective drug targeting or delivery of bioactive entitites (proteins, liposomes and nucleotides to name a few).

4.5 REFERENCES

1. Mukhopadhyay, S.; Maitra, U. Chemistry and biology of bile acids, *Curr. Sci.* **2004**, *87*, 1666,
2. Holm, R.; Müllertz, A.; Mub, H. Bile salts and their importance for drug absorption, *Int. J. Pharm.* **2013**, *453*, 44, doi: 10.1016/j.ijpharm.2013.04.003.

3. Wiedmann, T.S.; Liang, W.; Kamel, L. Solubilization of drugs by physiological mixtures of bile salts, *Pharm. Res.* **2002**, *19*, 1203, DOI: 10.1023/a:1019858428449

4. Zhao, Y.; Facial amphiphiles in molecular recognition: from unusual aggregates to solvophobically driven foldamers, *Curr. Opin. Colloid Interface Sci.* **2007**, *12*, 92, DOI: 10.1023/a:1019858428449.

5. Galantini, L.; di Gregorio, M. C.; Gubitosi, M.; Travaglini, L.; Tato, J. V.; Jover, A.; Meijide, F.; Tellini, V. H. S.; Pavel, N. V. Bile salts and derivatives: rigid unconventional amphiphiles as dispersants, carriers and superstructure building blocks *Curr. Opin. Colloid Interface Sci.* **2015**, *20*, 170, DOI: 10.1016/j.cocis.2015.08.004.

6. Qiao, Y.; Lin, Y.; Yang, Z.; Chen, H.; Zhang, S.; Yan, Y.; Huang, J. Unique temperature-dependent supramolecular self-assembly: from hierarchical 1D nanostructures to super hydrogel. *J. Phys. Chem. B* **2010**, *114*, 11725, https://doi.org/10.1021/jp1047369.

7. Terech, P.; Jean, B.; Ne, F. Hexagonally ordered ammonium lithocholate self-assembled nanotubes with highly monodisperse sections. *Adv. Mater.* **2006**, *18*, 1571, DOI: 10.1002/adma.200502358.

8. Wang, H.; Xu, W.; Song, S.; Feng, L.; Song, A.; Hao, J. Hydrogels facilitated by monovalent cations and their use as efficient dye adsorbents. *J. Phys. Chem. B* **2014**, *118*, 4693, doi: 10.1021/jp500113h.

9. Madenci, D.; Egelhaaf, S.U. Self-assembly in aqueous bile salt solutions, *Curr. Opin. Colloid Interface Sci.* **2010**, *15*, 109, https://doi.org/10.1016/j.cocis.2009.11.010.

10. Singh, J.; Unlu, Z.; Ranganathan, R. Aggregate properties of sodium deoxycholate and dimyristoylphosphatidylcholine mixed micelles, *J. Phys. Chem* **2008**, *112*, 3997, https://doi.org/10.1021/jp077380w.

11. Kiselev, M.A.; Janich, M.; Hildebrand, A.; Strunz, P.; Neubert, R.H.H.; Lombardo, D. Structural transition in aqueous lipid/bile salt [DPPC/NaDC] supramolecular aggregates: SANS and DLS study, *Chem. Phys.* **2013**, *424*, 93, DOI: 10.1016/j.chemphys.2013.05.014.

12. Mangiapia, G.; D'Errico, G.; Capuano, F.; Ortona, O.; Heenan, R.K.; Paduano, L.; Sartorio, R. On the interpretation of transport properties of sodium cholate and sodium deoxycholate in binary and ternary aqueous mixtures, *Phys. Chem. Chem. Phys*. **2011**, *13*, 15906, DOI: 10.1039/C1CP20922A.

13. Lopez, F.; Samseth, J.; Mortensen, K.; Rosenqvist, E.; Rouch, J. Micro- and Macrostructural studies of sodium deoxycholate micellar complexes in aqueous solutions, *Langmuir* **1996**, *12,* 6188, https://doi.org/10.1021/la960006v.

14. Blow, D. M.; Rich, A. Studies on the formation of helical deoxycholate complexes, *J. Am. Chem. Soc.* **1960**, *82*, 3566, https://doi.org/10.1021/ja01499a023.

15. Jover, A.; Meijide, F.; Rodríguez Núñez, E.; Vázquez Tato, J. Aggregation kinetics of sodium deoxycholate in aqueous solution, *Langmuir* **1998**, 14, 4359, https://doi.org/10.1021/la9712754.

16. Zhang, S.; Xie, J.; Liu, C. Microenvironmental properties and chiral discrimination abilities of bile salt micelles by fluorescence probe technique, *Anal. Chem.* **2003**, *75*, 91, DOI: 10.1021/ac020373d.

17. Clothier, J.G. Jr; Daley, L.M.; Tomellini, S.A. Effects of bile salt structure on chiral separations with mixed micelles of bile salts and polyoxyethylene ethers using micellar electrokinetic capillary chromatography, *J. Chromatogr. B* **1996**, *683*, 37, DOI: 10.1016/0378-4347(96)00174-0.

18. Nishi, H.; Fukuyama, T.; Matsuo, M; Terabe, S. Chiral separation of diltiazem, trimetoquinol and related compounds by micellar electrokinetic chromatography with bile salts, *J. Chromatogr. A* **1990**, *515*, 233, DOI: 10.1016/s0021-9673(01)89318-3.

19. Cole, R.O.; Sepaniak, M.J.; Hinze, W. L. Optimization of binaphthyl enantiomer separations by capillary zone electrophoresis using mobile phases containing bile salts and organic solvent, *J. High Resolut. Chromatogr.* **1990**, *13*, 579, https://doi.org/10.1002/jhrc.1240130814.

20. McNeel, K.E.; Siraj, N.; Negulescu, I.; Warner, I. M.; Sodium deoxycholate/TRIS-based hydrogels for multipurpose solute delivery vehicles: ambient release, drug release, and enantiopreferential release, *Talanta* **2018**, *177*, 66, doi: 10.1016/j.talanta.2017.09.025.

21. Hildebrand, A.; Garidel, P.; Neubert, R.; Blume, A. Thermodynamics of demicellization of mixed micelles composed of sodium oleate and bile salts, *Langmuir* 2004, *20*, 320, https://doi.org/10.1021/la035526m.

22. Nasrollahi, P.; Khajeh, K.; Tamjid, E.; Taleb, M.; Soleimani, M.; Nie, G. Sustained release of sodium deoxycholate from PLGA–PEG–PLGA thermosensitive polymer, *Artificial Cells, Nanomedicine, and Biotechnology* **2018**, *46*, 1170, DOI: 10.1080/21691401.2018.1481861.

23. Guo, Y.; Wang, R.; Shang, Y.; Liu, H. Effects of polymers on the properties of hydrogels constructed using sodium deoxycholate and amino acid, *RSC Adv.* **2018**, 8, 8699, DOI: 10.1039/C8RA00171E.

24. Avranas, A.; Tasopoulos, V. Aqueous solutions of sodium deoxycholate and hydroxypropylmethylcellulose: dynamic surface tension measurements, *J. Colloid Interface Sci.* **2000**, *221*, 223, https://doi.org/10.1006/jcis.1999.6574.

25. Stilbs P., Paulsen K., Griffiths P. C. Global least-squares analysis of large, correlated spectral data sets: application to component-resolved FT-PGSE NMR spectroscopy, *J. Phys. Chem.* **1996**, 100, 8180, https://doi.org/10.1021/jp9535607.

26. Claridge, High-resolution NMR techniques in organic chemistry, second ed., Elsevier, Oxford, UK, **2009**.

27. Vold, R.D.; McBain, J.W. The solubility curve of sodium deoxycholate in water, *J. Am. Chem. Soc.* **1941**, *63*, 1296, https://doi.org/10.1021/ja01850a043.

28. Garidel, P.; Hildebrand, A.; Neubert, R.; Blume, A. Thermodynamic characterization of bile salt aggregation as a function of temperature and ionic strength using isothermal titration calorimetry. *Langmuir* 2000, 16, 5267, https://doi.org/10.1021/la9912390.

29. Roda, A.; Hofmann, A.F.; Mysels, K.J. The influence of bile salt structure on self-association in aqueous solutions. *J. Biol. Chem.* **1983**, 258, 6362.

30. Small, D.M. Size and structure of bile salt micelles: influence of structure, concentration, counterion concentration, pH and temperature. Goddard ED, editor. Adv. Chem. Ser., vol. 84, Chapter 4. New York: Plenum Press; **1968**. p. 31–42.

31. Reis, S.; Moutinho C.G.; Matos, C.; de Castro, B.; Gameiro, P.; Lima J.L. Noninvasive methods to determine the critical micelle concentration of some bile acid salts. *Anal. Biochem.* **2004**, 334, 117, DOI: 10.1016/j.ab.2004.07.017.

32. Singh, J.; Unlu, Z.; Ranganathan, R.; Griffiths, P.C. Aggregate properties of sodium deoxycholate and dimyristoylphosphatidylcholine mixed micelles, *J. Phys. Chem. B* **2008**, *112*, 3997, https://doi.org/10.1021/jp077380w.

4.6 APPENDIX

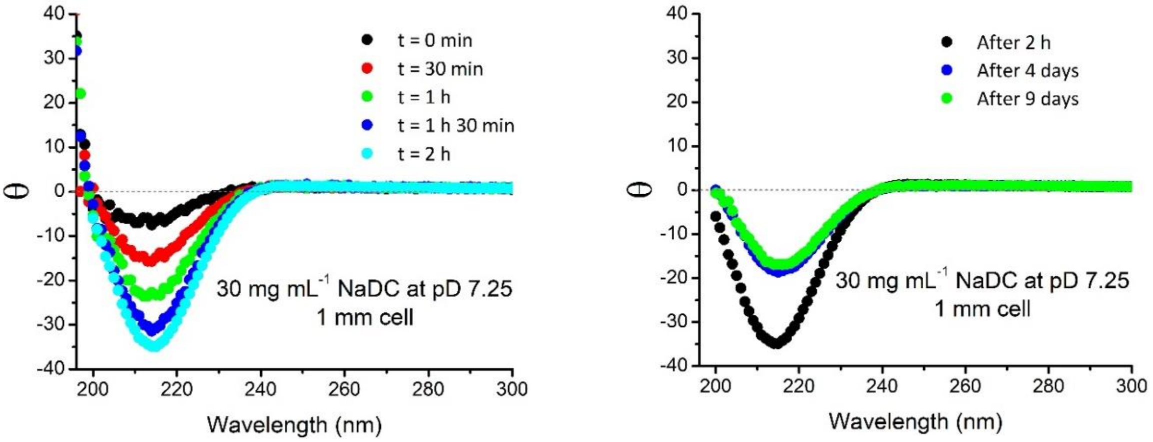

Figure A1. CD spectra of 30 mg mL^{-1} NaDC/water systems in 0.1 M NaCl and pH 7.30 as a function of time.

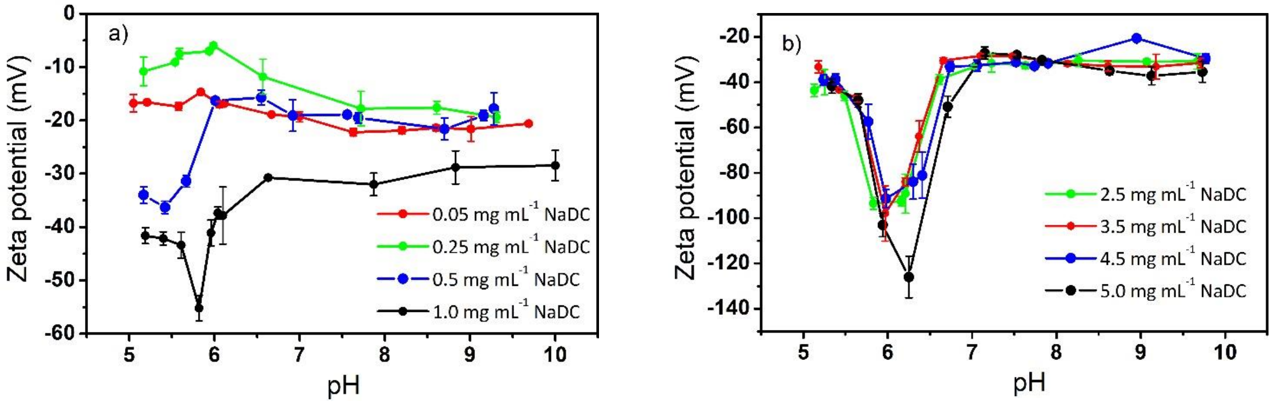

Figure A2. NaDC/water mixtures trend of ζ-values with pH and a) NaDC concentration between 0.05 – 1.0 mg mL^{-1} and b) NaDC concentration between 2.5 – 5.0 mg mL^{-1}. Data were collected in 0.1 M NaCl.

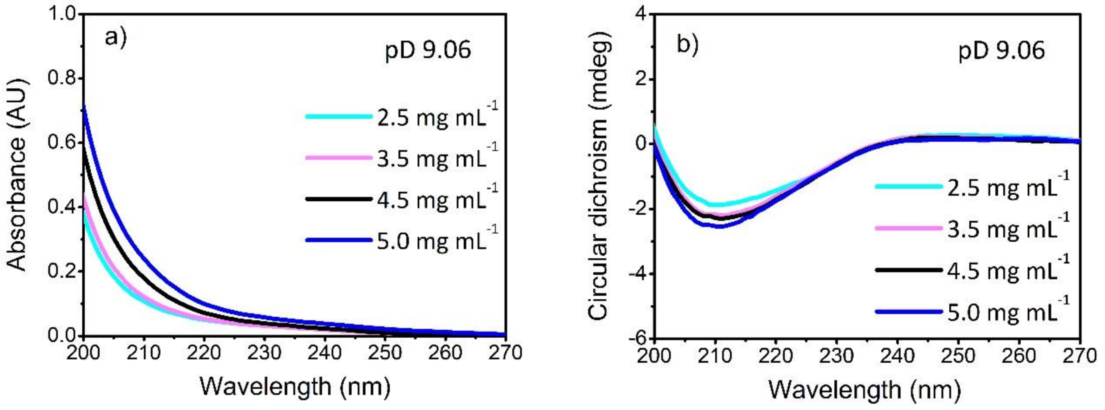

Figure A3. Concentration-dependence of a) UV-vis and b) CD spectra of NaDC/water systems, recorded at pD 9.06 in quartz-cell of 1 mm path length.

Table A1. Parameters obtained for NaDC/water as a function of concentration, using the hydrated ellipsoid mathematical model: scattering light density (SLD), polar and equatorial radii and charge. All values had a S.D. lower than 1 %.

C_{NaDC} (mg mL^{-1})	SLD (10^{-6} Å^{-2})	R_{polar} (Å)	$R_{equatorial}$ (Å)	Charge (e)
5	1.50	22.67	7.96	24.30
20	2.24	23.47	10.45	15.48
35	2.17	24.81	10.44	14.41
40	2.20	25.47	10.44	14.77
50	1.69	24.64	7.26	13.37
100	2.10	28.25	9.97	12.95

Table A2. pH-Dependent parameters obtained for NaDC/water systems using the hydrated ellipsoid and the hydrated elliptical cylinder mathematical model: scattering light density (SLD), radii and charge. All values had a S.D. lower than 1 %.

pD	Mathematical Model	SLD (10^{-6} Å^{-2})	R_{minor} (Å)	Axis ratio	Length (Å)	R_{polar} (Å)	$R_{equatorial}$ (Å)	Charge (e)
8.80	Hydrated Ellipsoid	1.50	---	---	---	22.67	7.96	24.30
7.30	Hydrated Elliptical Cylinder	3.87	8.36	2.98	482.82	---	---	53.31
6.80	Hydrated Elliptical Cylinder	1.42	22.94	5.26	630.49	---	---	60.78

Table A3. Parameters obtained for 5 mg mL^{-1} NaDC at pD 8.50-9.50 in presence of the polymers (*D*-, *L*-, *D,L*-ARGO7 and the equimolar mixture *D*-/*L*-ARGO7) using the hydrated ellipsoid mathematical model: scattering light density (SLD), polar and equatorial radii and charge. All values had a S.D. lower than 1 %.

C_{NaDC} (mg mL^{-1})	Polymers	C_{ARGO7} (mg mL^{-1})	SLD (10^{-6} Å^{-2})	R_{polar} (Å)	$R_{equatorial}$ (Å)	Charge (e)
5	*D*-ARGO7	0.5	1.60	29.36	6.08	11.19
5	*L*-ARGO7	0.5	1.34	23.24	8.07	22.96
5	*D,L*-ARGO7	0.5	2.40	22.29	8.48	17.06
5	*D*-/*L*-ARGO7	0.5	2.48	21.62	9.30	25.13

Table A4. Parameters obtained for 35 mg mL^{-1} NaDC at pD 8.50-9.50 in presence of 3.5, 35 or 70 mg mL^{-1} *D*-ARGO7: scattering light density (SLD), polar and equatorial radii and charge. All values had a S.D. lower than 1 %.

C_{NaDC} (mg mL^{-1})	$C_{D\text{-}ARGO7}$ (mg mL^{-1})	Mathematical Model	SLD (10^{-6} Å^{-2})	R_{polar} (Å)	$R_{equatorial\ minor}$ (Å)	$R_{equatorial\ major}$ (Å)*	Charge (e)
35	--	Hydrated Ellipsoid	1.85	22.00		8.50	14.00
35	3.5	Hydrated Ellipsoid	2.12	28.16		7.79	12.12
35	35	Hydrated Ellipsoid	3.50	44.38		5.48	3.69
35	70	Hydrated Triaxial Ellipsoid	3.53	5.39	51.87	29.66	0.001

* Defined as equatorial major radius in hydrated triaxial ellipsoids, whereas it is defined as equatorial radius in ellipsoid.

Table A5. Parameters obtained for 5 mg mL^{-1} NaDC solutions at pD 7.30-7.50 mixed with 0.5 mg mL^{-1} of *D*-, *D,L*-ARGO7 and the equimolar mixture *D*-/*L*-ARGO7 using the hydrated elliptical cylinder mathematical model: scattering light density (SLD), radius minor, axis ratio, length and charge. All values had a S.D. lower than 1 %.

Solutions	SLD (10^{-6} Å^{-2})	R_{minor} (Å)	Axis ratio	Length (Å)	Charge (e)
NaDC	3.87	8.36	2.98	482.82	53.31
NaDC/*D*-ARGO7	3.65	7.97	1.51	438.69	42.25
NaDC/*D,L*-ARGO7	3.32	4.29	4.96	1992.5	19.70
NaDC/*D*-/*L*-ARGO7	3.60	10.47	1.02	539.46	65.23

Table A6. Parameters obtained for 5 mg mL^{-1} NaDC/water/*L*-ARGO7 system at pD 7.30-7.50 using the shape independent mathematical function: correlation length, Porod exponent and Lorentz exponent. All values had a S.D. lower than 1 %.

Solutions	Correlation length (Å)	Porod's Exponent	Lorentz's Exponent (Å^{-2})
NaDC/*L*-ARGO7	10.62	2.73	1.95

Table A7. Parameters obtained for 5 mg mL^{-1} NaDC at pD 7.30-7.60 in presence of higher M_n *D*-, *L*-, *D,L*-ARGO7 and the equimolar mixture *D*-/*L*-ARGO7, using the hydrated elliptical cylinder mathematical model: scattering light density (SLD), radius minor, axis ratio, length and charge. All values had a S.D. lower than 1 %.

Solutions	**SLD (10^{-6} Å^{-2})**	**R_{minor} (Å)**	**Axis ratio**	**Length (Å)**	**Charge (e)**
NaDC	3.87	8.36	2.98	482.82	53.31
NaDC/*D*-ARGO7	2.14	6.90	1.84	586.81	34.75
NaDC/*D,L*-ARGO7	0.560	3.44	2.40	1908.9	50.71
NaDC/*D*-/*L*-ARGO7	3.15	5.94	3.68	2557.4	22.26

Table A8. Parameters obtained for NaDC/water/*L*-ARGO7 (higher M_n) mixture, at pD 7.3 – 7.6 using the hydrated ellipsoid mathematical model: scattering light density (SLD), polar and equatorial radii and charge. All values had a S.D. lower than 1 %.

Solutions	**SLD (10^{-6} Å^{-2})**	**R_{polar} (Å)**	**$R_{equatorial}$ (Å)**	**Charge (e)**
NaDC/*L*-ARGO7	2.54	8.73	17.71	4.85E-4

Table A9. Parameters obtained for 5 mg mL^{-1} NaDC at pD 6.6 – 6.9 in presence of *D*-, *D,L*-ARGO7 and the equimolar mixture *D*-/*L*-ARGO7, using the hydrated elliptical cylinder mathematical model: scattering light density (SLD), radius minor, axis ratio, length and charge. All values had a S.D. lower than 1 %.

Solutions	**SLD (10^{-6} Å^{-2})**	**R_{minor} (Å)**	**Axis ratio**	**Length (Å)**	**Charge (e)**
NaDC	1.42	22.94	5.26	630.49	60.78
NaDC/*D*-ARGO7	2.73	15.42	1.65	2364.7	10.02
NaDC/*D,L*-ARGO7	2.34	16.19	1.51	4027.4	3.67
NaDC/*D*-/*L*-ARGO7	2.67	15.69	1.53	12044	5.04

Table A10. Parameters obtained for NaDC/water/*L*-ARGO7 mixture, at pD 6.6 – 6.9, using the shape independent mathematical function: correlation length, Porod exponent and Lorentz exponent. All values had a S.D. lower than 1 %.

Solutions	**Correlation length (Å)**	**Porod's Exponent**	**Lorentz's Exponent (Å^{-2})**
NaDC/*L*-ARGO7	12.94	3.50	2.19

CONCLUSIONS

Different types of amino-acid deriving polymers, of the polyamidoamino acids family (PAACs), were synthesized by the stepwise Michael-type polyaddition of natural α-amino acids, and their stereoisomers, to *N,N'*-methylenebisacrylamides (MBA). Reactions were carried out in water, at 50°C and pH > 9 for 6 days. Differently from synthetic polymers obtained by radical polymerization of modified α-amino acids, PAACs retain the acid-base properties and the chirality of the parent amino acids.

The PAACs synthesized in this work can be classified based on the structural features of the α-amino acid residue: arginine derived PAACs (ARGO7), alkyl-substituted PAACs (M-*L*-Ala, M-*L*-Val, M-*L*-Leu), glutamine-derived PAAC (M-*L*-Gln), homo and copolymeric L-tryptophan-based PAACs (M-*L*-Trp and M-G-*L*-Trp).

i) Arginine-based PAACs

Cationic arginine-based PAACs were synthesized from the addition of *L*-arginine (*L*-ARGO7), *D*-arginine (*D*-ARGO7) and *D,L*-arginine (*D,L*-ARGO7). Acid-base properties were determined and showed a modest polyelectrolyte effect. Differently from common synthetic polyelectrolyte, pK_{a1} associated to -COOH/COO- equilibria decreased with increasing ionization degree, ascribed to the formation of inter-polyelectrolyte complexes. Circular dichroism spectroscopy indicated that *L*- and *D*-ARGO7 polymers were able to self-assemble in water into stable pH-dependent conformations, with mirror-image spectra. Differential molar ellipticity were reported as a function of pH, describing a sigmoidal curve affected by the ionization degree of the *tert*-amine groups in the main chains. Conformational changes induced by pH and temperature were quickly achieved and fully reversible. In addition, ARGO7 conformations resulted stable at ionic strength up to 2 M and presence of denaturating agents as guanidinium chloride and urea. Molecular dynamics studies carried out at Politecnico di Milano (Prof. Raffaini and Prof. Ganazzoli) revealed ARGO7 had a compact hairpin-like conformation (R_g 0.8-1.11 nm) whose main chain was organized into a transoid arrangement. These pH-dependent structures were held together by intramolecular interactions of electrostatic nature.

ii) Alkyl-based PAACs

Hydrophobic alkyl-substituted PAACs were synthesized from *L*-alanine (M-*L*-Ala), *L*-valine (M-*L*-Val) and *L*-leucine (M-*L*-Leu). Acid-base properties, self-structuring abilities and size in solutions indicated results comparable with ARGO7 polymers, with minor differences due to the amino acid side chain. Circular dichroism spectroscopy confirmed the formation of stable self-assembled structures, rapidly formed and interconverted with pH. Differently from ARGO7, these conformations were affected by the presence of guanidinium chloride. DLS measurements indicated R_hs stable for at least 1 month (25°C), unaffected by increasing concentration in the 0.5-20 mg mL^{-1} range, associated with the formation of intramolecularly self-assembled single chain nanoparticles. Molecular dynamics studies showed compact structure dictated mainly by intramolecular interactions in the polymer main chain, with minor dependence from the amino acids side chains.

iii) Glutamine-based PAACs

Polar glutamine-based PAAC was obtained from *L*-glutamine (M-*L*-Gln). Differently from the other PAACs, molecular dynamics showed a higher number of H-bonding, both along the main chain and the glutamine residues, responsible for the higher M_n and R_h recorded. Variable temperature NMR indicated that the side-chain amides groups were mainly involved in the formation of H-bonding, and they were as such responsible of the M-*L*-Gln stable conformation. Circular dichroism spectroscopy showed pH-dependent self-assembled structures, sensitive to the presence of urea, with time dependent spectral variations.

iv) Tryptophan-based PAACs

Amphipathic tryptophan-based homo- and copolymer were synthesized by Michael-type polyaddition of MBA with *L*-tryptophan, its isomer, and different molar ratio of *L*-tryptophan/glycine mixtures. They all showed composition- and pH-dependent solubility. Hydrodynamic radii resulted stable for at least 1 month, and unaffected by pH in the range 1–11 for M-G-*L*-Trp$_5$, M-G-*L*-Trp$_{10}$ and M-G-*L*-Trp$_{20}$ and pH range 7–11 for M-G-*L*-Trp$_{40}$ and M-*L*-Trp homopolymers. Tryptophan-based copolymers showed R_hs modestly affected by pH and tryptophan content, whereas they resulted sensitive to concentration in the range 1–30 mg·mL^{-1}. Similarly to the other PAACs, all tryptophan-based homo- and copolymers gave rise to pH dependent CD spectra, ascribed to their ability to self-assemble into stable structures governed by the main chain average ionization degree. Photoluminescence analyses, quantum yields, steady state and time-resolved fluorescence measurements, resulted governed solely by tryptophan photo physics. Both homo and copolymers showed pH-dependent quantum yields, lifetimes and emission maximum. Interestingly, fluorescence studies conducted on oxygen-free solution gave comparable results, indicating compact conformations where L-tryptophan moieties were not accessible to the quencher. Also, intermolecular quenching by approaching chains was evaluated and observed in M-*L*-Trp and M-G-*L*-Trp_{10}.

v) Chiral interactions in NaDC/water/ARGO7 mixtures

Sodium deoxycholate (NaDC), one of the components of bile salts, was chosen as a chiral model surface to detect chiral interactions with ARGO7 stereoisomers. In order to study chiral recognition, circular dichroism spectroscopy and small-angle neutron scattering were carried out on NaDC/water and NaDC/water/ARGO7 mixtures. Circular dichroism spectra were recorded at pD 9.06 and 7.30. Results indicated sign of chiral recognition only at pD 7.30, when NaDC/water/ARGO7 mixtures appeared as transparent gels. In fact, at pD 7.30, NaDC spectral pattern were modified in different ways by the presence of *L*- or *D*-ARGO7, whereas at pD 9.06, no significant modification of the CD spectra was recorded. This behavior indicated that the self-reorganization of NaDC into an ordered gel may trigger the chiral recognition of the different stereoisomers. Small angle neutron scattering was then performed to evaluate the changes in NaDC micelles morphology in presence of *L*- or *D*-ARGO7. At pD 8.5, SANS data collected in the 5 – 100 mg mL^{-1} NaDC concentration range were consistent with the presence of micelles, described by prolate ellipsoids. As expected from CD measurements, in these conditions NaDC/water/ARGO7 stereoisomers mixtures showed superimposable curves, described by the same mathematical model used for NaDC/water system, indicating absence of chiral discrimination. The conformation of NaDC micelles changed from prolate ellipsoids to elongated rods when pH was decreased. At pD 7.50, SANS data showed scattering curves differently affected by the presence of the ARGO7 stereoisomers. In particular, *D*- and *D,L*-ARGO7 changed SANS pattern in the same way, retaining the rod-like structure of NaDC micelles, whereas *L*-ARGO7 triggered the formation of NaDC ellipsoidal clusters. The same modification of the scattering pattern were observed even at pD 6.90, at the onset of NaDC flocculation.

In conclusion, results indicated PAACs showed potential for biotechnological applications due to their pH- and composition responsiveness, intermolecular self-assemble ability into compact nanostructures, fluorescent dependent properties, selective chiral interactions with biomolecules, opening the way for intracellular selective drug targeting or delivery of bioactive entities.